DYNAMIC MECHANICAL BEHAVIOR AND HIGH PRESSURE PHASE STABILITY OF A ZIRCONIUM-BASED BULK METALLIC GLASS AND ITS COMPOSITE WITH TUNGSTEN

A Thesis
Presented to
The Academic Faculty

by

Morgana Martin

In Partial Fulfillment
of the Requirements for the Degree
Doctor of Philosophy

School of Materials Science and Engineering
Georgia Institute of Technology
May 2008

DYNAMIC MECHANICAL BEHAVIOR AND HIGH PRESSURE PHASE STABILITY OF A ZIRCONIUM-BASED BULK METALLIC GLASS AND ITS COMPOSITE WITH TUNGSTEN

Approved by:

Professor Naresh N. Thadhani
Materials Science and Engineering
Georgia Institute of Technology, Advisor

Professor Min Zhou
Mechanical Engineering
Georgia Institute of Technology

Professor Thomas H. Sanders, Jr.
Materials Science & Engineering
Georgia Institute of Technology

Professor Mulalo Doyoyo
Civil & Environmental Engineering
Georgia Institute of Technology

Professor Mo Li
Materials Science & Engineering
Georgia Institute of Technology

Dr. Laszlo Kecskes
Weapons & Materials Research Directorate
U.S. Army Research Laboratory

Date Approved: February 26, 2008

Dedicated to my mom, an amazing role model.

ACKNOWLEDGEMENTS

This work was funded by ARO Grant No. E-48148-MS-000-05123-1 (Dr. Mullins program monitor), a NASA Jenkins Predoctoral Fellowship, and a Boeing Graduate Fellowship. This work was performed partially at the National Institute for Materials Science (NIMS) in Tsukuba, Japan while I was participating in the NSF East Asia and Pacific Summer Institute Program (summer 2006) and at the Technical University of Chemnitz in Germany while I was participating in the German Academic Exchange Service's (DAAD) Research Grant Program (fall 2007), so I'd like to acknowledge both NSF and DAAD as well, for both the funding and the international research opportunities and experiences. I'd also like to acknowledge Liquidmetal Technologies, Inc. and the Army Research Laboratory for providing the specimens.

I gratefully acknowledge all of the members of my committee including Professor Naresh Thadhani, Professor Mulalo Doyoyo, Dr. Laszlo Kecskes, Professor Mo Li, Professor Tom Sanders, and Professor Min Zhou for all of their feedback and guidance. In particular, I'd like to thank Dr. Laszlo Kecskes for use of ARL facilities and for discussion and feedback throughout the duration of this project, I'd like to thank Dr. Mo Li for discussions regarding the high pressure phase transformation work, and Professor Mulalo Doyoyo for discussions regarding the impact experiments with confinement sleeves. I'd also like to give special thanks to my advisor, Professor Naresh Thadhani, for all of his help and guidance over the last five years and for making it possible for me to travel to China, Japan, Germany, Hawaii, and many other domestic destinations over the past several years.

During my stay at NIMS, Dr. Toshimori Sekine and Dr. Takimichi Kobayashi were very helpful to me and integral in the completion of the high-pressure equation of state

work. I'd like to thank them for hosting me at NIMS and for the collaboration and the excellent opportunity. I'd also like to acknowledge Professor Lothar Meyer at the Technical University of Chemnitz (TUC) for hosting me. I'd like to thank Norman Herzig for making all of the arrangements for my visit and both he and David Musch for helping to coordinate my experiments. Additional thanks to Christoph Wollschlaeger, Herr Syla, Richard, Herr Muth, Frau Kavalir, Corinna Kuprin, Igor, Thorsten Halle, Matthias Hockauf, Kristin Sommer, Thomas Weirauch, Frau Glaeser, Frau Moore, Frau Faust, Frau Fritsche, Frau Wetzel, Anka, and everyone else at TUC for all of their help completing my experiments and for making me feel welcome at their university during my stay in Chemnitz.

I'd like to thank all of my group members for all of their help over the years. In particular, I'd like to thank Lou Ferranti and Dan Eakins for teaching me how to use everything in the lab when I first started. I'd also like to thank Anthony Fredenburg, Kit Neel, Chris Wehrenberg, Brad White, Dr. Dai, and all other group members and other students in the department who helped me along the way. I'd also like to thank Ryan Crawford, Jim Painter, and Phillip Draa for their assistance with experiments, and all undergrads who helped with setup and cleanup of the gas gun. I'd also like to acknowledge Todd Walters and Yolande Berta for help with the microscopy facilities, Mike Haluska for help with the XRD facilities, Paul Moy at ARL for use of mechanical testing facilities and assistance with performing compression tests, and Tusit Weerasooriya at ARL for his help with ultrasonic measurements.

My family has been very supportive throughout all these years of school and living far away from them. I'd like to thank them for their support and for always being there for me. I would especially like to acknowledge my mom for believing in me even when I didn't always believe in myself and for helping have the courage to survive grad school when I didn't think I would. She is quite an inspiration to me and I couldn't have gotten this far without her.

And last, but not least, I would like to thank my almost-husband, Matt, for being so

encouraging, supportive, and loving over the past fours years. I couldn't have done this without him and having a wedding to look forward to at the end of all of it certainly provided extra motivation when I needed it.

TABLE OF CONTENTS

LIST OF TABLES

LIST OF FIGURES

SUMMARY

An investigation of the high-strain-rate mechanical properties, deformation mechanisms, and fracture characteristics of a Zr-based bulk metallic glass (BMG) and its composite with tungsten was conducted through the use of controlled impact experiments and constitutive modeling. Because BMGs exhibit high strength and deform by shear banding, they are of interest for a number of applications in high strain-rate and impact loading. However, BMGs undergo catastrophic failure due to localized deformation. Thus, methods to restrict or control shear band propagation need to be developed via addition of reinforcement particles or alteration of microstructure by partial crystallization. The overall **objective** of this research was to determine the high-strain-rate deformation and failure mechanisms of a BMG and its composite as a function of stress state and strain rate, and describe the mechanical behavior over a range of loading conditions. The **significance** of this research is the advancement of the fundamental understanding of mechanical behavior, and the influence of strain rate on mechanical properties, of bulk metallic glasses and their composites that can be used for design of these materials for structural applications.

The research involved performing controlled impact experiments on BMG composites consisting of amorphous $Zr_{57}Nb_5Cu_{15.4}Ni_{12.6}Al_{10}$ (LM106 or Vitreloy106) with crystalline tungsten reinforcement particles. Monolithic LM106 was also examined to aid in the understanding of the composite. The mechanical behavior of the composite was investigated over a range of strain rates (10^{-3} s^{-1} to 10^{6} s^{-1}), stress states (compression, compression-shear, tension), and temperatures (RT to 600 °C) to determine the dependence of mechanical properties and deformation and failure modes (i.e., homogeneous deformation vs. inhomogeneous shear banding) on these parameters. Mechanical testing in the quasi-static to intermediate strain-rate regimes was performed using an Instron, Drop Weight Tower,

and Split Hopkinson Pressure Bar, respectively. High-strain-rate mechanical properties of the BMG-matrix composite and monolithic BMG were investigated using dynamic compression (reverse Taylor) and dynamic tension (spall) impact experiments performed using a gas gun instrumented with velocity interferometry and high-speed digital photography. These experiments provided information about dynamic strength and deformation modes, and allowed for validation of constitutive models via comparison of experimental and simulated transient deformation profiles and free surface velocity traces. Hugoniot equation of state measurements were performed on the monolithic BMG to investigate the high pressure phase stability of the glass and the possible implications of a high pressure phase transformation on mechanical properties. Specimens were recovered for post-impact microstructural and thermal analysis to gain information about the mechanisms of dynamic deformation and fracture, and to examine for possible shock-induced phase transformations of the amorphous phase.

For the composite, mechanical testing revealed positive strain-rate sensitivity of its yield stress and negative strain-rate sensitivity of its failure stress over the range of strain rates evaluated, and work-hardening decreased as strain-rate increased. Its deformation mode was found to transition from heterogeneous deformation below the glass transition temperature (of the BMG), to homogeneous deformation between the glass transition and crystallization temperatures, and then back to heterogeneous deformation behavior above the crystallization temperature. The composite exhibited a large susceptibility to shear failure, as evidenced by much decreased strain-to-failure in biaxial (compression-shear) specimens as compared to that in uniaxial (compression) specimens. Failure took place primarily in the glass matrix and at the tungsten particle interfaces at all strain rates. Overall, the deformation and failure behavior of the composite is dominated by that of tungsten, but characteristics of BMG deformation and failure are evident, especially between the glass transition and crystallization temperatures, and at extremely high strain rates.

For the monolithic BMG, fracture surfaces became increasingly more disorganized as

strain rate increased, with evidence of melting due to temperature rise during fracture. The deformation and elastic-plastic wave propagation and interaction response based on measured free surface velocity traces of the monolithic glass were quite well described by the pressure-hardening Drucker-Prager model. Likewise, the deformation response of the composite was described reasonably well considering a rule of mixtures combination of properties of the BMG and W. High-pressure equation of state experiments provided evidence of transition to a mixed phase region (at ~26 GPa) and then to a high-pressure phase (at ~67 GPa) with a bulk modulus of 288 GPa, 144% higher than that of the bulk modulus of the ambient pressure. Specimens obtained from recovery experiments did not reveal any crystallization, indicating that any crystallites that may have formed were too small and too few to detect. Alternatively, the transformation could be reversible or polyamorphic.

Mechanical testing performed on the BMG and composite over eleven orders of magnitude revealed a transition in the effect of strain-rate sensitivity at strain rates exceeding 10^4 s^{-1}. The yield and failure stresses of LM106 and the failure stress of W increased drastically as a function of strain rate above this transition point. The strengthening of the BMG above 10^4 s^{-1} is attributed to the transition to a higher modulus phase. The toughening of the BMG above 10^4 s^{-1} is attributed to effects of energy dissipation associated with the high-pressure phase transition.

CHAPTER I

INTRODUCTION

Bulk metallic glasses have become a subject of increasing interest due to their unique properties such as superior strength and hardness, and excellent corrosion and wear resistance [1]. However, the desirable properties of bulk metallic glasses are accompanied by their inability to undergo homogeneous plastic deformation. Bulk metallic glasses are known to deform by shear banding, which is of particular interest for many applications, but also causes them to be quite brittle and fail catastrophically due to propagation of these bands. If specially designed microstructures (intrinsically-formed crystalline phases or extrinsically-added reinforcement particles) can permit formation of multiple shear bands that do not propagate through the material and cause catastrophic failure, the plastic strain to failure can be significantly increased [2] from its otherwise negligible amount.

Microstructures can be tailored to control shear band propagation by addition of an extrinsic crystalline particulate phase to a BMG matrix. The addition of reinforcement particles to a metallic glass matrix has the potential to increase the plasticity of BMGs and completely change the properties and deformation response of the composite [2–7]. Addition of extrinsic reinforcements has the advantage of relatively easy processing. Reinforcement sizes and shapes (e.g. particles and wires) are limited by availability, but a variety of materials including heavy metals such as tungsten, tantalum, molybdenum, and niobium are candidates for reinforcements for fabricating BMG-matrix composites of high densities. By altering the composition, size, morphology, distribution, and amount of the reinforcement particles, there is potential to completely alter the behavior of the metallic glass, and therefore to design a material with a tailored deformation response.

This project focused on a BMG reinforced with tungsten particles which have been

identified as a favorable reinforcement material due to high strength, density, and strain-rate sensitivity. Previous work on similar BMG-W composites [2, 8, 9] has yielded promising results in a variety of low-strain-rate and penetration experiments. Tungsten, which is much denser than glass, is ductile and can interfere with shear band propagation in the glass matrix. Hence, the effect of the addition of crystalline tungsten particles to a BMG matrix was explored to determine if the deformation mode of BMGs at high-strain-rates can be significantly altered.

The mechanical properties of BMGs and their composites have been studied in some detail at low and intermediate strain rates, and constitutive models have been applied to describe this behavior. However, mechanical properties and deformation mechanisms in the high-strain-rate regime have only begun to be explored, and no previous attempts have been made to describe the high-strain-rate dynamic mechanical behavior through correlation with constitutive strength models. A constitutive model that relates stress to strain, strain rate and temperature, and that is valid over a wide range of these parameters will be useful and necessary when designing materials for penetrators or other applications. Hence, this work also addressed investigation of existing constitutive models to describe the deformation response of BMGs over a wide range of stress, strain rate and temperature.

The rationale for investigating high-strain-rate deformation and failure mechanisms of a BMG-matrix composite and the effects of pressure-induced crystallization include (a) the interest in these materials due to their ability to undergo deformation via shear-banding, resulting in self-sharpening and increased penetration upon impact; (b) the possibility of controlling the propagation of these shear bands via partial crystallization of the amorphous matrix and/or inclusion of crystalline reinforcement particles in order to promote formation of multiple shear bands, which would prevent immediate catastrophic failure; (c) the need to develop and validate a robust constitutive relationship that relates stress to strain, strain rate, and temperature in order to fully describe the mechanical behavior and

deformation mechanisms of these materials; and (d) the need for structure-property relationships that would allow microstructures to be specifically designed to exhibit desired mechanical properties for structural applications including kinetic energy penetrators.

Based on the above rationale, the overall objective of this research is to characterize the dynamic compressive and tensile responses of a W-LM106 bulk metallic glass composite and to correlate transient experimental deformation and failure with a constitutive model that describes the onset of plastic flow and subsequent fracture under high-strain-rate loading, while also accounting for the deformation mechanisms. The significance of the proposed research is that an understanding of the effects of impact loading and high strain rate deformation and failure of bulk metallic glass composites can be developed and applied for design and synthesis of microstructure. More specifically, the objectives of this research include:

- To determine the high-strain-rate dynamic compressive and tensile mechanical properties and deformation mechanisms and the high-pressure phase stability of a Zr-based bulk metallic glass and its composite with tungsten.

- To develop structure-property relations that utilize the understanding of effects of stress, strain rate, crystallinity and reinforcement-particle characteristics on deformation/fracture mechanisms of W-reinforced, Zr-based bulk metallic glass, for design and synthesis of high-strength metallic glass composites.

- To establish and validate constitutive equations describing the deformation and failure mechanisms of this metallic-amorphous composite based on models for homogeneous/inhomogeneous plastic/viscous flow in glassy materials and glass-crystalline composites using well-characterized and instrumented impact experiments.

A detailed understanding of the deformation and failure of BMGs and their composites during impact at high-strain-rates in conjunction with the validation of constitutive strength

models for these materials will lead to design of high strength BMG-matrix composite materials with customized and application-specific properties, for example as kinetic energy penetrators or in other structural applications.

In this dissertation, a brief background is provided in Chapter II on the synthesis of bulk metallic glasses and their composites, their deformation mechanisms, mechanical properties, constitutive behavior, and phase stability. Details of the materials investigated and experimental procedures are provided in Chapter III. Chapters IV-VII report the results of low to intermediate train-rate mechanical properties experiments on the composite, dynamic compression of the composite, dynamic compression of the monolithic glass, and high-pressure equation of state and phase stability of the glass, respectively. A summary and discussion in Chapter VIII compiles and analyzes the results on all materials and from all experiments and strain-rate regimes, culminating in the conclusions and recommendations for future work presented in Chapter IX.

CHAPTER II

BACKGROUND

Bulk metallic glasses and their composites are the focus of many scientific studies due to their unique mechanical and thermodynamic properties. The possibility of changing or controlling the mechanical deformation and fracture behavior of BMGs through the use of intrinsically-formed or extrinsically-added crystalline reinforcements has also recently been investigated. These microstructural modifications show promise in the area of design of BMG matrix composites with specifically tailored deformation behavior and mechanical properties. An overview of work done on processing and properties of metallic glasses and their composites will be described next.

2.1 Synthesis of Bulk Metallic Glasses

Amorphous solids are typically produced by rapid quenching, which hinders the crystallization kinetics [10]. The high heat transfer rate required limits these metallic glasses to thin samples produced by splat quenching or melt spinning. Some other methods for processing include solid-state amorphization [11] via hydrogen absorption [12, 13], mechanical alloying [14], or anomalous diffusion in crystalline bi-layers [15]. Also, creation of defects in a crystalline solid by intense plastic deformation [11], for example, can cause an increase in internal energy in excess of that of the amorphous phase, in which case it is energetically favorable for the crystal to amorphize. Recently, metallic glasses with slower nucleation kinetics in undercooled liquids have been processed by conventional casting at cooling rates of 10^{-1}-10^{2} K/s [16, 17]. This figure illustrates conditions for processing both the more recently developed bulk amorphous alloys as well as ordinary amorphous alloys developed before 1990. There is a clear tendency for the glass-forming ability to increase

with increasing T_g/T_m, and as such these alloys have slower critical cooling rates and larger possible bulk dimensions.

The criteria for slow crystallization kinetics, a stabilized supercooled liquid and high glass-forming ability include: (1) multi-component alloys of increased complexity and size of crystal unit cells such that the energetic advantage of an ordered structure is reduced by increasing the configurational entropy of the supercooled liquid phases; (2) atomic radius mismatch between elements, which leads to higher packing density and smaller free volume and requires a greater volume increase for crystallization, and also limits the solubility of these atoms in crystalline states; (3) negative heat of mixing between the elements, which increases the energy barrier at the solid-liquid interface and increases atomic diffusivity, thus slowing local atomic rearrangements and crystal nucleation rate, extending the supercooled liquid temperature; and (4) alloy composition close to deep eutectic, which forms a liquid stable at low temperatures [1, 18, 19]. Examples of metallic materials systems that have been made into an amorphous form are given in Figure 2.1 as a function of their critical cooling rate, maximum sample thickness and reduced glass transition temperature.

2.2 Deformation Mechanisms of Bulk Metallic Glasses

BMGs exhibit properties very different from those of crystalline materials. They do not strain harden, their plastic deformation is influenced by both shear and normal stresses, and deformation occurs inhomogeneously through plastic strains concentrated in localized shear bands [21]. As summarized by Lund and Schuh [22], macroscopic yield and failure of metallic glasses consists of many small-scale events, including: (1) nucleation of shear transformation zones, in which atoms rearrange to accommodate the applied shear strain; (2) propagation of shear localization, or shear banding [23, 24]; (3) adiabatic heating in deformed regions [19, 25]; (4) nucleation of nanocrystallites in or near shear bands [26]; (5) nucleation of nanovoids in shear bands [27]; and (6) coalescence of voids during failure [28, 29].

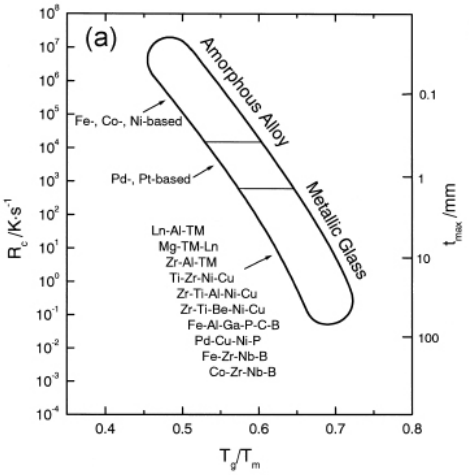

(b)

Typical bulk amorphous alloy systems reported up to date

Nonferrous alloy system	
Mg–Ln–M (Ln = lanthanide metal, M = Ni, Cu, Zn)	1988
Ln–Al–TM (TM = VI–VIII group transition metals)	1989
Ln–Ga–TM	1989
Zr–Al–TM	1990
Ti–Zr–TM	1993
Zr–Ti–TM–Be	1993
Zr–(Ti,Nb,Pd)–Al–TM	1995
Pd–Cu–Ni–P	1996
Pd–Ni–Fe–P	1996
Pd–Cu–B–Si	1997
Ti–Ni–Cu–Sn	1998
Ferrous alloy system	
Fe–(Al,Ga)–(P,C,B,Si,Ge)	1995
Fe–(Nb,Mo)–(Al,Ga)–(P,B,Si)	1995
Co–(Al,Ga)–(P,B,Si)	1996
Fe–(Zr,Hf,Nb)–B	1996
Co–(Zr,Hf,Nb)–B	1996
Ni–(Zr,Hf,Nb)–B	1996
Fe–Co–Ln–B	1998

Figure 2.1: (a) Relation between critical cooling rate (R_c), maximum sample thickness (t_{max}), and reduced glass transition temperature (T_g/T_m) for bulk metallic alloys and (b) list of typical amorphous alloy systems [20]. This figure illustrates conditions for processing both the more recently developed bulk amorphous alloys as well as ordinary amorphous alloys developed before 1990. There is a clear tendency for the glass-forming ability to increase with increasing T_g/T_m, and as such these alloys have slower critical cooling rates and larger possible bulk dimensions.

There are two basic modes of deformation in metallic glasses: homogeneous flow in which each volume element of the specimen contributes to the strain, and inhomogeneous flow in which the strain is localized in a few very thin shear bands [24]. The schematic deformation map given by Spaepen and shown in Figure 2.2 illustrates how the deformation behavior transitions as a function of strain rate and temperature. Homogeneous flow, which is close to Newtonian viscous ($\dot{\gamma} \propto \tau$), occurs at low stresses and high temperatures. In this deformation mode, the specimen thins uniformly and fracture occurs when some section of the specimen has narrowed to zero thickness. Inhomogeneous flow occurs at high stress levels. The stress is very strain-rate insensitive, so the flow is almost ideally plastic. The photographs shown in Figure 2.3 illustrate examples of two BMG specimens tested at different strain rates, one which exhibited homogeneous flow ($\dot{\varepsilon}$=3x10^{-5}) and shows a uniform deformation of the cross-section and one which exhibited inhomogeneous flow ($\dot{\varepsilon}$=10^{-3}) [30]. The deformation differences are simply a result of the change in strain rate.

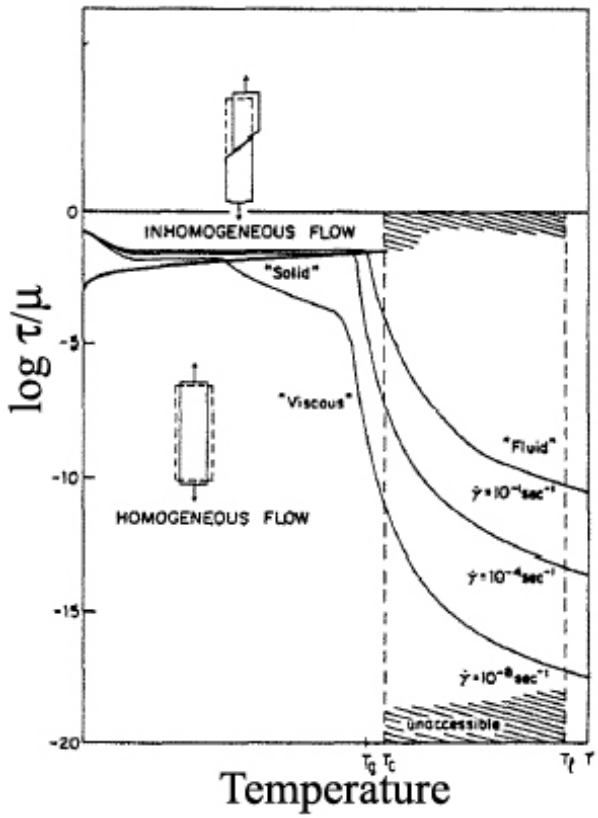

Figure 2.2: Schematic deformation map (flow stress normalized by temperature-dependent shear modulus, as a function of temperature) showing temperature and strain rate regimes when homogeneous and inhomogeneous deformation occur in metallic glasses [24]. Homogeneous deformation occurs at low stresses and high temperatures and inhomogeneous deformation occurs at high stresses.

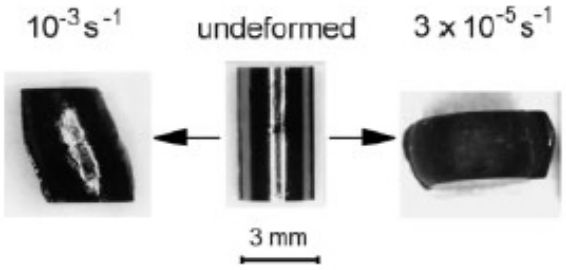

Figure 2.3: Photograph showing examples of a $Zr_{55}Cu_{30}Al_{10}Ni_5$ specimen which failed homogeneously ($\dot{\varepsilon}$=3x10^{-5}) and one which failed inhomogeneously ($\dot{\varepsilon}$=10^{-3}) due to the difference in strain rate [30]. The deformation differences are simply a result of the change in strain rate.

The fundamental unit of plasticity during inhomogeneous deformation of metallic glasses is the shear transformation zone (STZ), which is a small cluster of closely-packed atoms that spontaneously and cooperatively rearrange to accommodate the applied shear strain [22]. The continued propagation of this applied shear strain occurs when one STZ creates a localized distortion of the surrounding material, which triggers the formation of large planar bands of STZs, or shear bands.

According to the free volume model developed by Spaepen [24], macroscopic flow behavior is microscopically triggered by jumps of atoms into neighboring positions of equal space. The direction of these jumps is unbiased when no stress is applied, however a superimposed shear stress gradient causes the jumps to be biased in the direction of the stress, which leads to a microscopic plastic shear unit. When the neighboring atomic site is of a smaller size, the diffusing atom will create free volume by making the jump. This can lead to work softening during plastic deformation due to a macroscopic decrease in viscosity. There are two theories that explain this change in viscosity. A localized shear band is assumed to form due to the build-up of free volume created during the shearing of small groups of atoms [21, 31]; this then causes a decrease in the viscosity of the glass [21, 25]. The formation of free volume weakens the specimen locally by decreasing the cross-sectional area, and subsequently induces local softening of the material until fracture occurs along the plane of the shear bands [24].

Another explanation for the formation of shear bands is that local adiabatic heating occurs and the glass transition temperature is exceeded, thus decreasing the viscosity locally [19,32]. A vein-like pattern characteristically forms on the fracture surface of metallic glass; this pattern is the result of adiabatic heating in the shear band which causes softening of the glass [33]. The vein-like pattern that forms on fracture surfaces shows that the material within a shear band behaves like a liquid layer of reduced viscosity, which has been attributed to local dilatation of the glass in regions of high tensile stress [34]. The veinal pattern has been attributed to the Taylor instability [35], which occurs when a viscous fluid

is driven forward by another fluid of lower viscosity. The interface between the two fluids becomes unstable and "fingers" from the less viscous fluid penetrate into the more viscous fluid [33].

Lewandowski and Greer [36] and Zhang et al. [37] investigated the theory of adiabatic heating within shear bands by performing mechanical tests on several different BMGs coated with tin (T_m=207 °C above ambient) with the idea that if the local temperature rise exceeds the melting temperature of tin, the coating will melt and bead up. Micrographs of the melted tin on the surface of a fractured compression sample are shown in Figure 2.4 and results from calculations of temperature rise near a shear band are given in Figure 2.5. Temperature values were calculated based on a thin film solution of the diffusion equation:

$$\Delta T = \left(\frac{H}{2\rho C\sqrt{\pi\alpha}}\frac{1}{\sqrt{t}}exp\left(-\frac{x^2}{4\alpha t}\right)\right)$$

where ΔT is the temperature rise above ambient, H is the heat content (energy per unit area) of the band generated by shear, ρ is density, C is the specific heat capacity, α is the thermal diffusivity of the BMG, and t is the time elapsed since the end of shear. These studies quantified temperature rise near shear bands in an accurate manner and determined that temperature rise is a consequence of, not a cause of, shear bands [36].

2.3 Mechanical Properties of Bulk Metallic Glasses

2.3.1 Static Mechanical Properties of Bulk Metallic Glasses

Bulk metallic glasses have been shown to display elastic-perfectly plastic deformation behavior under compressive loading, with the plastic stress-strain response displaying sections of elastic loading followed by load drops, which correspond to the formation of shear bands [38, 39]. As the stress in a specimen increases to a critical value, a shear band is initiated and propagates across the specimen, producing abrupt deformation. The specimen then reloads elastically and the process repeats, resulting in a serrated flow pattern [39].

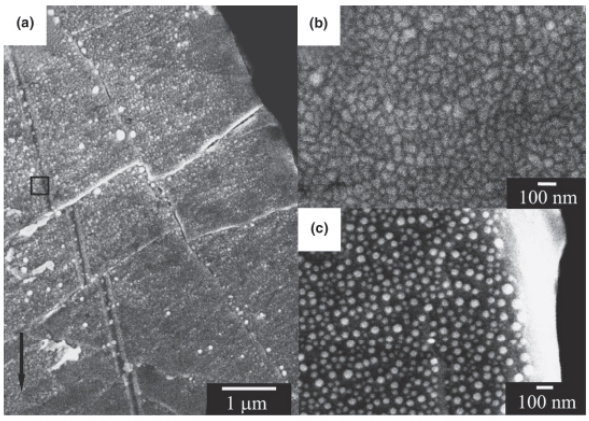

Figure 2.4: SEM micrographs of the tin-coated surface of partially-crystalline $Zr_{55}Ni_{10}Cu_{30}Al_5$ [37]. (a) intersecting cracks after compressive brittle fracture, (b) as-deposited tin pattern, and (c) close-up of boxed area in (a) showing tin beaded-up indicating temperature rise in excess of T_m of tin (207 ° above ambient).

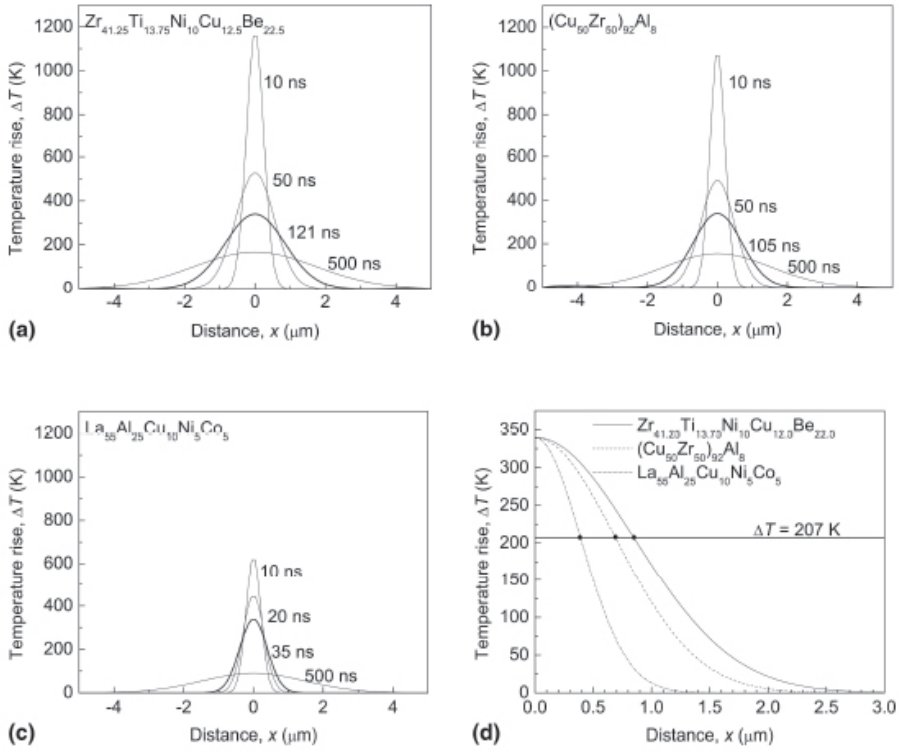

Figure 2.5: Calculated temperature profiles around a shear band at times after the end of shear in different BMGs- (a) $Zr_{41.25}Ti_{13.75}Ni_{10}Cu_{12.5}Be_{22.5}$, (b) $(Cu_{50}Zr_{50})_{92}Al_8$, (c) $La_{55}Al_{25}Cu_{10}Ni_5Co_5$ [37]. (d) shows a comparison of the maximum melting in tin for each BMG. Temperatures were calculated using a thin film solution of the diffusion equation. These studies quantified temperature rise near shear bands in an accurate manner and determined that temperature rise is a consequence of, not a cause of, shear bands [36].

Bulk metallic glasses have been shown to exhibit quite different behavior in tension than in compression [19,28], as illustrated in the stress-strain curves in Figure 2.6. Conner et al. [3] determined the quasi-static stress-strain response of $Zr_{57}Nb_5Cu_{15.4}Ni_{12.6}Al_{10}$ (LM106) BMG, which was studied in this work, and the resulting data is shown in Figure 2.8. These tests yielded a compressive yield strength of 1800 MPa and a tensile yield strength of 1200 MPa, and show similar features and differences between tensile and compressive behavior to those exhibited in Figure 2.6. The mechanistic reasons for these differences in behavior are as follows. In compression, shear bands can carry very large localized plastic strains, giving metallic glasses ductile properties. In tension, however, deformation usually occurs in a single shear band and the glass fails by shear rupture through this band with very little plastic strain [40]. Under compressive loading, the BMG displays some plasticity before fracture, and fracture occurs mainly along one shear band at an angle of ~42-43° from the loading axis [23, 41–45]. Also, the yield stress in plane strain compression is approximately equal to the yield stress in uniaxial compression [23]. Under tensile loading, the glass displays brittle fracture without yielding, and the tensile fracture angle is ~56° (50-65°) [19, 42, 43, 45, 46]. Images showing the difference in failure angles of specimens tested under compressive or tensile loading can be seen in Figure 2.7.

The fracture surfaces produced by tensile and compressive loads show different features, which can be seen in Figure 2.9. A compressive fracture surface is typically smooth with periodic bands in the direction of fracture, and a uniform vein-like structure within the bands [28, 47], as shown in Figure 2.9(a). In contrast, a tensile fracture surface shows a mixture of veins and radial cores, which can be seen in Figure 2.9(b). These differences are attributed to the role of the normal stress during tensile loading and the dominance of shear stress during compressive loading [28].

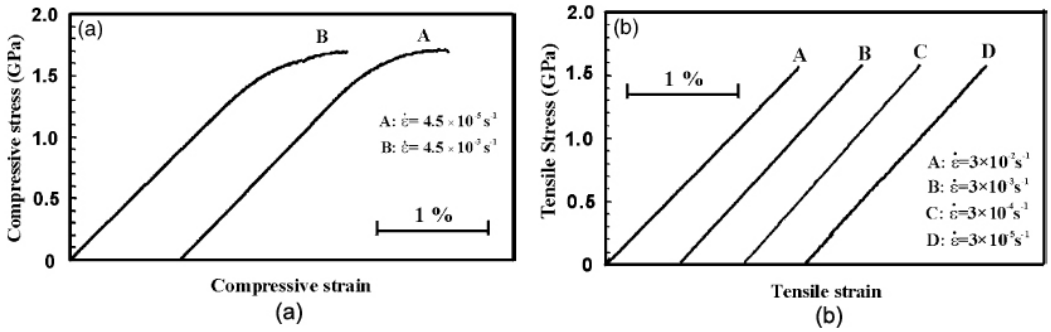

Figure 2.6: Stress-strain curves for $Zr_{59}Cu_{20}Al_{10}Ni_8Ti_3$ metallic glass under (a) compressive and (b) tensile loading [28] showing no plasticity under tensile loading, but a small amount under compressive loading due to the extra constraint provided in this configuration, thus prohibiting catastrophic failure as early. In compression, shear bands can carry very large localized plastic strains, giving metallic glasses ductile properties. In tension, however, deformation usually occurs in a single shear band and the glass fails by shear rupture through this band with very little plastic strain [40].

2.3.2 Dynamic Mechanical Properties of Bulk Metallic Glasses

Few studies have been performed on the dynamic mechanical properties of BMGs in the high-strain-rate regime; these studies are summarized next.

2.3.2.1 Dynamic Indentation of Bulk Metallic Glasses

Indentation studies have revealed that at low indentation rates, deformation occurs in discrete events of isolated shear banding which show prominent displacement bursts. At high indentation rates, however, deformation is continuous without any evidence of discrete events [38]. This difference is consistent with a kinetic limitation for shear bands; at high-strain-rates, a single shear band cannot accommodate strain rapidly enough, so multiple shear bands must operate simultaneously [38].

2.3.2.2 Fracture Toughness of Bulk Metallic Glasses

The dynamic failure mechanisms of a Zr-Ti-Ni-Cu-Be alloy were studied by Owen et al. [48]. Dynamic crack initiation and fracture toughness were investigated over nine orders of magnitude in loading rate. In the quasi-static range ($\dot{K}_I^d < 10^4$ MPa m$^{\frac{1}{2}}$ s^{-1}), the fracture

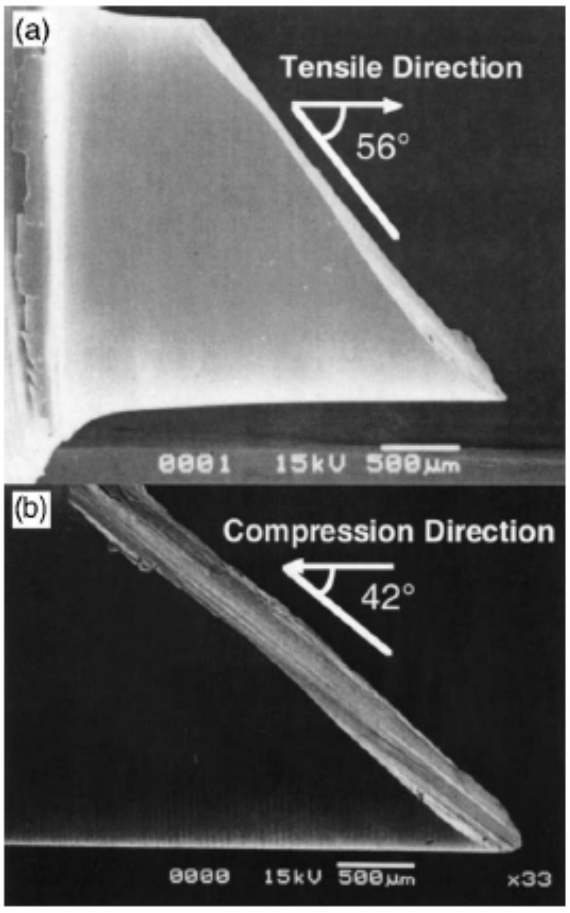

Figure 2.7: $Pd_{40}Ni_{40}P_{20}$ specimens fractured (a) in tension and (b) in compression, showing the difference in failure angles [45]. Under compressive loading, the BMG displays some plasticity before fracture, and fracture occurs mainly along one shear band at an angle of ~42-43° from the loading axis [23, 41–45]. Under tensile loading, the glass displays brittle fracture without yielding, and the tensile fracture angle is ~56° (50-65°) [19, 42, 43, 45, 46].

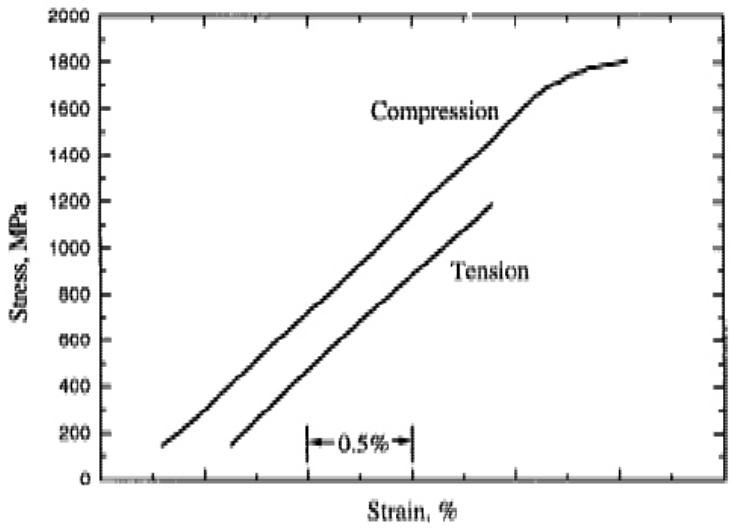

Figure 2.8: Stress-strain curves of $Zr_{57}Nb_5Cu_{15.4}Ni_{12.6}Al_{10}$ metallic glass under compressive and tensile loading [3].

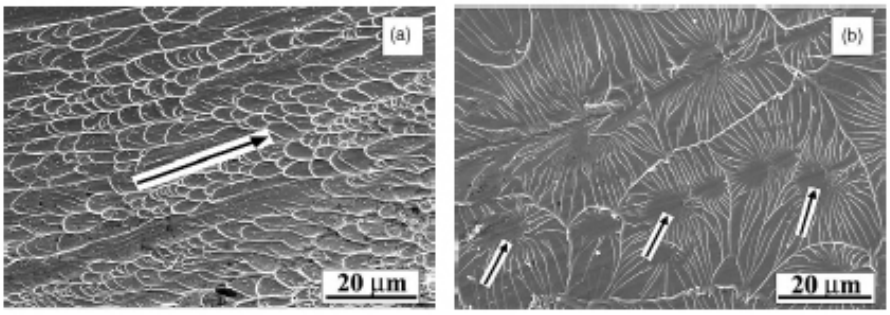

Figure 2.9: Comparison of typical (a) compressive and (b) tensile fracture surfaces of $Zr_{59}Cu_{20}Al_{10}Ni_8Ti_3$ [28]. The arrows indicate the direction of fracture. A compressive fracture surface is typically smooth with periodic bands in the direction of fracture, and a uniform vein-like structure within the bands [28, 47]. In contrast, a tensile fracture surface shows a mixture of veins and radial cores. These differences are attributed to the role of the normal stress during tensile loading and the dominance of shear stress during compressive loading [28].

experiments were conducted in three-point bending geometry using a hydraulic Materials Testing System and the displacement rate was varied systematically to yield a range of loading rates. The time history of the stress intensity factor, K_I^d, was calculated from the varying load and specimen geometry and the fracture toughness was taken as the peak value of K_I^d. The quasi-static loading rate, $\dot{K}_I^d$, was determined from the slope of K_I^d vs. time. In the dynamic range ($\dot{K}_I^d > 10^4$ MPa m$^{\frac{1}{2}}$ s^{-1}), a drop weight tower was used to load specimens in three-point bend geometry at impact velocities of 2-6 m/s. The mechanical fields in the vicinity of the dynamically-loaded crack tip were recorded with a high-speed camera with optical interferometry. From the interferograms, K_I^d and crack tip motion were measured, which allowed for determination of K_I^d at crack initiation (K_{IC}^d) and propagation toughness K_D associated with a given speed.

Toughness was found to increase four to six-fold from the quasi-static to dynamic regime, as can be seen in Figure 2.10. This drastic increase was attributed to effects of inertia and thermal softening on the dynamic crack initiation process. Materials exhibiting high toughness had a tendency for crack branching. Formation of shear bands was found to be a result of nucleation, growth and linkage of areas of highly localized temperature.

2.3.2.3 Dynamic Compression of Bulk Metallic Glasses

Dynamic compression of various BMGs has been investigated in several studies [3,8,9,45, 47,49–56]. The dynamic compressive strength of Vitreloy1 was determined to be between 1.8 and 2.0 GPa with a compressive failure strain of 2.5-3.5% [47] or as high as 3.5-4% [3,49].

The dynamic compressive behavior of Vitreloy1 was investigated by Bruck et al. [49] using Split Hopkinson Pressure Bar experiments coupled with a high-speed infrared thermal detector. These tests showed that the BMGs retained their elastic-perfectly plastic behavior at high strain rates and failure occurred in shear bands oriented at ~45° to the loading axis. They also found that temperature increases due to adiabatic heating occurred

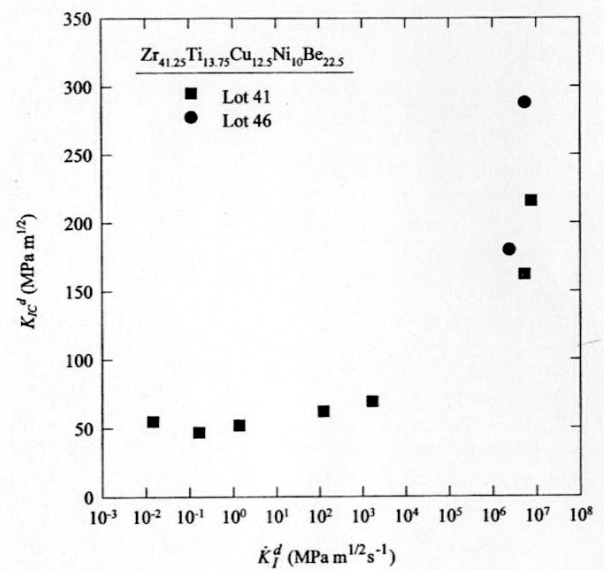

Figure 2.10: Dynamic fracture toughness of $Zr_{41.25}Ti_{13.75}Cu_{12.5}Ni_{10}Be_{22.5}$ as a function of loading rate [48] showing a four to six-fold increase in toughness from the quasi-static to dynamic regime, as can be seen in Figure 2.10. This drastic increase was attributed to effects of inertia and thermal softening on the dynamic crack initiation process.

after the onset of inhomogeneous deformation, and temperatures near the melting point were approached within the shear bands after specimen failure.

The fracture surface characteristics developed during dynamic loading have been observed to differ from those of quasi-static compression surfaces. Quasi-statically tested specimens show failure at ~45° with smooth fracture surfaces with well-developed veinal patterns in the direction of shear (Figure 2.9). In contrast, dynamically tested specimens fail nearly parallel to the loading axis, with multiple inclined planes, indicative of the action of multiple shear planes [45, 47, 50]. The dynamically fractured surfaces are more rough, with disorganized and randomly oriented veinal patterns and liquid droplets [45, 47, 50].

Taylor [57] impact tests have been performed by Cline and Reaugh [55, 56] on both Pd- and Zr-based metallic glass. Their goal was to determine the dynamic yield strengths of these materials using the relationship defined by Wilkins and Guinan [58], but in both studies they concluded that the Taylor test is not well-suited to determination of the dynamic yield strength of metallic glass since the material fractures and thus is not recoverable for

a final length measurement. However, preliminary observations of the fracture surfaces produced under dynamic loading were presented.

2.3.2.4 Strain-Rate Sensitivity of Bulk Metallic Glasses

Strain-rate sensitivity of bulk metallic glasses has been the subject of several studies. A few investigators have reported that BMGs exhibit positive strain-rate sensitivity [59, 60]. However, most studies on this topic have drawn the conclusion that BMGs exhibit negative strain-rate sensitivity, with the fracture stress decreasing as strain rate increases [8,9,45,49, 50,52–54,54,61]. Negative strain-rate sensitivity has been observed by Bruck et al. [49], but was attributed to experimental dispersion. However, after correcting for dispersion, these results have been determined to be realistic [54]. Gu et al. [54] have also found negative strain rate sensitivity for many BMGs, as shown in the plot of normalized failure stress as a function of strain rate in Figure 2.11. The mechanistic explanation given by Gu et al. [54] for the negative strain rate sensitivity of these materials is that adiabatic processes occur during failure of BMGs and higher strain rates favor adiabatic processes, thus leading to a lower failure strength at higher loading rates when adiabatic processes are more prevalent.

Li et al. [8,9] studied the compressive mechanical behavior of Zr- and Hf-based BMGs under quasi-static and dynamic ($\sim 10^3$ s^{-1}) loading. These studies yielded negative strain-rate sensitivity, as shown in the plot of fracture stress as a function of strain rate in Figure 2.12. This negative strain rate sensitivity was explained as follows [8]: shear bands in a BMG initiate well below the yield stress and grow upon continued quasi-static loading. Under dynamic loading conditions, cracks initiate immediately upon shear band initiation due to the excess energy that is available; these cracks lead to fracture of the specimen, and thus a lower fracture stress. This explanation for the negative strain-rate sensitivity of BMGs is further supported by work done by Mukai et al. [45], who observed this negative strain-rate sensitivity in $Pd_{40}Ni_{40}P_{20}$ BMG, with a quasi-static compressive strength of ~1.7 GPa and a dynamic strength of ~1.4 GPa (at $\dot{\varepsilon} = 5x10^{-2}$ s^{-1}). During this study, they

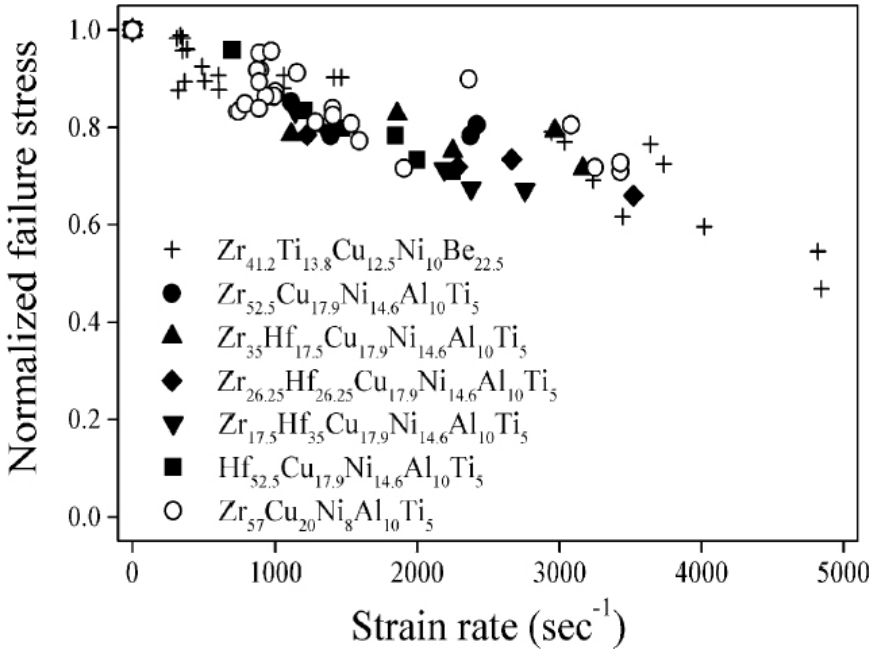

Figure 2.11: Normalized failure stress as a function of strain rate of $(Hf_x\text{-}Zr_{1-x})_{52.5}$-$Cu_{17.9}Ni_{14.6}Al_{10}Ti_5$ (x=0-1), $Zr_{41.2}Ti_{13.8}Cu_{12.5}Ni_{10}Be_{22.5}$ (from [49]), Zr_{57}- $Cu_{20}Ni_8Al_{10}Ti_5$ (from [53]) [54] showing decreasing failure stress with increasing strain-rate for several bulk metallic glasses.

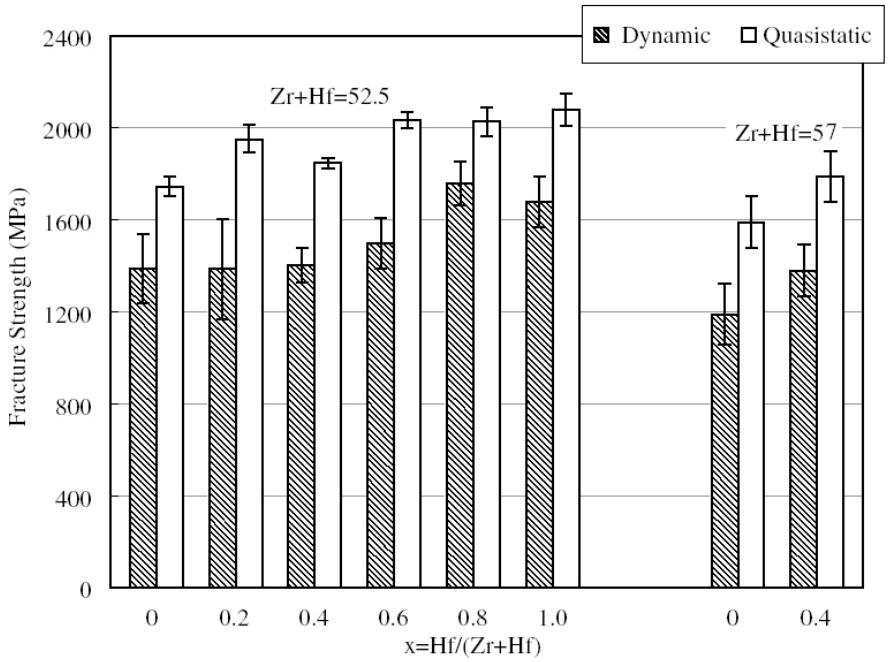

Figure 2.12: Fracture strengths of $(Zr_xHf_{1-x})_{52.5}Ti_5Ni_{14.6}Cu_{17.9}Al_{10}$ and $(Zr_xHf_{1-x})_{57}Ti_5Ni_8Cu_{20}Al_{10}$ BMGs under static and dynamic loading [8] showign higher fracture strengths under quasistatic than dynamic loading, indicating negative strain-rate sensitivity, for all composite compositions.

observed that although the quasi-statically tested specimens were failing at an "apparent" yield stress of ~1.7 GPa, they began to show serrations indicative of shear band formation (shown in Figure 2.13), which is the mechanism for accommodation of deformation in BMGs. As strain rate was increased, the specimens could no longer accommodate the deformation quickly enough, and the failure strength approached ~1.4 GPa, which is the stress level when shear band initiation begins. Mukai et al. [45] compiled stress as a function of strain rate data for a number of BMGs and this is shown in in Figure 2.14. This data reveals negative strain-rate sensitivity for several BMGs, but with a large degree of scatter at strain rates $\geq 10^3$ s^{-1}.

Lu et al. [62] investigated the effect of strain rate on the stress-strain behavior of Vitreloy1. Figure 2.15 shows stress-strain curves at a test temperature of 643 K (T_g ~ 623 K) and strain rates ranging from $2x10^{-4}$ to $1x10^{-1}$ s^{-1}. It was found that the specimens tested

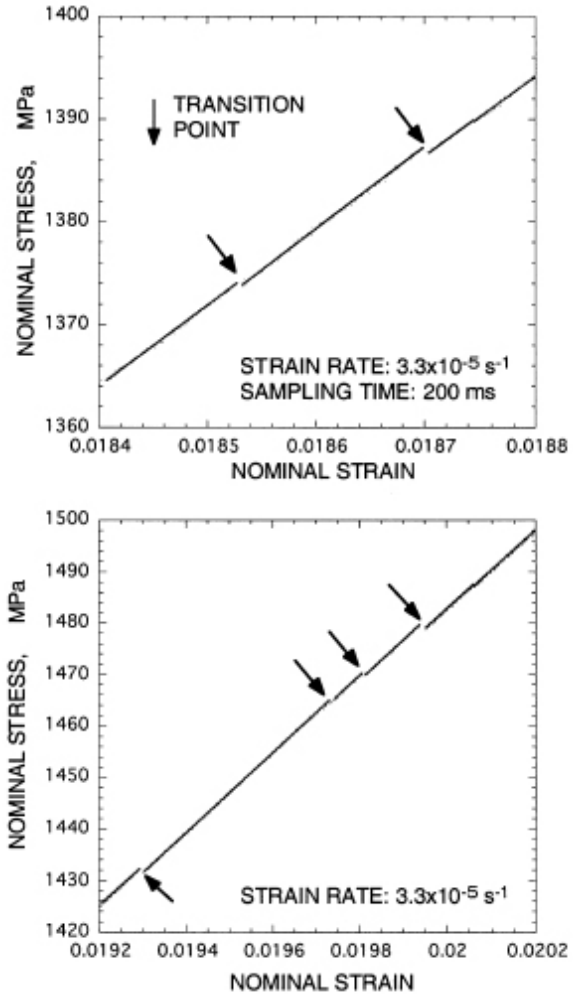

Figure 2.13: Stress-strain data for uniaxial compression of $Pd_{40}Ni_{40}P_{20}$ BMG tested at $\dot{\varepsilon}$=3.3x10^{-5} s^{-1} showing serrations indicative of shear band formation. The serrations appear at 1.35-1.45 GPa, which is the stress where this material fails under dynamic loading [45].

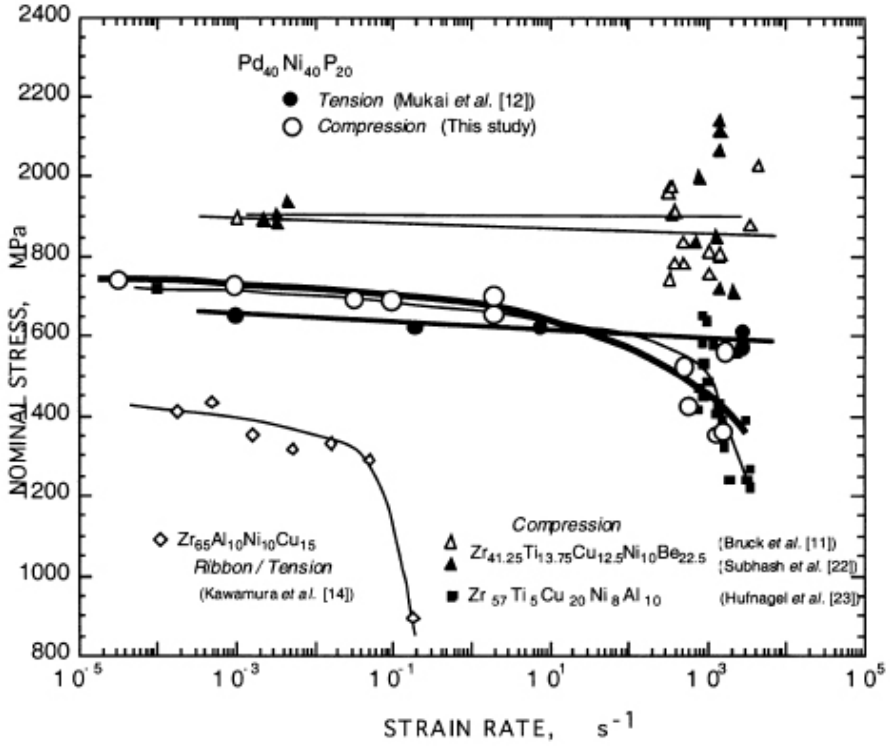

Figure 2.14: Stress as a function of strain rate data for several BMGs [45]. Data from [47, 49, 53] is also included. This data reveals negative strain-rate sensitivity for several BMGs, but with a large degree of scatter at strain rates $\geq 10^3$ s^{-1}. The rapid decrease in flow stress of $Zr_{65}Al_{10}Ni_{10}Cu_{15}$ ribbon at a strain rate of 10^{-1} s^{-1} was attributed to increased sensitivity to surface defects.

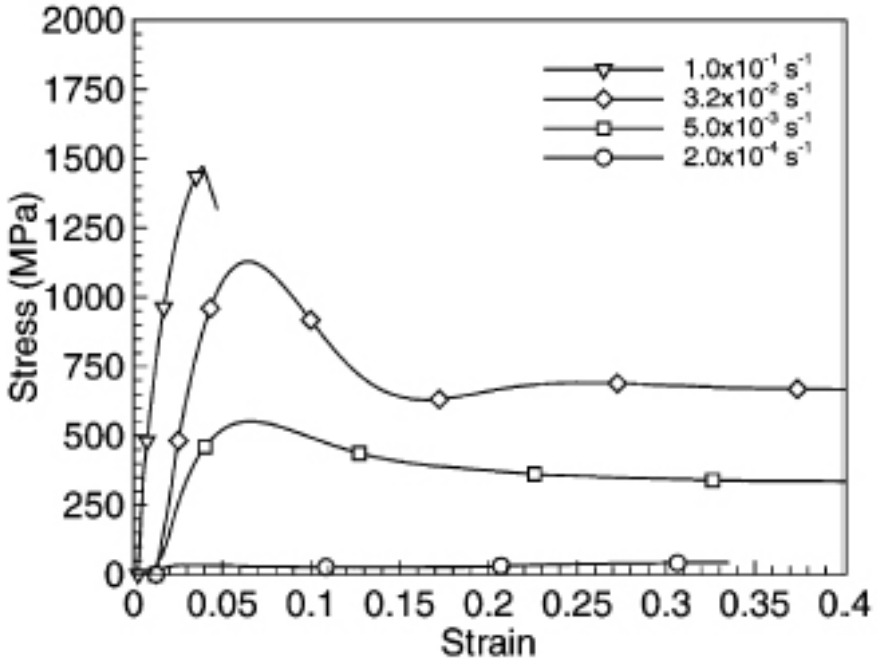

Figure 2.15: Effect of strain rate on the uniaxial stress-strain response of Vitreloy1 at a test temperature of 643 K. A transition from homogeneous to inhomogeneous flow can be observed as strain rate increases [62].

at the higher strain-rates ($\geq 10^{-1}$ s^{-1}) exhibited a linear slope until failure and no inelastic post-yielding, whereas specimens tested at lower strain rates showed more ductile behavior. These specimens were characterized by localized shear failure with veinal patterns on the fracture surfaces. It was also evident that as strain rate was increased, the deformation mechanism changed from homogeneous to inhomogeneous flow, as is indicated by Spaepen's [24] deformation map (Figure 2.2).

2.3.2.5 Dynamic Tensile Properties of Bulk Metallic Glasses

The dynamic tensile properties of bulk metallic glasses have received less attention and study in comparison to compressive properties. Work at Caltech [63] investigated the shock wave response of Vitreloy1 ($Zr_{41.25}Ti_{13.75}Ni_{10}Cu_{12.5}Be_{22.5}$) and its partially microcrystallized composite, α-Vitreloy1. In this study, plate impact experiments were performed and the wave profiles were captured by velocity interferometry (VISAR), as shown

in Figure 2.16. A spall signal was evident for both the monolithic glass as well as the composite; the spall strength (at $d\varepsilon/dt = 10^6\ s^{-1}$) of Vitreloy1 was found to be 2.35 GPa and that of α-Vitreloy1 was 2.11 GPa. Samples were analyzed upon recovery and it was found that Vitreloy1 underwent brittle fracture caused by shear localization and failure, with crack formation caused by the nucleation, growth and coalescence of microvoids within the shear bands. The α-Vitreloy1 composite, in contrast, showed evidence of a more ductile failure, with microvoids nucleating mostly at the boundaries between the amorphous matrix and the BCC crystals. The spall strength of Vitreloy1 was also investigated by Yuan et al. [64]. The free surface velocity traces recorded during this study are shown in in Figure 2.17. The spall strength at a shock input stress of 4.4 GPa was 3.5 GPa, whereas the spall strength at shock input stresses of 5.1, 6.0 and 7.0 GPa were 2.72, 2.35, and 2.33 GPa, respectively, as can be seen in Figure 2.18. Their investigation yielded the result that spall strength decreases with increasing normal (impact) stress. This trend is logical since microfracture in brittle materials can appear in the compression phase of impact. The degree of fracture increases as load intensity increases, and as a result, decreases the capacity of the brittle material to resist the tensile stresses that follow the initial compression [65].

2.3.2.6 Hugoniot Elastic Limit of Bulk Metallic Glass

The value of the Hugoniot elastic limit (HEL), or the critical threshold for the onset of elasticity, has been investigated for a few Zr-based bulk metallic glasses. Shock wave experiments were performed by Gupta et al. [66] on Zr-based bulk amorphous alloy samples. The specimens, which had a composition of $Zr_{56.7}Cu_{15.3}Ni_{12.5}Nb_5Al_{10}Y_{0.5}$, were determined to have an HEL of 7.1 ± 0.3 GPa, corresponding to an elastic strain of ~4%. Experiments performed at a peak stress exceeding the HEL yielded a two-wave structure consisting of an elastic precursor and a plastic wave, as shown in Figure 2.19. This study led to the conclusion that the shear strength of this amorphous alloy is reduced as it is shocked above the HEL. In another study using plate impact experiments instrumented with VISAR velocity

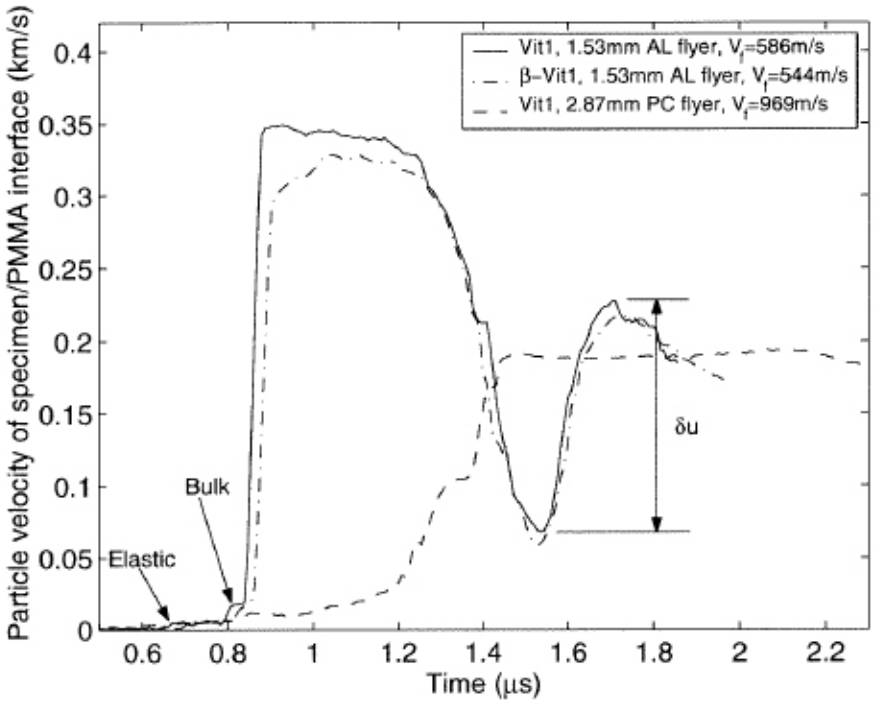

Figure 2.16: Particle velocity profiles obtained during plate impact experiments of Vitreloy1 and its partially crystallized composite, α-Vitreloy1 [29]. The wave profiles show drops in free surface particle velocity (δu) indicative of spall in both materials. The spall strengths were determined to be 2.35 GPa for Vitreloy1 and 2.11 GPa for β-Vitreloy1.

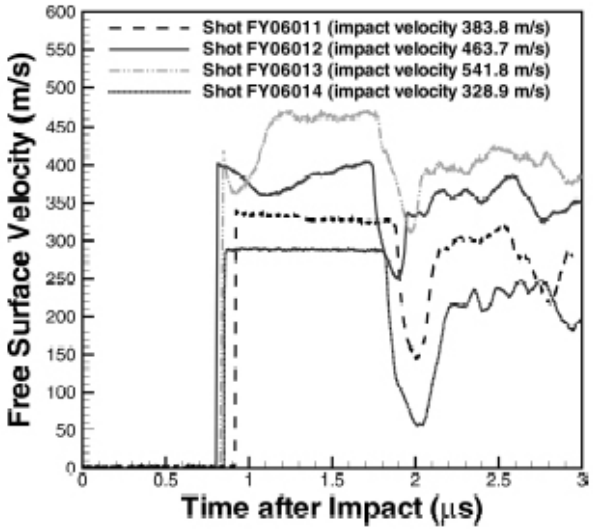

Figure 2.17: Free surface velocity traces from plate impact of Vitreloy1 showing drops in free surface velocity indicative of spall failure [64]. Spall strengths were determined to be 3.5, 2.72, 2.35, and 2.33 GPa at shock input stresses of 4.4, 5.1, 6.0 and 7.0 GPa, respectively.

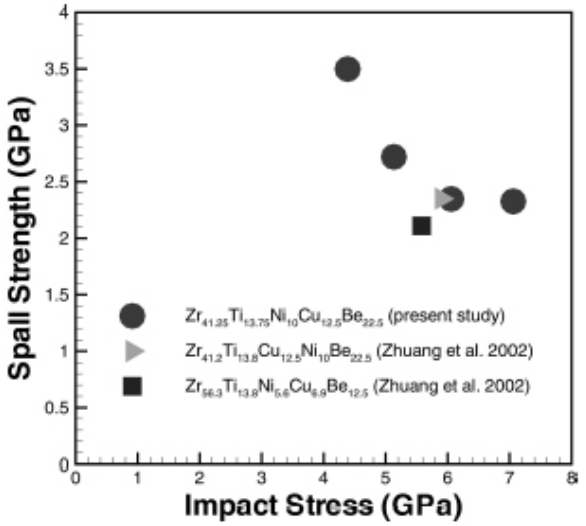

Figure 2.18: Dependence of spall strength on impact stress for Zr-based BMGs [64] showing a decrease in spall strength with increasing impact stress.

interferometry, the HEL of Vitreloy1 ($Zr_{41.25}Ti_{13.75}Ni_{10}Cu_{12.5}Be_{22.5}$) BMG was determined to be 6.15 GPa [64]. The free surface velocity profiles from these experiments are shown in Figure 2.20. In both studies, the VISAR traces showed characteristics typical of an ideal elasto-isotropic solid, in which shear strength is catastrophically lost above the HEL [67], as shown schematically in Figure 2.21. Additionally, the peak at the elastic precursor front seen in the VISAR traces recorded by Yuan et al. [64] (Figure 2.20) becomes sharper with increasing impact velocity, as is typical for shock wave measurements on elasto-isotropic solids lacking strain-hardening capability [64, 67]. Mashimo et al. [68] observed a kink in streak camera images corresponding to an HEL of 6.2 GPa in $Zr_{55}Al_{10}Ni_5Cu_{30}$ BMG. Similar to the experiments utilizing velocity interferometry, experiments performed at a peak stress exceeding the HEL yielded a two-wave structure consisting of an elastic precursor and a plastic wave.

2.3.3 Temperature Dependence of Mechanical Properties of Bulk Metallic Glasses

At high temperatures, a dynamic equilibrium can be established between the creation of free volume due to stress-driven shearing and annihilation of free volume due to diffusional rearrangement [24, 30, 69]. As a result of this equilibrium, homogeneous Newtonian flow with a dependence of stress on strain rate is expected at temperatures near T_g. This strain rate dependence at temperatures near T_g was shown in Figure 2.15. An increase in strain rate or decrease in temperature prevents diffusional rearrangement from keeping up with creation of free volume and establishment of this equilibrium will not take place, thus leading to inhomogeneous flow with localized shear deformation [24]. A detailed understanding of the deformation mechanisms and mechanical properties of bulk metallic glasses as a function of temperature has been the topic of several studies, which are discussed here.

The deformation mechanisms of $Zr_{55}Cu_{30}Al_{10}Ni_5$ BMG in the supercooled liquid state were studied by Heilmaier and Eckert [30]. It was observed that the stress levels reached during compressive loading were much lower than those reached during room temperature

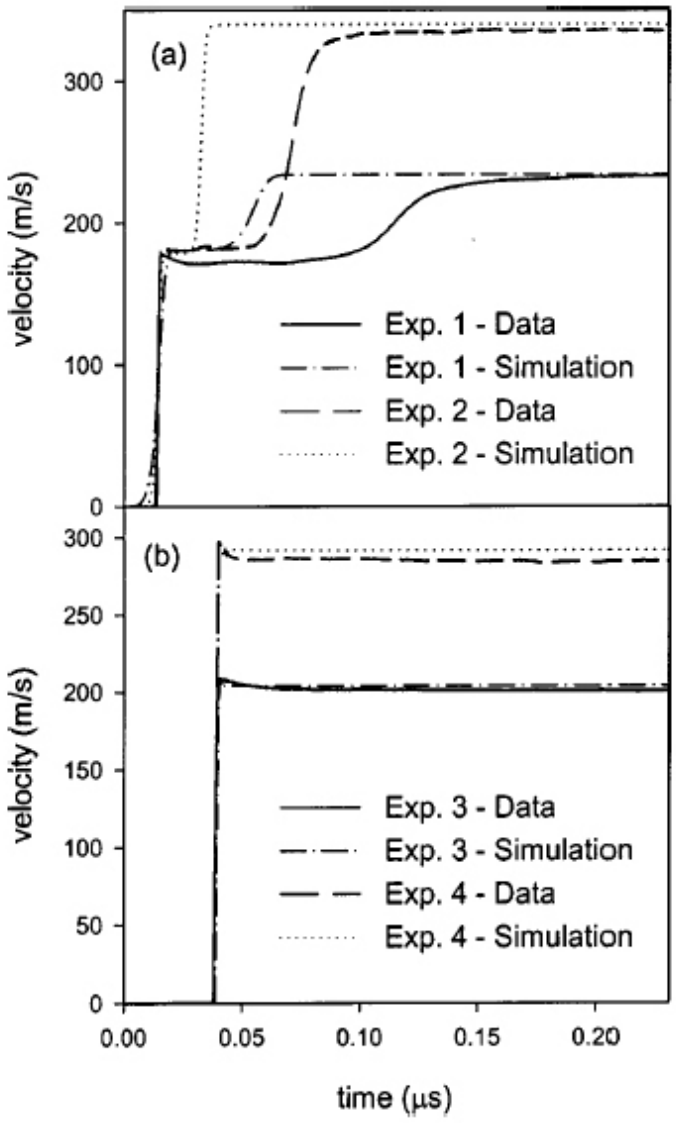

Figure 2.19: Velocity as a function of time profiles showing two-wave structures consisting of an elastic precursor, indicative of HEL, and plastic wave [66]. The wave profiles are characteristic of a material in which shear strength is reduced as it is shocked above the HEL. The HEL was determined to be 7.1 ± 0.3 GPa.

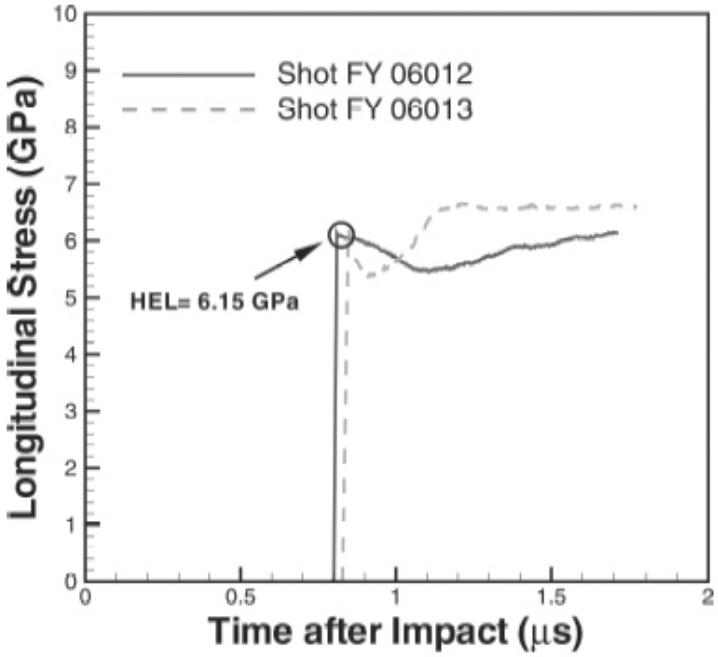

Figure 2.20: Longitudinal stress as a function of time profiles showing the HEL of Vitreloy1 BMG [64]. The HEL peaks get increasingly sharper with impact velocity, which is characteristic of an ideal elasto-isotropic solid, in which shear strength is catastrophically lost above the HEL [67], as shown schematically in Figure 2.21.

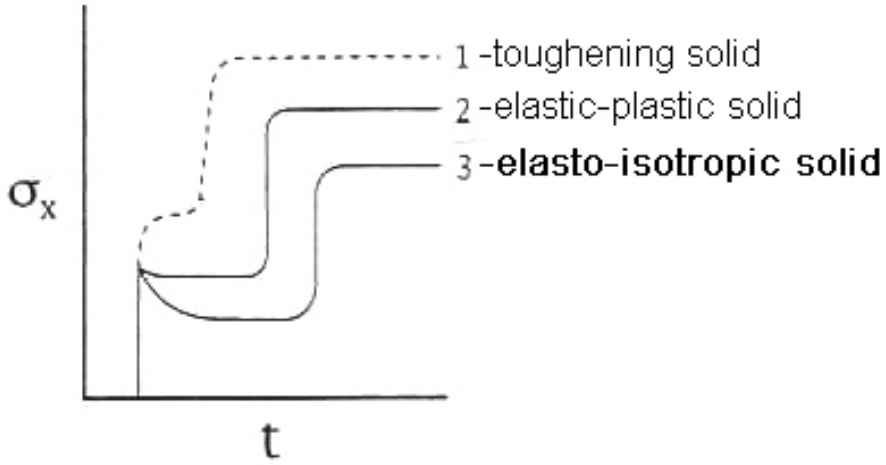

Figure 2.21: Schematic profiles of longitudinal stress as a function of time comparing a toughening solid, elastic-plastic solid and elasto-isotropic solid, which loses shear strength above its HEL [67]. The wave profiles of BMGs show characteristics of the elasto-isotropic solid.

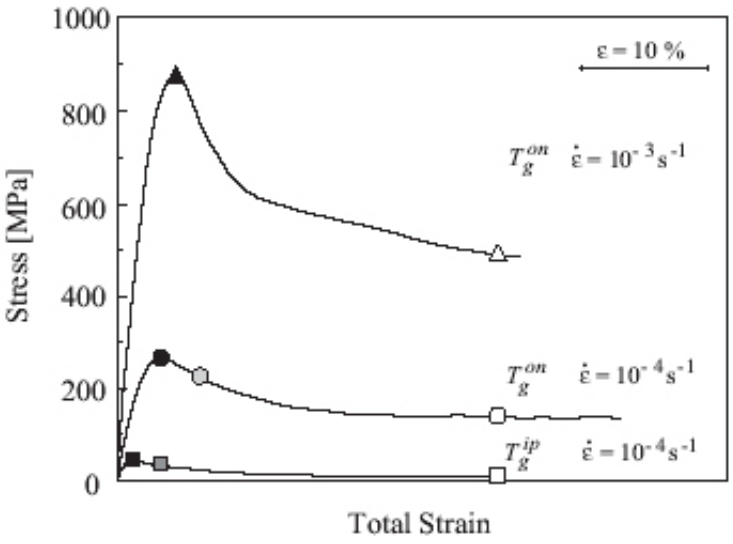

Figure 2.22: Compressive stress-strain response of $Zr_{55}Cu_{30}Al_{10}Ni_5$ BMG the onset of T_g and the inflection point of T_g at varying strain rates. The curves show the overshoot stress that is commonly observed in high temperature testing as well as the pronounced strain rate sensitivity [30].

testing, and a large dependence on strain rate was observed, as can be seen in Figure 2.22. It was also observed that the BMGs exhibited an increased amount of plasticity such that the tests were stopped after 30% strain without failure, in comparison to a room temperature elastic limit on the order of ~1-2% [3]. Additionally, a peak stress, or stress overshoot, was observed in all tests. This stress represents the stress level at which the internal shear stresses are sufficiently large to create additional free volume, and thus lead to a decrease in viscosity. The atomic jumps cause a decrease in the stress level until diffusional rearrangement catches up and dynamic free volume equilibrium is attained.

Wang et al. [70] studied the compressive fracture characteristics of $Zr_{41.25}Ti_{13.75}Ni_{10}$-$Cu_{12.5}Be_{22.5}$ at the glass transition temperature (616 K) and in the supercooled liquid region. Under uniaxial compressive loading slightly above T_g (T=636 K), the deformation behavior of this BMG was found to transition from homogeneous deformation to inhomogeneous deformation as the strain rate was increased, as is suggested by the deformation

map (Figure 2.2) created by Spaepen [24]. This mechanistic change resulted in a ductile to brittle transition with increasing strain rate.This transition occurred at strain rates of $1x10^{-2}$, $1x10^{-1}$, and $7.4x10^{-1}$ s^{-1} for test temperatures of 616, 636, and 656 K, respectively. At a test temperature of 676 K, catastrophic failure did not occur at strain rates up to 1 s^{-1}. Failure stress was also found to decrease from 1545 to 1360 to 1219 MPa as test temperatures increased from 616 to 636 to 656 K, respectively. These stresses are all significantly less than the failure stress at room temperature (1906 MPa). The failure angles of the specimens increased from 40° to 56° over the temperature range of 616 to 656 K, indicating a change in the role of normal stress. This change in failure angle was attributed to an increase in cohesive strength with increasing strain rate, based on the Mohr-Coulomb criterion. Additionally, as the test temperature increased beyond the glass transition, the characteristics observed on the fracture surfaces changed. Radial cores, which are typical of tensile fracture surfaces at room temperature [28], as well as large areas of disorganized flow, appeared on compressive fracture surfaces which were tested at 636 and 656 K, in contrast to the organized veinal pattern observed on the fracture surface of the 616 K test specimens, and likewise at room temperature.

The temperature-dependent deformation of an alloy of nearly the same composition ($Zr_{41.2}Ti_{13.8}Ni_{10}Cu_{12.5}Be_{22.5}$, Vitreloy1) was studied by Wang et al. [71]. The glass transition temperature of this material was determined to be 355 °C using differential scanning calorimetry. Quasi-static compression experiments at a strain rate of $5x10^{-4}$ s^{-1} and test temperatures ranging from 346 to 373 °C revealed a decrease in strength with increasing temperature, as expected. The variation in the stress-strain response at a constant strain rate and varying test temperature can be seen in Figure 2.23. In agreement with the deformation map (Figure 2.2) made by Spaepen [24], non-Newtonian flow was observed at low temperatures and high strain rates, whereas increases in temperature or decreases in strain rate caused the BMG to undergo Newtonian flow.

Lu et al. [62] used Split Hopkinson Bar experiments to study the dynamic deformation

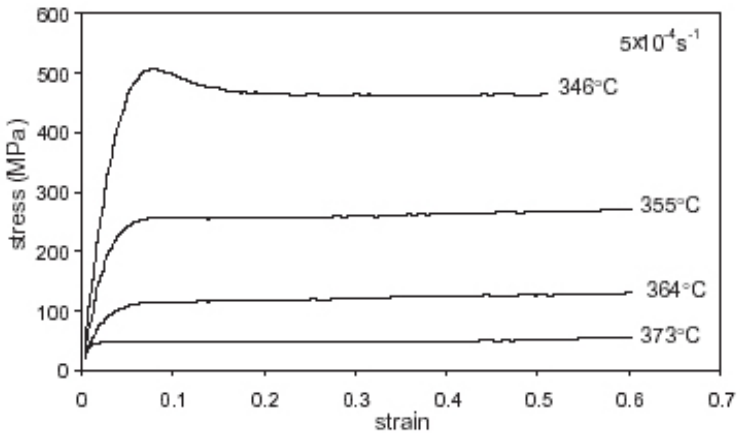

Figure 2.23: Compressive stress-strain response of $Zr_{41.2}Ti_{13.8}Ni_{10}Cu_{12.5}Be_{22.5}$ at a strain rate of $5x10^{-4}$ s^{-1} and test temperatures of 346, 355, 364, and 373 °C [71] revealing a decrease in flow stress with increasing test temperature.

behavior of Vitreloy1 (T_g~623 K) over a range of strain-rates and temperatures. Figure 2.24 shows the compressive stress-strain response of Vitreloy1 at a strain rate of $1x10^{-1}$ s^{-1} and test temperatures of 295, 523, 643, 663, and 683 K. It is evident from the change in the stress-strain response (brittle to ductile) that the deformation mechanism is changing from inhomogeneous (failure along a single shear plane) to homogeneous (uniform macroscopic deformation, no macroscopic shear) as temperature increases. A decrease in the elastic modulus was also observed as the test temperature increased, and stress overshoot (due to the free volume-induced structural relaxation) became evident at 663 K. This study showed strain-rate sensitivity only in the temperature range near T_g, as can be seen in Figure 2.25, however this sensitivity was insignificant at high strain rates (10^2-10^3 s^{-1}). Strain rate sensitivity was previously discussed in more detail in Section 2.3.2.4, but the overall results from this study by Lu et al. [62] show that the effects of strain rate and temperature on the deformation of bulk metallic glasses show opposing trends- as strain rate increases, deformation changes from homogeneous to inhomogeneous, and as temperature increases, deformation changes from inhomogeneous to homogeneous deformation.

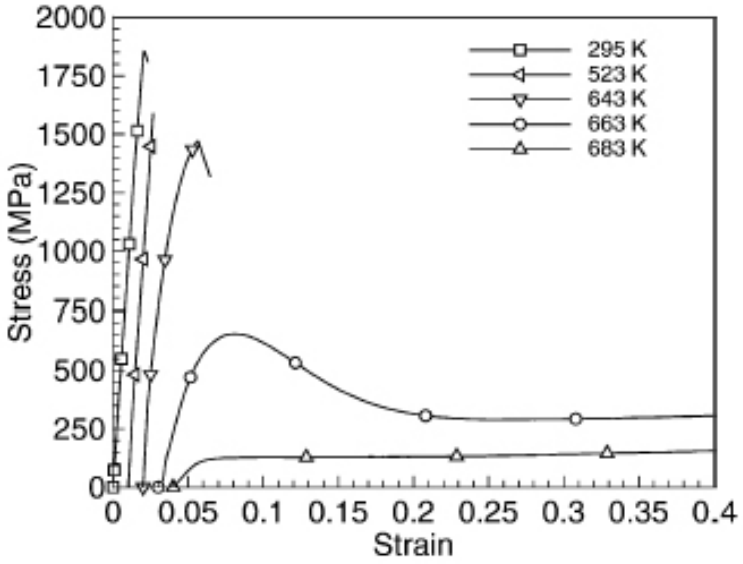

Figure 2.24: Effect of temperature on uniaxial stress-strain behavior of Vitreloy1 at a strain rate of $1x10^{-1}$ s^{-1} and temperatures ranging from 295 to 683 K. A chance in deformation mode from inhomogeneous to homogeneous can be seen between test temperatures of 643 and 663 K [62]. Stress overshoot due to free volume-induced structural relaxation was evident at and above a temperature of 663 K.

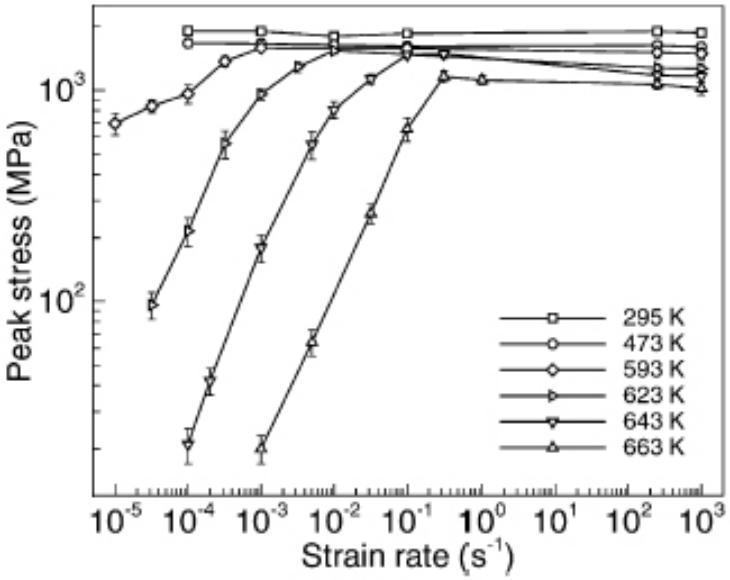

Figure 2.25: Peak stress as a function of strain rate for test temperatures ranging from 295 to 663 K. This data shows significant strain-rate sensitivity at high test temperatures, but this sensitivity becomes negligible at high strain rates [62].

2.4 Constitutive Mechanical Behavior of Bulk Metallic Glasses

Both the tensile and compressive failure angles of metallic glasses deviate from the maximum shear stress plane (45°) [19, 25, 31, 42, 43, 45, 46]. As previously mentioned (Section 2.3.1), the compressive failure angle of BMGs is ~43° from the loading axis [19, 21, 22, 28, 31, 38, 42, 43, 45, 72] and the tensile failure angle is ~56° (50-65°) [19, 42, 43, 45, 46]. This deviation has been the basis of the premise that BMGs exhibit a normal stress dependence [19, 21–23, 25, 28, 31, 38, 42–44, 72] and that their failure does not follow the von Mises criterion [21, 23, 28, 31, 38, 45, 72–74]. The von Mises criterion, which incorporates only shear stresses, predicts that yield will occur on any plane when the resolved shear stress reaches a certain critical value. The Mohr-Coulomb (or a similar) criterion has been found to be applicable to deformation and failure of BMGs [22, 23, 31, 38, 45, 72, 74, 75]. The Mohr-Coulomb criterion, which is given in Equation 1, incorporates the normal stress, which activates the flow on the slip-plane:

$$\tau_y = k_0 - \alpha\sigma_n \tag{1}$$

In this equation, τ_y is the effective shear yield stress, k_0 is the shear resistance of the glass, σ_n is the stress normal to the plane of yielding, and α corresponds to the normal stress coefficient, which is related to the deviation of the fracture surface from 45°.

Verification of the applicability of this type of criterion has been provided by Donovan [23] on tests performed on $Pd_{40}Ni_{40}P_{20}$ which showed that the yield strengths in uniaxial and plane strain compression are nearly the same, as expected from the criterion. Additionally, indentation studies coupled with simulations have been used by Vaidyanathan et al. [75] to gain further insight into the deformation of bulk metallic glasses. Comparisons were made between the experimental data and simulations utilizing elastic theory, and the von Mises and Mohr-Coulomb yield criteria. The Mohr-Coulomb yield criterion provided the closest approximation to the experimental data and this serves as further verification

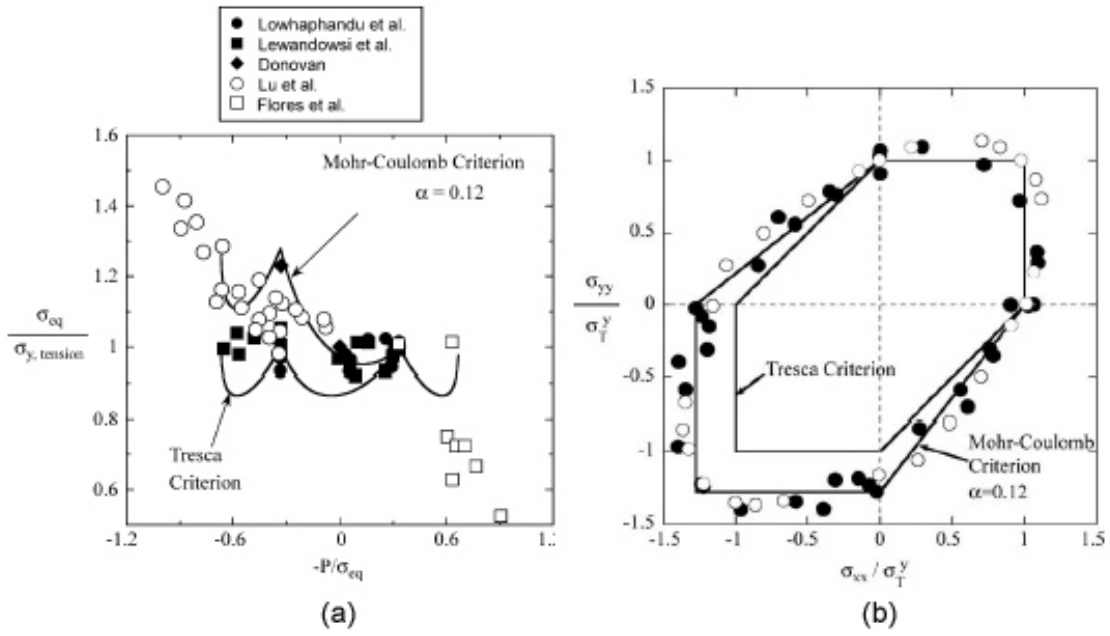

Figure 2.26: (a) Compilation of experimental data for multiaxial yield of metallic glasses prepared by Lund and Schuh [22]; original data is from [31, 42, 72, 77, 78]. Plot of equivalent stress, normalized by tensile yield stress, as a function of the triaxiality parameter. The Mohr-Coulomb and Tresca criterion are shown, and the Mohr-Coulomb criterion shows the appropriate negative trend with pressure and offers a reasonable description of the data. (b) Simulation data produced by Lund and Schuh [22] for the biaxial yield surface of amorphous materials including simulated Cu-Zr (•) [38] and a simulated glassy polymer (○) [76]. This shows that the Mohr-Coulomb criterion is a better descriptor than the Tresca criterion for the yield of amorphous materials.

that metallic glasses do not follow von Mises yield criterion.

Lund and Schuh [22] compiled a review of the experimental and simulation-based evidence for asymmetric yielding in metallic glasses, concluding that there is indeed a measurable influence of normal stress on the plastic yielding of metallic glasses, and that the Mohr-Coulomb criterion describes the appropriate negative trend with pressure, as shown in Figure 2.26(a). Furthermore, simulations performed to gain insight into the yielding of amorphous materials, including Cu-Zr metallic glasses [38] and a glassy polymer [76] have shown that the data for the biaxial yield surface exhibits a clear asymmetry for both sets of materials and this asymmetry was well-described by the Mohr Coulomb criterion, as shown in Figure 2.26(b).

The Drucker-Prager [79] constitutive model considers pressure-dependence of a material and can be made to closely approximate the Mohr-Coulomb yield function. Because of its similarities to Mohr-Coulomb and its inclusion of normal stress, the Drucker-Prager model has been used to model the deformation of metallic glasses [74]. Indentation studies of Vitreloy1 coupled with simulations employing the extended Drucker-Prager model have shown that this model is capable of capturing the material response during dynamic indentation [29, 74]. Because this model shows potential for modeling the deformation of a BMG composite, it was used in this work.

Because of the interest in understanding the failure criterion of metallic glasses, a few studies have investigated the effects of pressure or normal stress on yield in the quasi-static regime. Lu et al. [78] conducted experiments on $Zr_{41.2}Ti_{13.8}Cu_{12.5}Ni_{10}Be_{22.5}$ BMG and reported that critical shear stress is not necessarily a function of normal stress, but hydrostatic pressure, as can be seen by the plot of shear stress as a function of pressure shown in Figure 2.27. In contrast, Lewandowski et al. [42, 72] reported evidence of a normal stress dependence, with no significant dependence on hydrostatic pressure, for the same BMG, as shown in Figure 2.28. Further investigation of these effects is undoubtedly necessary; additionally, these effects have not yet been investigated in the high strain-rate regime. So although there is a general agreement that the failure of BMGs is better described by a Mohr-Coulomb type criterion in comparison to a von Mises type, many questions remain about the constitutive behavior of BMGs.

2.5 Phase Stability of Bulk Metallic Glasses

2.5.1 Thermal Stability of Bulk Metallic Glasses

Bulk metallic glasses undergo several transitions with increasing temperature. When in range of the glass transition temperature (T_g), crystallization temperature (T_x), and melting temperature (T_m), the properties of BMGs can be affected, and as such it is important that these transitions are well characterized. Differential Scanning Calorimetry (DSC) has

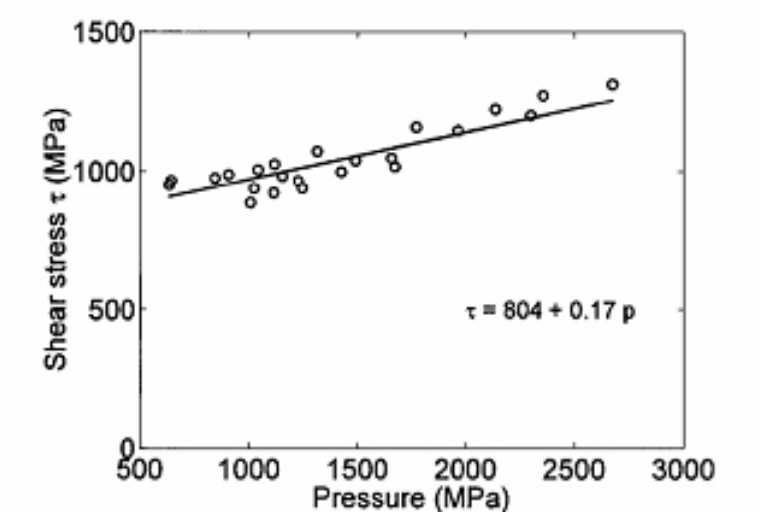

Figure 2.27: Critical shear stress as a function of pressure data for Vitreloy1 suggesting that critical shear stress is a function of hydrostatic pressure [78].

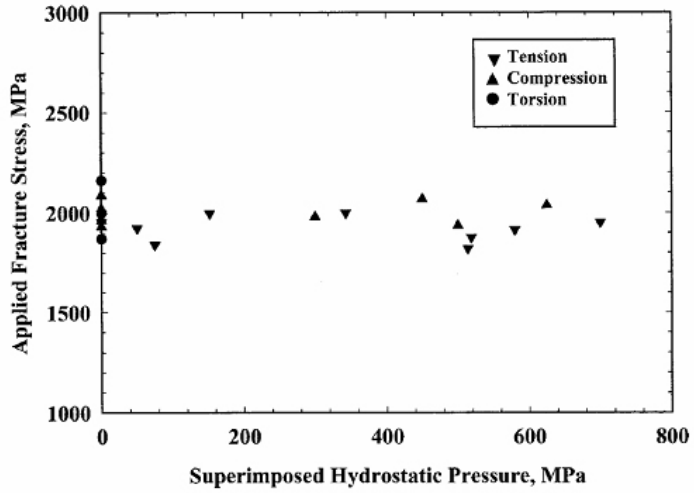

Figure 2.28: Fracture stress as a function of superimposed hydrostatic pressure data for Vitreloy1 suggesting no dependence of failure on hydrostatic stress [72].

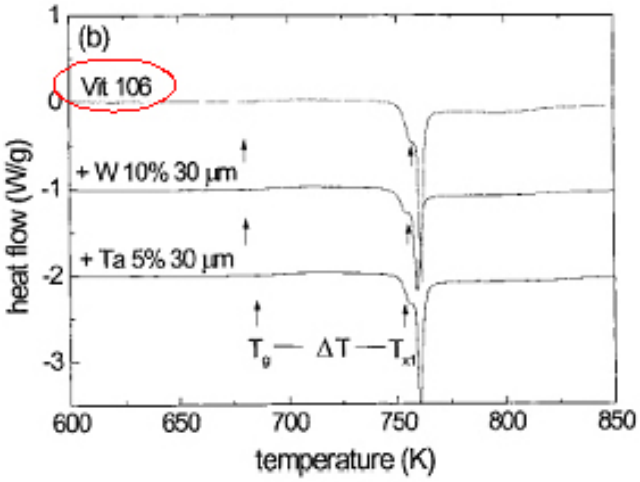

Figure 2.29: DSC curves for LM106 (and various composite compositions) revealing a glass transition temperature of 405-414 °C and a crystallization temperature of 478-480 °C [7]. As is shown by the comparison of the curves for the monolithic glass and the glass containing 10% W, these transition temperatures were not affected by the addition of tungsten particles.

been used to investigate the thermal properties of Zr-based BMGs, as shown in the Figures 2.29 and 2.30. Figure 2.29 shows the DSC curves for LM106 as well as various composite compositions revealing a glass transition temperature of 405-414 °C and a crystallization temperature of 478-480 °C [7]. This study also demonstrated that these transition temperatures were not affected by the addition of tungsten particles. Figure 2.30 shows DSC curves of a slightly different BMG, $Zr_{55}Cu_{30}Ni_{10}Al_5$. The thermal properties of this BMG were studied as a function of heating rate and it was shown that the glass transition temperature was unchanged but the crystallization temperature increased with heating rate.

2.5.2 Stress and Strain-rate-induced Crystallization

It is known that BMGs crystallize with the availability of thermal energy. The phenomenon of stress-induced crystallization in BMGs has also been investigated in a few studies. Stress-induced nano-crystallization of bulk metallic glasses has been observed by Kim et al. [80] and Boucharat et al. [81] using nanoindentation and high-stress (6 GPa) torsion

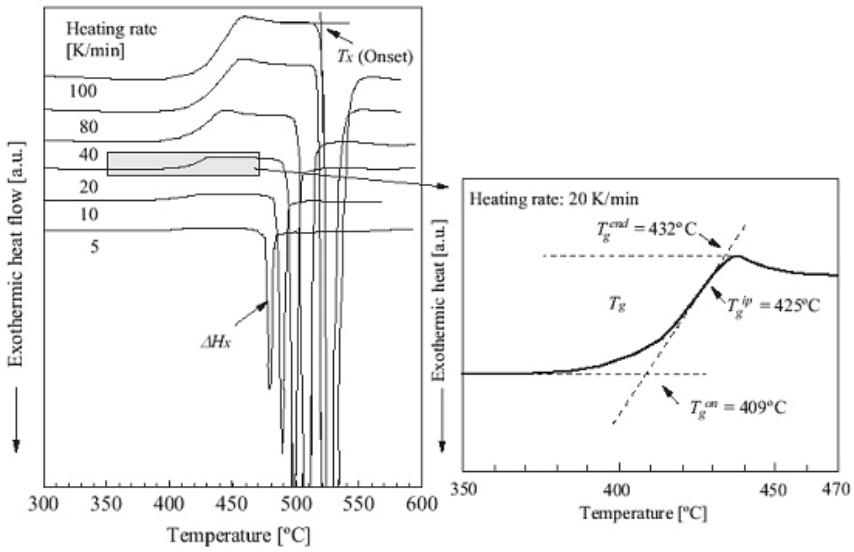

Figure 2.30: DSC curves of $Zr_{55}Cu_{30}Ni_{10}Al_5$ at different heating rates showing an increase in crystallization temperature with heating rate, but no effect on the glass transition temperature [30].

straining, respectively. Kim et al. [80] took extreme caution to insure that the nanocrystallites that formed were a result of stress and not thermal effects; for example, the indentations were performed at 2mN/s and TEM specimens were thinned from the side opposite the indent. TEM images of indents made by Kim et al. [80] and corresponding single area diffraction patterns showing nanocrystallites are shown in Figure 2.31. This phenomenon of stress-induced crystallization was described as a consequence of flow dilatation in shear bands and radically enhanced diffusional mobility. The nanocrystals observed by Boucharat et al. [81] were observed to appear predominantly in the shear bands, but also in the surrounding amorphous matrix, which is an indication that there is another process besides enhanced mobility within the shear bands that is contributing to deformation-induced crystallization. The phenomenon of stress-induced crystallization in BMGs has not previously been investigated at high stresses (above 6 GPa). Furthermore, the effect of stress-induced crystallization on mechanical properties has yet to be investigated.

Lohwongwatana et al. [82] observed strain-rate-induced crystallization during splat cooling. Whereas a purely amorphous specimen could be produced at low strain rates,

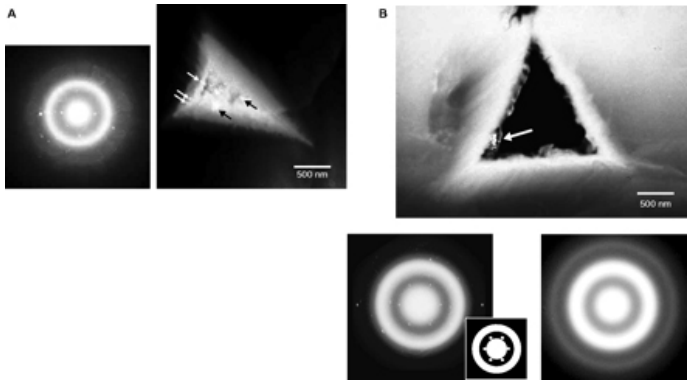

Figure 2.31: TEM images of indents and corresponding single area diffraction patterns showing nanocrystallites formed as a result of applied stress (and with no temperature rise) [80].

increases in rate caused the final alloy to be only partially amorphous. A phase separation process was suggested to explain the crystallization behavior, but this could simply be an effect of changes in cooling rate at different strain rates.

2.5.3 Equation of State and High Pressure Phase Transformations

As discussed in previous sections, the high-strain-rate behavior of bulk metallic glasses have been investigated in some detail, but few studies have been conducted to investigate the high-pressure equation of state (EOS), phase stability behavior, and shock wave response of monolithic bulk metallic glasses. When studying the shock response of amorphous materials, it is not unexpected for stress traces to show considerable dispersion in the shock front in the rising part of the waveform, as shown schematically in Figure 2.32, due to their negative first pressure derivative of elastic modulus [67]. Additionally, when evaluating the equation of state of bulk metallic glasses in shock velocity-particle velocity (U_s-U_p) space, the effects of the dispersed elastic shock front are evidenced by a negative slope in the elastic region, as shown schematically in Figure 2.33.

The shock wave response of $Zr_{41.2}Ti_{13.8}Cu_{12.5}Ni_{10}Be_{22.5}$ (LM1) has been investigated by Zhuang et al. [63] up to stresses of 24 GPa and by Yuan et al. [64] in the stress range of 5-7 GPa using planar impact experiments instrumented with VISAR to capture the wave

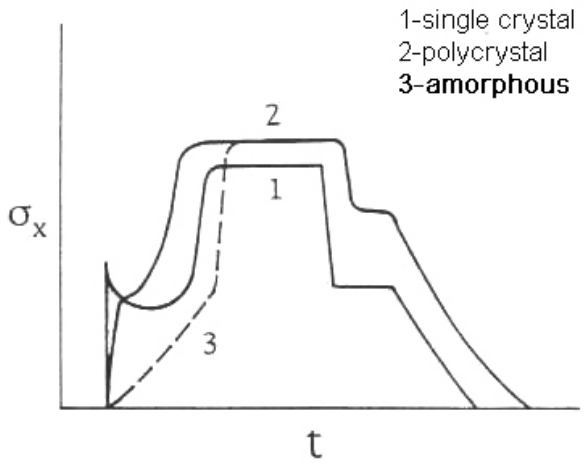

Figure 2.32: Schematic profiles of longitudinal stress as a function of time for a single crystal, polycrystal and amorphous material, which shows dispersion in its shock front due to the negative first pressure derivative of elastic modulus [67].

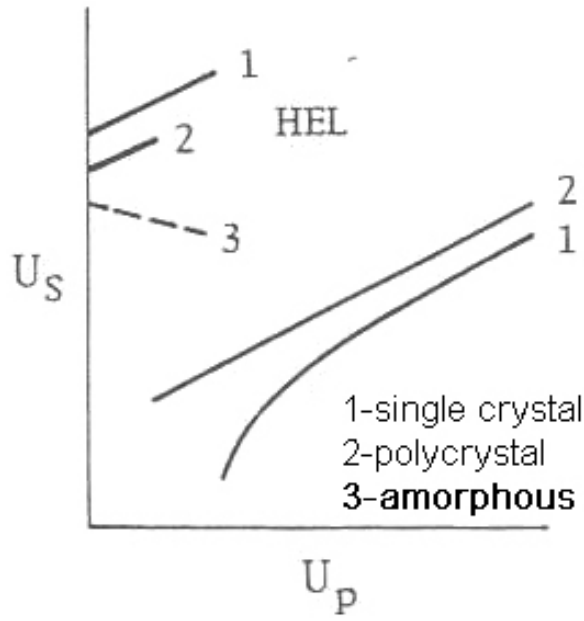

Figure 2.33: Schematic of shock velocity as a function of particle velocity for a single crystal, polycrystal and amorphous material [67]. An amorphous material commonly exhibits a negative slope in the elastic regime due to the dispersion in the rising part of the shock front (Figure 2.32) due to the negative first pressure derivative of elastic modulus.

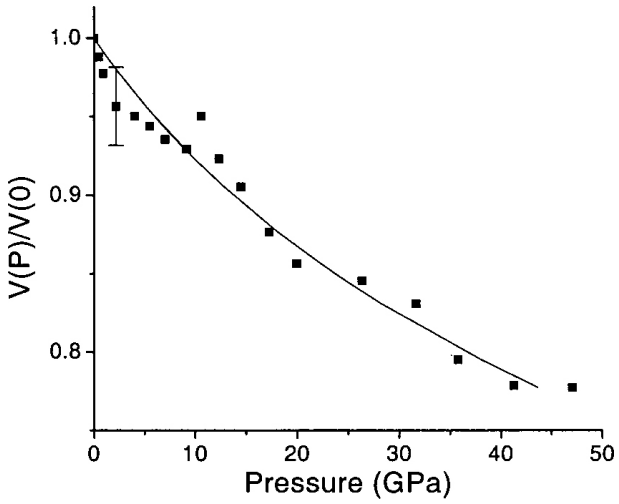

Figure 2.34: Compression data of $Zr_{41.2}Ti_{13.8}Cu_{12.5}Ni_{10}Be_{22.5}$ at room temperature obtained using synchrotron x-ray diffraction measurements. Solid curve is the Birch equation of state [83].

profiles. This same BMG ($Zr_{41.2}Ti_{13.8}Cu_{12.5}Ni_{10}Be_{22.5}$) was also studied by Jiang et al. [83] using high-stress x-ray diffraction measurements with synchrotron radiation up to a stress of ~47 GPa. Results from this study are shown in Figure 2.34. The pressure-volume equation of state of a slightly different BMG, $Zr_{41}Ti_{14}Cu_{12.5}Ni_{10}Be_{22.5}$, was studied by Pan et al. [84] using a piston-cylinder displacement technique up to a stress of 4.5 GPa; the authors observed remarkable non-linear characteristics in the low stress regime, indicative of the existence of a large amount of free volume. Results from the study by Pan et al. [84] are shown in Figure 2.35. Similarly, Wang et al. [85] noticed pressure-induced structural relaxation of the BMG, which gave rise to rapid volumetric changes in $Pd_{39}Ni_{10}Cu_{30}P_{21}$ up to 23.5 GPa in their investigation using high pressure energy dispersive x-ray diffraction with a synchrotron radiation source.

Turneaure et al. [66] studied the shock wave response of $Zr_{56.7}Cu_{15.3}Ni_{12.5}Nb_5Al_{10}Y_{0.5}$ in the stress range of 9-13 GPa using planar impact experiments instrumented with VISAR. The compression behavior of $Zr_{44}Nb_7Cu_{13.5}Ni_{10.8}Be_{24.3}$ was investigated by Gong et al. [86] using high-stress energy dispersive x-ray diffraction with a synchrotron radiation source coupled with calculations of the radial distribution function at stresses up to 39 GPa.

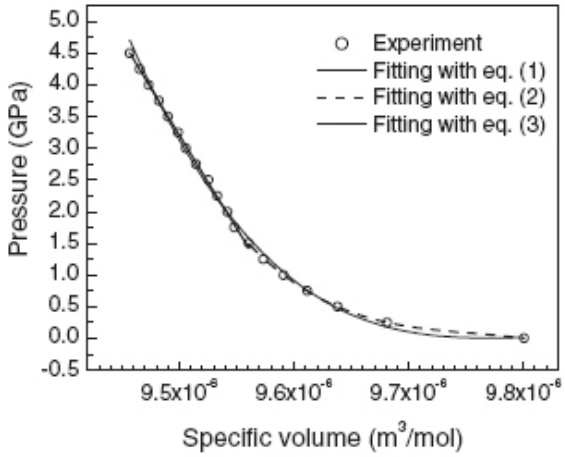

Figure 2.35: Compression data of $Zr_{41}Ti_{14}Cu_{12.5}Ni_{10}Be_{22.5}$ obtained using a piston-cylinder technique [84]. Equations 1-3 are polynomial fits to the data. The non-linear characteristics in the low stress regime indicate existenc eof a large amount of free volume.

Mashimo et al. [68] have recently investigated the Hugoniot compression curve of amorphous $Zr_{55}Al_{10}Ni_5Cu_{30}$ and a fully crystalline alloy of the same composition (consisting of crystals of cF-Zr_2Ni, tIZr_2Cu, and hP-$AlCu_2Zr$) up to stresses of 50 GPa using the inclined mirror technique. This study by Mashimo et al. [68] revealed a kink in the U_s-U_p data for the BMG at approximately 14 GPa, which was attributed to a probable phase transition. The crystalline alloy did not show any kink indicative of a phase transition. This data is shown in Figure 2.36. Although the U_s-U_p data indicated a phase transformation, samples recovered by Mashimo et al. [68, 87] after shock experiments up to 40 GPa still showed amorphous diffraction patterns. The authors suggested that this discrepancy was either because the transition was to a crystalline phase which didn't grow large enough during the nano-microsecond duration of shock wave experiments to be identified by x-ray diffraction, or because the transition was to a more dense amorphous phase followed by a return to the original amorphous phase [87]. This discrepancy between recovered specimens and shock-compression data is analogous to what was observed by Wackerle [88] during an investigation of the Hugoniot of quartz in which recovered specimens seemed to be unchanged from their starting state, although $U_s - U_p$ data indicated a phase change.

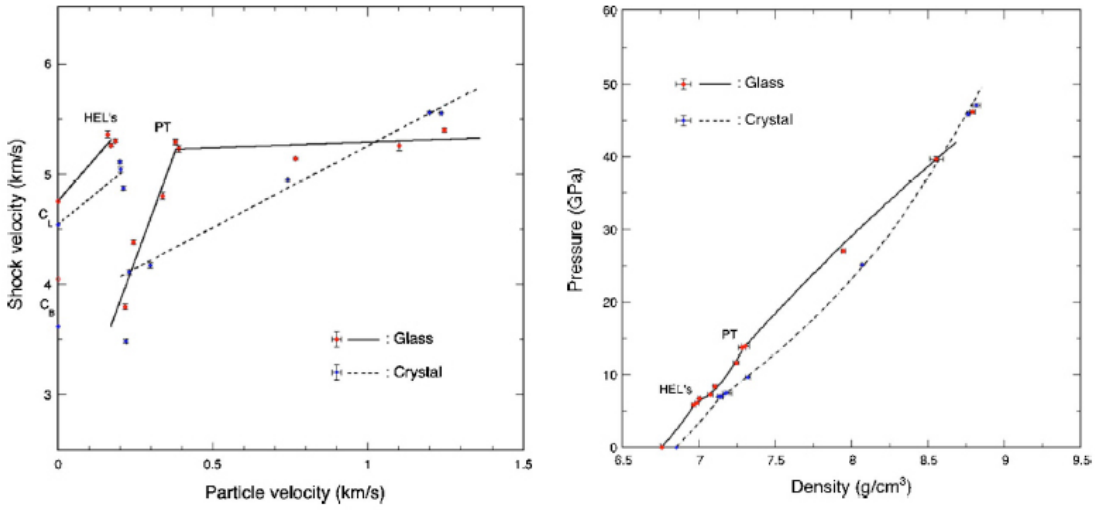

Figure 2.36: Hugoniot data of $Zr_{55}Al_{10}Ni_5Cu_{30}$ BMG and its fully-crystalline alloy up to 50 GPa. (a) U_s-U_p data revealing a kink, which is indicative of phase transformation, at 14 GPa in the BMG data. The crystalline alloy did not show any deviations from linearity indicative of phase changes. (b) Pressure-density data again showing the phase change in the amorphous alloy, but not its crystalline counterpart [68].

Under static high pressure to 30 GPa, the high pressure phase stability of $Ce_{55}Al_{45}$ BMG was investigated using a diamond anvil cell and in situ x-ray diffraction [89]. The authors found that $Ce_{55}Al_{45}$ exhibited polyamorphism over this pressure range, evidenced by a shifting of the diffraction peak to higher momentum transfer and changes in the diffraction intensity maximum, as shown in Figure 2.37. Perhaps this work helps to elucidate the nature of some of the high pressure phase changes observed in amorphous metals under shock loading since no crystalline phases have been detected in recovered materials but there is evidence of phase transformation from shock experiments- the transitions are possibly occurring from one amorphous phase to another.

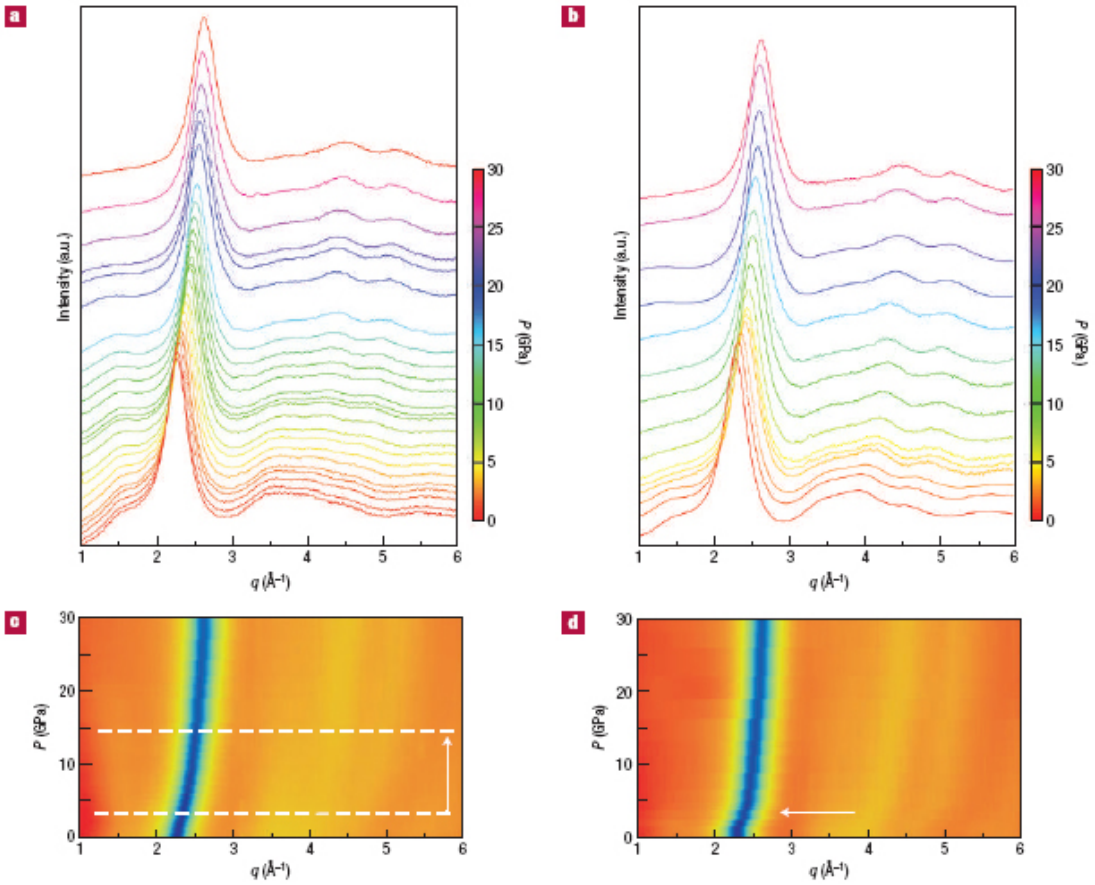

Figure 2.37: X-ray diffraction patterns of $Ce_{55}Al_{45}$ BMG as a function of pressure in a diamond anvil cell. (a) Data collected during compression, and (b) data collected during decompression, and (c,d) intensity peak shift as a function of pressure [89]. Data shows shifting of the diffraction peak to higher momentum transfer and changes in the diffraction intensity maximum indicating transition from one amorphous state to another, or polyamorphism.

2.6 Mechanical Behavior of Bulk Metallic Glass Matrix Composites

2.6.1 Mechanical Behavior of Intrinsic Composites

During processing of metallic glasses, nanoscale crystalline particles can be formed in the amorphous phase due to: (1) multistage crystallization process; (2) existence of homogeneous nucleation sites in the amorphous phase and a high nucleation rate; (3) suppression of growth of solute element at nanocrystal/amorphous interface (low growth rate); and (4) high thermal stability of the remaining amorphous phase by the redistribution of the solute elements at the amorphous/crystalline interface [90].

An increase in the strength of amorphous alloys has been observed in alloys with nanocrystals, formed by annealing the melt-spun amorphous single-phase, dispersed in an amorphous matrix. The effects of nanocrystallites on the mechanical properties of a Zr-Nb-Cu- Al alloys were investigated by Fan et al. [91]. The structures contained a homogeneous dispersion of nanocrystals (<15 nm in size) in the amorphous matrix. The results, which are presented in Figure 2.38, show a linear increase in tensile fracture strength (σ_f) and Vicker's hardness (H_v) with increasing volume fraction of nanocrystallites. This trend continued up to 50 vol%, where good bending ductility was still maintained. The value of σ_f increased from 1550 MPa with 0% nanocrystallites to 1910 MPa with 50 vol% nanocrystallites. The value of H_v increased from 470 to 524 when the volume fraction of nanocrystallites was increased from 0 to 50%. These effects have been seen in similar studies on many other Zr-based alloy systems [20, 90–93]. The addition of nanocrystallites to amorphous alloys has also been shown to increase plasticity. An example of compressive-strain curves of a Zr-Cu-Pd-Al alloy containing varying amounts of nanocrystals can be seen in Figure 2.39. This figure illustrates an increase in plasticity (nearly double) upon 27% nanocrystallization (Figure 2.39, curve (c)) of $Zr_{60}Cu_{20}Pd_{10}Al_{10}$ compared to the as-quenched material (Figure 2.39, curve (b)). This plasticity does not increase further with increasing amount of nanocrystals (> 27%), but an increase in compressive strength can be seen.

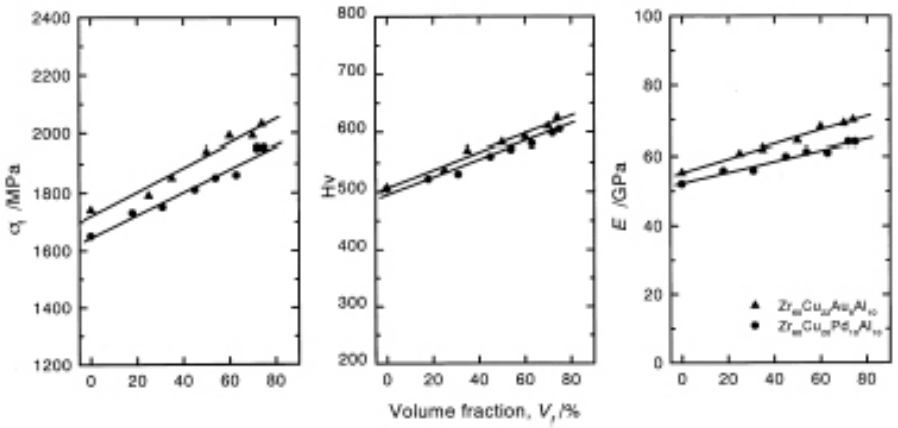

Figure 2.38: Increases in tensile fracture strength (σ_f), Vicker's hardness (H_v), and Young's modulus (E) with volume fraction (V_f) Zr_2(Cu,Pd) nanocrystalline compound in $Zr_{60}Al_{10}Cu_{20}Pd_{10}$ and $Zr_{60}Al_{10}Cu_{22}Au_8$ amorphous alloys [20].

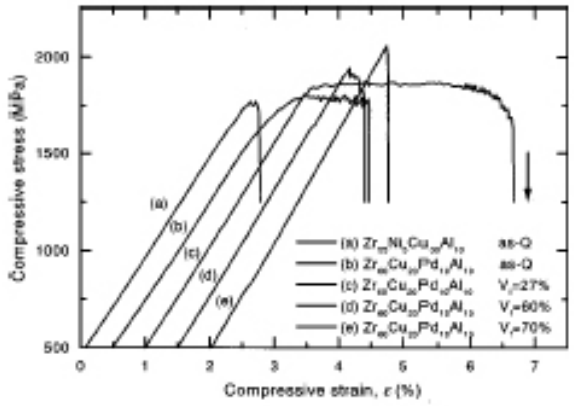

Figure 2.39: Compressive stress-strain curves for (a) bulk $Zr_{55}Ni_5Cu_{30}Al_{10}$ metallic glass; and (b), (c), (d), and (e) as-quenched and nanocrystalline bulk $Zr_{60}Cu_{20}Pd_{10}Al_{10}$ [92]. An increase of ~100% in plasticity upon 27% nanocrystallization is evident, but no further increase is observed with >27% nanocrystallites. However, compressive strength continues to increase with increasing volume fraction of nanocrystallites.

A change in the tensile fracture plane from ~45° to perpendicular to the loading direction has been observed when the volume fraction of nanocrystallites was increased over 40% [1,20,90]. Aside from this difference, the fracture surfaces of these amorphous alloys containing nanocrystalline phases are very similar to those of amorphous alloys, indicating that good plastic deformability is retained before final fracture [1,90].

The superior mechanical properties of amorphous alloys containing nanoscale crystals has been explained by a combination of three factors: (1) the amorphous phase contains a large amount of free volume due to annealing in the supercooled liquid region followed by water quenching; (2) the glassy/amorphous interface has a highly dense-packed atomic configuration due to a much lower energy at the solid/liquid interface compared to the solid/solid interface; and (3) the crystals have a very small size and disperse homogeneously and isolatedly in the amorphous matrix [94]. The increased ductility in these nanocrystalline composites has been attributed to the high interface-to-volume ratio of the nanocrystals [92]. Nanocrystallites have also been shown to inhibit shear band propagation and prevent failure along localized regions of shear [95]. The shear deformation of the material can be effectively suppressed by the high-strength nanocrystalline particles, which leads to the increase in fracture stress [1,92,93].

Aside from crystallization within a monolithic BMG, crystallization and reaction at the matrix/particle interface in particle-reinforced BMG composites has also been documented. The effect of these interfacial nanocrystals on mechanical properties has not been examined, but these nanocrystals potentially have the same positive effect on mechanical properties. Previous studies on processing of BMG-matrix composites have shown that the composites can be successfully made without significantly affecting the glass-forming ability of the glass, resulting in retention of its amorphous character [3,7]. However, composites are commonly found to contain small amounts of new crystalline phases present at the particle/matrix interfaces due to either partial crystallization of the matrix or interfacial reaction [4,7]. In a study of W-Vitreloy106 composites, crystals were believed to

have formed during the cooling process as a result of either heterogeneous nucleation at the W/Vitreloy106 interface or reduced glass-forming ability of the matrix in the vicinity of the W particles due to increased W concentration near the particles and decreased W concentration in the remainder of the matrix [4, 7]. In another study, W particles diffused into the matrix forming 50-100 nm crystals similar to the matrix composition, but depleted of Ni [96].

In a study of Vitreloy106 reinforced with 50 or 80 vol% W particles or wires, the interfacial characteristics and crystallinity of the matrix were examined after processing at two different temperatures. It was found that the tungsten dissolves during processing, so higher processing temperatures lead to more tungsten dissolution into the matrix. The amorphous nature of the matrix was mostly retained after processing at 1150 K, but became more crystalline after processing at 1425 K. The resulting microstructures suggested that upon cooling the solubility of tungsten in the glass is exceeded, and it precipitates into the matrix [5]. In another case, the matrix penetrated grains of W fiber, which was evidence of grain boundary attack on the fiber by the melt [97].

If the crystallization during processing of composites can be controlled, the crystals, and especially nanocrystals that form at the particle/matrix interface could potentially be a tool for controlling the propagation of shear bands, in addition to the external reinforcement provided by the W particles (described in following section). This would provide another controllable factor that can be used to tailor the mechanical properties and deformation mechanisms of BMG composites.

2.6.2 Mechanical Behavior of Extrinsic Composites

It is desirable to form BMG-matrix composites in order to improve upon the properties of the monolithic BMG. Zr-Nb-Cu-Ni-Al alloys (Vitreloy family) are among the best glass formers and are very resistant to heterogeneous nucleation at surfaces or interfaces, which makes them an ideal matrix material for particle reinforced composites [4, 7]. Thus, many

studies have investigated the mechanical properties of this alloy reinforced with various materials (including WC, W, Ta, steel) [3, 5–7, 16, 98]. Crystalline materials are attractive as reinforcement materials because they have the potential to improve the fatigue properties of the BMG and toughen the material, in addition to hindering propagation of shear bands and small cracks [3, 7, 16]. Reinforcement materials in BMG-matrix composites need to have limited reactivity with the matrix [7], and the surface area of reinforcement particles is also an important consideration since heterogeneous nucleation sites increase with surface area [4]. Another consideration for reinforcement materials is the coefficient of thermal expansion [7] since CTE mismatch with the matrix can induce additional stresses in the composite.

Composites show an increase in ductile behavior with increasing volume fraction and decreasing size of reinforcement [5]. Monolithic metallic glass shows only ~0.5% plastic deformation, whereas particle reinforced BMG-matrix composites have shown up to 16% plastic strain before failure [3–7, 16, 42]. Compression tests performed on Vitreloy106-particulate (WC, W, Ta) composites showed plastic elongation of 3-7%, as can be seen in Figure 2.40, in comparison to 0.5% inelastic deformation of the pure glass, which was shown in Figure 2.8. The tensile and compressive strengths were also shown to increase from the addition of these reinforcement particles [7, 16]. The mechanism of tensile fracture was found to be affected by the addition of reinforcement particles; pure Vitreloy106 fails following propagation of the first shear band, but with W particles present, the failed composite had rims on its edges and a fracture surface similar to that observed in ductile materials. The changes in the fracture surface, in addition to the increase in plastic strain to failure, have suggested that the addition of particles increases the fracture toughness of the BMG [7, 16]. There are two factors contributing to the increase in toughness: the restriction that the particles place on the propagating shear band, causing it to slow and change direction, and an increase in the surface area over which the fracture occurs [3, 5]. The critical shear stress for shear band formation is larger in the composite than in the monolithic

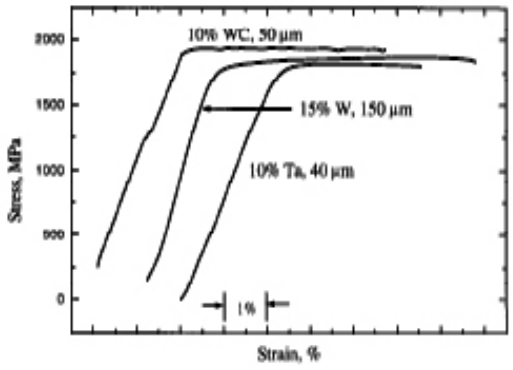

Figure 2.40: Stress-strain response of LM106 containing W, Ta, or WC particulate reinforcements. The composites show much more inelastic deformation (~3-7%) than the monolithic glass (~0.5%) [3].

glass because the particle/matrix interaction provides an additional restraint. If the shear stress remains equal, the energy required to fracture a composite is greater than that for a monolithic BMG because of the additional surface area [16].

The strain-to-failure and ultimate strength of a BMG composite are much greater in compression than in tension. In tension, the load is carried primarily by the matrix after the particles yield. The applied stress approaches the UTS of the glass (1200 MPa for Vitreloy106 [4, 16]), triggering shear band initiation and propagation. Since the material is not constrained, shear bands become unstable and fracture occurs. Under compressive loading, the composite is constrained so cracks cannot open and the distance a shear band can propagate is limited, which encourages formation of multiple shear bands. Additionally, the particle/matrix interfacial bond plays more of a role in tension because a tighter bond is needed to transfer load or adhere the matrix to the reinforcement. As a result, the tensile strength of a BMG composite is much less than its compressive strength and very similar to the failure strain of the pure matrix material [4].

The compressive properties of $Zr_{57}Nb_5Al_{10}Cu_{15.4}Ni_{12.6}$ reinforced with 60 vol% W particles have been studied over strain rates ranging from 10^{-4} to 10^4 s^{-1} and compared to the compressive properties of monolithic glass [2]. The stress-strain curves for the composite, monolithic tungsten, and monolithic glass at quasi-static and dynamic strain rates are

shown in Figure 2.41(a) and (b). The composite shows substantial plastic deformation at all strain rates, with failure after 30% in the quasi-static regime and after 20-30% plastic strain in the dynamic regime. In contrast to the glass, the composite shows strain-rate hardening behavior, with a strain-rate hardening exponent of m=0.016, as shown in Figure 2.41(c). This strain rate sensitivity, m, is close to a rule of mixtures approximation value based on the strain rate sensitivities of monolithic glass (m=0) and tungsten (m=0.025). The strain-rate dependence is more characteristic of the BCC tungsten phase, which dominates due to the large volume fraction of tungsten as well as the restraint of the failure mode of the amorphous matrix. At all strain rates, shear bands develop in the amorphous matrix, and the tungsten particles provide obstacles to shear band propagation. The obstacles lead to formation of multiple shear bands and allow for development of large plastic strains. The final failure of the composites under dynamic loading ($d\varepsilon/dt = 10^3$-10^4 s^{-1}) has been explained by adiabatic heating, which decreases the strength of the particles, thus reducing the constraint for shear band formation and allowing shear bands to form and propagate to macroscopic failure.

As previously mentioned, the introduction of particulates into a BMG has been shown to interfere with the propagating shear bands, causing them to slow and deflect, which delays failure and improves the toughness of the material [4, 7, 16]. Monolithic glass fails due to the propagation of a single catastrophic shear band, but the plastic strain in a particle-reinforced composite is due to formation of multiple shear bands since the particles plastically deform and interfere with the nucleation and propagation of any single shear band in the matrix [4, 16]. The restriction of shear band propagation provided by a W particle can be seen in Figure 2.42. The characteristic vein-like structure is attributed to localized melting within shear bands, and the direction of the veins is indicative of the direction of fracture. This image shows a reduced size of the vein pattern, which indicates that the flow of the material has slowed in front of the particle, and the particle has therefore slowed the propagation of the shear band [7, 16]. Around the sides and front of the particle, smooth

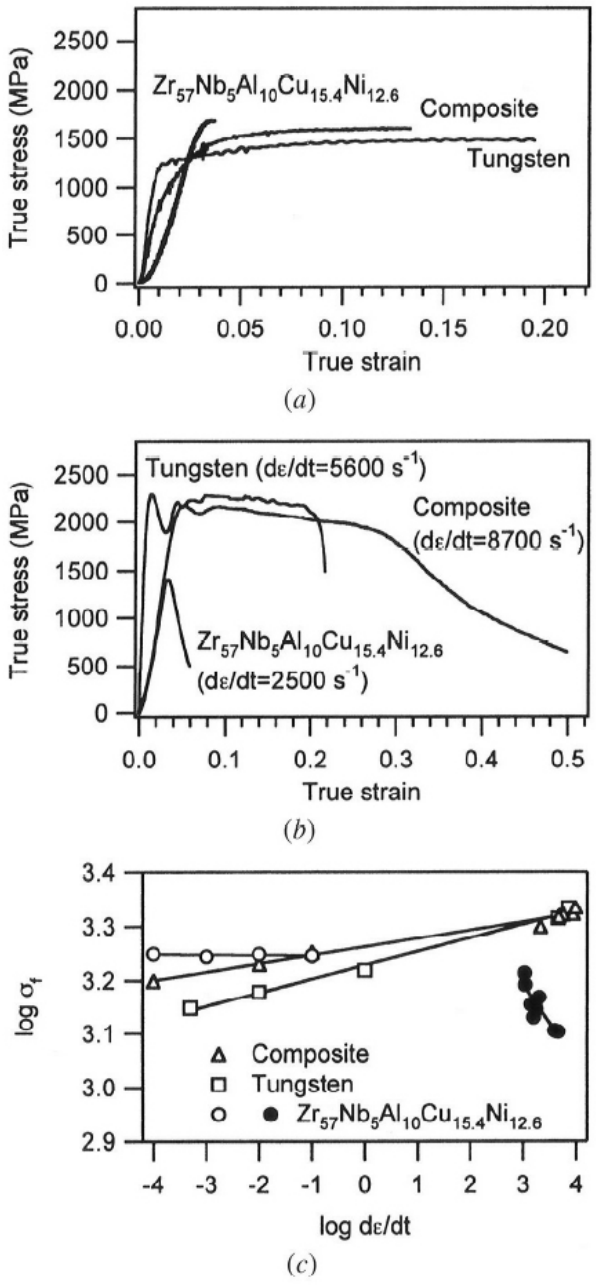

Figure 2.41: Uniaxial compressive behavior of $Zr_{57}Nb_5Al_{10}Cu_{15.4}Ni_{12.6}$ + 60 vol% W particle composites, monolithic W, and monolithic glass [2]. (a) Quasi-static loading ($d\varepsilon/dt = 10^{-4}$ s^{-1}), and (b) Dynamic loading. Unloading in the composite at ~0.3 strain is due to fracture, and unloading in W at ~0.2 strain is due to elastic unloading. Both the quasi-static and dynamic loading conditions show the composites to exhibit an increase in plasticity over Vit106. (c) Determination of the strain-rate sensitivity exponent, m. The open symbols correspond to the logarithm of the flow stress at 5% strain for W and the composite and 0.2% strain for the glass. The closed circles correspond to the logarithm of the fracture stress of the pure glass.

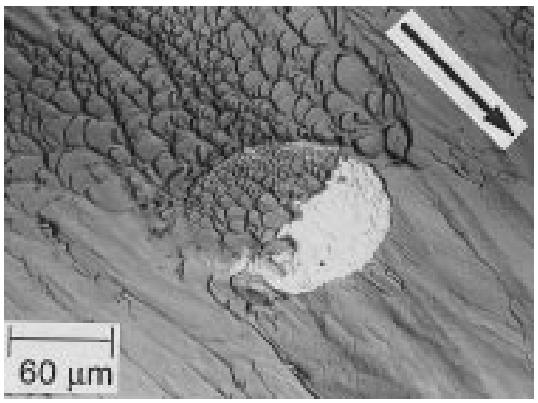

Figure 2.42: SEM micrograph of a compressive fracture surface of a Vitreloy106-matrix composite with 5% W reinforcement particles [7]. The vein-like morphology is typical of shear band failure, and it can be seen that the particle restricts the shear band propagation since the size of the vein pattern in front of the particle is reduced. The arrow indicates the direction of shear band propagation.

surfaces can be seen, which is a sign of fast fracture [16]. This image also shows flow of the BMG over the particle, indicating a reduced viscosity of the glass inside the shear band [7].

The mechanism by which reinforcement particles inhibit shear band propagation has been attributed to be as follows. The BMG matrix carries most of the load during yielding, which triggers the onset of shear band formation. The residual stresses in the matrix then guide the shear bands toward the reinforcement particles. For example, in a BMG-matrix composite containing W wires, there will be high radial compressive stresses on the wires since the CTE of the glass is nearly twice that of tungsten, so the tensile matrix hoop stress guides the fracture path toward and through W wires [6].

Choi-Yim et al. [7] showed that as a BMG-matrix composite deforms, multiple shear bands are formed, which suggests a change in the deformation mechanism as compared to monolithic glass. They concluded that the constraint that the reinforcement particles provide on the matrix prevents catastrophic failure and leads to formation of secondary shear bands parallel to the initial band. This explanation is logical because the difference in elastic properties between a metallic glass matrix and crystalline reinforcements can cause stress concentrations to promote shear band initiation in the glass. Because the Poisson′s

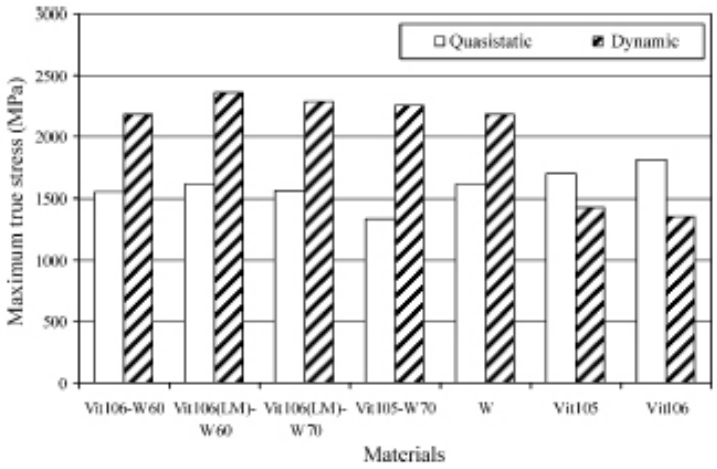

Figure 2.43: Comparison between maximum stress felt by BMGs, W and W-BMG composites under quasistatic and dynamic loading. This plot illustrates that the W and the composites exhibit positive strain-rate sensitivity, but the BMGs exhibit negative strain-rate sensitivity [9].

ratio of the reinforcement (ν=0.28 for tungsten) is lower than that of the metallic glass (ν=0.38 for Vitreloy106), confinement of the particles will lead to initiation of additional shear bands, and the increased shear band density will allow much larger plastic strains to develop than a monolithic glass can sustain [2]. Therefore, extended plasticity observed in BMG-matrix composites can be attributed to the formation of multiple shear bands.

Li et al. [9] have also studied the mechanical behavior of W preform-reinforced BMGs under quasistatic and dynamic (4000 s^{-1}) loading. This study showed positive strain-rate sensitivity for W and all of the composites, but negative strain-rate sensitivity for the monolithic BMGs, as discussed previously (Section 2.3.2.4). These results are shown graphically in Figure 2.43. Dalla Torre et al. [52] found negative strain-rate sensitivity for both Vitreloy105 and a Vitreloy105-graphite (6%) composite, although the strain rates investigated only ranged up to 10^{-2} s^{-1}.

Ballistic penetration tests performed on BMG-matrix composite rods have shown that localized shear banding results in self-sharpening behavior [6, 98], and that reinforced BMG-matrix composites have a higher penetrating capability than tungsten heavy alloys

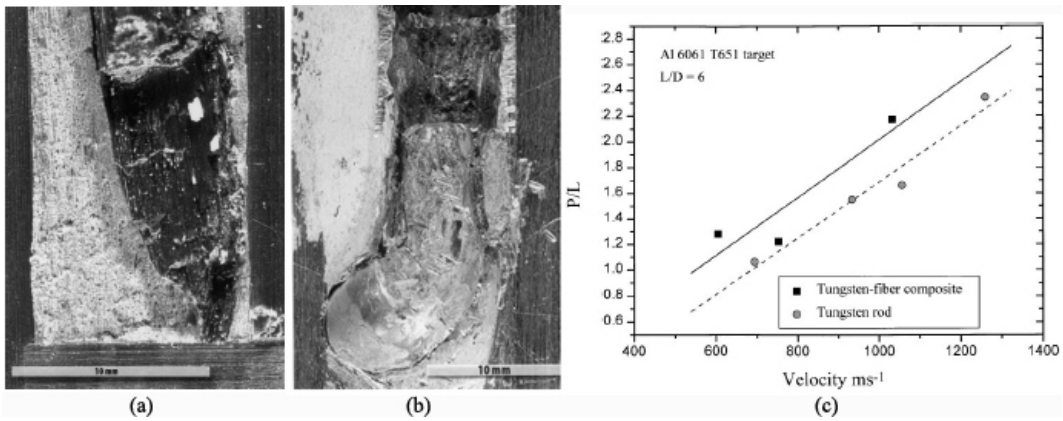

Figure 2.44: Reverse ballistic impact of (a) a BMG composite containing 85 vol% W fiber in a $Zr_{41.25}Ti_{13.75}Cu_{12.5}Ni_{10}Be_{22.5}$ matrix and (b) WHA into a 6061 Al target. (a) Self-sharpening behavior with the diameter of the penetration hole smaller than the initial diameter of the specimen and (b) mushrooming with the diameter of the penetration hole being larger that the initial specimen diameter. (c) Normalized penetration depth (P/L) as a function of impact velocity for ballistic impact tests [98]. This plot shows the increased penetration depth that the BMG-composite can achieve due to its self-sharpening behavior.

(WHA) in both Al and steel targets [6, 98]. An example of results from a ballistic impact test with a BMG composite versus a tungsten alloy can be seen in Figure 2.44. This plot shows that the composite penetrators perform 10-20% better than the WHA penetrators.

The prior work that has been done on mechanical properties and phase stability of bulk metallic glasses and their composites indicates the need to further investigate these properties in the high-strain rate and high pressure regimes. This will be the focus of the current study.

CHAPTER III

MATERIALS AND EXPERIMENTAL PROCEDURES

3.1 Overview

The main objective of this work was to determine the deformation and failure mechanisms of $Zr_{57}Nb_5Cu_{15.4}Ni_{12.6}Al_{10}$ (LM106) BMG and its composite with tungsten as a function of stress state and strain rate and ultimately develop a complete understanding of deformation and failure mechanisms that can be used to develop a constitutive model that describes the mechanical behavior over a range of loading conditions. It was a goal of this work to develop structure-property relationships valid over a wide range of strain rates and stress states for both the monolithic glass and the composite such that a complete understanding of mechanical behavior and deformation mechanisms can be utilized when designing materials for specific structural applications.

The overall approach for this work included a combination of experimental and analytical techniques. Mechanical testing experiments were performed at strain rates ranging 11 orders of magnitude. Testing techniques and apparatuses included quasi-static compression, drop weight tower, Split Hopkinson Pressure Bar, Reverse Taylor impact, spall, and plate impact. Diagnostics including high-speed photography, velocity interferometry, streak photography, and stress and strain gauges were utilized during experiments. Additionally, effects of altering stress state, through use of sleeved specimens and compression-shear specimens, were explored. The effects of temperature on mechanical behavior were also explored. Finite element modeling was utilized to assess validity of existing constitutive models and to obtain additional information from experiments by correlating simulations with experimental results. The details of all of these techniques are described in this chapter.

Table 3.1: Density and sound speeds of monolithic LM106 and LM106-70W composite. Densities were measured using Archimedes method, sound speeds for LM106 were calculated from elastic properties data in the literature [3, 4], and sound speeds for LM106-70W were measured using ultrasonic testing.

Material	ρ_0 (g/cm^3)	C_l (m/s)	C_s (m/s)	C_B (m/s) $\left(= \sqrt{C_l^2 - \frac{4}{3}C_s^2}\right)$	C_0 (m/s) $\left(= \sqrt{\frac{E}{\rho_0}}\right)$
LM106	6.70±0.01	4903	2144	4232	3597
LM106-70W	15.58±0.09	4925±84	2588±40	3914±97	4187±59

3.2 Materials

3.2.1 LM106 Bulk Metallic Glass

The material under examination in this study is a Zr-based bulk metallic glass ($Zr_{57}Nb_5$-$Cu_{15.4}Ni_{12.6}Al_{10}$) known as LM106 (or Vitreloy106). The BMG was processed by Liquidmetal Technologies, Inc. and provided in the form of rods of 10.12 mm diameter. The values of density (6.70 g/cm^3) and sound speeds were measured using the archimedes method and ultrasound, respectively, and are reported in Table 3.1. Each specimen was lapped with 25 μm diamond suspension to insure parallel surfaces (within ~1%). This BMG has been previously studied and the compressive and tensile strengths have been reported to be 1800 and 1200 MPa, respectively [3]. Prior work on thermal analysis of LM106 was shown in Section 2.5.1 and reveals a T_g of ~400 °C, T_x of ~480 °C, and T_m of ~815 °C.

3.2.2 Sleeved LM106 Bulk Metallic Glass

For some experiments, it was desirable to test the BMG surrounded by a confinement sleeve to evaluate the effects of the altered stress state. For these experiments, $Zr_{57}Nb_5Cu_{15.4}Ni_{12.6}$-$Al_{10}$ (LM106) bulk metallic glass was fabricated by Liquidmetal Technologies by casting into 316 stainless steel sleeves of ~0.9 mm thickness, forming a thin layer (3 μm) of brittle intermetallic between the BMG and the steel. Micrographs of the sleeve-specimen interface are shown in Figure 3.1, revealing some porosity/cracking at the interface layer, but it is believed that this physically bonded interface still provides better coupling than shrink

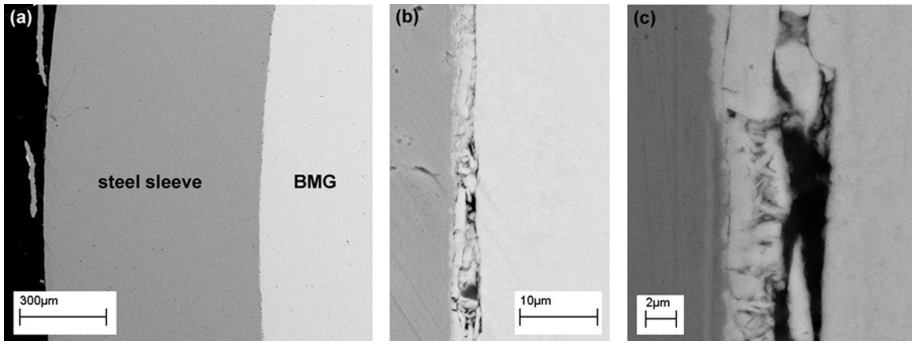

Figure 3.1: SEM micrographs of the steel sleeve-BMG interface at increasing magnifications. The intermetallic interface layer measures ~3 μm. At the lowest magnification (a), the sleeve/BMG interface looks clean, but at 30X higher magnification (b) it is obvious that the interface has some imperfections, in the form of voids and cracking, and the scale of these imperfections can be seen in more detail in (c).

fitting or pressing the specimen into the sleeve would have. Specimens in the form of rods (~12.7 mm outer diameter, including sleeve) were cut to approximately 50 mm length (~4:1 length:diameter) and lapped with 45 μm diamond suspension to ensure parallelism within ±0.004 mm. In order to evaluate the effect of the confining stress from the sleeve, one specimen from this batch was prepared without a sleeve to allow for comparison. For this specimen, the steel sleeve was removed using a lathe to reduce the thickness of the steel sleeve until it could be peeled away from the BMG. The surface finish of the BMG was then refined by grinding. All specimens included in this study were cast in the same batch during processing, which eliminated any compositional or processing variability.

3.2.3 Tungsten-reinforced Bulk Metallic Glass Composite

The composite under investigation was a BMG-matrix composite consisting of a $Zr_{57}Nb_5$-$Cu_{15.4}Ni_{12.6}Al_{10}$ (LM106) matrix with 70 vol% crystalline tungsten reinforcement particles (~5 μm nominal size). The tungsten preforms were fabricated by SpectraMat and were pressure infiltrated with BMG by Liquidmetal Technologies, Inc. The samples were then provided by the Army Research Laboratory. The fabrication of these materials has been

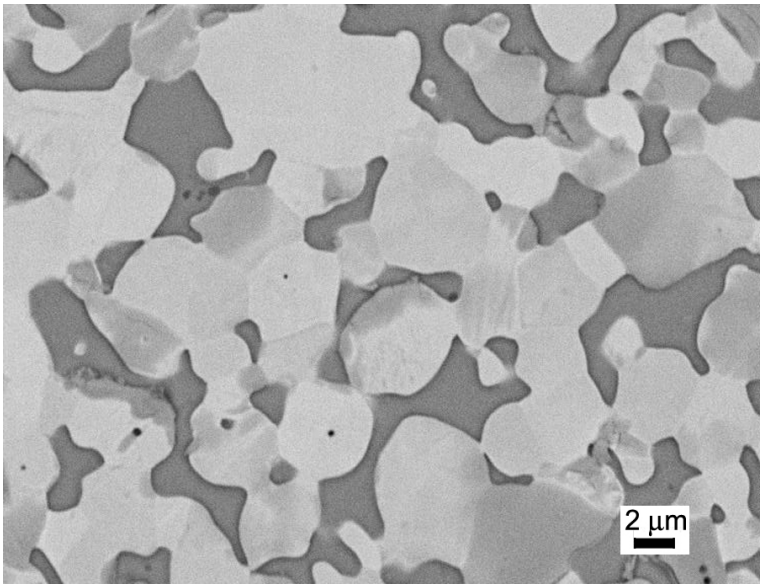

Figure 3.2: SEM micrograph showing the composite microstructure in its as-received form. The light gray phase is the crystalline tungsten particles and the dark gray phase is the amorphous BMG. The variation in intensity in the W is due to different intensities of backscattered electrons of different crystal facets.

described in detail by Li et al. [9]. Briefly, at SpectraMat the W powder was cold isostatically pressed at 30,000 psi and sintered above 900 °C in hydrogen. The infiltration of the W preforms with BMG was done at Liquidmetal by heating the preform and BMG (encased in a steel tube) above the liquidus of LM106 (842 °C) while under vacuum, applying argon gas pressure to force the viscous BMG into the preform, and finally quenching the steel tube in water.

Composite samples studied in this work were from two different processing batches, Lot 114 and Lot 092905, and although these two batches should have been identical, some differences in mechanical behavior of samples between the two batches were observed, as will be discussed later. The microstructure of the as-received composite is shown in Figure 3.2. The values of density and sound speeds for the composite are reported in Table 3.1.

3.2.3.1 *Differential Scanning Calorimetry and Differential Thermal Analysis*

Differential Scanning Calorimetry (DSC) and Differential Thermal Analysis (DTA) were used to investigate the thermal properties of the composite material. The DTA was done in a Perkin Elmer DTA7 at a heating rate of 10 °C/min with Al_2O_3 as a baseline material. The DTA results are shown in Figure 3.3 and reveal a T_x of ~470-480 ^{circ}C and a T_m of ~816 ^{circ}C. In the DSC, the specimen was heated and cooled twice at 10K/min. The DSC results are shown in Figures 3.4 and 3.5 below. The results in Figures 3.4 show a possible indication of a glass transition (during the first heating only, red curve) beginning at 348.5 °C and lasting through 418 °C, although the signal is not clear. The melting event is clearly seen in all four curves, and is shown more clearly in Figure 3.5, in which the temperature scale is adjusted to focus on the melting event. The onset of melting was measured to occur at 816.6 °C, on average. These measured values for T_g and T_m agree with what other researchers have reported for the monolithic LM106 and LM106 + 10% W [7, 99]. It is unknown why the crystallization event was not captured during these measurements, but it is believed that it was due to the small sample size, 70% of which was W. Due to this, thermal properties values from other studies (T_g ~400 °C, T_x ~480 °C, and T_m ~815 °C) were used as guidelines for determination of relevant temperatures for mechanical testing.

3.3 Mechanical Testing at Low and Intermediate Strain Rates

This work explores the mechanical behavior of LM106 BMG and its composite with tungsten over a wide range of strain rates and loading conditions. This section describes the experimental procedures and details for the mechanical testing performed on the composite material in the low to intermediate strain rate regimes ($\sim 10^{-3}$ to 10^3 s^{-1}). These experiments were performed in collaboration with Professor Lothar Meyer at the Technical University of Chemnitz in Chemnitz, Germany.

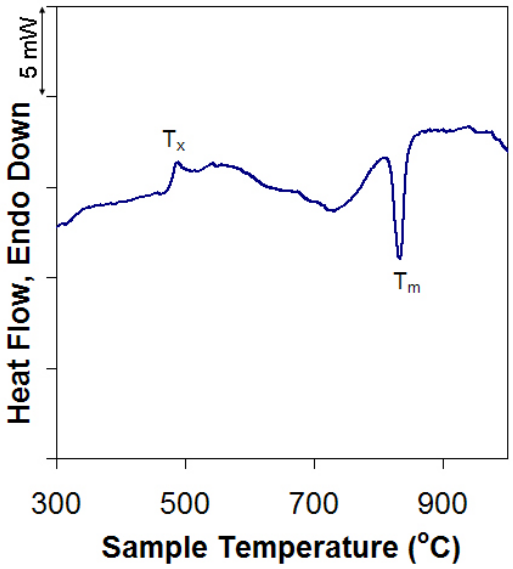

Figure 3.3: DTA curve showing heat flow as a function of temperature for LM106-70W. The heating rate was 10 °C/min. The onset of crystallization (T_x) was observed between 470-480 °C and the onset of melting (T_m) at approximately 816 °C. The glass transition was not observed.

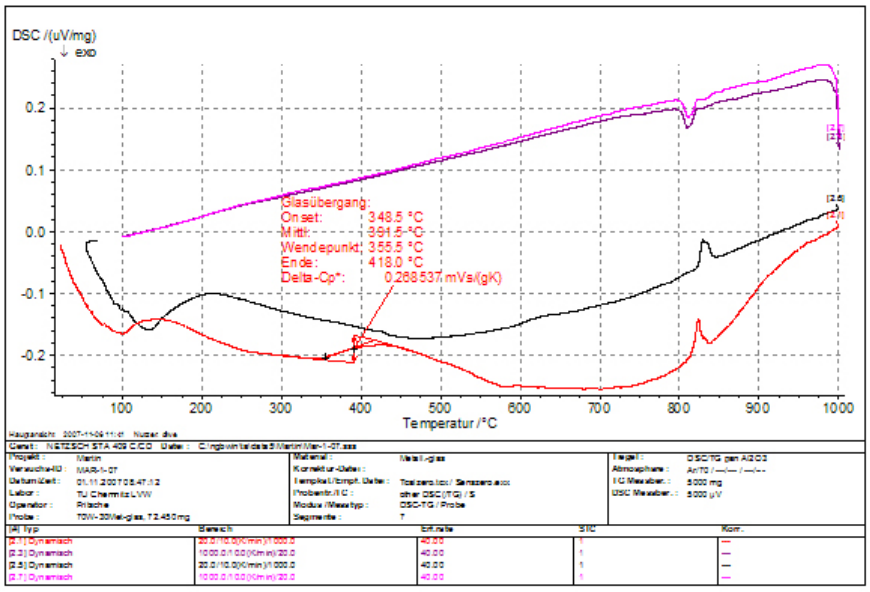

Figure 3.4: DSC curves showing heat flow as a function of temperature for LM106-70W. Two heating curves are shown in red and black, and two cooling curves are shown in pink and purple. The heating and cooling rates were 10 K/min. A possible signature of the T_g was observed at ~348-418 °C during the first heating (red) and melting was clearly observed at an average of ~816.6 °C in all four curves.

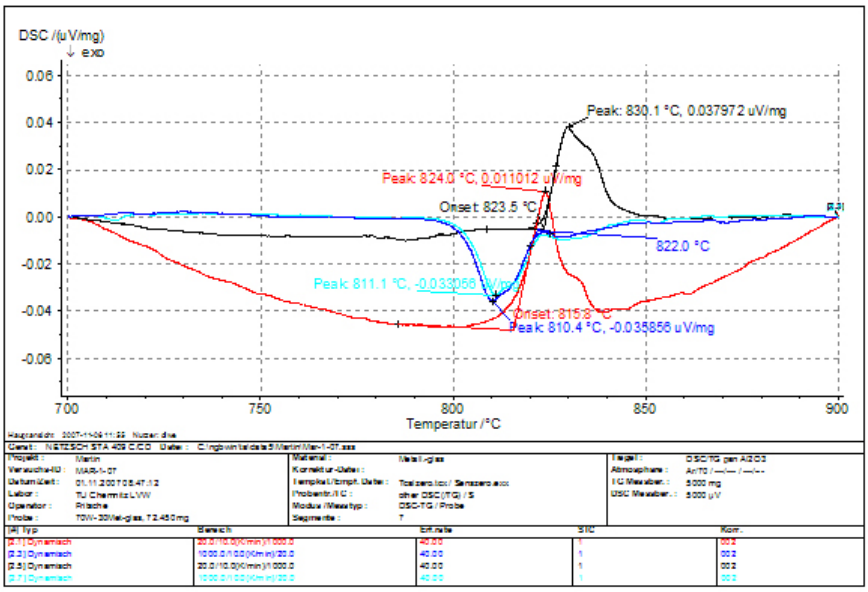

Figure 3.5: DSC curves (two on heating and two on cooling) showing heat flow as a function of temperature for LM106-70W showing the temperature range of interest for the melting event. Melting was measured to occur at 816.6 °C on average.

3.3.1 Specimen Preparation

The stress and strain distributions in materials are often inhomogeneous during high-strain rate scenarios, leading to localized regions of increased shear deformation [100]. Additionally, adiabatic shear failure often occurs in high-strength materials during uniaxial compression tests. Pure shear or pure compression states are rare, and thus it is important to study material response under not only uniaxial, but also biaxial loading to understand the susceptibility of a material to adiabatic shear failure. Behavior of LM106-W specimens under biaxial loading is of particular interest due to the tendency of BMGs to deform by adiabatic shear banding [21, 23, 24], as was discussed in Section 2.2.

LM106-70W specimens for compression and compression-shear experiments conducted under low and intermediate strain rate conditions were 6 mm in height and 6 mm in diameter. Compression-shear specimens were oriented with an inclination of 6° off the loading axis, as shown in the schematic in Figure 3.6, which illustrates the uniaxial and biaxial

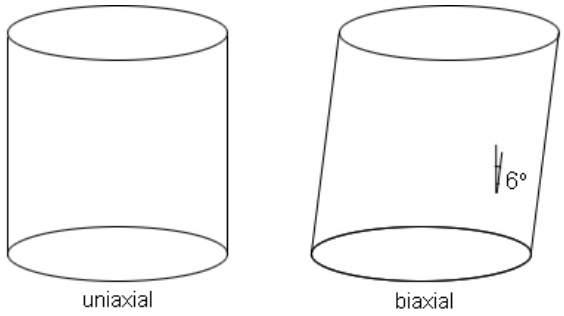

Figure 3.6: Schematic showing the uniaxial and biaxial (6° off-axis) specimen configurations. The biaxial specimens resulted in 10.4% additional shear loading.

specimen configurations. As shown by Meyer and Krueger [100], the 6° inclination resulted in additional shear loading of ~10.4% of the axial compression load:

$$\frac{\sigma}{\tau} = \frac{\frac{F}{A}cos\theta cos\phi}{\frac{F}{A}} = cos(6°)cos(84°) = 10.4\%$$

The inclined specimen provides a dynamic biaxial stress state, allowing the material to respond with its specific sensitivity to adiabatic shear failure. An example of varying stress-strain responses of a Ti-6Al-4V with varying degrees of inclination is shown in Figure 3.7. Specimen ends (uniaxial specimens only) were prepared by turning against a coarse pad to create shallow circular grooves, which reduced friction effects. Specimens were then cleaned in an ultrasonic bath with acetone.

Two strain gauges were applied to each uniaxial compression specimen, exactly opposite each other (9.4 mm apart around circumference of sample). To apply strain gages, specimens were slightly sanded on the sides in the area where strain gauges were applied and then the application sites were cleaned with propanol. The sample surface was then treated with M-Prep conditioner and neutralizer (Vashay Micro Measurements). Strain gauges were then positioned using tape and M-bond 610 Adhesive was applied to the specimen surface and the bonding side of the gauge. The adhesive was allowed to dry by solvent evaporation for at least half an hour, but no more than four hours, before the gauges were affixed to the specimen with the partially-dry adhesive. Specimens were then fixed in a clamp and heated in a furnace for 2 hours to complete the curing process, following which

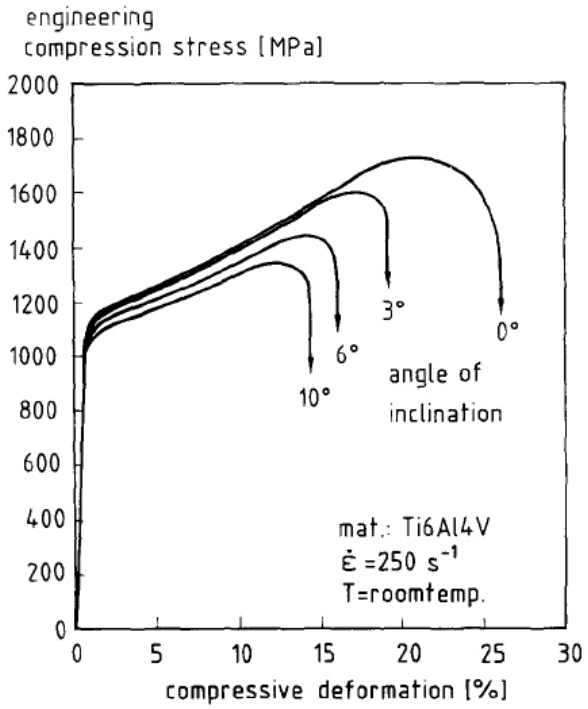

Figure 3.7: The variation in stress-strain response of Ti-6Al-4V due to different specimen inclinations [100]. Increasing the angle of inclination resulted in increasing degrees of additional shear stress during loading, and thus lower strains-to-failure.

the specimens were allowed to cool in the furnace. The tape was then removed and excess adhesive was scraped of the specimen ends. Two cables were soldered to each strain gauge and the connections were sealed with a polyurethane coating after checking the continuity of each connection with a voltmeter and verifying the 120 Ω resistance.

3.3.2 Quasi-Static Compression and Compression-Shear Testing (10^{-3} – 10^{0} s^{-1})

Quasi-static mechanical testing for evaluation of the properties of the composite both under uniaxial compression and biaxial compression-shear was performed using an Instron 8503 servo-hydraulic universal testing machine with a 250 kN load capacity. This technique was used for testing at strain rates of 10^{-3}, 5x10^{-2}, and 10^{0} s^{-1}, which corresponded to loading rates of 0.006, 0.3, and 6 mm/sec, respectively. The specimen was centered between two hardened steel platens which were lubricated with MoS_2 (Klüber Lubrication) to reduce friction. On either side of the platens was an inductive (electronic proximity) sensor, which detects metallic objects without touching them via sensing of the current flowing through an inductive loop. These sensors were used to measure the displacement of the cross-head. When compression-shear specimens were tested, it was important to orient the specimens such that the platens would not shift toward the inductive sensors, possibly damaging them, during the test. The free ends of the strain gauge cables were soldered to their corresponding terminals for measurement and continuity was checked using a voltmeter to verify the 120 Ω resistance. A battery was used to supply voltage through the strain gages and as the area of the strain gauges changed as the specimen was compressed, the resistance of the gauges increased. The strain gauges were set up in a Half Wheatstone Bridge configuration, in which the total resistance is measured over a bridge consisting of four resistors, two of which (the strain gauges) have unknown values. A diagram of a half Wheatstone bridge is shown in Figure 3.8, illustrating a schematic of the circuit in which the two strain gauges served as resistors with unknown resistance values. The signals from the strain gauges were passed through an AM 502 Differential Amplifier (100X) and a filter (1 kHz for 10^{-3} s^{-1}

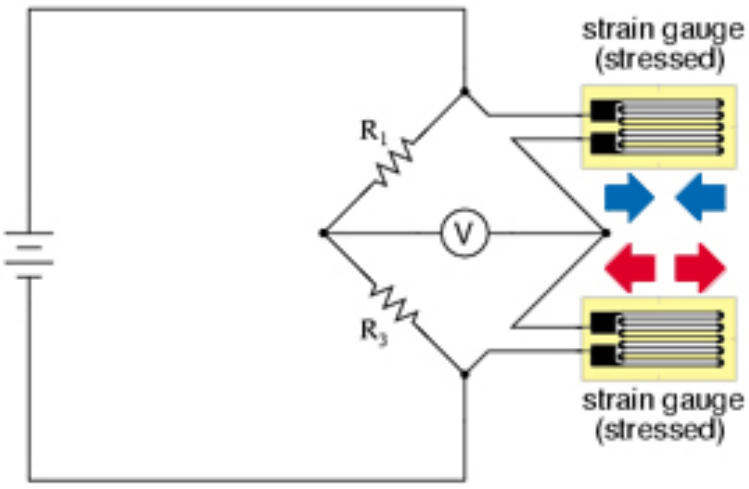

Figure 3.8: Diagram of a half Wheatstone bridge incorporating two resistors with precisely known resistance values and two unknown resistors (strain gauges) whose resistance values were measured during the experiment [101].

and 10 kHz for $5x10^{-2}$ and 10^{0} s^{-1}). The data was recorded using Labview-based software at a recording rate of 20 scans/sec for the 10^{-3} s^{-1} experiments and 5000 scans/sec for the $5x10^{-2}$ and 10^{0} s^{-1} experiments. The recorded data included the time, load, cross-head displacement (set s.t. 1V=1mm) measured with the average of the two inductive sensors, and the voltage measured from the average of the two strain gauges. Two of each of the inductive sensors and strain gauges were used to compensate for any bending such that if bending did occur the two complimentary measuring devices would have opposite signals which would average out.

Examples of the raw data obtained from compression testing using the Instron machine can be seen in Figure 3.9. Data analysis was performed using FAMOS software to convert load to stress ($\sigma = P/A_0$) and displacement to strain ($\varepsilon_{cross-head} = \Delta l/l_0 = displacement/l_0$). The strain gauge signal was converted to strain according to: $\varepsilon_{SG} = \frac{B \cdot U_b \cdot 100\%}{U_i \cdot K_{amp} \cdot K_{SG}}$ where B is the type of the Wheatstone Bridge (in this case, $B = 2$ for half bridge), U_b is the measured voltage signal, U_i is the voltage running through the circuit immediately before the start of the test, K_{amp} is the amplification (100 X), and K_{SG} is the K-factor of the strain gauge, which is the proportionality factor between the relative change of the resistance (K_{SG}=1.98). The

strain gauges typically measured up to ~5% strain, and this data was used for determination of elastic modulus. After the strain gauge expired, the data from the inductive sensors was used, after correcting it for the compliance of the testing machine. Strain gauges were not used for the compression-shear specimens, since it has been observed in previous work that the elastic portion of the curves from the uniaxial and biaxial specimens is identical, so it was unnecessary. The data from these experiments was likewise corrected for compliance. This data analysis procedure is described in more detail in Appendix A.1.

3.3.3 Drop Weight Compression and Compression-Shear Testing ($\dot{\varepsilon} \approx$200 s^{-1})

A drop-weight tower consists of a 600 kg weight which drops on a specimen, which is resting on an anvil [100]. Below the weight, a small hammer head is affixed to ensure precise loading conditions. An advantage of this experimental configuration is that large amounts of stored energy can be applied such that strain-rate history of the specimen material is not influenced by its strain hardening. For this study, drop weight tests were performed at a strain rate of 200 s^{-1}, which required a drop height of approximately 80 mm, according to the following relationships:

$$V = \sqrt{2Gh} \tag{2}$$

and

$$\dot{\varepsilon} = \frac{V}{h_0}, \tag{3}$$

such that

$$h = \frac{(\dot{\varepsilon} h_0)^2}{2G} \tag{4}$$

where V is the impact velocity, G is gravity, h is the fall height, $\dot{\varepsilon}$ is strain rate, and h_0 is the sample height. Strain gauges (with 700 Ω resistance) were affixed on the hammer head to record load-time history. Displacement was measured with a light gate system in which each gate passed generated a peak in the signal and the distance between peaks was proportional to a known displacement. The optical gate system also served as the trigger

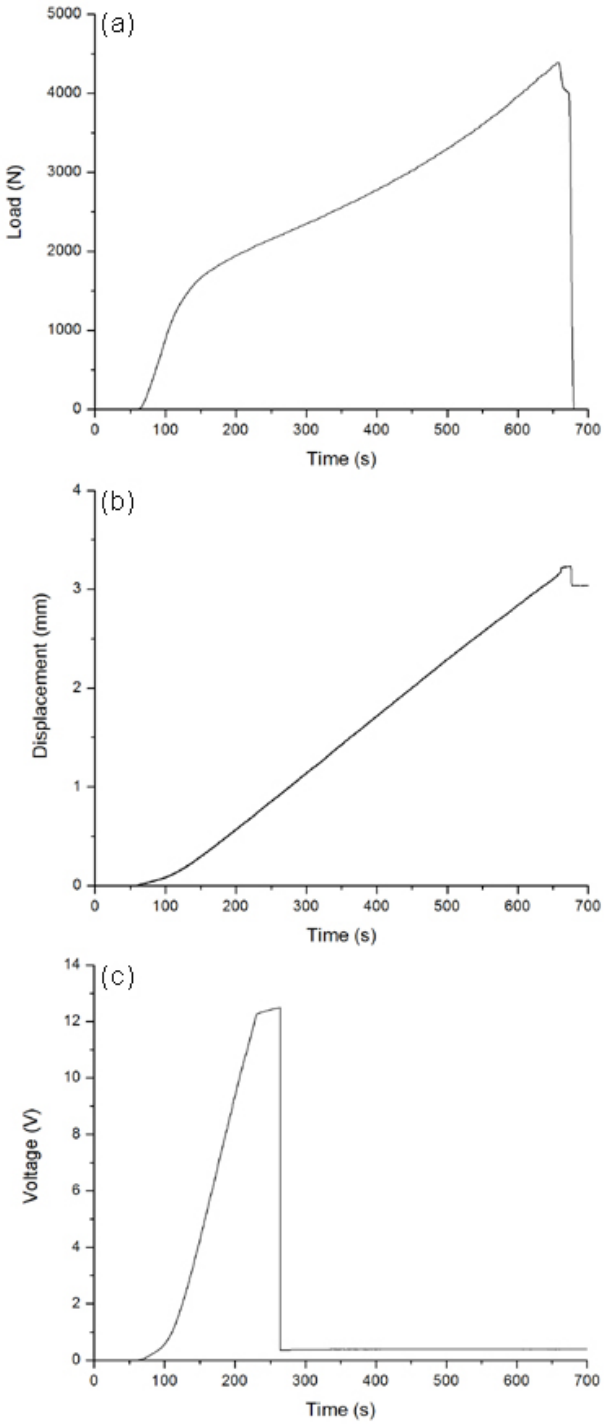

Figure 3.9: Raw data obtained from the Instron testing machine. (a) Load, which was measured by the load cell and was used to calculate stress, (b) displacement, which was measured by the inductive sensor (1 V= 1 mm) and was used to calculate stress after removing the machine compliance, and (c) voltage which was measured from the strain gauges on the specimen through a half Wheatstone Bridge and was used to calculate strain during the early stages of deformation.

for the Textronix TDS744A Oscilloscope, which recorded the data. Strain rate was calculated from the recorded measurements. Examples of the raw data (load, displacement, and voltage) obtained from these tests can be seen in Figure 3.12. Data analysis was performed using FAMOS software. The scripts used to perform the calculations can be found in Appendix A.2. This setup also allowed for specimen recovery during any stage of deformation since it is equipped with high-speed brakes and special stopping devices. After analysis of the initial data, stopped tests were performed approximately at yield, failure, and at stages in between for both the uniaxial and biaxial specimens. The dropped weight was stopped, thus preventing further specimen deformation, using precision measured hardened steel blocks. A schematic of this setup can be seen in Figure 3.10 and a photograph is shown in Figure 3.11.

3.3.3.1 High Temperature Testing

Investigations of the compressive mechanical behavior of both uniaxial and biaxial specimens were also explored as a function of test temperature using the drop weight testing facility at a strain rate of 200 s^{-1}. These tests were performed in the same way as those at room temperature, but the specimens had a thermocouple point-welded onto their surface to measure specimen temperature. The specimens were heated with inductive heating coils which were positioned around the area where the sample was setup and where impact took place. The heating coils can be seen in the photograph in Figure 3.11. The heating rate was approximately 3 °C/s and experiments were performed at test temperatures of 200, 380, 450, 550, and 600 °C. These test temperatures allowed for investigation of the changes in compressive mechanical behavior over a range of temperatures, beyond the glass transition temperature (T_g~405-414 °C [7, 99]), between T_g and and the crystallization temperature (T_x~478-480 °C [7,99]), and above T_x of LM106. (See Section 3.2.3.1 for thermal analysis of this W-LM106 composite). Thus, the effects of these thermodynamic transitions on the mechanical behavior of the composite could be evaluated.

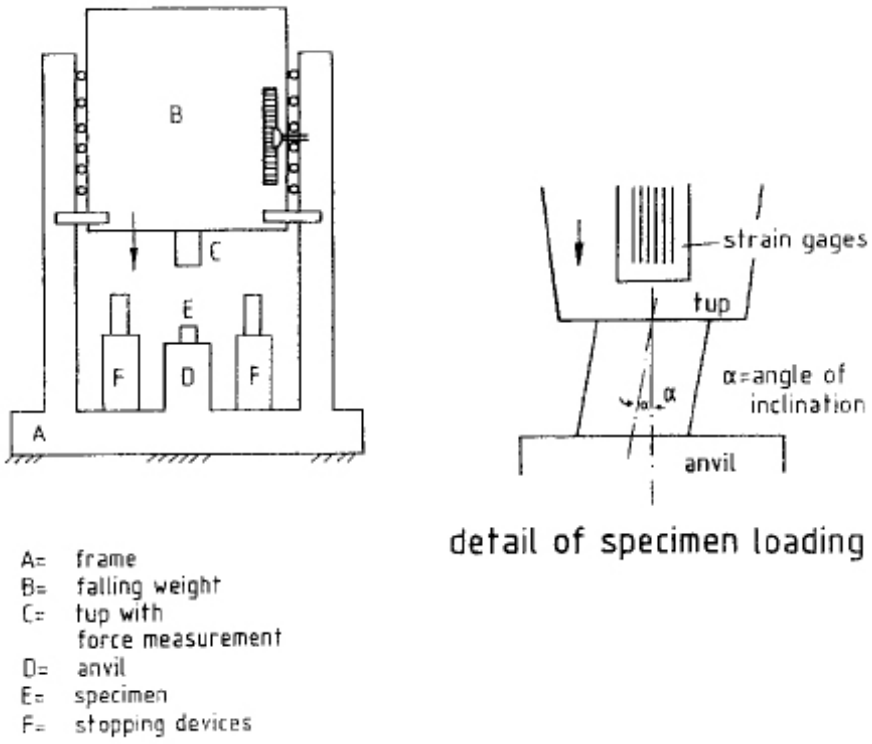

Figure 3.10: Schematic of the drop weight testing apparatus showing a weight (B) which is dropped onto a specimen (E) resting on an anvil (D). Stopping devices (F) allowed for specimen recovery at any stage of deformation. On the right is a schematic showing details of the weight-specimen-anvil loading on an inclined specimen.

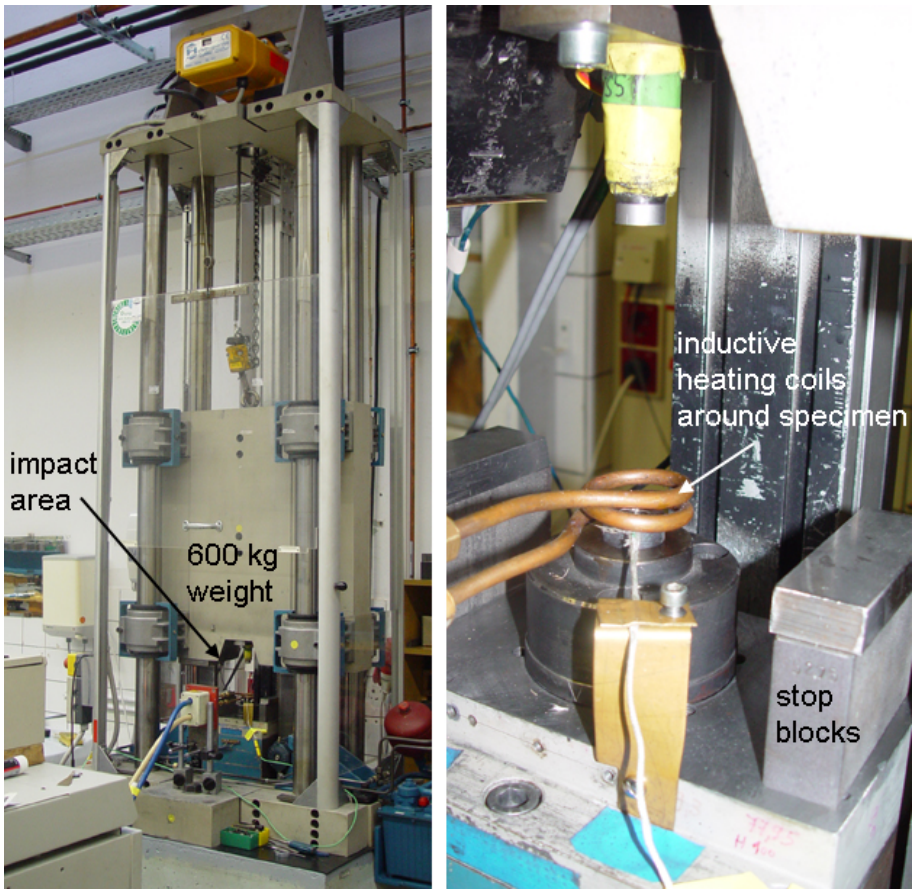

Figure 3.11: Photographs of the drop weight testing apparatus. The photograph on the left shows the 600 kg weight which is dropped on the specimen from a height specified by Equations 2-4. The photograph on the right shows details of the specimen loading area setup for a high temperature experiment with inductive heating coils positioned around the specimen. Stop blocks used to stop deformation at any specified stage can be seen on the right of the photograph.

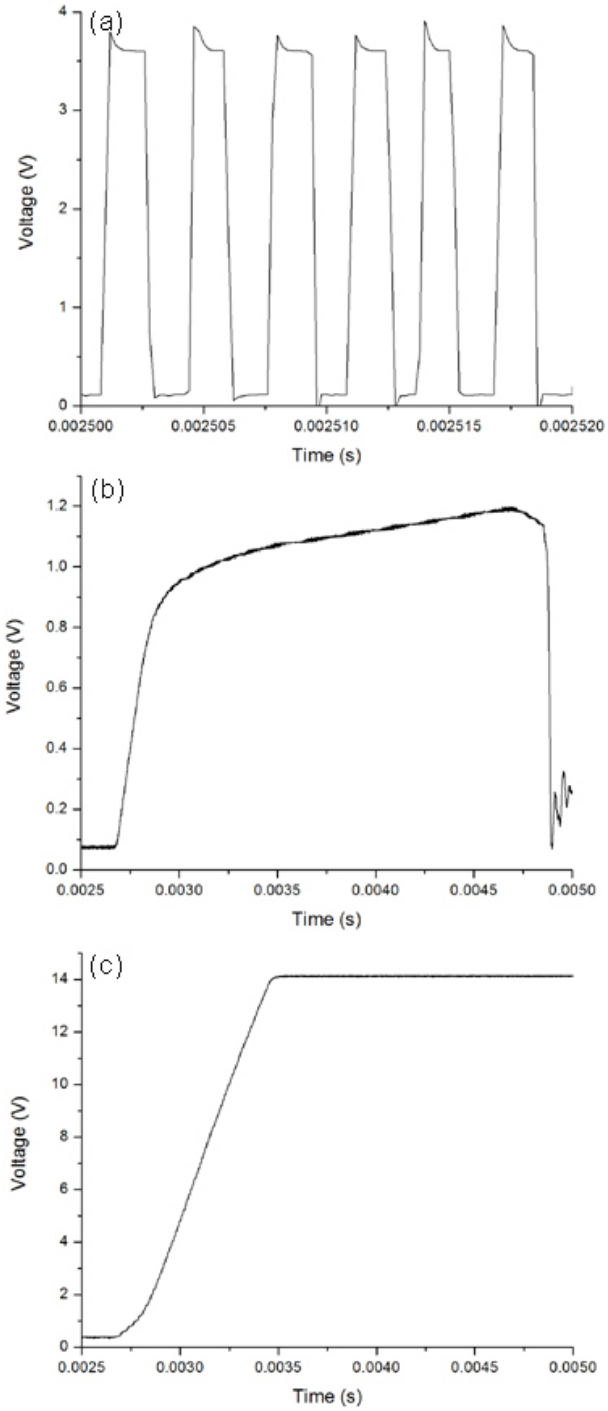

Figure 3.12: Raw data obtained from the Drop Weight testing machine. (a) Voltage measured by the optical gate system used to calculate displacement (only a small time window shown so peaks are clear), (b) voltage measured by the strain gauge on the machine, which was used to calculate strain, and (c) voltage measured by the strain gauges on the specimen through a half Wheatstone Bridge, used to calculate strain in the early stages of deformation.

3.3.4 Split Hopkinson Pressure Bar Experiments ($\dot{\varepsilon} \approx$1400-1800 s^{-1})

The Hopkinson (Kolsky) Bar is a commonly used experimental technique for probing material behavior in the intermediate to high strain-rate regime [102]. In this setup, which is shown schematically in Figure 3.13, a striker bar impacts the incident bar, which produces a pulse in the incident bar that has a large length with respect to the specimen size. A small piece of lead (3 mm diameter, <1 mm thick) was placed on the end of the incident bar with grease to provide damping in the signal. After traveling through the incident bar, the elastic wave reaches the specimen, which was lubricated with MoS_2 on its ends and held between the incident and transmitted bars. Removable hardened steel platens were used on the ends of the incident and transmitted bars (on either side of the sample) to prevent damage of the bars. These platens were replaced between each experiment. The plastic wave is imparted to the specimen due to the amplitude of the wave. Strain gauges on the incident and transmitted bars allow for measurement of a direct incident pulse, a reflected pulse, and a transmitted pulse, which were recorded using an LDS Nicolet Digital Oscilloscope Workstation, which was triggered by the force increase in the input bar. From these three pulses, stress, strain, and strain rate for the specimen were derived as follows. Strain rate is calculated as [103]:

$$\dot{\varepsilon} = \frac{d\varepsilon}{dt} = \frac{V_1(t) - V_2(t)}{L}$$

where V_1 and V_2 are interface velocities at the incident bar/specimen interface and the specimen/transmitted bar interface (shown schematically in Figure 3.13), respectively, and L is the length of the specimen. The interface velocities can be defined as $V_1 = C_0\varepsilon_I$ (at t=0) and $V_2 = C_0\varepsilon_T$. At $t > 0, V_0$ decreases due to the reflected wave according to:

$$V_1 = C_0(\varepsilon_I - \varepsilon_R)$$

By substitution,

$$\frac{d\varepsilon}{dt} = \frac{C_0(\varepsilon_I - \varepsilon_R) - C_0\varepsilon_T}{L}$$

or,

$$\dot{\varepsilon}(t) = \frac{C_0}{L}(\varepsilon_I - \varepsilon_R - \varepsilon_T)$$

Strain can then be found by integrating the above equation:

$$\varepsilon(t) = \frac{C_0}{l}\int_0^t [\varepsilon_I(t) - \varepsilon_R(t) - \varepsilon_T(t)]dt$$

Stress can be found as follows:

$$\sigma = \frac{P_1(t) + P_2(t)}{2A}$$

where P_1 and P_2 are the forces acting on the incident bar/specimen interface and the specimen/transmitted bar interface, respectively, and are defined as:

$$P_1(t) = A_0E_0(\varepsilon_I + \varepsilon_R)$$
$$P_2(t) = A_0E_0\varepsilon_T$$

which gives:

$$\sigma = \frac{A_0E_0}{2A}[\varepsilon_I(t) + \varepsilon_R(t) + \varepsilon_T(t)]$$

where E_0 is the elastic modulus of the bars and A_0 is the cross-sectional area of the bars. At equilibrium, $P_1(t) = P_2(t)$ and $\varepsilon_I(t) + \varepsilon_R(t) = \varepsilon_T(t)$, which gives:

$$\sigma(t) = E_0\frac{A_0}{A}\varepsilon_T(t)$$
$$\dot{\varepsilon}(t) = -\frac{2C_0}{L}\varepsilon_R$$
$$\varepsilon(t) = -\frac{2C_0}{L}\int_0^t \varepsilon_R dt$$

The deformation and failure during impact were imaged using a Redlake MotionXtra high-speed camera (maximum recording rate of 100,000 frames/sec) to record 250 images (including a 50 image pre-trigger setting) at a rate of 30,000 frames/sec (330 μs interframe time) utilizing two Dedocool lights to enhance the imaging. The camera was triggered by

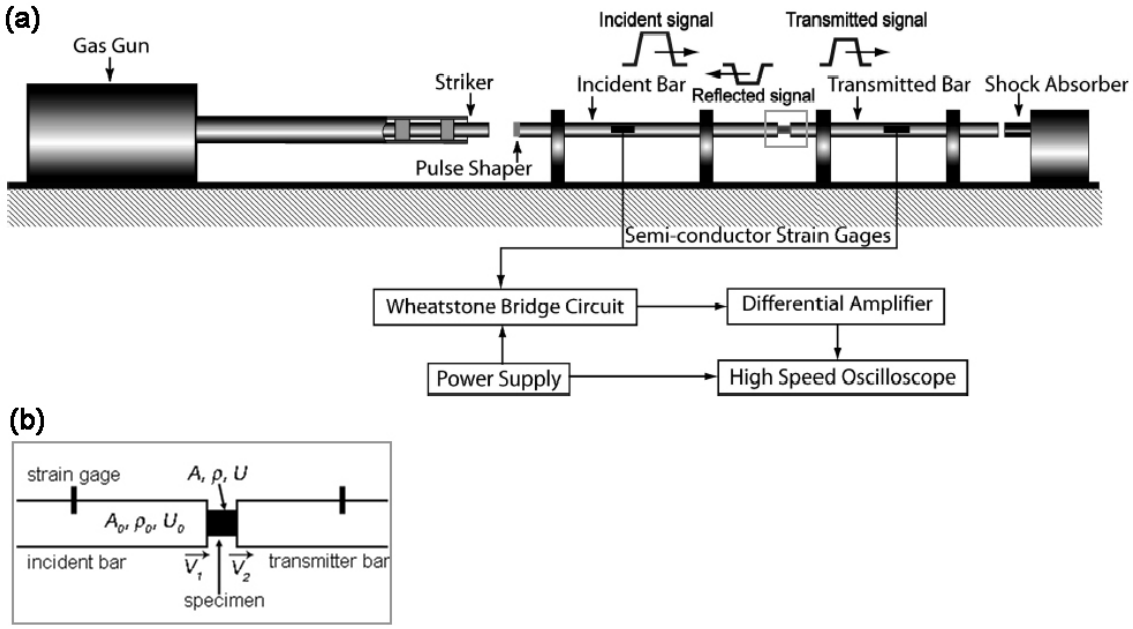

Figure 3.13: (a) Schematic of the setup of the Hopkinson bar experiments [104,105] showing the striker bar, which impacts the incident bar producing a pulse, which subsequently travels through the specimen. (b) Schematic closeup view of area where specimen is held during the experiment (marked with gray box in (a)) showing the interfaces between the incident bar, sample, and transmitted bar and the corresponding variables.

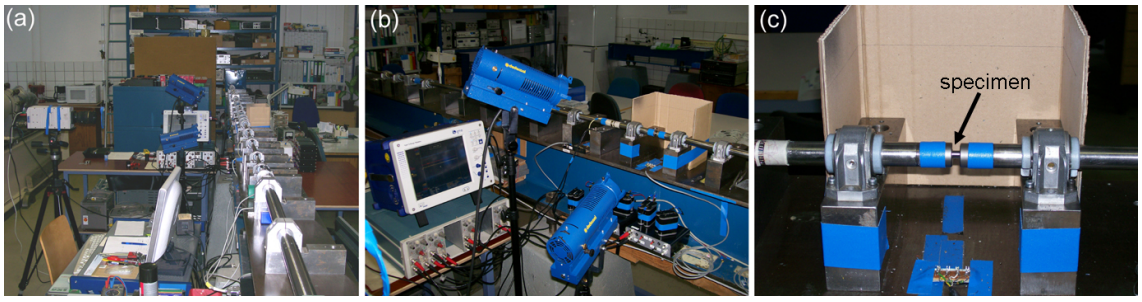

Figure 3.14: Photographs of the Hopkinson bar apparatus at TU Chemnitz. (a) The entire length of the apparatus, with the diagnostics to the left side, (b) the two lights used for imaging, the oscilloscope, and power source for the strain gauge measurements, and (c) a close-up of the specimen between the removable platens attached to the incident and transmitted bars.

the oscilloscope. Photographs of the Hopkinson Bar apparatus at TU Chemnitz which was used for these experiments are shown in Figure 3.14.

For the uniaxial specimens, a pair of strain gauges were mounted on opposite sides of the specimen in order to obtain the correct stiffness and correct for the compliance of the testing apparatus. The signal from the strain gauge was used to calculate strain according to the procedure which was described in Section 3.3.2 for the quasi-static tests. Examples of the raw data obtained from these tests can be seen in Figure 3.15. Data analysis was performed using FAMOS software. The scripts used for perform the calculations can be found in Appendix A.3.

After analysis of the initial data, stopped tests were performed approximately at yield, failure, and at stages in between for both the uniaxial and biaxial specimens. The incident bar was stopped, thus preventing further specimen deformation, using precision-machined hardened steel rings which were placed around the sample (using glue to attach to the platen) and were machined in 0.1 mm increments in order to stop tests at nearly any strain increment desired.

3.3.5 Conversion to True Stress and Strain

Due to the high ductility of LM106-70W and the large strains experienced by the specimens under some testing conditions, all engineering stress and strain data (for all strain rates) was converted to true stress and strain. This conversion ensured that the material properties were being measured and analyzed and not component properties. The conversion to true stress and strain is based on the assumption of constant volume.

3.4 High Strain Rate Regime (10^3-10^5 s^{-1})

The high-strain rate (10^3-10^5 s^{-1}) and very high-strain rate ($>10^5$ s^{-1}) impact experiments were performed using a single-stage helium-driven gas-gun at Georgia Tech (with the exception of five experiments performed at the NIMS in Japan, which will be discussed in

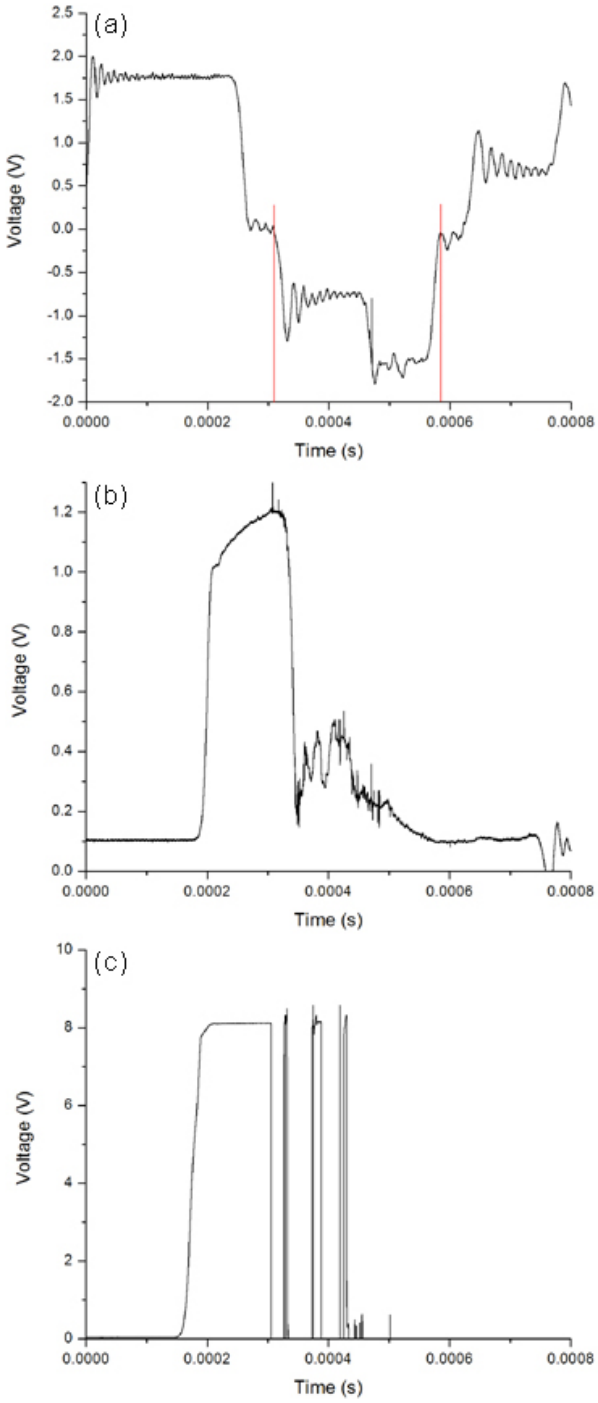

Figure 3.15: Raw data obtained from the Split Hopkinson Pressure Bar testing. (a) Voltage measured by the strain gauge affixed to the incident bar. The reflected wave (between the red lines) was used to calculate strain. (b) Voltage measured by the strain gauge affixed to the transmitted bar, which was used to calculate stress. (c) Voltage measured by the strain gauges on the specimen through a half Wheatstone Bridge, used to calculate strain in the early stages of deformation.

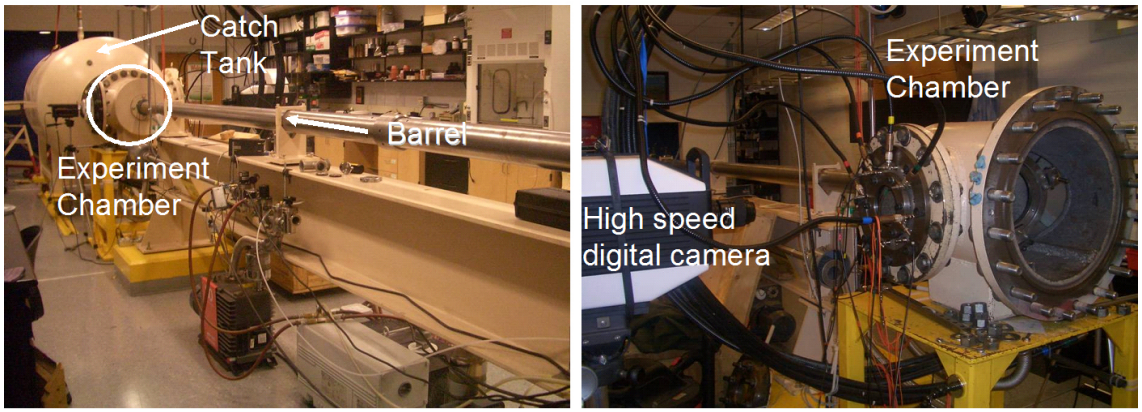

Figure 3.16: Photographs of the single-stage gas gun at Georgia Tech. Diagnostics included high-speed photography and velocity interferometry (VISAR). Samples were recovered post-impact from the soft-catch tank. The photograph on the left shows the 25 ft. long barrel leading to the experiment chamber and catch tank. The photograph on the right shows the experiment chamber with the high-speed camera positioned to capture images through a window and cables connected from oscilloscopes to velocity pins through BNC feed-throughs.

Section 3.5.1.2). Photographs of the GT gas gun are shown in Figure 3.16. The gun has an 80 mm diameter, 25 ft. long barrel, and is capable of impact velocities of 50 to 1150 m/s, utilizing a wrap around breach firing mechanism for the lower end of the velocity range and a double-rupture diaphragm firing mechanism for the higher impact velocities. During experiments, the barrel and experiment chamber were evacuated to below 100 mtorr. The experiment chamber is sealed from the catch tank with a thin (0.1778 mm) Mylar polyester diaphragm to prevent necessity of evacuating the entire catch tank to the same vacuum level. For each experiment, a series of shorting pins was used to measure the velocity of the projectile (impact velocity) by dividing the measured distance between the pins by the time between the electrical signal generated when the projectile shorted each pin. Two crush pins (for redundancy) extending ~3 mm in front of the impact face were used to trigger the oscilloscopes and diagnostics. The velocity and triggering signals were passed through an experiment chamber door with BNC feed-throughs. The velocity pin signals were recorded on a series of HP 53131A counters, as well as a TDS 784D Tektronix oscilloscope for redundancy.

3.4.1 Reverse Taylor Impact (Dynamic Compression) Tests

Dynamic compression experiments were performed using the reverse Taylor [57] anvil-on-rod impact configuration. The rod-on-rigid-anvil impact experiment developed by G.I. Taylor [57] in 1948 has become a standard method for investigating the high-strain rate ($\sim 10^3$-10^5 s^{-1}) deformation response of materials. In Taylor's impact experiment, a rod-shaped specimen is accelerated to impact a rigid anvil and deformation propagates through the cylinder as a wave. Because of the dynamic nature of this experiment, the part of the cylinder experiencing the impact undergoes a higher deformation and a higher strain rate than the subsequent sections of the cylinder. After impact, the specimen is recovered and the changes in its dimensions are used to infer its dynamic flow strength based on the assumption of a rigid, perfectly plastic material response [57, 58, 106–108]. According to Taylor's analysis, conservation of mass across the elastic-plastic interface is given as:

$$A_0(U + v) = Av, \rho_0 = \rho \tag{5}$$

where A is the cross-sectional area of the rod, U is the impact velocity, and v is the velocity of the deformed material. If the stress on either side of the interface is σ_{yd}, the amplitude of the elastic wave, then the conservation of momentum gives:

$$\rho A_0(U + v)U = \sigma_{yd}(A - A_0) \tag{6}$$

Combining Equations 5 and 6 and knowing that

$$\varepsilon = \frac{L_0 - L}{L_0} = \frac{V_0/A_0 - V_0/A}{V_0/A_0} = 1 - \frac{A_0}{A} \tag{7}$$

we get:

$$\frac{\rho U^2}{\sigma_{yd}} = \frac{\varepsilon^2}{1 - \varepsilon} \tag{8}$$

Equation 7 is Taylor's definition of strain, which will be used for analysis of results of impact experiments in a subsequent chapter (Section 5.4.1.3). Equation 8 is Taylor's definition of the dynamic yield stress of a material. Although not a particularly useful value

in an absolute sense, this dynamic strength represents the average yield stress of the material during the particular conditions of that impact (including a range of stresses and strain rates) and is typically significantly greater than the static yield strength of the material.

In 1973, Wilkins and Guinan [58] provided a new analysis of Taylor's impact experiment. This analysis assumed that the change in length with time was equal to the instantaneous velocity of the rod:

$$\frac{dL}{dt} = -U \tag{9}$$

Application of Newton's 2nd Law to obtain the force exerted on the rigid wall by the specimen gave:

$$\sigma_{yd} A = -\rho_0 L A \frac{dU}{dt} \tag{10}$$

where $\rho_0 LA$ is the specimen's mass and $\frac{dU}{dt}$ is its deceleration. Substitution of Equation 9 into Equation 10 gives:

$$\frac{dL}{L} = \frac{\rho_0 U}{\sigma_{yd}} dU$$
$$\ln \frac{L_1}{L_0} = -\frac{\rho_0 U^2}{2\sigma_{yd}}$$

which is another definition of dynamic yield strength, and seems to give a more reasonable, although still largely only an average measurement of dynamic strength of materials. The definition of strain used by Wilkins and Guinan [58], however, is used in analysis of Taylor impact experiments in Section 5.4.1.3.

Instrumented Taylor tests have also been used to generate stress-strain-strain-rate curves [107, 109] and investigate the constitutive response of materials by comparing the experimental and simulated final deformed shapes of the specimen through use of a constitutive model [58, 110–120]. The correlation of simulations with experiments provides validation of constitutive models, often after extracting the constants from the experiment, by matching the simulated final profile to that of the recovered specimen obtained during the

impact experiment. However, matching the final shape of the specimen does not necessarily provide a robust validation of the constitutive model since the deformation path is not considered [121]. More recently, the Taylor impact test has been performed in its reverse configuration, with the rigid anvil impacting a stationary rod-shaped sample, allowing for simultaneous velocity interferometry of the free (back) surface velocity [121–126] and high-speed photography of the impact and specimen deformation throughout the entire impact event. The implementation of multiple time-resolved diagnostics which monitor the entire time-dependent deformation event and the elastic-plastic wave propagation and interaction not only provides more information about the deformation history, but allows for more robust validation of constitutive models [121, 122, 126]. For these reasons, dynamic compression experiments were performed in the reverse Taylor impact configuration with both high-speed photography and velocity interferometry.

A schematic of the reverse Taylor anvil-on-rod impact test setup can be seen in Figure 3.17. The projectile consisted of an 80 mm diameter Al sabot with a 10 mm thick high strength AF1410 (Eglin) steel rigid anvil plate secured to the front surface. A cylindrical rod (D=9 mm, L=50 mm) of W-LM106 composite, which was epoxy-mounted at ~10 mm from its back end to an 1/8 in. thick Acrylic target ring in the experiment chamber, served as the target. The brittle epoxy and Acrylic target ring fractured immediately upon impact and did not interfere with deformation and fracture of the specimen. Specimens were lapped with 25 μm diamond suspension to insure planar and parallel surfaces, and a laser was used to align the specimen to insure planar impact within 3 mrad of tilt using a two-axis adjustment (mounted to the gun muzzle) on the target ring and a laser alignment system.

An Imacon-200 High-Speed Digital Camera captured images (16 frames) of the transient deformation of the specimen during impact. The images had a resolution of 1200 pixels by 980 pixels, which corresponds to approximately 18 pixels/mm in the field of view used for these experiments. An example of the 16 frames captured is shown in Figure

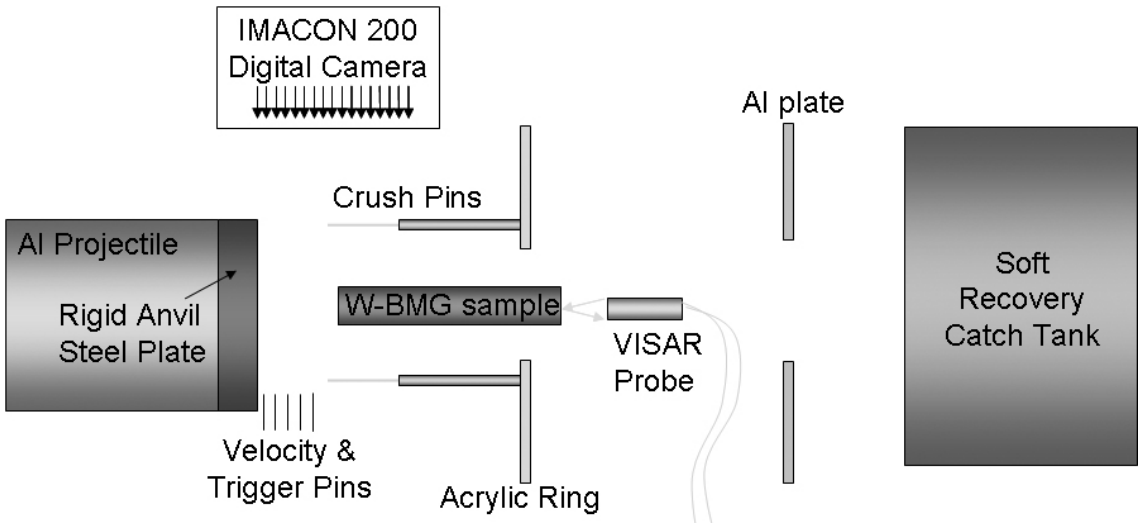

Figure 3.17: Schematic of anvil-on-rod impact (reverse Taylor) test setup used in a gas gun with high-speed digital photography, velocity interferometry and soft recovery of the sample. The projectile-flyer assembly accelerates down the barrel, first passing a series of velocity and trigger pins (to trigger the flash) and then crush pins (to trigger the camera and VISAR) before impacting the specimen. The high-speed camera captures 16 images during deformation. The specimen is held in place with epoxy into an acrylic target ring, which fractures immediately upon impact so as not to interfere with deformation. The VISAR probe holding two optical fibers is positioned behind the specimen. A laser is shined onto the back (free) surface of the specimen and the reflected light is collected into the second fiber. The deformed or fractured specimen was recovered from the soft recovery catch tank following impact.

3.18 (frame 10 did not capture an image in this particular experiment). Shown in the center of these images is the rod-shaped specimen and the Acrylic target ring (appears as a thick line in the side view) which held it in place. The crush pins can be partially seen above and below the specimen rod. The Al sabot with steel flyer plate mounted to its front surface can be seen approaching from the left in each frame. These frames progress from left to right starting in the upper left corner and ending in the lower right corner. Frames were typically captured beginning immediately before impact and over a time duration of ~100 μs. To obtain quantitative dimensional and strain data from these images, measurements of the specimen's dimensions along its entire length and radius were performed. To make these measurements, the profile of the deforming specimen was isolated from the image using Adobe Photoshop software. Next, ImageJ software (National Institute of Health) was used to create a vertical or horizontal profile along the entire specimen, and the length of each line drawn by the ImageJ macro was subsequently measured in pixels and converted to mm. Images showing examples of the image isolation and profile drawing are shown in Figure 3.19. Measurements of the dimensions of the rod-shaped specimen during deformation were taken from the images and the error associated with these measurements is derived in Appendix B.1.

The VISAR (velocity interferometry system for any reflector) system [127] (Valyn International) was used to capture the free surface velocity of the composite rod during each experiment. This system utilized an input laser, which was placed ~30 μm from the rear surface of the specimen and was focused in a 200 μm spot on its back (free) surface. The specimen's back surface was polished such that the light from the laser was reflected, and some of this reflected light was captured by an output optical fiber. When the light was transported back to the interferometer, it underwent a Doppler shift proportional to the velocity of the specimen. Photomultiplier units then transduced the changes in light amplitude to changes in electrical voltage, and the digitizing oscilloscope recorded the voltage histories. These electrical histories were then processed using an algorithm in the PlotData

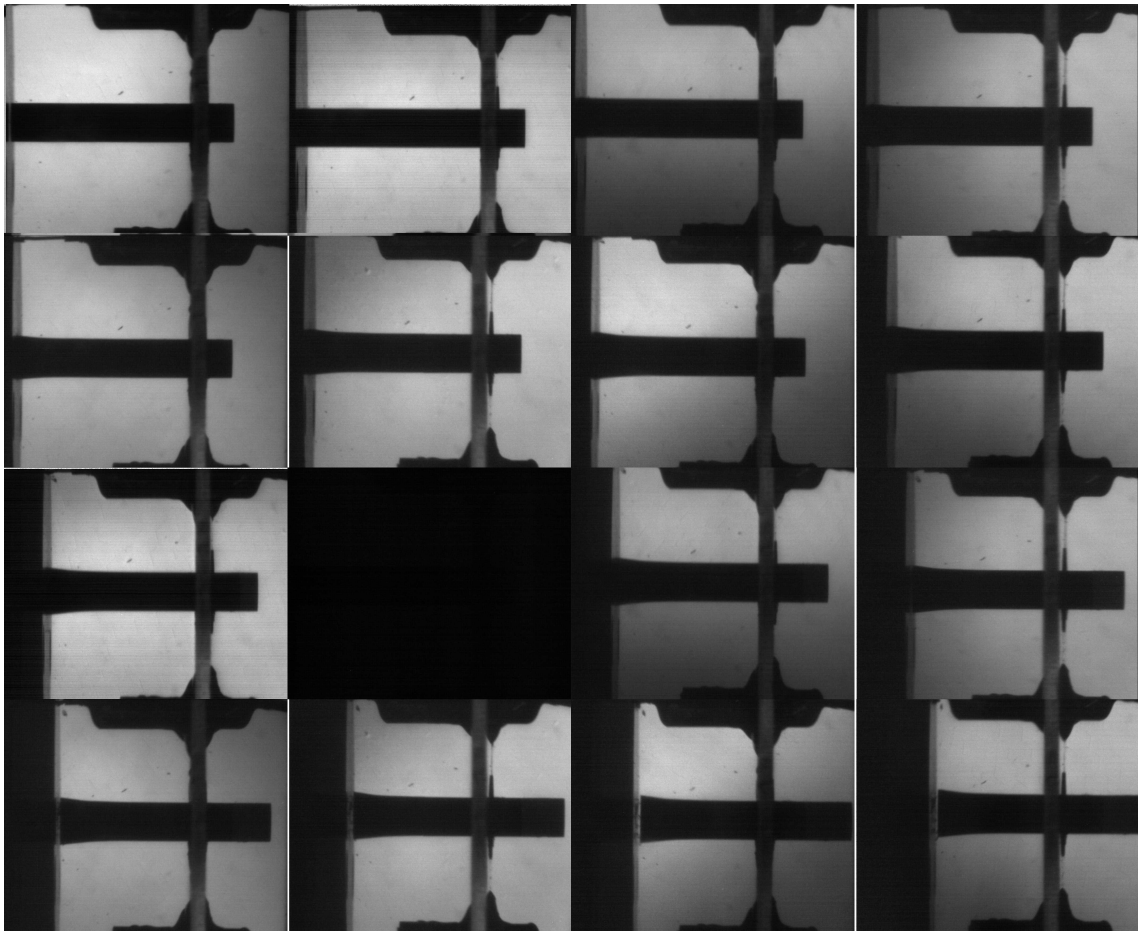

Figure 3.18: Example of 16 high-speed images captured by the Imacon-200 high-speed digital camera during a dynamic compression experiment. These frames progress from left to right starting in the upper left corner and ending in the lower right corner. Frames were typically captured beginning immediately before impact and over a time duration of ~100 μs. Frame 10 is dark because it did not capture an image in this particular experiment.

Figure 3.19: Example of the process of isolating the specimen profile from the high speed image and processing it with an ImageJ macro to obtain the specimen dimensions along the entire deforming rod.

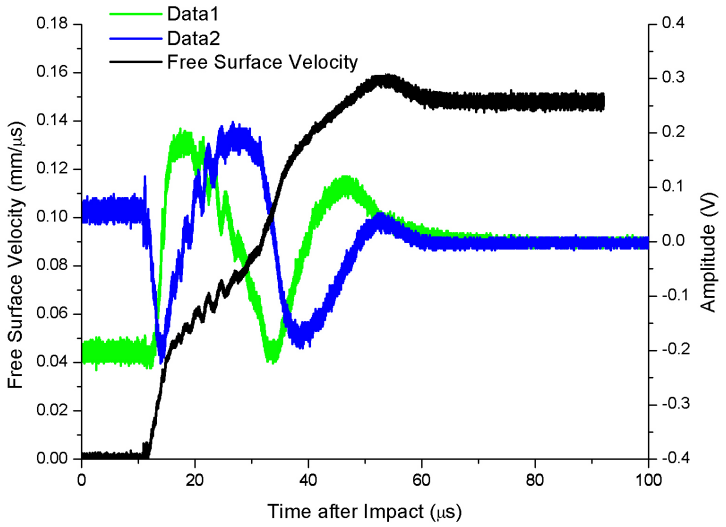

Figure 3.20: Example of the two voltage traces generated by the VISAR system and the free surface velocity trace that resulted after processing with PlotData software.

software (Sandia National Laboratories) to obtain the measured specimen surface velocity history. An example of the data obtained from the VISAR system and the resulting free surface velocity trace after post-processing is shown in Figure 3.20.

3.4.1.1 AUTODYN-2D Modeling of Reverse Taylor Impact Tests

Finite element simulations using the AUTODYN hydrocode were performed and correlated with many of the impact experiments. A general description of the setup for these simulations is described here. The simulations were set up in an axisymmetric configuration with a gauge on the back surface of the sample rod which monitored the free surface velocity, as shown in Figure 3.21, for correlation with experimentally-captured free surface velocities. For model validation, the deformed specimen profiles generated by the simulations were captured at times corresponding to those of the images captured during each experiment. The simulated and experimental transient profiles and sample back (free) surface velocity traces were compared to verify model applicability at all velocities and to extract additional information about deformation and failure by analyzing the simulation results in

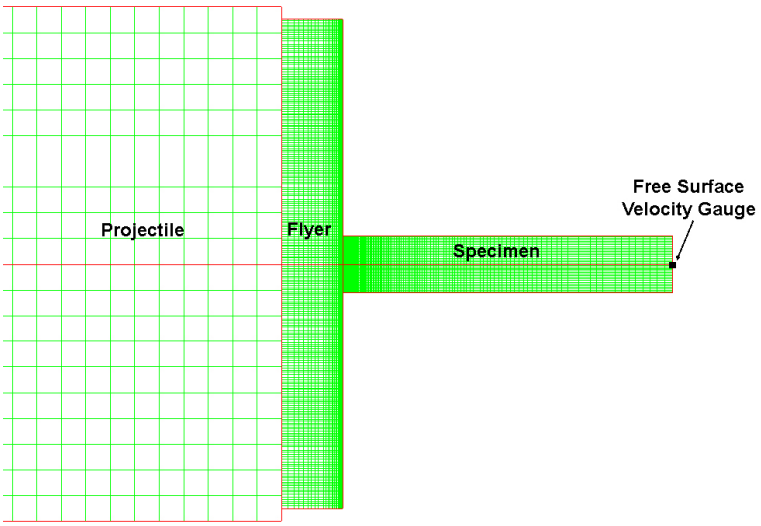

Figure 3.21: 2-D axisymmetric problem setup and mesh in AUTODYN-2D showing the projectile (partial), rigid anvil, and specimen rod. The gauge on the back (free) surface of the specimen tracks the free surface velocity.

conjunction with experimental results. Details of the models used and the specific goals for using these simulations will be discussed in later chapters in correlation with the respective results.

3.5 Very High Strain Rate Regime ($\dot{\varepsilon} \geq 10^5\ s^{-1}$)

The stress required to generate strain rates on the order of $\sim 10^6\ s^{-1}$ is generally much in excess of the dynamic flow strength of a material, allowing for the shear stresses to be neglected and the problem to be essentially one-dimensional. These conditions lead to a shock wave, which is defined as a discontinuity in pressure, temperature (internal energy), and density. The calculations of shock wave parameters are based on the Rankine-Hugoniot [128, 129] conservation equations. The assumptions governing these conservation equations and calculations are (1) discontinuity of the shock front, (2) negligible shear modulus, (3) negligible body forces, (4) no elasto-plastic behavior, and (5) no phase transformations [103]. The conservation of mass across the shock front is described as follows [103]:

mass in = mass out

mass moving toward the front: $A\rho_0(U_s - U_0)dt$

mass moving away from the front: $A\rho(U_s - U_p)dt$

Hence,

$$A\rho_0(U_s - U_0)dt = A\rho(U_s - U_p)dt$$

and if $U_0 = 0$,

$$\rho_0 U_s = \rho(U_s - U_p) \tag{11}$$

The conservation of momentum across the shock front has the stipulation that the difference in momentum is equal to the impulse per unit area [103]:

Momentum=mass×velocity

Impulse=Fdt

Difference in momentum=$(\text{momentum})_1$-$(\text{momentum})_0$ =

$\rho A(U_s - U_p)dt - \rho_0 A(U_s - U_0)dtU_0)$

Impulse=Fdt=$(PA - P_0A)dt$

Then equating the difference in momentum with impulse:

$$A\rho(U_s - U_p)U_p dt - A\rho_0(U_s - U_0)U_0 dt = (P - P0)Adt$$

$$\rho_0(U_s - U_0)(U_p - U_0) = P - P_0$$

and if $U_0 = 0$,

$$(P - P_0) = \rho_0 U_s U_p \tag{12}$$

The difference in total energy between the two sides of the shock front is equal to the difference in work done by P and P_0, which is equal to [103]:

$$\Delta W = (PA)(U_p dt) - (P_0 A)(U_0 dt)$$

The difference in total energy is equal to:

$$\Delta E = \tfrac{1}{2}[\rho A(U_s - U_p)dt]U_p^2 + EA\rho(U_s - U_p)dt - (\tfrac{1}{2}[\rho_0 A(U_s - U_0)dt]U_0^2 + E_0 A\rho_0(U_s - U_0)dt)$$

Setting $\Delta W = \Delta E$ and taking $U_0 = 0$,

$$PU_p dtA = \left[\tfrac{1}{2}\rho A(U_s - U_p)dt\right] U_p^2 + EA\rho(U_s - U_p)dt - E_0 A\rho_0(Us)dt$$
$$PU_p = \tfrac{1}{2}\rho(U_s - U_p)U_p^2 - E_0\rho_0 U_s + E\rho(U_s - U_p)$$

Making substitutions from the conservation of mass equation (Equation 11),

$$PU_p = \frac{1}{2}\rho U_s U_p^2 - E_0\rho_0 U_s + E\rho_0 U_s = \frac{1}{2}\rho U_s U_p^2 \rho_0 U_s (E - E_0) \tag{13}$$

The conservation of energy equation can be simplified [103]:

$$E - E_0 = \tfrac{PU_p}{\rho_0 U_s} - \tfrac{1}{2}\rho_0 \tfrac{U_s U_p^2}{\rho_0 U_s}$$

Making substitutions from the conservation of momentum (Equation 12),

$$E - E_0 = \frac{P(P - P_0)}{\rho_0^2 U_s^2} - \frac{1}{2}\frac{(P - P_0)^2}{\rho_0^2 U_s^2} \tag{14}$$

And with further substitutions from the conservation of mass (Equation 11),

$$(\rho_0 - \rho)U_s = -\rho U_p = -\frac{\rho(P-P_0)}{\rho_0 U_s}$$
$$\rho_0 U_s^2 = -\rho(P - P_0)\frac{1}{\rho_0 - \rho}$$

Since $1/\rho = V$,

$$\rho_0^2 U_s^2 = \frac{(P-P_0)}{V_0 - V}$$

And substituting back into Equation 14 gives:

$$E - E_0 = P(P - P_0)\frac{V_0 - V}{P - P_0} - \frac{1}{2}\frac{(P-P_0)^2}{P-P_0}(V_0 - V)$$

which simplifies to the more common form of the conservation of energy equation:

$$E - E_0 = \frac{1}{2}(P + P_0)(V_0 - V) \tag{15}$$

In the above three conservation equations (Equations 12-14) there are five variables: pressure, P, particle velocity, U_p, shock velocity, U_s, specific volume, V, or density, ρ, and energy, E. Therefore, an additional equation is necessary in order to determine all unknowns as a function of one parameter. A fourth equation, which relates shock velocity and particle velocity, can be experimentally determined, and is referred to as the equation of state (EOS).

3.5.1 Equation of State Experiments

The EOS often has the form:

$$U_s = C_0 + S_1 U_p + S_2 U_p^2 + ...,$$

where S_1, S_2, etc. are empirical parameters and C_0 is the sound speed in the material at zero pressure. For most metals, the EOS reduces to a first order (linear) relationship. Once this EOS has been determined, and one or more of the variables has been measured, all of the

other parameters can be calculated. It should be noted that if the material undergoes any phase transformations within the pressure range of interest, a new EOS is required for the new phase. Since BMGs are relatively new materials and their EOSs have not been well-characterized, it was of interest to determine the EOS of LM106 up to very high pressures (~120 GPa) to learn about the phase stability of this material. Two different techniques were utilized to perform these EOS experiments and these are described in the following sections.

3.5.1.1 Low Pressure Regime Experiments Utilizing Stress Gauges + VISAR Diagnostics

The equation of state data in the relatively low stress regime (<26 GPa) were obtained using the single-stage gas gun at Georgia Tech. Experiments were performed using a plate impact configuration in which a (W-6Cu-4Ni alloy or Cu) flyer plate (~50.8 mm diameter and ~5.1 mm thickness) impacted a (304 stainless steel or Cu) driver plate (~57.15 mm diameter and ~2.8 mm thickness), which was backed by a ~10 mm diameter and 2-2.5 mm thickness BMG sample. In this configuration, the equation of state properties were measured using in situ polyvinylidine fluoride (PVDF) stress gauges (Ktech Corporation) and VISAR [127] velocity interferometry (Valyn International), as illustrated in the schematic shown in Figure 3.22. The PVDF gauge packages consist of a Bauer-type PVDF gauge enclosed within two insulating films of 0.0001" PTFE, totaling 75 μm. The PVDF gauge mounted along the driver-sample interface was used to record the input stress, P, and the arrival time of the shock wave at the sample front. The gauge mounted on the sample's back surface was used to measure the propagated stress and arrival time of the shock wave at the rear surface of the sample. In some cases, a back gauge was not used, and the VISAR signal was instead used to measure the arrival of the shock wave at the rear surface of the sample. The sample thickness divided by the travel time of the shock wave through the sample (less the time of travel through the 75 μm gauge package thickness) allowed for determination of the shock velocity, U_s. The details of the experimental setup for each

equation of state experiment are reported in Table 7.1. The experimental setup has been described in greater detail by Eakins [130] for a powder specimen.

Construction of the gauge packages and specimen assembly in the present work were performed as follows. First, all mating surfaces are lapped to within 1% parallelism . Next, a single PTFE film was attached to the back surface of the driver using Loctite Hysol thin-film epoxy, and cured for 12 hours. During the cure stage, the films were placed under approximately 7 kg of weight. The input PVDF gauge was then placed on the film, positive lead (+) toward impact, and covered with a second PTFE film, ensuring that all air pockets were removed. After curing of that layer, the specimen was then fixed (again with Loctite Hysol thin-film epoxy) on top of the input gauge package. After curing of that layer, the PTFE film-gauge-PTFE film procedure was repeated on the rear of the specimen. The input and propagated gauges were aligned such that the they were oriented at 90° to one another to prevent interference between them. Photographs taken during each stage of the driver-gauge-specimen package assembly can be seen in Figure 3.23. The driver-gauge-specimen package was mounted in a 3/8 in. thick PMMA ring, which was mounted to the muzzle of the gun using 2 in. thick standoff blocks. Figure 3.23(d) shows a photograph of the entire specimen assembly mounted inside the experiment chamber, with the VISAR probe behind the specimen and CVRs attached to the PVDF gauges.

The mechanism by which the PVDF stress gauges measure stress is as follows [130]. The stress gauges are composed of PVDF films which had been polarized by the Bauer process (U.S. patent #4684337). This polymer is piezoelectric and develops a bias (potential) in response to stress [131], and when placed in a circuit, the film produces current flow proportional to the lattice strain. Applied stress and electrical response are related through a well-characterized empirical relationship up to 100 GPa [132, 133]. The PVDF gauges are placed in parallel with a current-viewing resistor (CVR) which provides precise resistance on the time scale of these impact experiments. A Tektronix 1040A 4-channel GHz

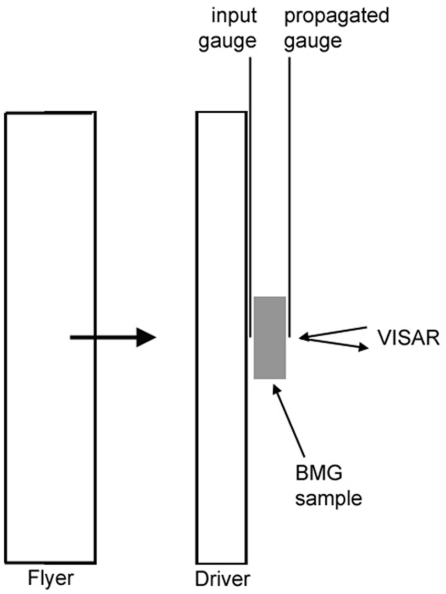

Figure 3.22: Plate impact setup with PVDF stress gauges and VISAR velocity interferometry diagnostics. The flyer plate impacts a driver plate, which has a BMG specimen mounted on its rear surface. PVDF stress gauges are attached to the sample's front and rear surfaces to measure the magnitudes of the input and propagated stresses. VISAR was used to capture the free surface velocity on the rear surface of the BMG specimen.

frequency oscilloscope (1 ns/point resolution, triggered on an auxiliary line by the crush-pins) monitors the potential (voltage) across the CVR after it has been channeled through isolated BNC connections through the side of the experiment chamber. The input and propagated PVDF signals are each split into low and high sensitivity channels such that the low sensitivity channel captures the peak magnitude and the high sensitivity channel is used to resolve the peak base. Using an algorithm within the Labview-based software, PlotData (Sandia National Laboratories) [133], voltage is then converted into charge density [131] according to:

$$V = \frac{I}{R}$$

$$\rho_I = \frac{I}{A}$$

$$\rho_Q = \int_0^t \rho_I(t)dt$$

where V is the measured voltage, I is the current, R is the CVR value and ρ_I is the current

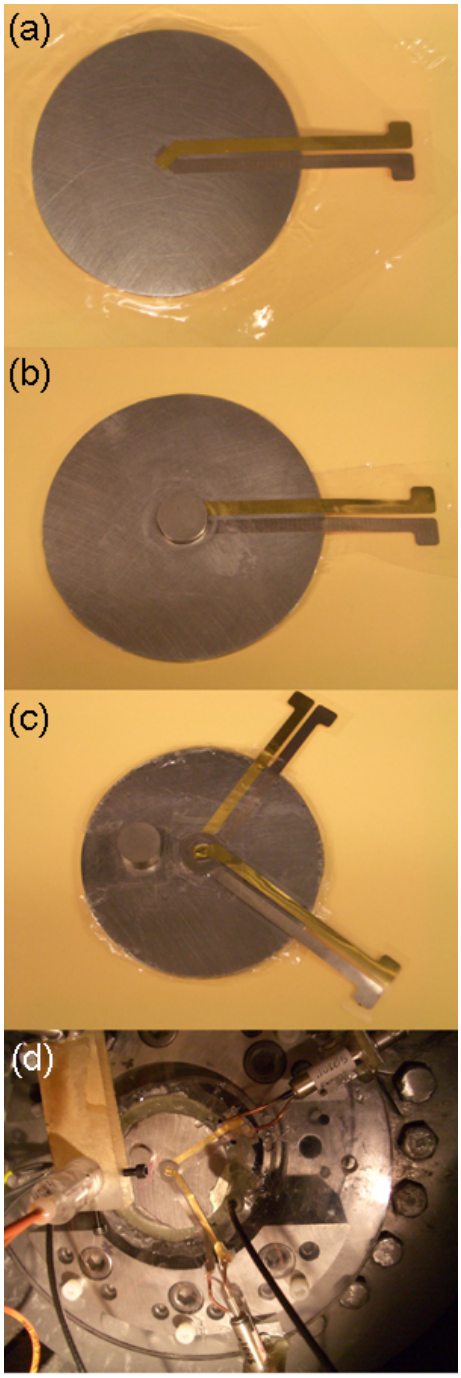

Figure 3.23: (a-c) Photographs taken at different stages of setup of driver-gauge- specimen package. (a) Driver with Teflon film and input PVDF gauge, (b) sample, and (c) propagated PVDF gauge and an extra specimen for redundancy or to measure a spall signal. (d) Photograph of the entire specimen assembly mounted in the experiment chamber. The VISAR probe can be seen behind the specimen and the CVRs can be seen attached to the PVDF gauges.

density, A is the active area of the gauge, and ρ_Q is the charge density. An example of this data reduction is shown in Figure 3.24.

VISAR was used to measure the free surface velocity, U_{fs}, from which the particle velocity, U_p, was deduced according to:

$$U_p \approx \frac{1}{2} U_{fs} \tag{16}$$

Deducing the particle velocity from the VISAR free surface velocity, U_{fs}, is a valid assumption under the conditions that the entropy increase associated with the shock state is small, and that the un-shocked material and that which has been shocked (moving at U_{fs} and returned to zero stress) have the same properties [134]. The experimentally measured U_p values were also compared with calculations utilizing the impedance matching technique [103, 135], which is described in Section 7.3.3 in conjunction with the presentation of the results. This experimental method therefore allowed for measurement of three variables, U_s, U_p and P. Details of these measurements are described elsewhere [121,136,137]. The derivation of the error propagation associated with these measurements is given in Appendix B.2.

3.5.1.2 Inclined Mirror + Streak Camera Technique

The high stress equation of state experiments were performed on the two-stage light-gas gun [138] at the National Institute for Materials Science (NIMS) in Tsukuba, Japan. The shock velocity and particle velocity were measured using the inclined mirror technique [134] and the experiments were instrumented with a streak camera (Ultranac FS 501) with a streak rate of ~55 ns/mm. Experiments were performed at impact velocities of ~3000-4700 m/s, which corresponded to stresses in the range of ~26-123 GPa. Impact velocity was measured (within ±0.3%) using the x-ray beam cutting method, in which three parallel beams are used to detect acceleration [138]. This was coupled with NaI scintillators and photmultiplier tubes (PMTs), which are also used for triggering signals. Flash

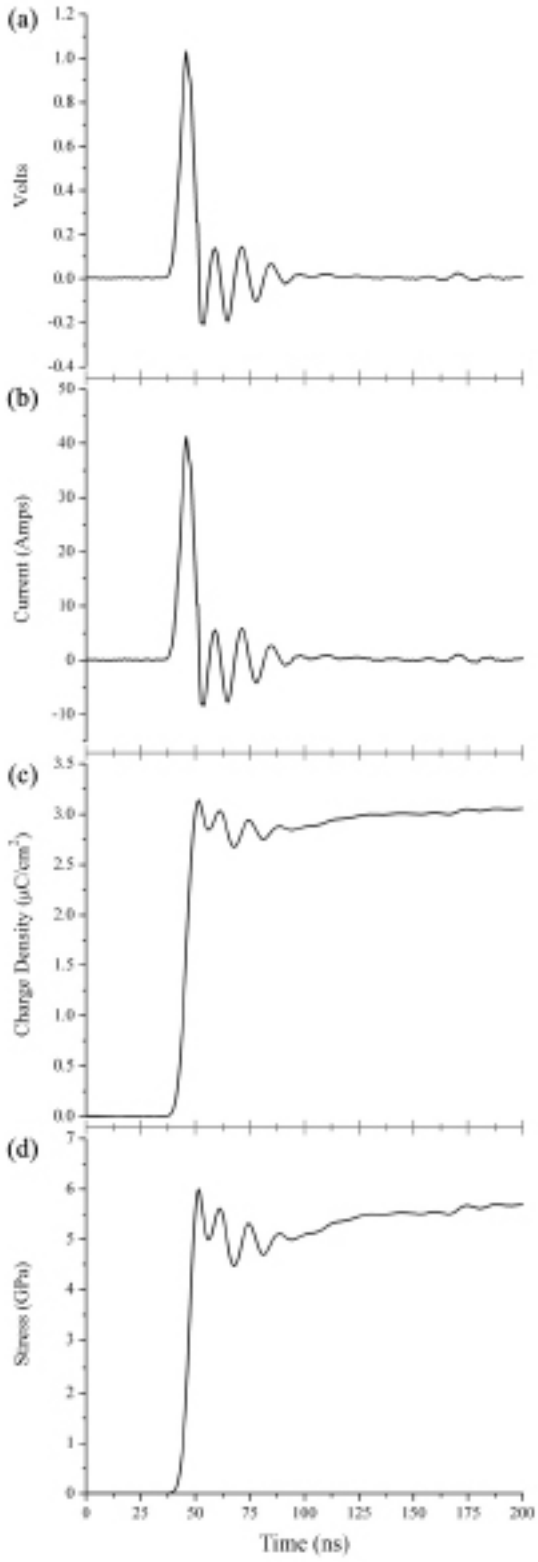

Figure 3.24: Examples of the sequence of (a) the raw voltage data obtained from the PVDF gauges and the subsequent reduction to (b) current, (c) charge density, and (d) stress [130]. The oscillations are caused by reverberations within the gauge package.

Figure 3.25: Photographs of the two-stage gas gun at the National Institute for Materials Science in Tsukuba, Japan. The photograph on the left shows the entire length of the gas gun. The photograph on the right shows the experiment chamber and the streak camera positioned to record reflected light during experiments.

x-ray shadowography was used to photograph the projectile during free flight to confirm planarity of impact [138].

The NIMS specimen setup consisted of a BMG sample (2-2.5 mm thickness) which was epoxy-mounted to a driver plate (Al or 304 Stainless Steel). Five mirrors were then epoxy-mounted to the sample + driver setup: one inclined mirror on the center of the sample, two flat mirrors on either side of the inclined mirror, and two flat mirrors on the driver plate adjacent to the sample, as can be seen in the schematic in Figure 3.26. The angle, α, between the inclined mirror (IM) and the sample was measured using a laser reflection technique. A trigger pin, which was used to trigger the streak camera, was epoxy-mounted to the driver plate such that about 10 mm of the pin was protruding from the impact face. The sample assembly was fixed to a steel target plate and hung in the experiment chamber. The target was aligned using an indicator to insure parallel impact. Photographs of the setup of these high-pressure plate impact experiments can be seen in Figure 3.27.

Figure 3.26 shows a schematic of the streak camera technique for recording extinction times of light reflected off various mirrors mounted on the sample. As can be seen in the schematic, a flash lamp is used to generate light during impact and this light is reflected off of all five mirrors. The schematic and streak camera image in Figure 3.28 illustrate how

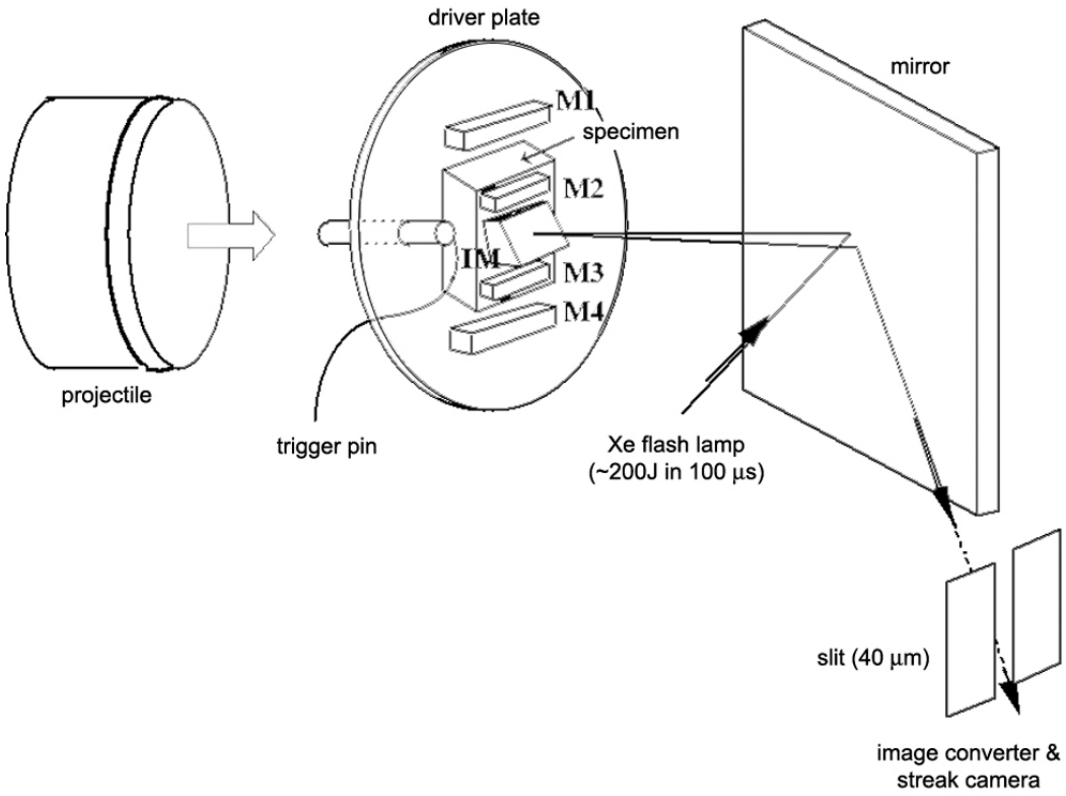

Figure 3.26: Schematic of the streak camera and inclined mirror setup for measurement of shock velocity and free surface velocity. The specimen was mounted on the back of a driver plate, along with five mirrors (M1-M4 and IM). A streak camera recorded light reflected off the mirrors during the experiment.

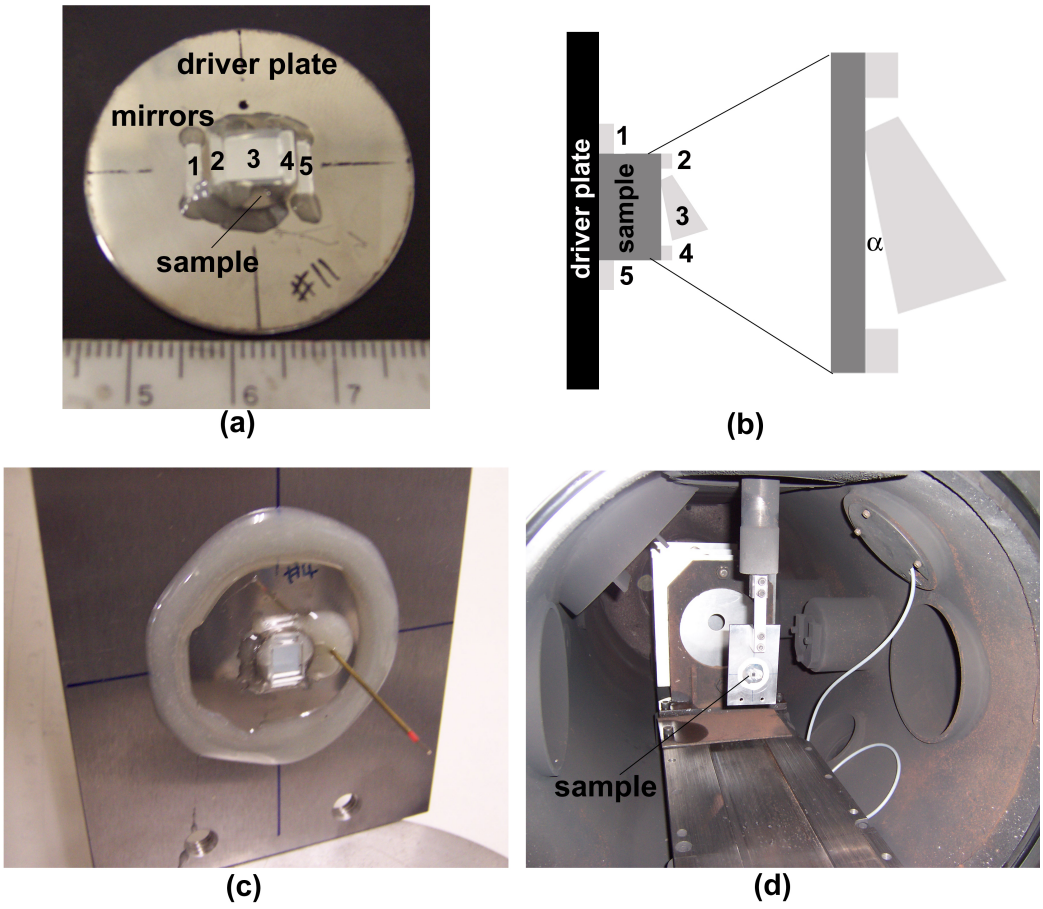

Figure 3.27: EOS experiment setup images. (a) Photograph of mirrors mounted on the sample and driver plate. (b) Schematic side view of the mirror, sample, and driver plate assembly. The angle α is between the sample and inclined mirror. (c) Photograph of sample assembly (back side) with trigger pin on target plate. (d) Photograph of sample assembly hanging in experiment chamber.

streak photography and the inclined mirror method are used to measured shock velocity and particle velocity. Upon arrival of the shock wave at the back of the driver plate, the light reflected off mirrors 1 and 4 (M1 & M4) becomes extinct. Similarly, when the shock wave reached the back surface of the specimen, the light reflected from mirrors 2 and 3 (M2 & M3) becomes extinct. The time difference between the extinction of light from M1/M4 and M2/M3 is the travel time of the shock wave through the specimen thickness. Dividing the sample thickness by the shock wave travel time yields the shock velocity, U_s. The free surface velocity of the specimen was related to the light reflected off the inclined mirror (IM) by:

$$U_{fs} = \frac{W}{M}\frac{tan\alpha}{tan\gamma} \tag{17}$$

where W is the camera streak rate, M is the magnification of the streak camera image, α is the angle between the inclined mirror and the sample (shown in the schematic in Figure 3.28), and γ is the angle produced on the streak record from the extinction of the light reflected off IM (shown in Figure 3.28). The particle velocity was then determined using Equation 16, and was compared with values calculated using the impedance matching technique [103,135]. The error associated with these measurements is derived in Appendix B.2.

3.6 Recovery Experiments

Recovery experiments were performed on the single-stage gas gun at NIMS at impact velocities of 794-1894 m/s and pressures of ~8-60 GPa, which were estimated using 2D axisymmetric AUTODYN simulations after the experiments. The recovery specimens were discs of 10.12 mm diameter and 1-1.5 mm thickness. Each disc was lapped to ensure that its surfaces were parallel. The discs were placed inside a 304 stainless steel capsule with a 304 stainless steel ring surrounding the sample since the inner diameter of the capsule

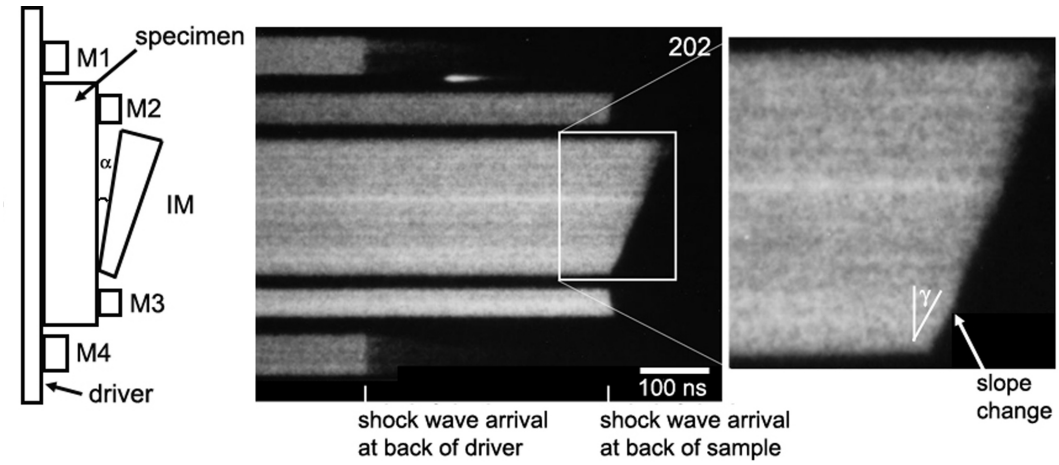

Figure 3.28: Schematic of driver plate+specimen+mirror setup showing flat mirrors (M1-M4) and an inclined mirror (MI). An example of a streak image is also shown. Upon arrival of the shock wave at the back of the driver plate, the light reflected off mirrors 1 and 4 (M1 & M4) becomes extinct. Similarly, when the shock wave reached the back surface of the specimen, the light reflected from mirrors 2 and 3 (M2 & M3) becomes extinct. The time difference between the extinction of light from M1/M4 and M2/M3 is the travel time of the shock wave through the specimen thickness. The free surface velocity of the specimen was related to the light reflected off the inclined mirror (IM) by $U_{fs} = \frac{W}{M}\frac{tan\alpha}{tan\gamma}$. The inset shows a change in slope (change in γ) in the streak image, which is indicative of a phase transition.

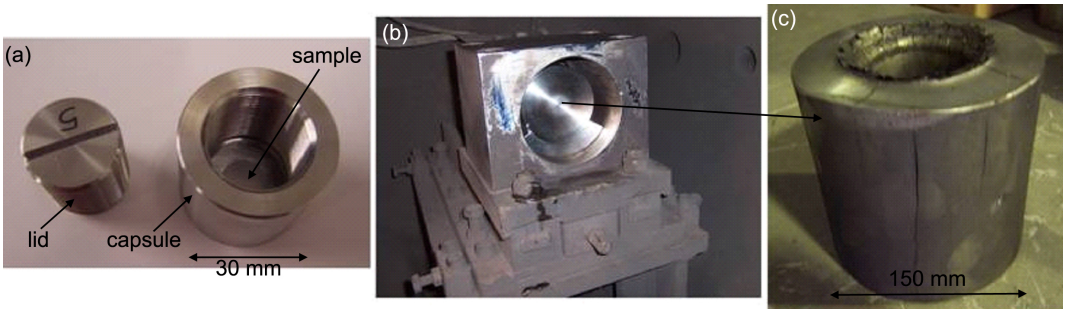

Figure 3.29: (a) Steel capsule with BMG sample disc inside. (b) Inside experiment chamber before experiment. The capsule is inside the momentum trap, which is the cylindrical part in the center of the photograph. (c) Momentum trap after the experiment showing deformation due to impact.

was larger than the diameter of the specimens. This setup is shown in Figure 3.29(a). Figure 3.29(b) shows the inside of the experiment chamber before an experiment, and Figure 3.29(c) shows the momentum trap after an impact experiment. After each experiment, the capsule was recovered and the specimen was removed and analyzed using x-ray diffraction and scanning electron microscopy.

CHAPTER IV

UNIAXIAL AND BIAXIAL COMPRESSIVE RESPONSE OF LM106-70W OVER A RANGE OF STRAIN RATES AND TEMPERATURES

4.1 Overview

The uniaxial and biaxial compressive responses of LM106-70W composite were investigated over a range of strain rates ($\sim 10^{-3}$ to 10^{3} s^{-1}) using an Instron universal testing machine ($\sim 10^{-3}$ to 1 s^{-1}), Drop Weight tester ($\sim$200 s^{-1}), and Split Hopkinson Pressure Bar ($\sim 10^{3}$ s^{-1}). The temperature dependence of the mechanical behavior was investigated at temperatures ranging from RT to 600 °C using the instrumented Drop Weight testing apparatus, mounted with an inductive heating device. After testing, the deformed and fractured specimens were examined using optical and scanning electron microscopy. Stopped experiments were used to investigate deformation and failure mechanisms at specified strain intervals in both the Drop Weight and Split Hopkinson Bar tests. These stopped specimens were also subsequently examined using optical and scanning electron microscopy to observe shear band and crack formation and development after increasingly more strain.

The overall results showed an increase in yield strength with strain rate and a decrease in failure strength, plasticity, and hardening with strain rate. Comparison of uniaxial and biaxial loading gave evidence of a strong susceptibility to shear failure since the additional 10% shear stress caused failure at much lower strains in all cases. Results also showed a decrease in flow stress and plasticity with increased temperature. Also notable was the anomalous behavior at 450 °C, which lies between the T_g and T_x and as such is in a temperature regime where homogeneous flow, as opposed to heterogeneous deformation via

shear banding, is the dominant mechanism in the BMG.

4.2 Introduction and Motivation

Because of the dependence of the deformation mechanism (homogeneous vs. inhomogeneous) of BMGs on temperature and strain rate, it was of interest to investigate the dependence of not only BMGs, but also their composites, as a function of both of these variables.

Strain-rate sensitivity in bulk metallic glasses has been the subject of several studies. A few investigators have reported that BMGs exhibit positive strain-rate sensitivity [59, 60]. However, most studies on this topic have drawn the conclusion that BMGs exhibit negative strain-rate sensitivity, with the fracture stress decreasing as strain rate increases [8, 9, 45, 49, 50, 52–54, 54, 61]. The mechanistic explanation given by Gu et al. [54] for the negative strain rate sensitivity of these materials is that adiabatic processes occur during failure of BMGs and higher strain rates favor adiabatic processes, thus leading to a lower failure strength at higher loading rates when adiabatic processes are more prevalent. Another explanation has been provided by Li et al. [8] suggesting that shear bands in a BMG initiate well below the yield stress and grow upon continued quasi-static loading. Under dynamic loading conditions, cracks initiate immediately upon shear band initiation due to the excess energy that is available; these cracks lead to fracture of the specimen, and thus a lower fracture stress. This explanation for the negative strain-rate sensitivity of BMGs was further supported by work done by Mukai et al. [45], in which they observed that although the quasi-statically tested specimens were failing at an "apparent" yield stress of ~1.7 GPa, they began to show serrations indicative of shear band formation, which is the mechanism for accommodation of deformation in BMGs. As strain rate was increased, the specimens could no longer accommodate the deformation quickly enough, and the failure strength approached ~1.4 GPa, which is the stress level when shear band initiation began.

The strain-rate sensitivity of BMG-matrix composites has also been investigated in a few studies [2, 9, 52]. In a study by Jiao et al. [2], $Zr_{57}Nb_5Al_{10}Cu_{15.4}Ni_{12.6}$ reinforced with

60 vol% W particles showed strain-rate hardening behavior with a strain-rate hardening exponent of m=0.016, which is close to a rule of mixtures approximation using the strain rate sensitivity of the two respective phases [2]. As expected, the rate-dependence in this composite is more characteristic of the BCC tungsten phase, which dominates due to the large volume fraction of tungsten as well as the restraint of the failure mode of the amorphous matrix. Mechanistically, it was found that shear bands develop in the amorphous matrix, and the tungsten particles provide obstacles to shear band propagation, which leads to formation of multiple shear bands and allows for development of large plastic strains. Similarly, Li et al. [9] studied W preform-reinforced BMGs and found positive strain-rate sensitivity for W and all composites, but negative strain-rate sensitivity for the monolithic BMGs.

Several studies have investigated the temperature dependence of the deformation and mechanical properties of BMGs [24, 30, 62, 70, 71], although the effects of temperature on BMG-matrix composites have yet to be investigated. In general, as the temperature is raised past the glass transition of the BMG, a change in the stress-strain response from brittle to ductile behavior can be observed as the deformation mechanism changes from inhomogeneous (failure along a single shear plane) to homogeneous (uniform macroscopic deformation, no macroscopic shear).

This study aimed to investigate the strain-rate sensitivity of the BMG composite containing 70% W particles in the LM106 metallic glass matrix. In addition to probing the effects of strain rate, different stress states were also investigated over the range of strain rates by utilizing a cylindrical specimen for uniaxial loading and a 6° inclined cylindrical specimen for biaxial loading. Additionally, the temperature dependence of the composite material was investigated for both stress states.

4.3 Approach

Investigation of the compression and compression-shear (6° inclined samples) response of LM106-70W over a range of strain rates (~10^{-3} s^{-1} to 10^{3} s^{-1}) and temperatures (RT to 600 °C) was done using an Instron Universal testing machine, a Drop Weight testing machine, and a Split Hopkinson Pressure Bar at the Technical University of Chemnitz in Germany. The details of the experiments and analysis for each of these tests are discussed in Sections 3.3.2, 3.3.3, and 3.3.4, respectively. Investigations of the temperature dependence of the mechanical response was done using the Drop Weight tower with an inductive heating device at temperatures of RT, 200, 380, 450, 550, and 600 °C, as described in Section 3.3.3.1. This temperature range exceeds the glass transition (~400 °C) and crystallization temperatures (~480 °C) of the BMG (Sections 2.5.1 and 3.2.3.1 give thermal analysis results for the monolithic glass and composite, respectively) and allows for determination of changes in mechanical properties and deformation mechanisms due to these transitions.

4.4 Results and Discussion

4.4.1 Stress-Strain Response as a Function of Strain Rate

Compression tests were performed on both uniaxial and biaxial (6° off-axis) specimen configurations at nominal strain rates of (a) 10^{-3}, (b) $5x10^{-2}$, (c) 1, (d) 200, and (e) 10^{3} s^{-1}. The true stress-strain response of both uniaxial and biaxial specimens is shown in Figure 4.1 for each strain rate investigated. This figure shows that the uniaxial and biaxial flow stresses are generally the same. Uniaxial and biaxial specimens typically show similar flow stresses until the point when more force becomes concentrated on the shear plane, which is exaggerated in the biaxial specimens, and as a result the flow stress of the biaxial geometry is less than that of the uniaxial geometry. At low rates, uniaxial failure occurs at a lower stress and strain than biaxial failure, whereas at intermediate to high rates, uniaxial and biaxial failures occur at similar stress levels, but the biaxial specimens fail after less plasticity. Also, failure was not observed in the data collected from the 1 s^{-1} (true strain

rate of 0.79 s^{-1}) data (Figure 4.1 (c)). This is believed to be due to either to being at the upper limit of the Instron load cell's sensitivity or the fact that the failure occurred in small vertical cracks around the periphery of the specimen, which possibly did not affect the top and bottom specimen surfaces and specimen height, at least enough to be detected at that rate.

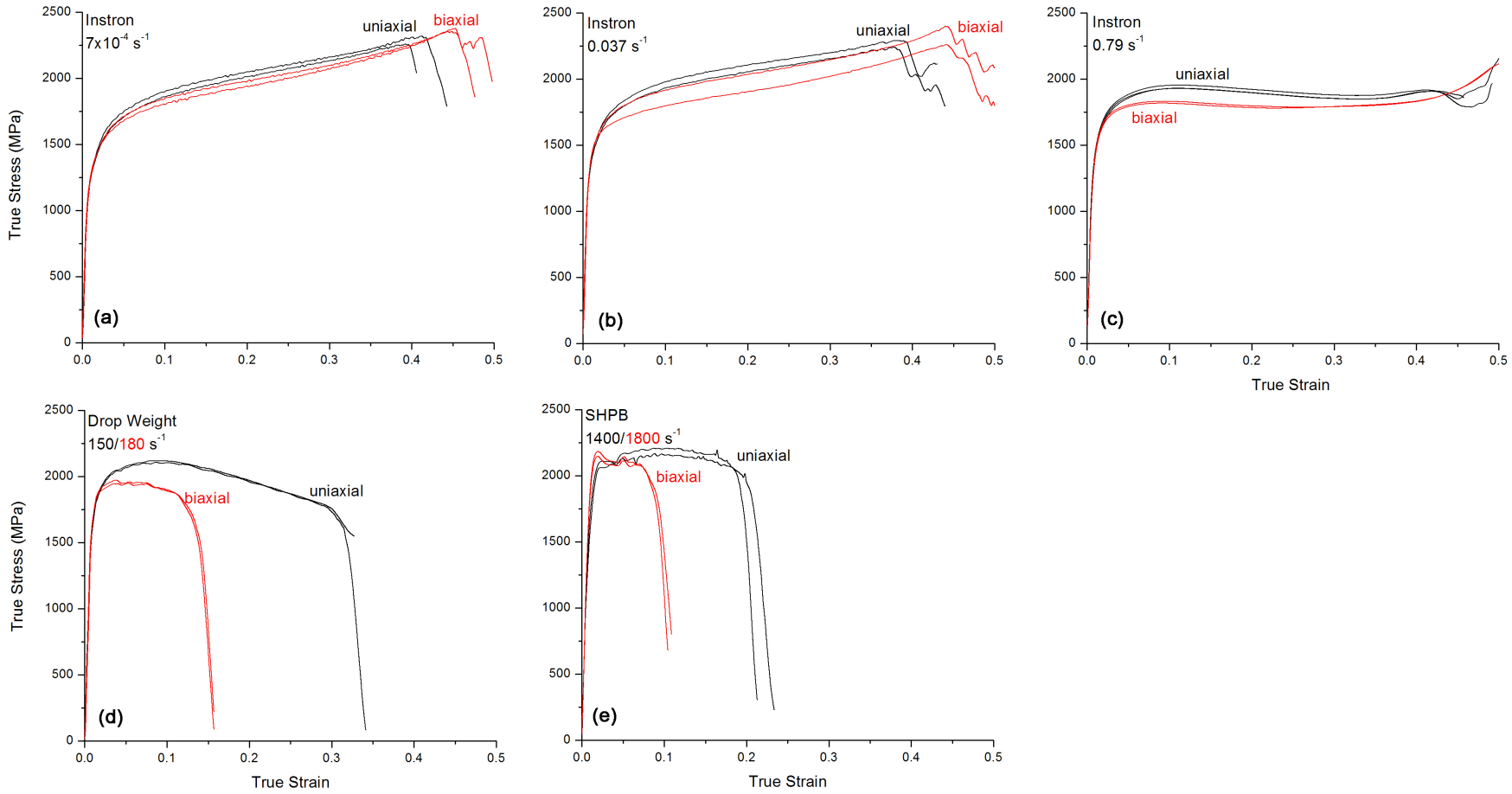

Figure 4.1: True stress-strain response of uniaxial and biaxial LM106-70W over a range of strain rates. (a) $7x10^{-4}$ s^{-1}, (b) 0.037 s^{-1}, (c) 0.79 s^{-1}, (d) 150 s^{-1} (uniaxial), 180 s^{-1} (biaxial), (e) 1400 s^{-1} (uniaxial), 1800 s^{-1} (biaxial). Data shows similar flow stresses for uniaxial and biaxial specimen configurations, but a lower strain-to-failure in the biaxial case.

Comparison of the true stress-strain response of (a) all uniaxial and (b) all biaxial specimens over the range of strain rates is shown in Figure 4.2. These plots reveal that with increasing strain rate there is an increase in yield stress, a decrease in failure stress (except from drop weight to SHPB), a decrease in plasticity, and a decrease in strain hardening, with the data at intermediate and high rates showing some softening behavior. Figure 4.3 shows the strain rate sensitivity of LM106-70W over the range of $\sim 10^{-3}$ to 10^{3} s^{-1}. The plot shows log σ as a function of log $\dot{\varepsilon}$ and the stresses plotted are measured at 5% strain in each case. The uniaxial specimens show a consistently higher stress than the biaxial specimens at each strain rate. Both the uniaxial and biaxial specimens show a slope of 0.015. For materials exhibiting a power law relationship, $\sigma_f \propto \left(\frac{d\varepsilon}{dt}\right)^m$, where σ_f is flow stress, $\frac{d\varepsilon}{dt}$ is the strain rate, the slope defines the strain-rate sensitivity exponent, m. This is comparable to the value m=0.016 determined by Jiao et al. [2] for a composite of LM106 and 60% W. We would expect the 70% tungsten composite to show a higher rate sensitivity due to the larger content of BCC tungsten, but the difference is believed to be within experimental error. Several investigators have observed negative strain-rate sensitivity of the monolithic BMG [8, 9, 53], but no strain-rate sensitivity values have been reported. If the rule of mixtures is used in reverse to solve for the strain-rate sensitivity of the BMG phase, this yields a strain-rate sensitivity, m, of -0.008 to -0.009 for the LM106 BMG.

Figure 4.4 shows the dependence of 0.2% flow stress and strain, and failure stress and strain, on strain rate. At 7.2x10^{-4} s^{-1} (quasi-static), the 0.2% yield stress was measured to be 1082 ± 21 MPa , which agrees well with a Rule of Mixtures value of 1065 MPa (0.7∗750 MPa + 0.3∗1800 MPa [3]). The stress and strain at yield both increase with strain rate, with the biaxial specimens showing more strain-rate sensitivity. Failure stress and strain both decrease with increasing strain rate (except from drop weight (0.79 s^{-1}) to SHPB (1400/1800 s^{-1}), where an increase in failure stress is seen). The uniaxial and biaxial specimens show similar strain-rate sensitivity with respect to failure stress, but biaxial specimens show a more rapid decrease in failure strain with increasing strain rate than uniaxial specimens

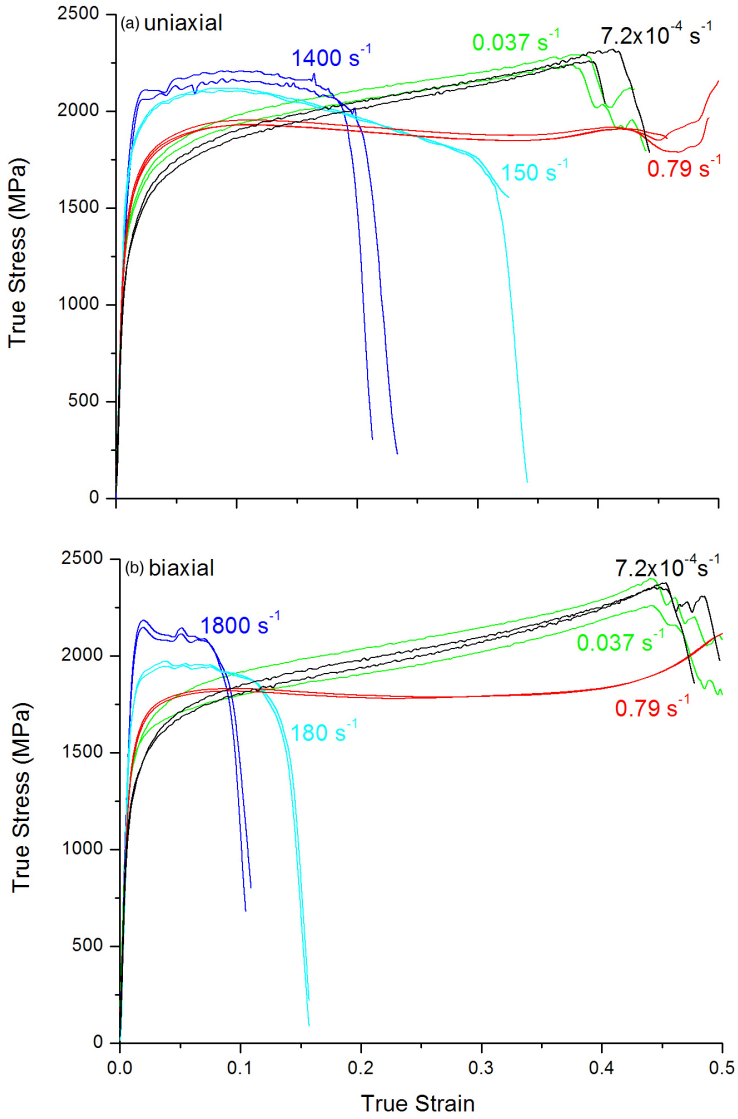

Figure 4.2: True stress-strain response of (a) uniaxial and (b) biaxial LM106-70W over a range of strain rates. This is the same data as in Figure 4.1 plotted such that variation in either uniaxial or biaxial behavior be compared over a range of strain rates. These plots reveal that with increasing strain rate there is an increase in yield stress, a decrease in failure stress (except from drop weight to SHPB), a decrease in plasticity, and a decrease in strain hardening, with the data at intermediate and high rates showing some softening behavior.

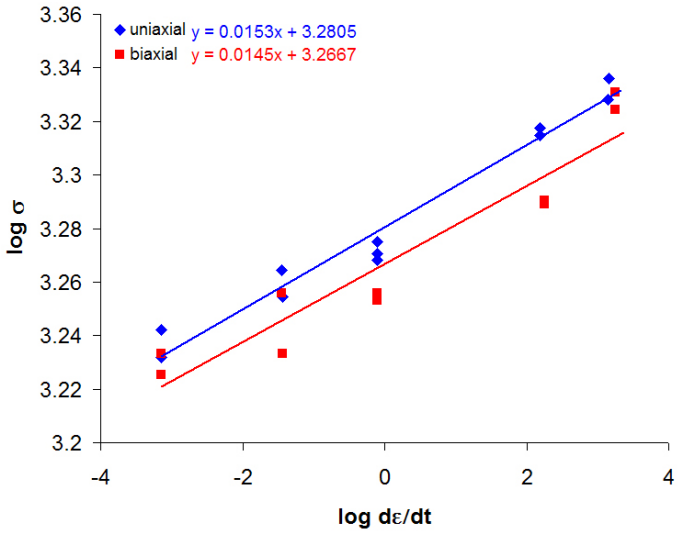

Figure 4.3: Strain rate sensitivity of LM106-70W. Plot shows log σ as a function of log $\dot{\varepsilon}$ and the stresses plotted are measured at 5% strain in each case. Both the uniaxial biaxial specimens show a strain rate sensitivity of 0.015, but the uniaxial specimens show a consistently higher stress than the biaxial specimens at each strain rate.

do. Figure 4.5 shows the 0.2% yield stress and failure stress plotted together as a function of strain rate. Yield stress increases with strain rate and failure stress decreases with strain rate, so the two are approaching one another. At a strain rate of 10^3 s^{-1} the two stress values are nearly the same, particularly in the case of the biaxial specimens, which show a more rapid increase in yield stress than do the uniaxial specimens.

The hardening behavior of LM106-70W as a function of strain rate is shown in Figures 4.6 and 4.7. Figure 4.6(a) shows the natural log of true stress as a function of natural log of true strain for determination of the hardening exponent, n, in the power law $\sigma \propto \varepsilon^n$. The dependence of n on strain rate is shown in Figure 4.6(b). For each rate, n was measured from ln ε values of -4 to -2, which corresponds to strains of 1.8 to 13.5%. The trend shows a decrease in hardening with increasing strain rate. It can be seen that the ln σ-ln ε relationship is not perfectly linear and that the power law fit is not perfect, although it illustrates the trend of decreasing hardening with increasing rate well. To further investigate the hardening behavior, the stress at specified strain increments of 5, 10, 15, 20, and 25% (when applicable) were measured for each rate and plotted as a function of true strain rate,

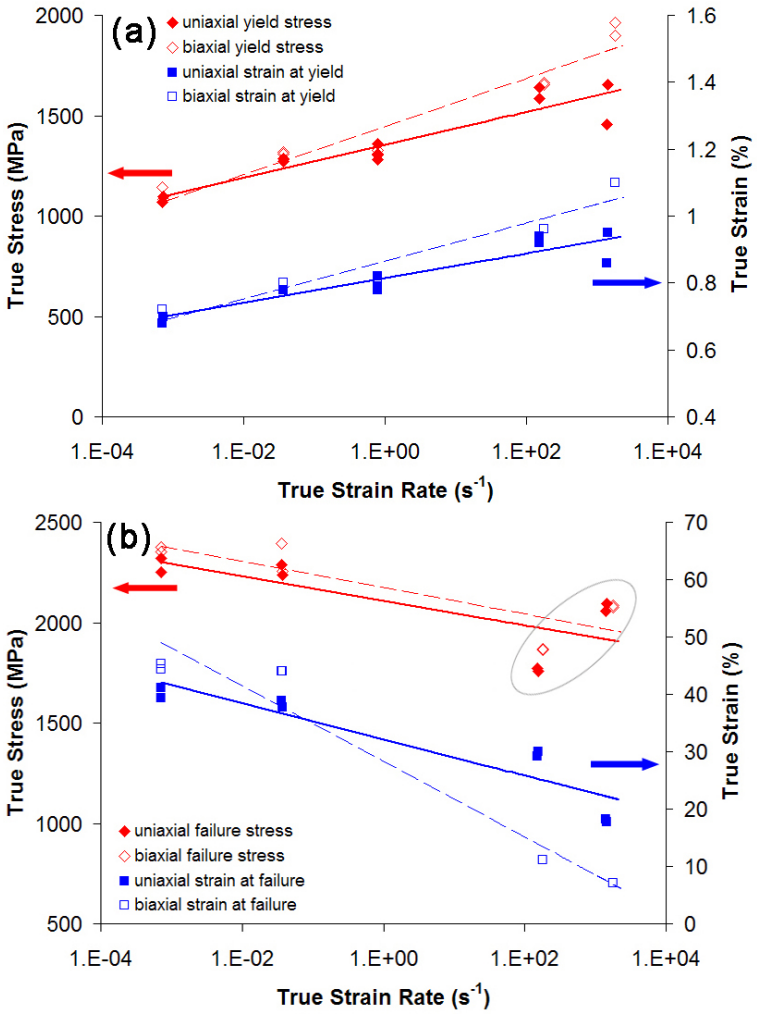

Figure 4.4: (a) Plot of 0.2% flow stress and strain as a function of strain rate. The stress and strain at yield both increase with strain rate, with the biaxial specimens showing a higher degree of strain-rate sensitivity. (b) Plot of failure stress and strain as a function of strain rate. Failure stress and strain both decrease with increasing strain rate (except from drop weight (0.79 s^{-1}) to SHPB (1400/1800 s^{-1}), where an increase in failure stress is seen-indicated with gray circle). The uniaxial and biaxial specimens show similar strain-rate sensitivity with respect to failure stress, but biaxial specimens show a more rapid decrease in failure strain with increasing strain rate than uniaxial specimens do.

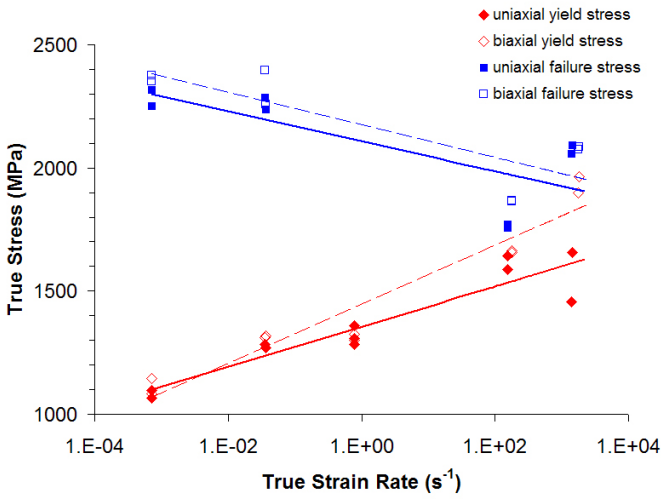

Figure 4.5: Plot of yield stress and failure stress as a function of strain rate. Yield stress increases with strain rate and failure stress decreases with strain rate, so the two are approaching one another. By $10^3 s^{-1}$ the two stress values are nearly the same, particularly in the case of the biaxial specimens, which show a more rapid increase in yield stress than the uniaxial specimens.

as shown in Figure 4.7(a). The corresponding incremental $d\sigma/d\varepsilon$ values are plotted as a function of true strain rate in Figure 4.7(b). These figures illustrate that hardening occurs from 5-10% ε at all $\dot{\varepsilon}$, but the slope ($d\sigma/d\varepsilon$), or degree of hardening, decreases as strain rate increases. This indicates that the ability of LM106-70W (specifically the tungsten particles) to accommodate dislocations decreases as strain rate increases. The 10^{-3} and $5x10^{-2}$ s^{-1} experiments show hardening at all strains, and experiments at rates of ≥ 1 s^{-1} show softening after 10% strain. The decrease in hardening with increasing strain rate can be explained by the increased temperature generation at higher rates of deformation, which causes increased softening behavior.

Figure 4.8 shows examples of high-speed images captured during Split Hopkinson Pressure Bar impact of (a) a uniaxial specimen and (b) compression-shear biaxial specimen. The three frames shown in each case illustrate the stages immediately before catastrophic failure, during failure, and after failure, at which time light-emitting sparks can be seen. Even at this high rate of compression, the uniaxial specimen is failing along its maximum

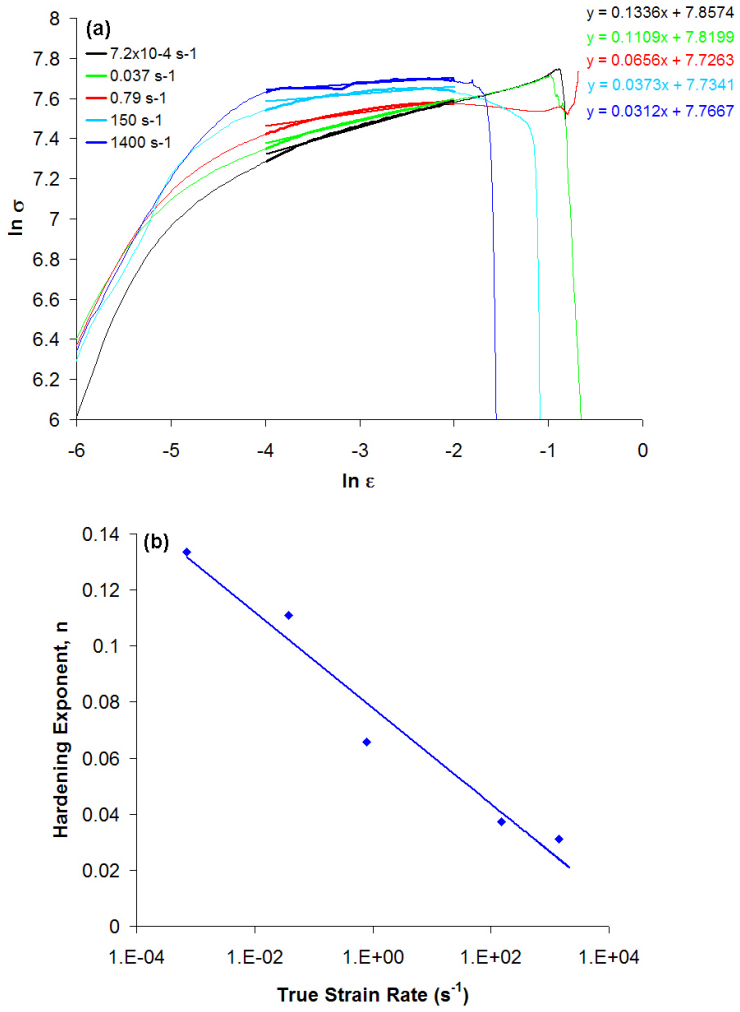

Figure 4.6: (a) Natural log of true stress as a function of natural log of true strain. (b) Hardening exponent, *n*, as a function of true strain rate. In all cases, *n* was measured from ln ε of -4 to -2, which corresponds to strains of 1.8 to 13.5%. The trend shows a decrease in hardening with increasing strain rate. The decrease in hardening with increasing strain rate can be explained by the increased temperature generation at higher rates of deformation, which causes increased softening behavior.

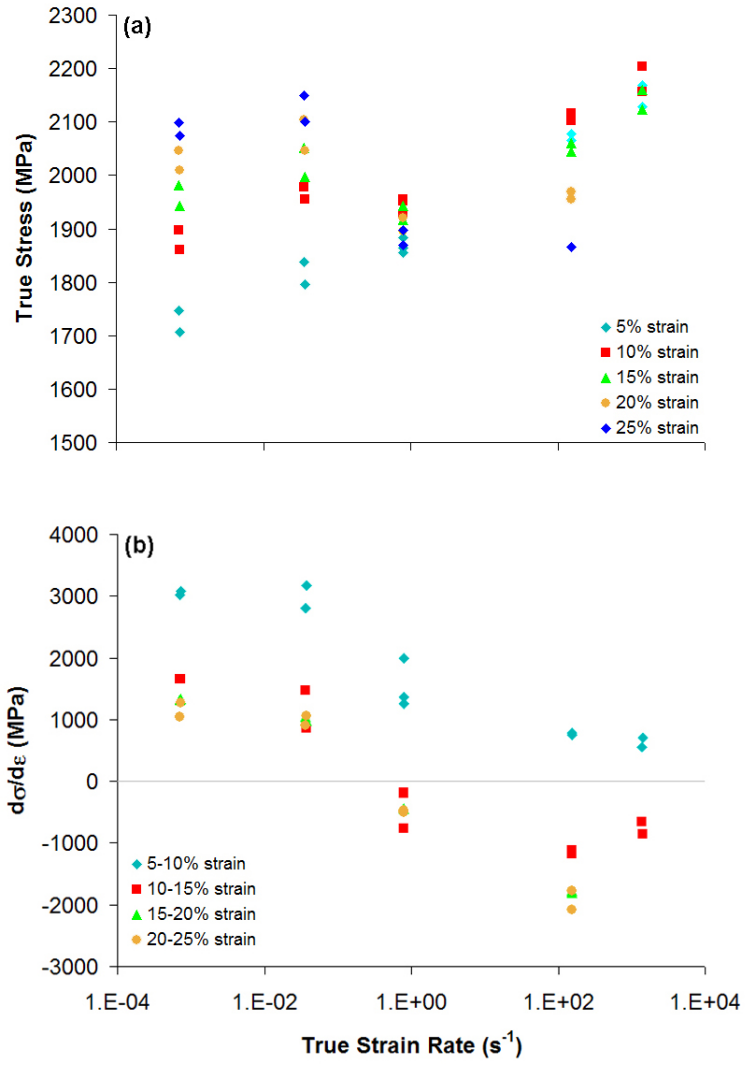

Figure 4.7: (a) True stress at specified strain values of 5, 10, 15, 20, and 25% (when applicable) and (b) $d\sigma/d\varepsilon$ at strain increments of 5-10, 10-15, 15-20, and 20-25% strain showing the evolution of hardening with strain. These figures illustrate that hardening occurs from 5-10% ε at all $\dot{\varepsilon}$, but the slope ($d\sigma/d\varepsilon$), or degree of hardening, decreases as strain rate increases. This indicates that the ability of LM106-70W (specifically the tungsten particles) to accommodate dislocations decreases as strain rate increases. The 10^{-3} and $5x10^{-2}$ s^{-1} experiments show hardening at all strains, and experiments at rates of ≥ 1 s^{-1} show softening after 10% strain.

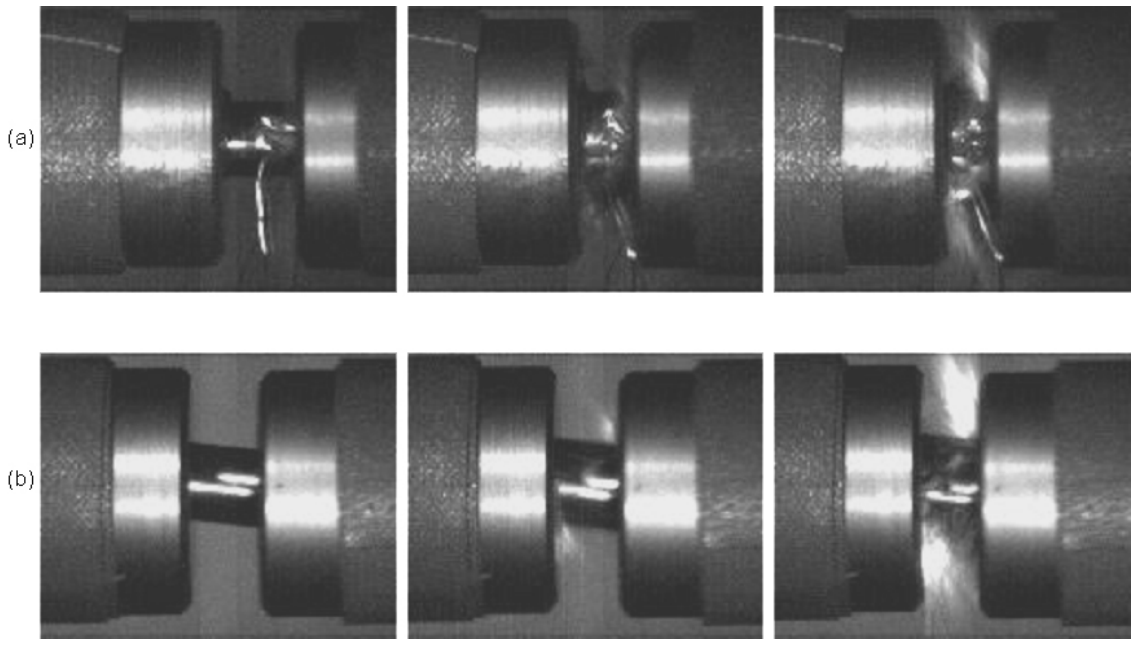

Figure 4.8: High-speed images captured during Split Hopkinson Pressure Bar impact testing of (a) uniaxial specimen and (b) biaxial specimen. Interframe time is 330 μs. The three frames shown in each case illustrate the stages immediately before catastrophic failure, during failure, and after failure, at which time light-emitting sparks can be seen. Even at this high rate of compression, the uniaxial specimen is failing along its maximum shear stress planes at ~45° from the loading axis, forming a conical region at either end, and the biaxial specimen is failing along its maximum shear stress plane connecting the two 96° corners of the specimen.

shear stress planes at ~45° from the loading axis, forming a conical region at either end, and the biaxial specimen is failing along its maximum shear stress plane connecting the two 96° corners of the specimen.

4.4.2 Microstructural Analysis

Uniaxial specimens tested at strain rates from 10^{-3} to 1 s^{-1} showed vertical cracking around the outside of the specimen and failure in the form of a forging cross, or 45° shear planes that originated at the outer edges of the top and bottom of each specimen and intersected in the center of the specimen's height, as shown in Figure 4.9(a). Examination of the cross sections of these specimens showed extensive shearing, as can be seen in the last image in Figure 4.9(a). Biaxial specimens tested in this same strain rate regime showed

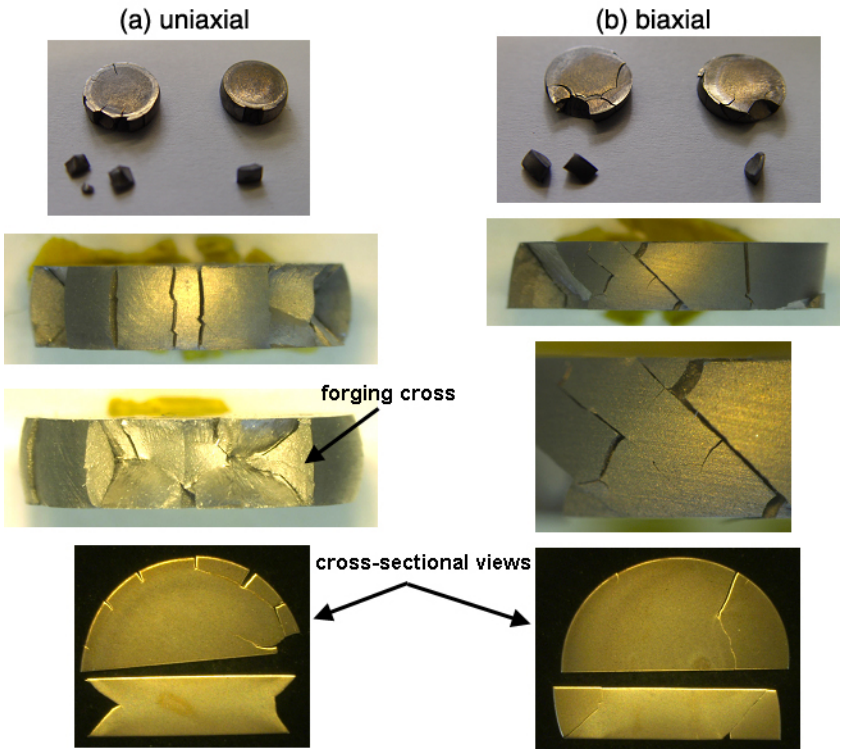

Figure 4.9: (a) Uniaxial and (b) biaxial specimens recovered after compressive testing on the Instron at ~1 s^{-1}. Uniaxial specimens show forging cross features from 45° shear fracture and vertical cracks around the periphery of the specimen resulting from tensile stress. Biaxial specimens show parallel shear cracks originating from the 96° corners of the specimens.

parallel, diagonally-oriented shear cracks around the specimen peripheries, as illustrated in the photograph in Figure 4.9(b). There are also notable differences in the cross-sections of the biaxial specimens (last image in Figure 4.9(b)). The biaxial cross-sections show qualitatively less damage and all visible damage is localized into the maximum shear stress region.

In order to learn about the deformation and failure mechanisms, stopped experiments were performed on both uniaxial and biaxial specimens using the Drop Weight and Split Hopkinson Pressure Bar techniques, as described in Sections 3.3.3 and 3.3.4, respectively. After the experiments, which were stopped at varying strain levels, specimens were sectioned and polished and examined using microscopy. The results from the stopped experiments performed using the Drop Weight Tower are shown in Figure 4.11 and the results

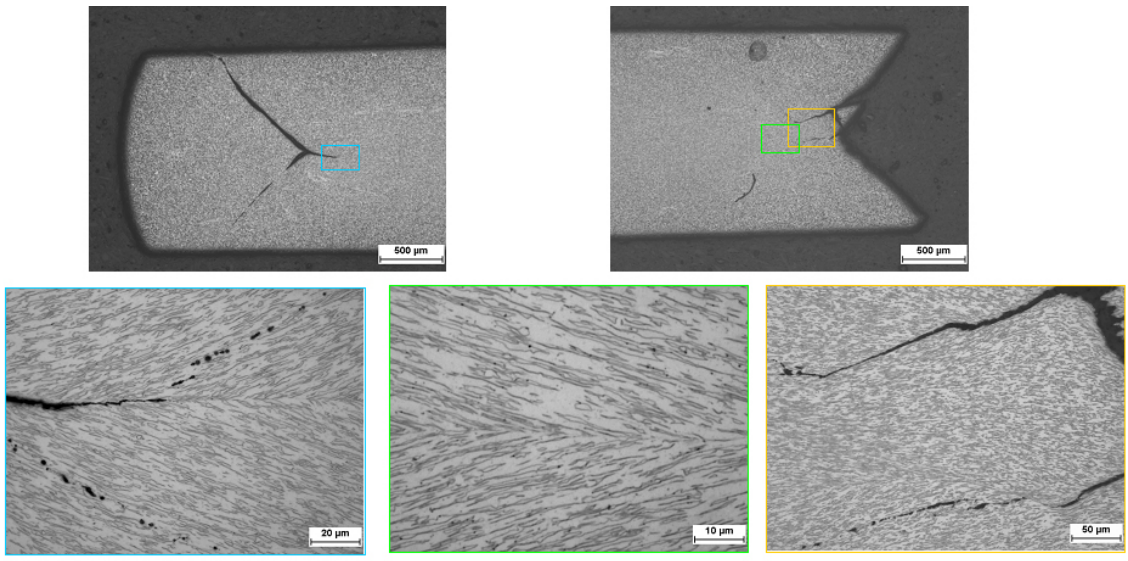

Figure 4.10: Examination of the microstructure of the cross-section of a specimen tested at ~1 s^{-1} under uniaxial compression. The macroscopic cross-sectional views show that the shear has been localized into symmetric regions at ~45° from the loading axis and the higher magnification micrographs show extensive shear deformation of the tungsten particles.

from the stopped experiments performed using the SHPB technique are shown in Figure 4.12. Specimens stopped at strains near the onset of failure showed shear bands in the expected locations (based on specimen geometry). The uniaxial specimens each showed two 45° bands connecting opposite corners and the biaxial specimens showed a single band connecting the 96° corners of the specimens. In general, the shear bands were found to be more pronounced at higher strain rates, and the shear bands in the biaxial specimens were more pronounced than those in the uniaxial specimens. Higher magnification views show a shear band width on the order of 100 μm develops at a (nominal) strain rate of 200 s^{-1} and ~10-20 μm at a strain rate of ~1400-1800 s^{-1}, regardless of specimen geometry. At 200 s^{-1}, failure in uniaxial specimens begins with a tensile crack in the top center of the specimen, and the crack propagates through mostly the BMG matrix and around the W particles, as illustrated in Figure 4.11. After the onset of failure, the shear bands evolve into cracks and the tensile crack in the center of the specimen continues to grow. It appears that

the simultaneous shear cracking from the corners and tensile cracking through the center (lengthwise) cause failure in the uniaxial specimens, whereas the shear deformation alone is responsible for failure in the biaxial specimens.

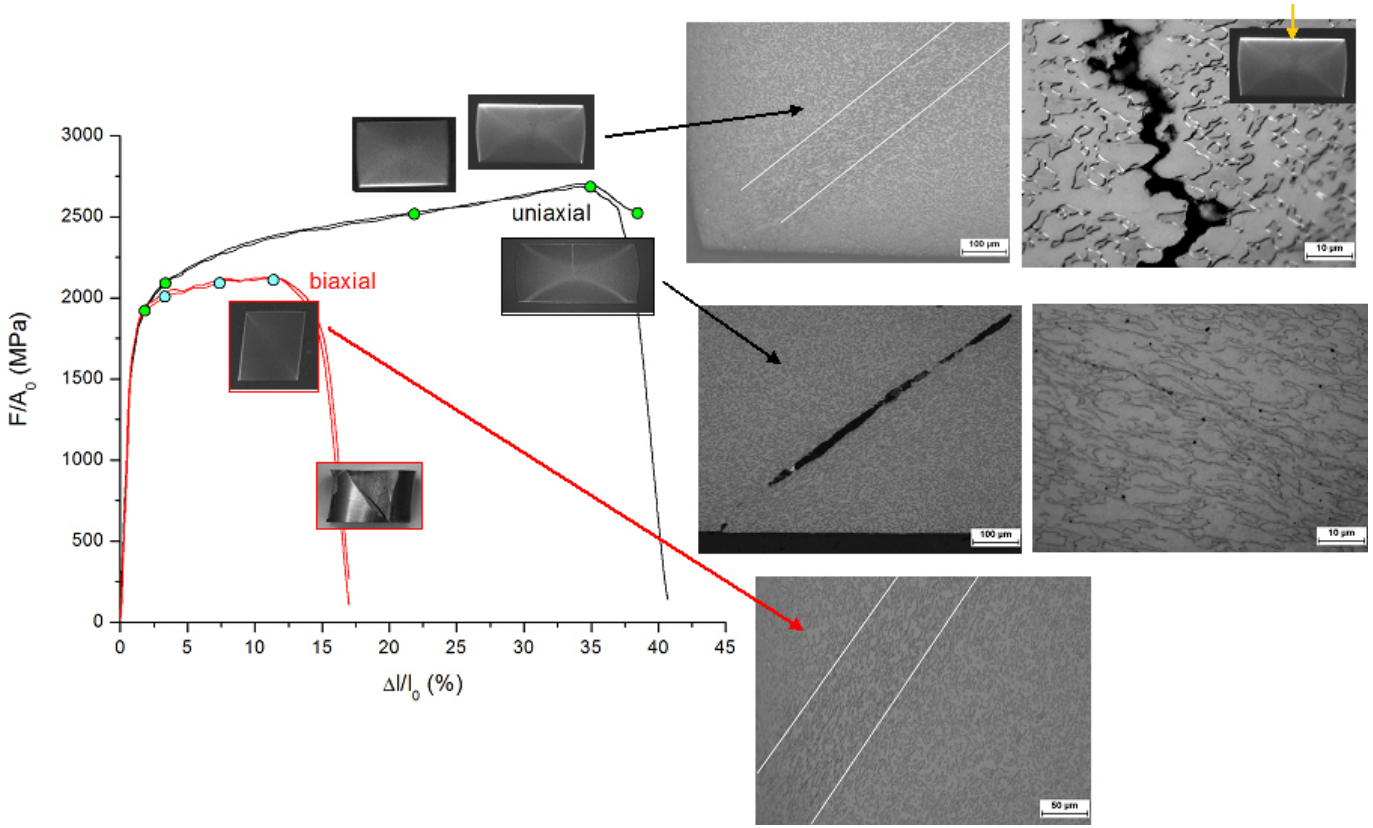

Figure 4.11: Stress-strain curves obtained from Drop Weight testing. Circles along the curves show strain levels at which the tests were stopped and the specimen was examined for microstructural evidence of the deformation and failure processes. Micrographs of stopped specimen sections which revealed shear bands are shown as well as photographs of failed specimens. The top two micrographs reveal a shear band in the uniaxial specimen just before failure and the beginning of a crack in the center of the specimen. The two micrographs in the middle show shear bands that have evolved into cracks after the onset of failure. The last micrograph shows a shear band in a biaxial specimen just before failure. The white lines indicate the approximate boundaries of the shear bands. The width of shear bands developed during Drop Weight testing were on the order of ~50-100 μm.

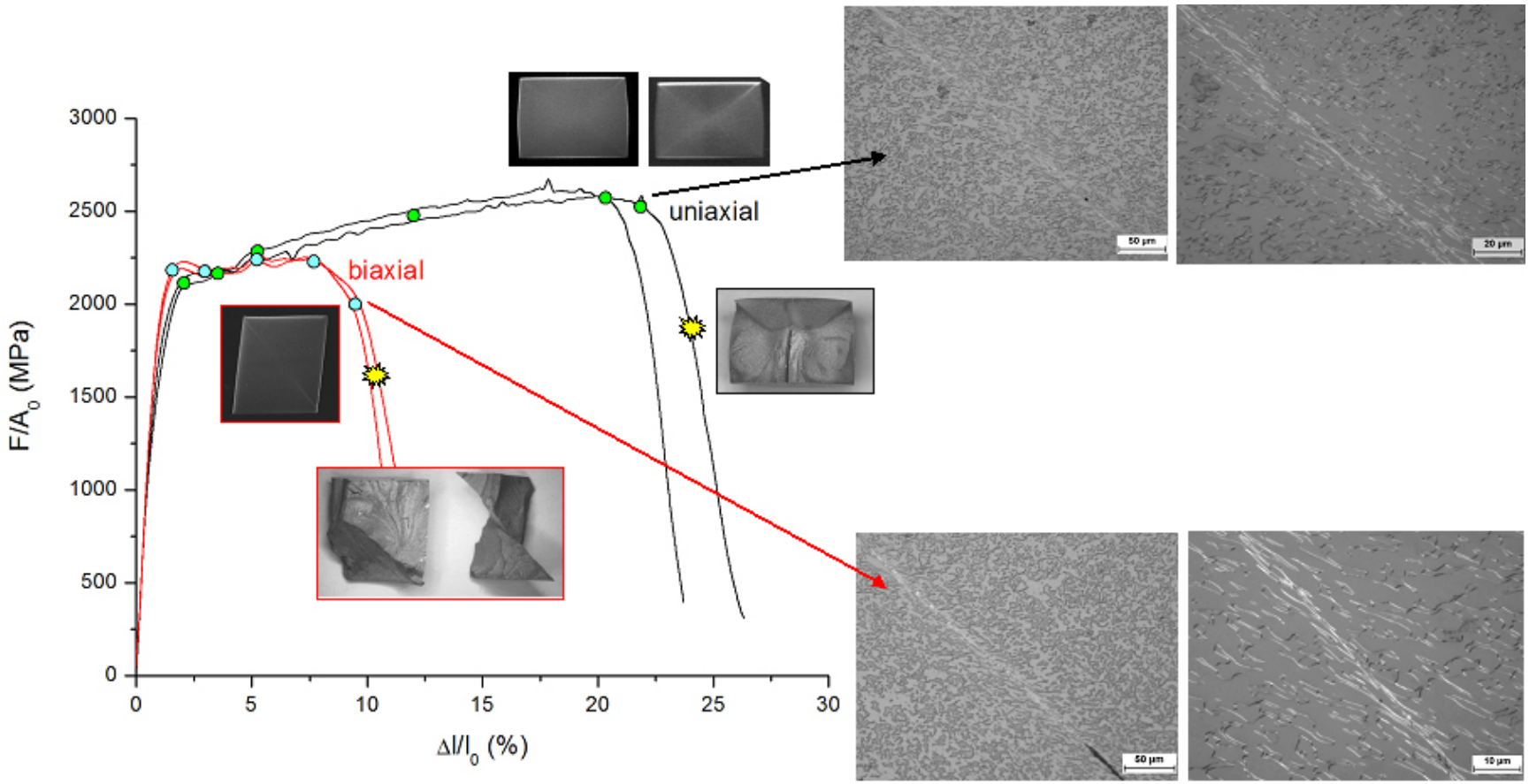

Figure 4.12: Stress-strain curves obtained from Split Hopkinson Pressure Bar testing. Circles along the curves show strain levels at which the tests were stopped and the specimen was examined for microstructural evidence of the deformation and failure processes. Micrographs of stopped specimen sections which revealed shear bands are shown as well as photographs of failed specimens (indicated with yellow symbols on curves). The width of shear bands developed during Drop Weight testing were on the order of ~10-20 μm.

SEM micrographs of the shear planes and tensile fracture surfaces of specimens tested with drop weight and SHPB techniques are shown in Figures 4.13-4.15. Figure 4.13 shows the shear planes of both a compression and a compression-shear specimen. These two shear planes look fairly similar, although the uniaxially loaded specimen exhibits a slightly smoother surface since they failed at a higher strain. The uniaxially loaded specimen also developed a tensile failure plane oriented parallel to loading, whereas the biaxially-loaded specimen failed only along its maximum shear stress plane, which connected the two 96° corners of the specimen. The tensile fracture surface of the uniaxial specimen shows quite different features from those of the shear plane. The deformation and elongation of the tungsten particles is quite evident, as is the flow of the BMG around the tungsten. There are a few fractured tungsten particles, but in general the fracture has occurred in the BMG matrix.

The shear and fracture surfaces of a uniaxially-loaded SHPB specimen are shown in Figure 4.14. The macroscopic image of the specimen shows the areas where each of the micrographs was taken. This specimen shows conical shear failure, as would be expected for this specimen geometry. The surfaces of the cone are quite smooth, as can be seen in the micrograph on the upper left. The micrograph on the lower left shows a higher magnification image of the conical shear surface and there are no apparent W particles, just a continuously smooth surface that appears as if a liquid layer has formed and covered it. Zhang et al. [37] quantified temperature rise near shear bands (as discussed in Section 2.2) and found increases in temperature in excess of 1100 K in a Zr-based system, so the possibility of some melting of LM106, which has a T_m of approximately 815 °C, is likely, especially considering there is additional energy available from the fracture process that will also cause a temperature rise.

The tensile failure surface is shown in the two micrographs on the right of Figure 4.14. These surfaces are more rough, with ridges apparent at low magnification, and distinct particles at higher magnification. This fracture surface shows more fractures through tungsten

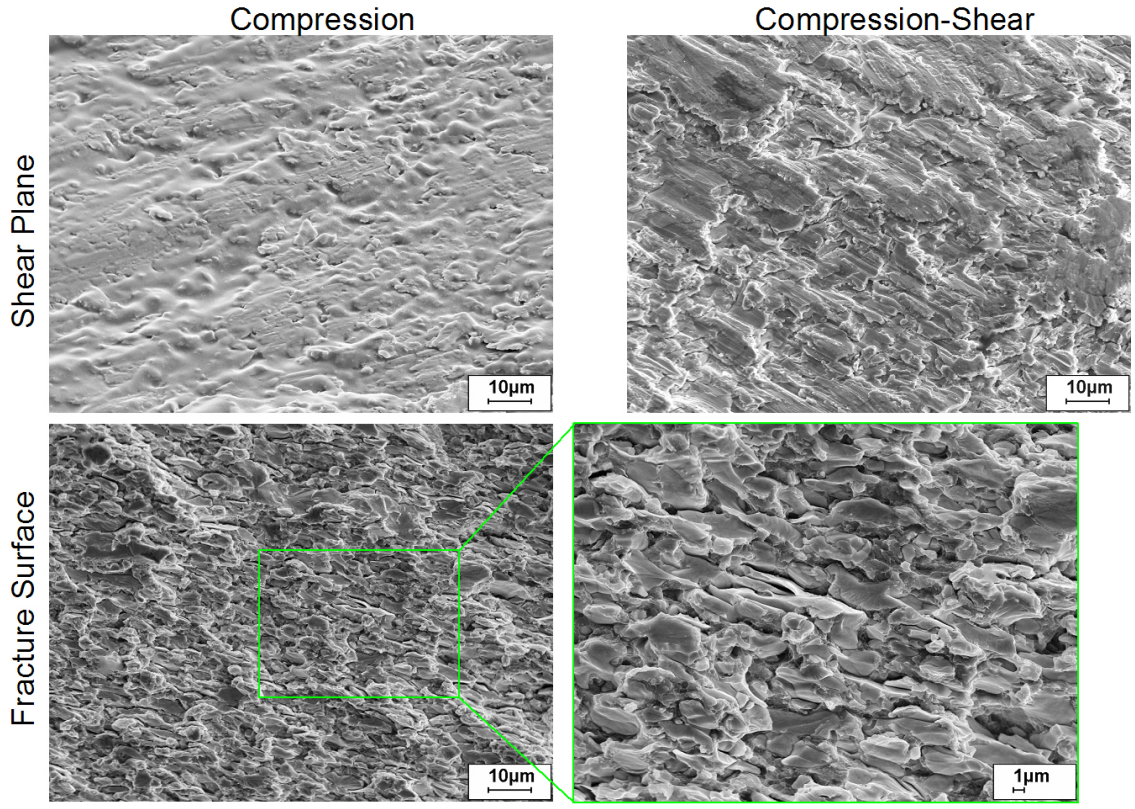

Figure 4.13: SEM micrographs of the shear planes of uniaxally and biaxially-loaded drop weight tested specimens, and the secondary (tensile) fracture surface of a uniaxially-loaded drop weight tested specimen. Uniaxially loaded specimens exhibited a slightly smoother surface due to failure at a higher strain, and they developed a tensile failure plane oriented parallel to loading, whereas the biaxially-loaded specimen failed only along its maximum shear stress plane, which connected the two 96° corners of the specimen. The tensile fracture surface of the uniaxial specimen shows quite different features from those of the shear plane. The deformation and elongation of the tungsten particles is quite evident, as is the flow of the BMG around the tungsten. There are a few fractured tungsten particles, but in general the fracture has occurred in the BMG matrix.

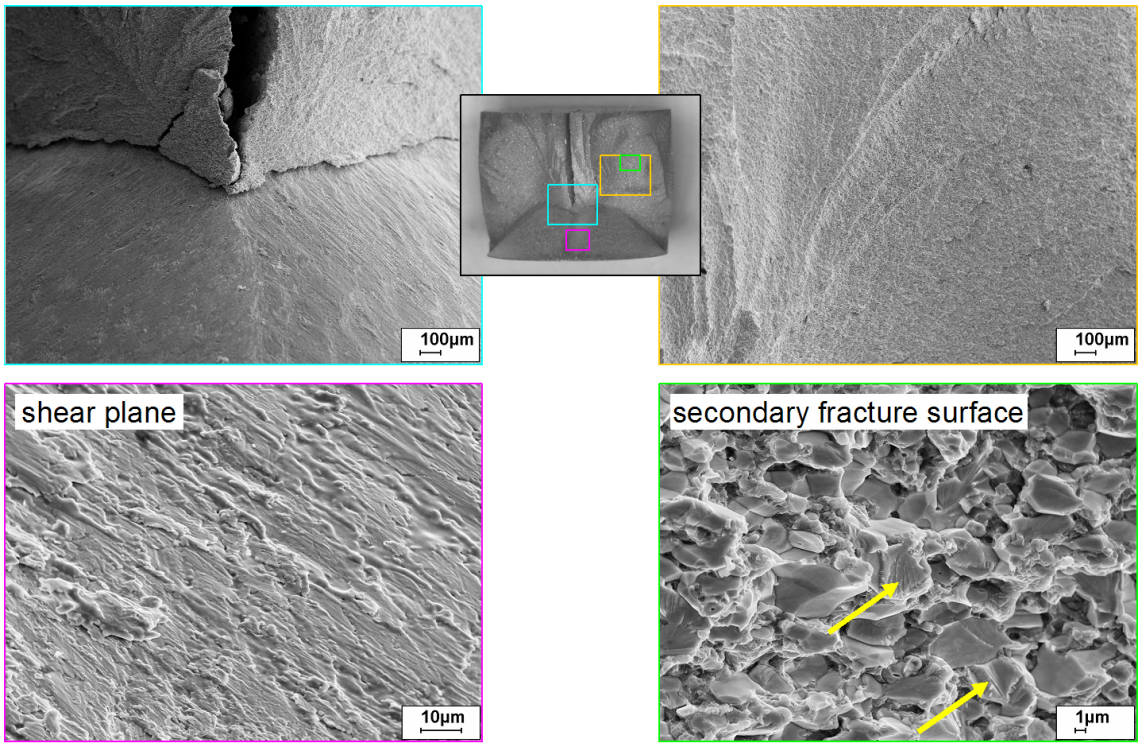

Figure 4.14: SEM micrographs of the conical shear surface and secondary (tensile) fracture surface of a uniaxially-loaded SHPB specimen. The surfaces of the cone are quite smooth, as can be seen in the micrograph on the upper left. The micrograph on the lower left shows a higher magnification image of the conical shear surface and there are no apparent W particles, just a continuously smooth surface that appears as if a liquid layer has formed and covered it. The tensile failure surface shown in the two micrographs on the right are more rough, with ridges apparent at low magnification, and distinct particles at higher magnification. This fracture surface shows more fractures through tungsten particles (examples indicated with yellow arrows) than were seen on the fracture surface of the drop weight specimen, which is logical due to the higher rate.

particles (examples indicated with yellow arrows) than were seen on the fracture surface of the drop weight specimen, which is logical due to the higher rate. Also noticeable is that the tungsten particles appear to be less deformed and elongated than they were in the drop weight specimens. Again, this is logical since the drop weight specimens failed at ~35% strain whereas the SHPB specimens failed at ~20-25% strain.

Shear and fracture surfaces of a biaxially-loaded SHPB specimen are shown in Figure 4.15. The macroscopic image of the specimen clearly shows the diagonal failure along the maximum shear stress plane, as well as tensile failure. The biaxial shear plane is less smooth than that of the uniaxial specimen, consistent with what was seen on the surfaces of the drop weight specimens. This is likely because the uniaxial specimens are strained more than the biaxial specimens, so there is more deformation/strain along the shear plane, thus giving it a more smooth appearance (Figure 4.15). The tensile fracture surface shows little deformation or elongation in the tungsten particles, although there are some that have fractured, as can clearly be seen in the high magnification image. The biaxial SHPB specimens failed at ~10% strain, so it is not unexpected for the tungsten particles to appear undeformed. The fracture appears to have taken place predominantly through the BMG matrix, which shows evidence of dimple-like structure, indicative of flow and ductility.

4.4.3 Temperature Dependence of Compressive Response

The temperature dependance of of the uniaxial and biaxial compressive behavior of LM106-70W was investigated at a nominal strain rate of 200 s^{-1} using the drop weight tower setup (described in Section 3.3.3) with inductive heating and specimen temperature measurement, as described in Section 3.3.3.1. Tests were performed on both uniaxial and biaxial specimens at room temperature as well as at temperatures of 200, 380, 450, 550 and 600 °C. The stress-strain curves generated from the high temperature tests are shown in Figure 4.16. The specimens tested at room temperature showed softening behavior, whereas the specimens tested at higher temperatures showed almost no softening, which is contrary to

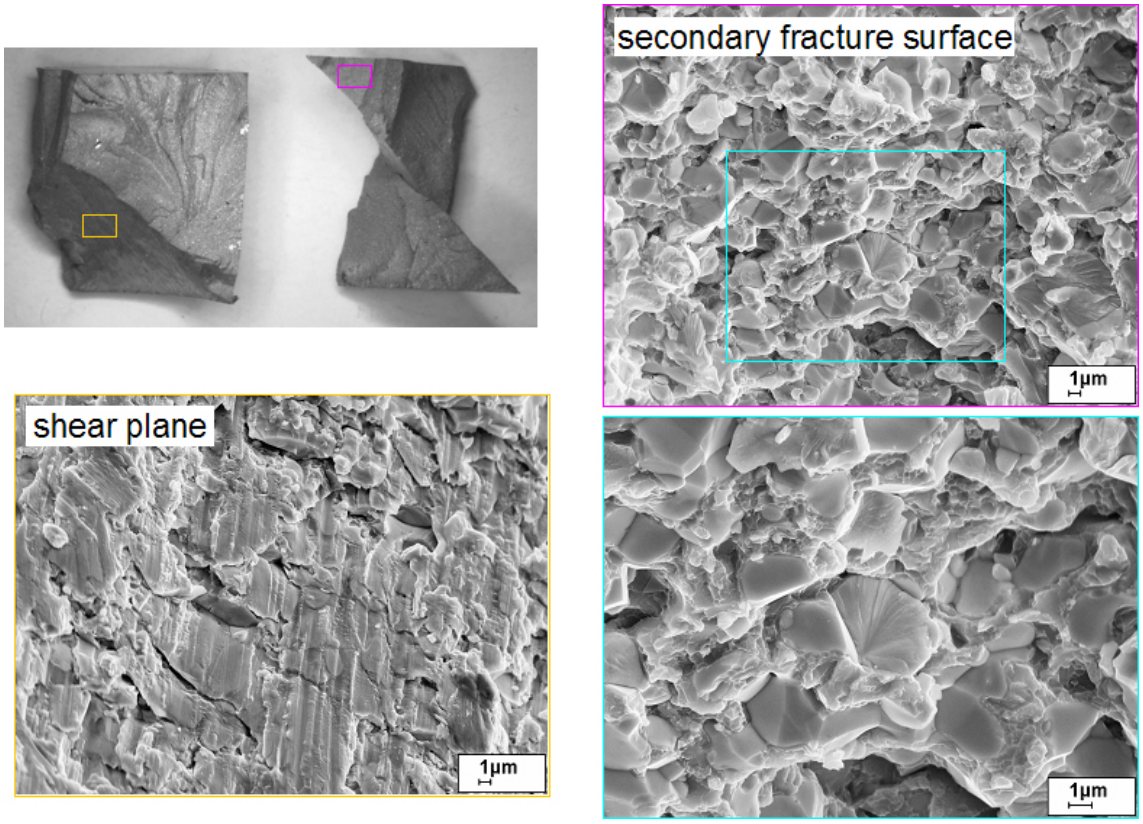

Figure 4.15: SEM micrographs of the diagonally-oriented shear surface and secondary (tensile) fracture surface of a biaxially-loaded SHPB specimen. The biaxial shear plane is less smooth than that of the uniaxial specimen because the uniaxial specimens are strained more than the biaxial specimens, so there is more deformation/strain along the shear plane, thus giving it a more smooth appearance. The tensile fracture surface shows little deformation or elongation in the tungsten particles, although there are some that have fractured, as can clearly be seen in the high magnification image. The biaxial SHPB specimens failed at $\sim$10% strain, so it is not unexpected for the tungsten particles to appear undeformed. The fracture appears to have taken place predominantly through the BMG matrix, which shows evidence of dimple-like structure, indicative of flow and ductility.

what would be expected. The uniaxial specimen tested at 450 °C shows unique behavior in comparison to the responses observed at other test temperatures. 450 °C is between in the glass transition temperature and crystallization temperature of LM106 BMG (see thermal analysis data in Appendices 3.2.3.1 and 2.5.1), and between these two transitions is the only temperature range where the BMG will deform homogeneously, and not by localized shear banding (when tested at high strain rates). Although the BMG is still in its amorphous state, it has gone through its "brittle to ductile" transition, and is behaving in more of a ductile ("rubbery") manner, as evidenced by the different trend evident in its stress-strain response (Figure 4.16 (a)). As the test temperature was increased further (550 °C), the crystallization temperature was surpassed and the BMG transformed to a crystalline phase (although probably not fully due to the fast heating rate). At this test temperature, the composite again showed behavior analogous to that at lower test temperatures. Because the behavior at all temperatures (except 450 °C) is similar in response, although not in magnitude, it appears as if the tungsten may be dominating the mechanical response of the composite, except in the temperature range (between T_g and T_x) where the BMG exhibits more ductile or "rubbery" behavior, in which case the deformation of the BMG dominates the material response. The compression-shear specimens recovered after high temperature testing are shown in Figure 4.17. All specimens show shear failure in the form of a crack connecting the 96° corners of the specimen. A vertically-oriented tensile crack also formed at all test temperatures.

Figure 4.18 shows comparisons of uniaxial and biaxial stress-strain response for each test temperature. This presentation of the plots reveals the similarity in flow stress between the uniaxial and biaxial cases at most temperatures. At room temperature, however, the flow stress of the biaxial specimens is somewhat lower than that of the uniaxial specimens. This can be attributed to the development of shear bands in the BMG at stresses below yield [8], which is more prevalent in the 6° specimen due to its stress state and susceptibility to shear. At higher temperatures there was no significant difference between the flow stresses

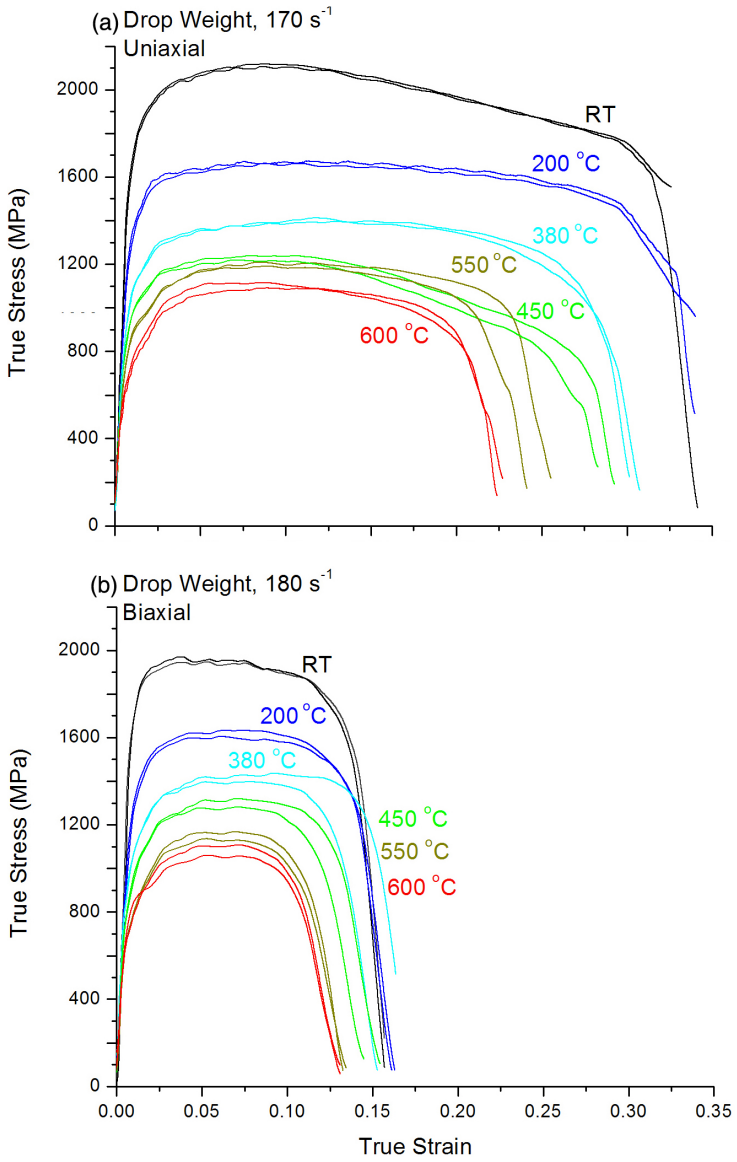

Figure 4.16: Stress-strain curves generated during high temperature testing of (a) uniaxial and (b) biaxial specimens at ~200 s^{-1}. The specimens tested at room temperature showed softening behavior, whereas the specimens tested at higher temperatures showed almost no softening. The uniaxial specimen tested at 450 °C shows unique behavior in comparison to the responses observed at other test temperatures. 450 °C is between in the glass transition temperature and crystallization temperature of LM106 BMG, and between these two transitions is the only temperature range where the BMG will deform homogeneously, and not by localized shear banding (when tested at high strain rates).

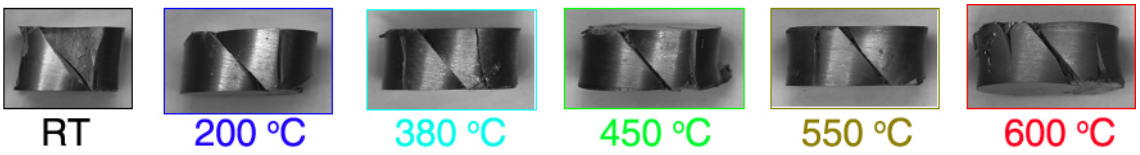

Figure 4.17: Compression-shear specimens after drop weight testing at ~200 s^{-1} over a range of temperatures. All specimens show shear failure in the form of a crack connecting the 96° corners of the specimen. A vertical tensile crack has also formed at all test temperatures.

measured for the uniaxial and biaxial specimens, so the increase in temperature of the glass phase must be causing a transition toward more homogeneous deformation and less heterogeneous and localized deformation by shear band formation. If the response is more homogeneous, it would be similar to that of the uniaxial specimen since the tendency to develop shear bands would be expected to decrease, therefore making the additional shear stress less significant. At 450 °C, the biaxial specimen shows a higher flow stress than the uniaxial case, which is quite unusual, but the difference is not considered to be enough to be significant.

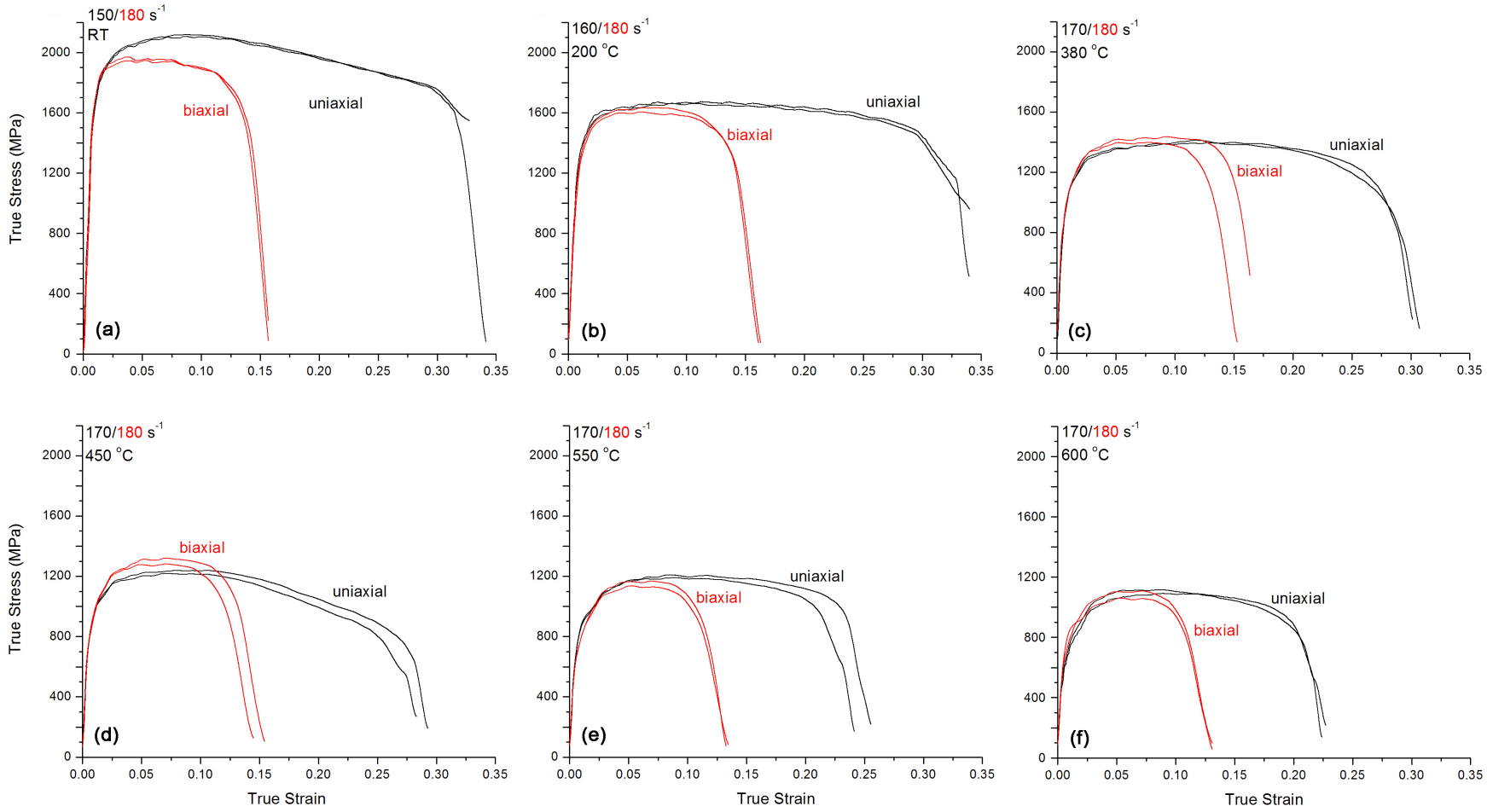

Figure 4.18: True stress-strain curves for uniaxial and biaxial specimens tested at 200 s^{-1} and temperatures of (a) room temperature, (b) 200, (c) 380, (d) 450, (e) 550 and (f) 600 °C. These plots reveal similar flow stresses when comparing the uniaxial and biaxial specimen configurations, but much less strain-to-failure in the biaxial specimens.

Plots of the 0.2% yield stress and failure stress as well as yield and failure strains are shown in Figure 4.19. Because of the lack of clearly defined failure points in the true stress-strain curves, the engineering stress-strain curves were used to investigate trends in yield and failure since these curves show hardening up to a maximum stress, which could easily be consistently measured, followed by failure. So although the values reported are in engineering stress and strain, the trends are the same in true stress and strain. Several obvious trends emerge from the yield and failure data. As shown in Figure 4.19(a), the uniaxial and biaxial specimens yield at the same stress throughout the entire temperature range investigated. For both uniaxial and biaxial specimens, yield stress decreases with increasing test temperature, as expected, and this decrease occurs at the same rate, regardless of specimen configuration. Additionally, failure stress decreases with increasing test temperature, again as expected, but the uniaxial failure stress, which is always above that of the corresponding biaxial specimen, decreases at a much higher rate such that at 600 °C the uniaxial and biaxial failure stresses are approximately the same. Both the failure stress and failure strain measured for the 450 °C test temperature deviated from the otherwise nearly linear trend; these data points are circled in the plots shown in Figure 4.19(a) and (b). This deviation can be explained from the difference in the deformation mechanism of the glass in that temperature range.

As shown in Figure 4.19(b), strain to failure decreases with increasing test temperature. This trend was the opposite of what was expected since typically in metals an increase in test temperature results in an increase in strain to failure. However, in an investigation of W single crystals with various crack orientations, Gumbsch [139] showed that the fracture toughness reaches a maximum at ~100-200 °C after which it decreases. The mechanistic explanation provided for this behavior was a transition from a process limited by dislocation nucleation to one limited by dislocation mobility. At the peak fracture toughness (at ~100-200 °C), dislocation nucleation is at a maximum, but mobility is at a minimum such that dislocations are keeping cracks from propagating. However, as temperature continues

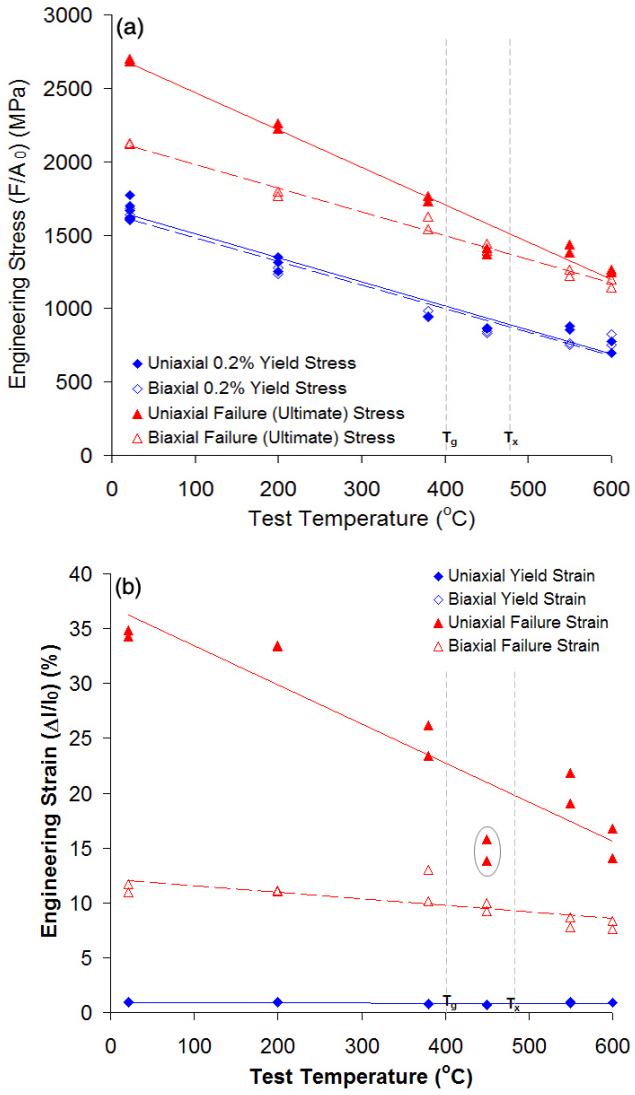

Figure 4.19: Temperature dependance of mechanical behavior of uniaxial and biaxial LM106-70W specimens tested at ~200 s^{-1}. (a) Yield and failure stresses as a function of test temperature and (b) yield and failure strains as a function of temperature. In (a) and (b) the data from the 450 °C tests (circled) deviates from the otherwise linear trend. For both uniaxial and biaxial specimens, yield stress decreases with increasing test temperature, and this decrease occurs at the same rate, regardless of specimen configuration. Additionally, failure stress decreases with increasing test temperature, but the uniaxial failure stress, which is always above that of the corresponding biaxial specimen, decreases at a much higher rate such that at 600 °C the uniaxial and biaxial failure stresses are approximately the same. AS seen in (b), strain to failure decreases with increasing test temperature. Both the failure stress and failure strain measured for the 450 °C test temperature deviated from the otherwise nearly linear trend; these data points are circled. This deviation can be explained from the difference in the deformation mechanism of the glass in that temperature range.

to increase, dislocation mobility increases, which allows cracks to propagate, and as a result decreases fracture toughness. Although this work was done on a single crystal, this decrease in fracture toughness explains the decrease in plasticity of the BMG-W composite with increasing temperature. Additionally, in work on a tungsten heavy alloy (95W-3.5Ni-1.5Fe), Islam et al. [140] found a considerable decrease in ductility at high temperatures (> 500°C) which they attributed to a loss of bonding between the tungsten grains and the matrix and an increase in the percentage of intergranular cleavage. Both the increase in dislocation mobility in the tungsten allowing cracks to propagate and the loss of bonding at the W/BMG interfaces could be contributing to the decrease in plasticity with increasing temperature.

The temperature sensitivity of LM106-70W can be seen in Figure 4.20(a). This plot shows the stress at 5, 10, 15, and 20% strain as a function of temperature for both uniaxial and biaxial (5 & 10% strains only) specimens. The temperature sensitivity of this material shows nearly the same slope at each measured strain, for both uniaxial and biaxial cases. Also notable is that the stress values measured for the 450 °C specimen (circled in Figure 4.20) at each strain deviate from the otherwise linear trend, which is again due to this temperature being between the T_g and T_x. Figure 4.20(b) shows the incremental slope of the stress-strain curve ($d\sigma/d\varepsilon$) at specified strain intervals (5-10%, 10-15%, 15-20%) and reveals the hardening behavior as a function of temperature. The uniaxial specimens show slight hardening from 5-10% strain followed by softening at further strains, whereas the biaxial specimens show softening in the 5-10% strain range. Although the slopes in the 10-15% and 15-20% ranges are negative for all temperatures for the uniaxial specimens, there is less softening in the 200 °C and 380 °C specimens than at room temperature, which was unexpected. Above T_g the softening increases for all test temperatures, as expected, with the most softening seen at 450 °C when the glass is in its "rubbery" phase.

Figure 4.21 shows the dependence of elastic modulus (obtained from slope of elastic portion of stress-strain curves) on test temperature. An overall decrease in elastic modulus

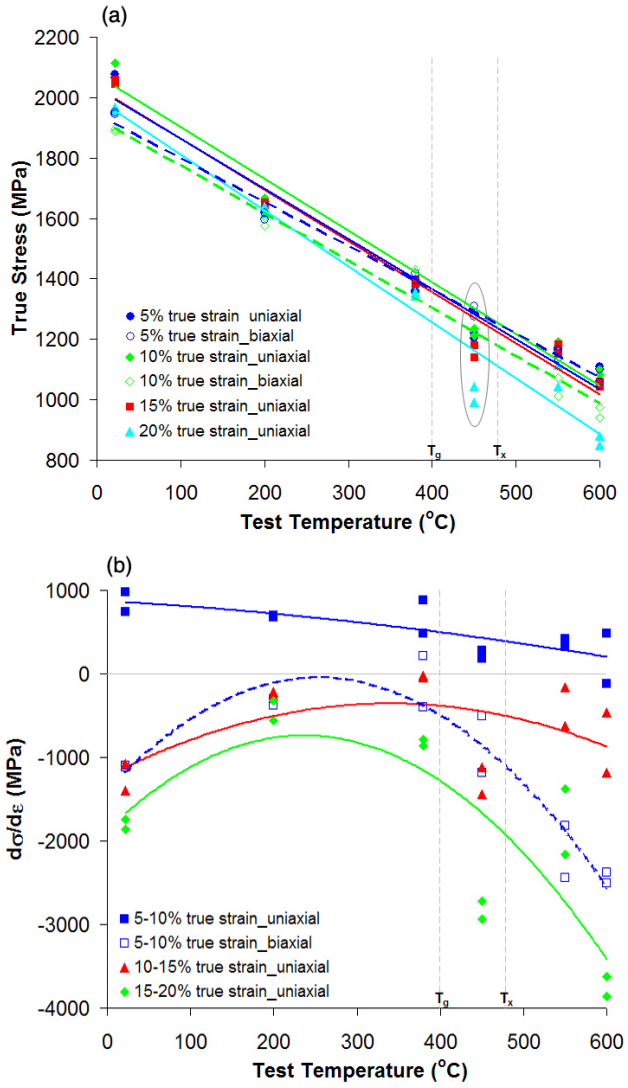

Figure 4.20: (a) Stress at 5, 10, 15, and 20% strain as a function of temperature. The stress values measured for the 450 °C specimen (circled) at each strain deviate from the otherwise linear trend, which is due to this temperature being between the T_g and T_x. (b) Slope of the stress-strain curve ($d\sigma/d\varepsilon$) at specified strain intervals (5-10%, 10-15%, 15-20%) showing hardening behavior as a function of temperature. The temperature sensitivity of this material shows nearly the same slope at each measured strain, for both uniaxial and biaxial cases. The uniaxial specimens show slight hardening from 5-10% strain followed by softening at further strains, whereas the biaxial specimens show softening in the 5-10% strain range. Although the slopes in the 10-15% and 15-20% ranges are negative for all temperatures for the uniaxial specimens, there is less softening in the 200 °C and 380 °C specimens than at room temperature. Above T_g the softening increases for all test temperatures, as expected, with the most softening seen at 450 °C when the glass is in its "rubbery" phase.

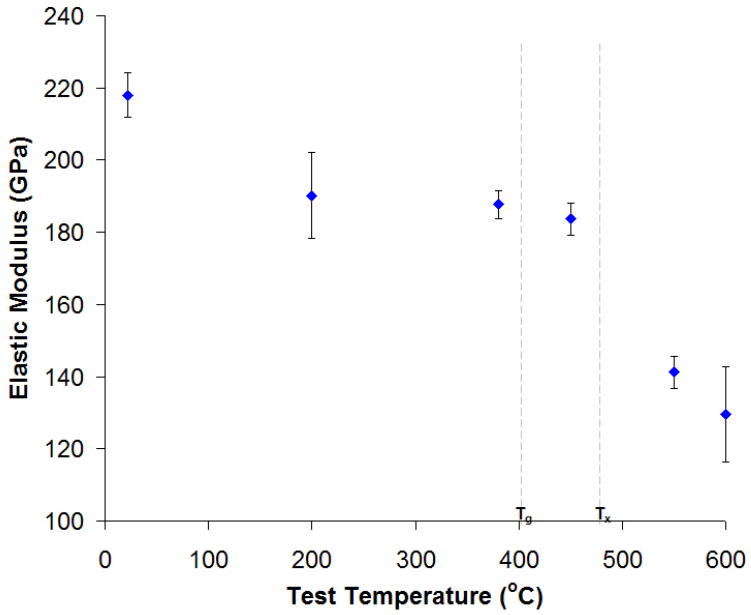

Figure 4.21: Temperature dependence of elastic modulus showing an overall decrease in E with increasing temperature. A plateau was observed from ~200-450°, so the glass transition temperature was exceeded without any apparent effect on E. However, a drastic decrease in elastic modulus was observed above the crystallization temperature of the BMG.

was observed. The elastic modulus at room temperature was 220 GPa, and at 200 °C it dropped to ~190 GPa, where it plateaued, with no obvious decrease above the glass transition temperature. However, a drastic decrease in elastic modulus was observed above the crystallization temperature of the BMG.

Figure 4.22 shows (a) the calculated temperature rise in each uniaxial specimen during testing and (b) the specimen temperature as a function of strain, taking ΔT into account. These values were calculated according to $\Delta T = \frac{0.9}{\rho c_p} \int \sigma d\varepsilon$. Accordingly, the specimen tested at 380 °C should have reached T_g with ~4-5% strain, and thus would have been expected to show marked changes in its behavior as it transitions from heterogeneous to homogeneous deformation in the glass phase, as was observed in the 450 °C specimens. However, the anomalous behavior was not observed, possibly due to the rapid rate of heat buildup, which may not provide enough time for the specimen to transform to the "rubbery"

phase.

4.5 Summary

Investigation of the compressive behavior of LM106-70W over a range of strain rates (10^{-3} to 10^{3} s^{-1}) showed an increase in yield strength and a decrease in failure strength, plasticity, and hardening with increasing strain rate. Comparison of uniaxial and biaxial loading gave evidence of a strong susceptibility of this material to shear failure since the additional 10% shear stress inherent with biaxial loading caused failure at much lower strains in all cases. Investigation of the compressive response of LM106-70W over a range of temperatures (up to 600 °C) showed a decrease in flow stress and plasticity with increased temperature. Also notable was the anomalous behavior at 450 °C, which lies between the T_g and T_x and is in a temperature regime where homogeneous flow, as opposed to heterogeneous shear banding, is the dominant deformation mechanism in the BMG. Overall, it can be generalized that the tungsten dominates the deformation behavior of the composite given the hardening and large degree of plasticity, which are characteristic of the BCC metal and not the BMG. This is not surprising given that the tungsten is 70 vol% of the composite. However, the additional shear stress during biaxial loading causes the BMG to play a strong role. Additionally, at temperatures between T_g and T_x, the BMG deforms homogeneously and this mechanistic change is so significant that the deformation of the BMG plays a significant role in the overall deformation of the composite in spite of its minor volume content (~30%).

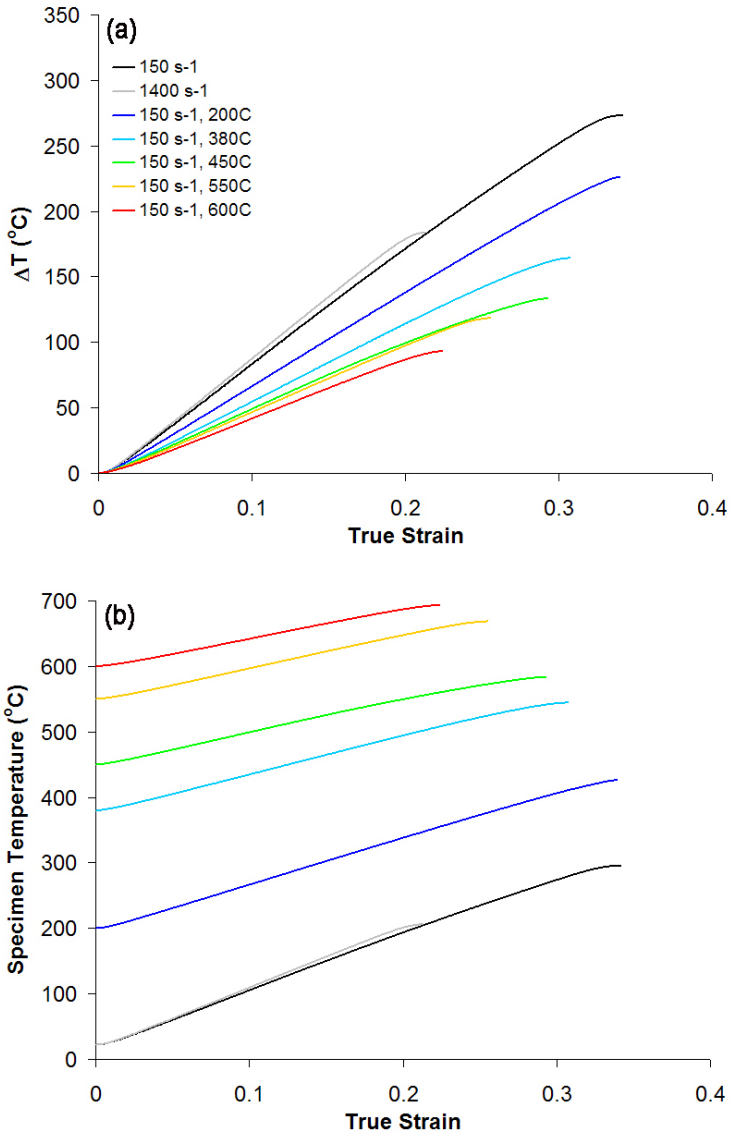

Figure 4.22: (a) ΔT calculated for uniaxial specimens in each type of experiment performed using $\Delta T = \frac{0.9}{\rho c_p} \int \sigma d\varepsilon$. (b) Specimen temperature (incorporating ΔT) as a function of strain. Accordingly, the specimen tested at 380 °C should have reached T_g with ~4-5% strain, and thus would have been expected to show marked changes in its behavior as it transitions from heterogeneous to homogeneous deformation in the glass phase, as was observed in the 450 °C specimens. However, the anomalous behavior was not observed, possibly due to the rapid rate of heat buildup, which may not provide enough time for the specimen to transform to the "rubbery" phase.

CHAPTER V

DYNAMIC COMPRESSIVE RESPONSE OF LM106-70W

5.1 Overview

The mechanical properties, deformation mechanisms, and fracture characteristics of LM106-70W composite were investigated at strain rates of 10^3 to 10^5 s^{-1} using gas gun anvil-on-rod impact experiments instrumented with velocity interferometry (VISAR) and high-speed digital photography [141]. The time-resolved elastic-plastic wave propagation response obtained through VISAR and the transient deformation states captured with the camera provided information about dynamic strength and deformation response of the composite. Comparison of experimental measurements with AUTODYN-simulated transient deformation profiles and free surface velocity traces allowed for validation of the pressure-hardening Drucker-Prager model, which was used to describe the deformation response of the composite and elucidate which phase dominates the deformation response- the glass matrix, tungsten reinforcement, or a combination of properties of the two phases. The microstructures of the recovered impacted specimens were analyzed to learn about the mechanisms of dynamic deformation and their fracture characteristics. The overall results from experiments and modeling revealed a strain to failure of ~45% along the length and ~7% in area, and the fracture initiation stress was found to decrease with increasing impact velocity due to the negative strain-rate sensitivity of the BMG in this regime.

5.2 Introduction and Motivation

The mechanical properties of BMGs and their composites have been studied in some detail at low and intermediate strain rates, including tests performed under uniaxial and biaxial loading as described in the previous section. Constitutive models have also been applied to describe their behavior at low strain rates, however the high-strain-rate dynamic mechanical behavior and fracture criterion are yet to be established. In addition, a constitutive model (that relates stress as a function of strain, strain rate and temperature over a wide range of parameters) is needed for design BMG-matrix composite materials with customized and application-specific properties.

5.3 Approach

5.3.1 Dynamic Compression Experiments

The high-strain-rate mechanical properties and deformation mechanisms of a BMG-matrix composite were investigated using reverse Taylor [57] anvil-on-rod impact experiments performed on the Georgia Tech 80 mm single-stage gas gun. The impact experiments were instrumented with high-speed digital imaging and VISAR [127] (velocity interferometry system for any reflector) to provide information about the dynamic yield strength and allow for validation of constitutive equations via correlation of numerically-simulated transient deformation profiles and free surface velocity traces with those captured in real time during the experiment.

Reverse Taylor [57] anvil-on-rod impact tests were performed on rod-shaped specimens of the composite using a gas gun at impact velocities of Reverse Taylor (anvil-on-rod) impact tests were performed on the composite material at 124, 130, 134, 146, 155, 186, and 244 m/s. These impact velocities correspond to maximum strain rates (at the impact face during the initial stage of impact and deformation) of ~3000 s^{-1} for the 130-155 m/s experiments, ~4000 s^{-1} for the 186 m/s experiment, and ~10,000 s^{-1} for the 244 m/s experiment. The range of velocities was chosen to examine processes involved in the early stages of

deformation and failure during impact.

5.3.2 Constitutive Modeling

In addition to studying the dynamic compressive and fracture behavior of this W-BMG composite, constitutive modeling utilizing existing constitutive relationships was performed to assess model validity for describing the deformation of this material at a range of impact velocities, and to extract more information from the experimental data by coupling simulations with experiments.

Numerical simulations using AUTODYN-2D (axisymmetric problem setup shown in Figure 2(b)) were first performed and correlated with the sample back (free) surface velocity trace and the final, recovered deformed state of the impacted sample at 134 m/s, to determine if the deformation response of the composite is dominated either by the matrix or the reinforcement phase, or a rule of mixtures combination of properties. The Steinberg-Guinan [142] strength model or von Mises yield criterion were used for tungsten and the Drucker-Prager [79] (Mohr-Coulomb) or von Mises yield criterion were used for the BMG. Model parameters for tungsten were obtained from the AUTODYN library and those for the BMG were obtained from the literature [4, 92]. The von Mises and Drucker-Prager yield criteria were also used to model the composite based on properties obtained from the rule of mixtures. The properties used for the composite are shown in Table 5.2. The von Mises yield criterion and Steinberg-Guinian strength model were utilized in their standard forms with a perfectly plastic flow rule. In the Steinberg-Guinan model, shear modulus and yield strength are represented as functions of equivalent plastic strain, pressure and internal energy (temperature) using the following equations [142]:

$$G = G_0 \left[1 + \left(\frac{G'_p}{G_0} \right) \frac{P}{\eta^{\frac{1}{3}}} + \left(\frac{G'_T}{G_0} \right) (T - 300) \right] \tag{18}$$

$$Y = Y_0 \left[1 + \beta \left(\varepsilon + \varepsilon_i\right)\right]^n \left[1 + \left(\frac{Y'_p}{Y_0}\right)\frac{P}{\eta^{\frac{1}{3}}} + \left(\frac{G'_T}{G_0}\right)(T - 300)\right] \tag{19}$$

$$s.t. Y_0 \left[1 + b \left(\varepsilon + \varepsilon_i\right)\right]^n \leq Y_{max} \tag{20}$$

where η is the compression ratio (v_0/v), β is the work hardening parameter, ε_i is the initial equivalent plastic strain,G_p' and Y_p' are *dG/dP* and *dY/dP*, respectively, at the reference state and G_T' and Y_T' are *dG/dT* and *dY/dT*, respectively, at the reference state. The subscript, *0*, corresponds to the reference state where T=300 K, P=0 and ε=0. The Drucker-Prager yield criterion was used with the Stassi (pressure hardening) option and is given as [143]:

$$J_{2Y} = \frac{Y_0}{3}[kY_0 + 3(k-1)p] \tag{21}$$

where J_{2Y} is the second invariant of the deviatoric stress at yield, Y_0 is the strength in simple tension, k is the ratio between the yield strengths in compression and tension, and p is the pressure. The Drucker-Prager yield criterion was used with a non-associated, volume independent flow rule. It should be noted that none of the models considers strain rate effects, and while the Steinberg-Guinan does not incorporate strain hardening of BCC-W, the strain-softening effect observed in the BMG [8,53] is not included in the models for the glass.

5.4 Results and Discussion

5.4.1 Dynamic Compression Experiments

All specimens used in impact experiments were taken from Lot 114, except those tested at impact velocities of 124 and 146 m/s, which were taken from Lot 092905. All of the

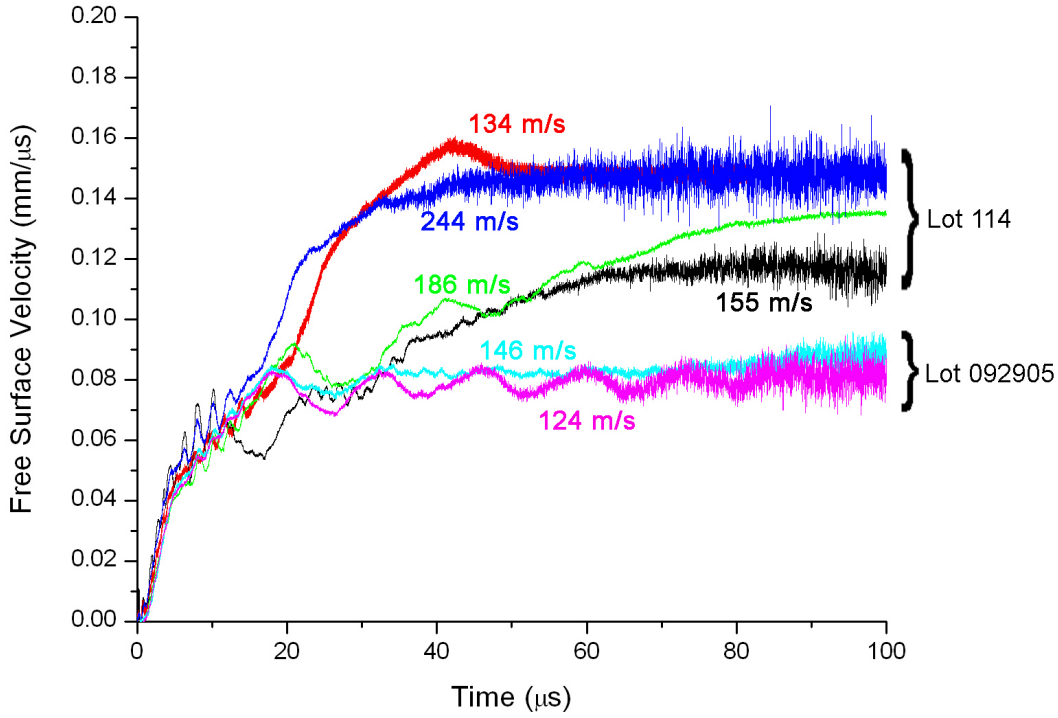

Figure 5.1: Free surface velocity traces captured using the VISAR velocity interferometry system. Specimens from two different processing lots were tested. Impact velocities ranged from 124-244 m/s and showed a trend of decreasing free surface velocity with increasing impact velocity due to fracture. This trend held true within each lot, with Lot 092905 showing lower overall free surface velocities than those observed in Lot 114.

free surface velocity traces captured using VISAR velocity interferometry are shown in Figure 5.1. It can be seen that free surface velocity decreased as impact velocity increased due to energy loss because of fracture, and resulting changes in wave propagation due to creation of new surfaces. This trend held true within each lot, with Lot 092905 showing lower overall free surface velocities than those observed in Lot 114. The overall lower free surface velocities for the specimens in Lot 092905 suggest some subtle differences between the two processing batches of specimens.

Because of the observed differences in mechanical responses of the two specimen lots, analysis and comparison was done within one processing lot (Lot 114). The 130 and 134 m/s impacts resulted in nearly identical transient deformation and recovered specimens

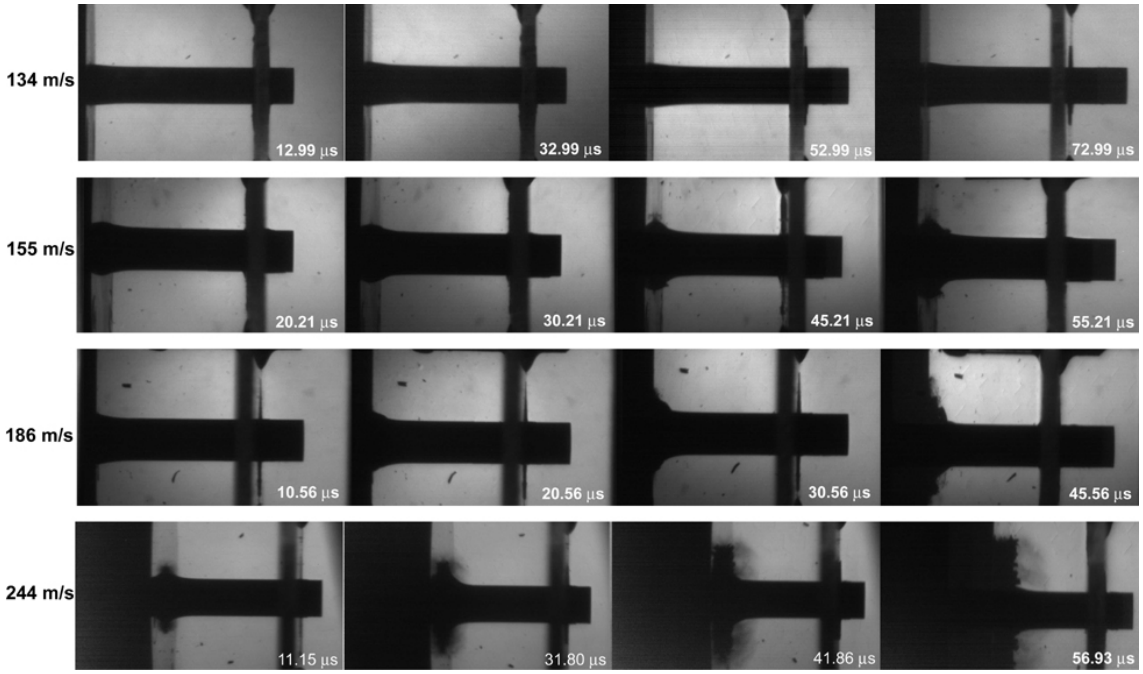

Figure 5.2: Four of 16 high-speed images captured during impact at 134, 155, 186, and 244 m/s. Impact at 134 m/s showed deformation with no failure whereas higher impact velocities showed increasing degrees of deformation and fracture with increasing impact velocity. Impact at 244 m/s led to immediate, catastrophic failure with the front half of the specimen rod disintegrating nearly to powder form.

with very similar features, so results from only one of these two experiments will be presented for each type of analysis. The 244 m/s specimen fractured nearly immediately, making analysis from camera images difficult, thus excluding it from much of the analysis. Examples of four of 16 high speed images captured during experiments performed at impact velocities of 134, 155, 186, and 244 m/s are shown in Figure 5.2. Comparison of these images shows differences in the material behavior caused by increases in impact velocity over the range investigated. It can be seen that when impacted at 134 m/s, the sample underwent deformation at the impact face, but remained intact with no catastrophic failure, which was true upon recovery of the sample. On the other hand, samples impacted at 155 and 186 m/s showed deformation followed by fracture to increasing degrees as impact velocity was increased. Impact at 244 m/s led to immediate, catastrophic failure with the front half of the specimen rod disintegrating nearly to powder form.

5.4.1.1 Analysis of Recovered Specimens

Photographs of specimens recovered post-impact are shown in Figure 5.3(a-c). The samples impacted at 155, 186, and 244 m/s resulted in fracture (Figure 5.3(b-d)), whereas the lower velocity impact experiments (130 & 134 m/s) showed mushrooming typical of dynamic impact of ductile metals (Figure 5.3(a)). The specimens recovered after impact at 130 and 134 m/s also showed radial cracking on the impact face due to the tension caused by the radial expansion, and shear cracks oriented at ~45° to the loading axis on the outer surface away from the impact face, as can be seen in Figure 5.3(a).

Microstructural analysis of the recovered specimens performed using scanning electron microscopy yielded several interesting characteristics, which are shown in Figure 5.4(a-f). Extensive deformation of the W particles was observed in regions along the crack tips on the impact face (Figure 5.4(a & b)) of the 130 m/s specimen. The cracks were observed to travel primarily through the glass matrix and around the W particles, which acted as obstacles to crack propagation. Fracture surfaces of the 155 and 186 m/s impacted samples

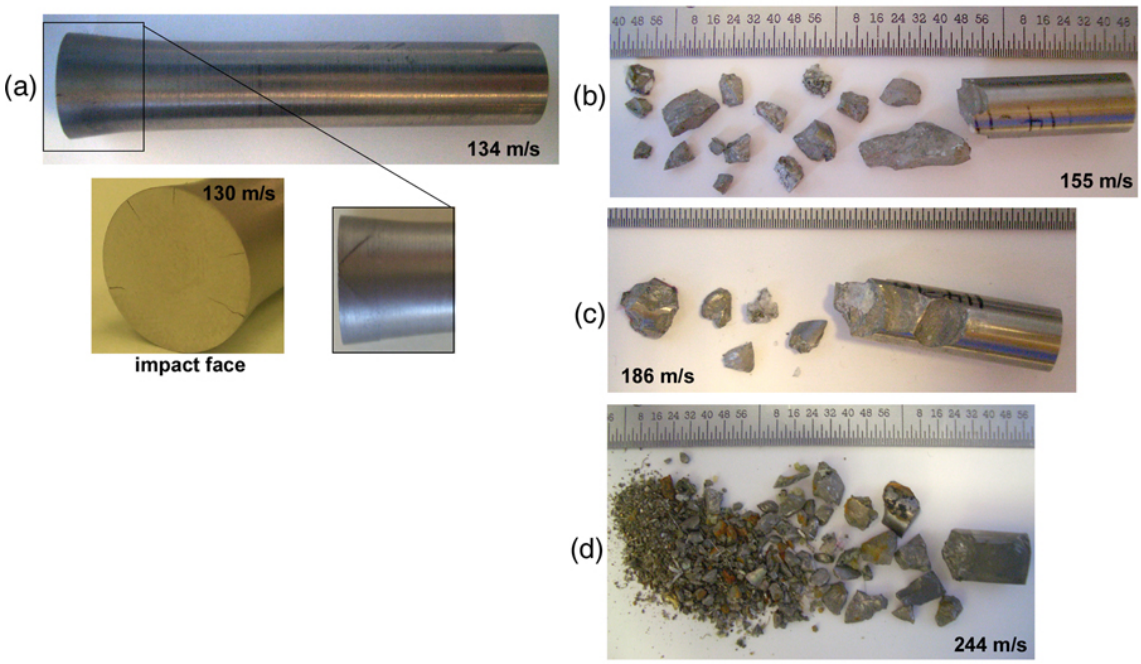

Figure 5.3: Specimens recovered from reverse Taylor impact tests at 130/134, 155, 186 and 244 m/s. (a) The specimens impacted at 130 and 134 m/s showed mushrooming at the impact face and did not result in fracture. This specimen also showed radial tensile cracks on the impact face and shear cracks on its outer surface. (b), (c), and (d) The specimens impacted at 155, 186, and 244 m/s, respectively, fractured as a result of the impact. All specimens have an initial diameter of 8.9 mm.

were very similar to one another and revealed extensive flow in the glass. Cracking was observed to occur primarily through the BMG matrix and at BMG-tungsten boundaries, although a few fractured tungsten particles can be seen; an example is indicated by the black arrow in Figure 5.4(c). Figure 5.4(d) reveals heavily deformed and sheared regions with elongated and deformed W particles and flow of the BMG over the W particles. The veinal pattern typical of BMG fracture surfaces is evident in some areas, as seen in Figure 5.4(d). Figure 5.4(e & f) show images of cracks propagating through the BMG matrix, traveling primarily around the W particles, but occasionally fracturing the W, as indicated by the white arrows.

Vicker's Hardness indentation tests were performed across the impact face and along the axial length of the specimen recovered after impact at 130 m/s to investigate the effects of strain and strain-rate hardening as a function of location in the specimen. The results of the indentation tests are shown in Figure 5.5. The hardness of the starting as-cast composite was 4.32±0.10 GPa. Strain hardening was evident in the recovered sample, as can be seen from the increase in hardness along the impact face and length of the recovered specimen, which is shown in the plot in Figure 5.5(a). The center of the impact face exhibited a hardness value of ~4.8 GPa and the impact end of the longitudinal section exhibited a hardness of ~4.9 GPa. An SEM micrograph showing a typical indentation is shown in Figure 5.5(b). The indentation encompasses several particles/regions of each phase and thus is representative of the composite, although the strain hardening behavior is attributed to the W phase alone. Hardness contour plots shown in Figure 5.5(c & d) were constructed using the MATLAB script given in Appendix C.1 to better characterize the hardening behavior in this impacted specimen. The contour plots of the axial length and impact face show the same trends as seen in the plots in Figure 5.5(a). Figure 5.5(e) shows the impact face of the recovered specimen, which shows several cracks. This image reveals that the hardness values may be correlated with the position of the radial cracks. Since extreme deformation was observed at the crack tips on the impact face, it is believed that the W particles became

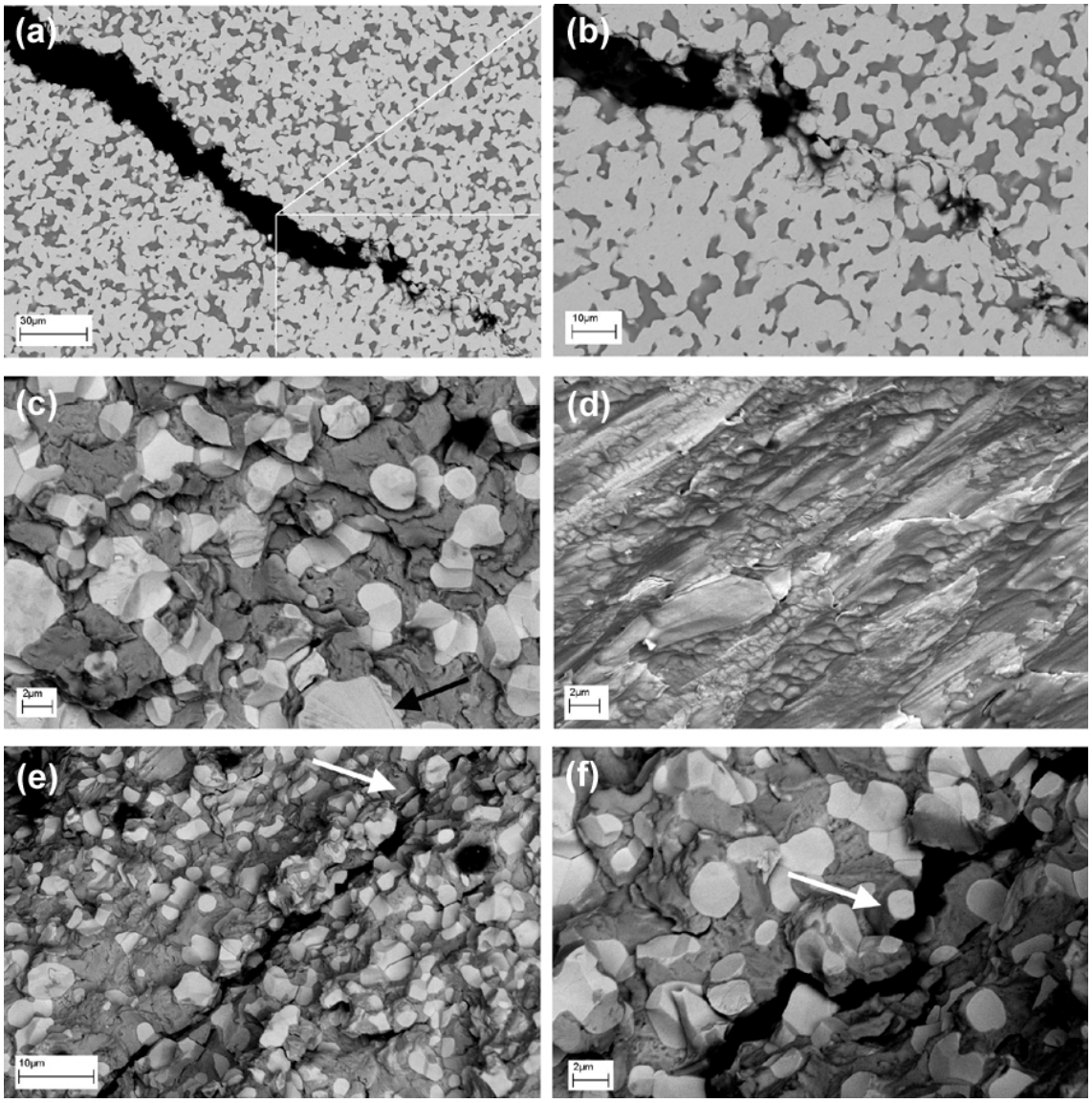

Figure 5.4: SEM micrographs of recovered specimens. (a & b) Crack on impact face of specimen impacted at 130 m/s. (c-f) Fracture surface of specimen impacted at 155 m/s, which exhibits similar features to the fracture surface from the 186 m/s impact experiment. (c) Flow in the glass and evidence that the fracture typically occurs in the matrix around the W boundaries, but occasionally through a W particle (indicated by the black arrow). (d) A region where the W particles have become extremely deformed and elongated and there is extensive flow of the BMG over the W particles. (e & f) Cracks propagating through the glass matrix, showing that the W particles act as obstacles to the crack propagation. In a few cases, however, the cracks propagate through the W particles, splitting them into two, as indicated by the white arrows.

extremely strained in this region and thus experience the most strain hardening, which may explain the regions of high hardness that protrude out from the center of the impact face.

5.4.1.2 Free Surface Velocity and Yield Stress

Analysis of the free surface velocity data obtained by the VISAR system gave valuable information about the dynamic mechanical behavior of these composites. VISAR traces from experiments at impact velocities of 134, 155, 186 and 244 m/s are plotted together in Figure 5.6. Comparison of these four traces shows that they all have the same initial slope, as expected since this region represents elastic wave reflections. It is also notable that the peak free surface velocity decreases with increasing impact velocity as a result of fracture, which results in an energy loss. Dynamic material data can be determined from these free surface velocity traces based on wave theory, as described in more detail by Rohr et al. [124]. For each experiment, the dynamic yield stress can be calculated as $\sigma_y = \frac{1}{2} c_L \rho \Delta u_{fs}$, where $c_L = \sqrt{\frac{E}{\rho}}$ is the longitudinal wave speed, ρ is density, and Δu_{fs} is the rise in free surface velocity during the first linear portion of the free surface velocity trace before the slope changes (indicated in the inset schematic Figure 5.6). The strain at yield can be calculated as: $\varepsilon = \frac{\partial u}{\partial x} = \frac{u_{fs}}{2c_L}$, and the strain rate at yield can be calculated as: $\frac{d\varepsilon}{dt} = \frac{\Delta\varepsilon}{\Delta t}$. The values σ_y, ε, and $\frac{d\varepsilon}{dt}$ for each experiment are reported in Table 5.1. These results show an increase in yield stress with increasing impact velocity (strain rate), which was expected due to the large fraction of BCC tungsten, which is highly strain-rate sensitive. The experiment at 186 m/s deviates slightly from the trend, which is possibly due to a material heterogeneity. It should be noted that the strain rates reported in Table 5.1 are lower than those reported earlier in the description of the experiments. The aforementioned values correspond to maximum strain rates, which are experienced during the initial stages of impact. The strain rate at yield is expected to be lower than that during initial impact, the significance of which will be discussed in more detail later.

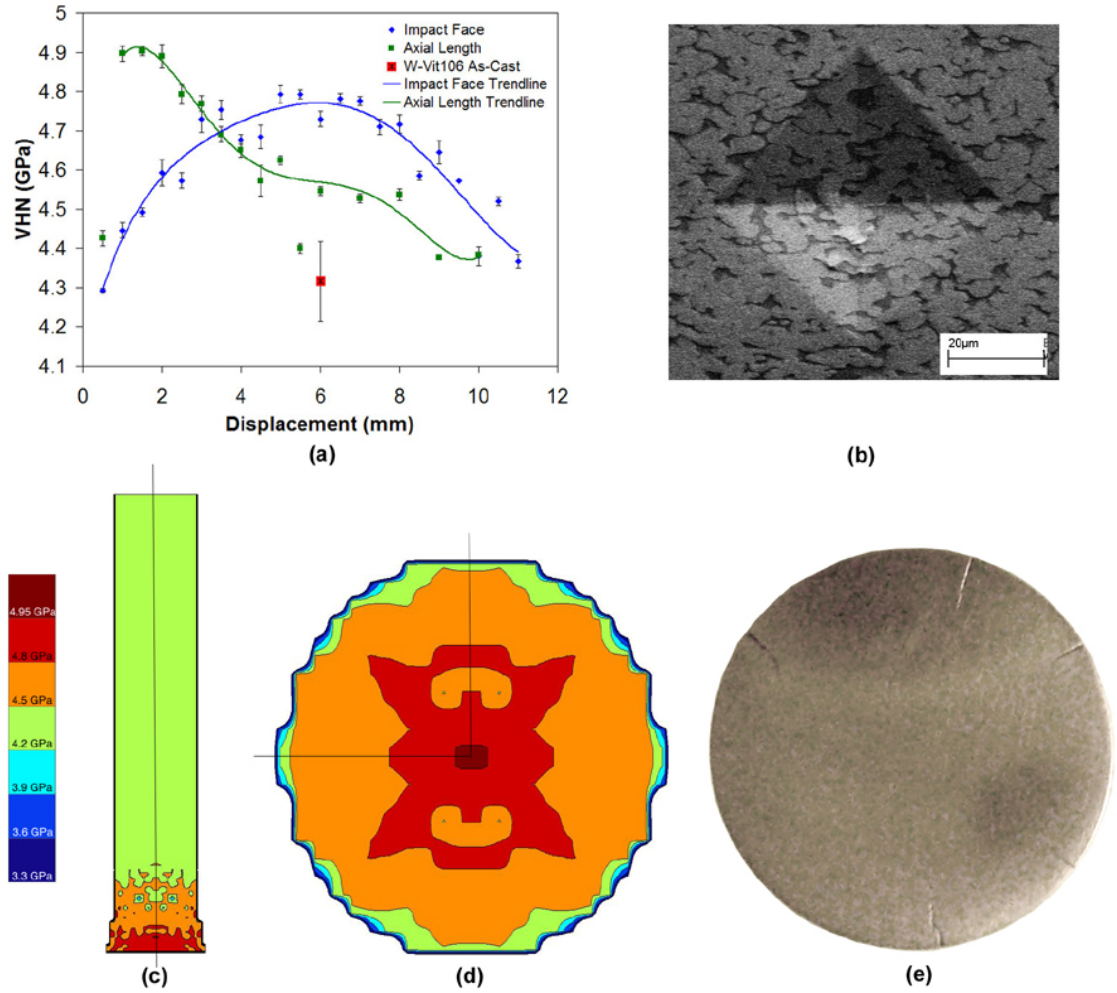

Figure 5.5: Vicker's hardness data from the composite specimen recovered from impact at 130 m/s. (a) Plot of hardness as a function of position along the center of the impact face of the rod and along the center of a longitudinal section. These measurements showed increased hardness values near the center of the impact face and at the impact end of the longitudinal section. (b) SEM micrograph of an indent showing the relative size of the indentation. (c) Hardness contour plot of a longitudinal section of the recovered specimen made from indents in a 0.5 mm grid on half of the longitudinal section (the other half is a mirror). (d) Hardness contour plot of the impact face of the recovered specimen made from indents in a 0.5 mm grid on one quarter of the impact face (the remaining $\frac{3}{4}$ of the impact face is mirrored). (e) The impact face of the specimen in the same orientation as was used for the hardness measurements. This image shows that the regions of higher hardness may correlate with the extremely strained regions at the crack tips.

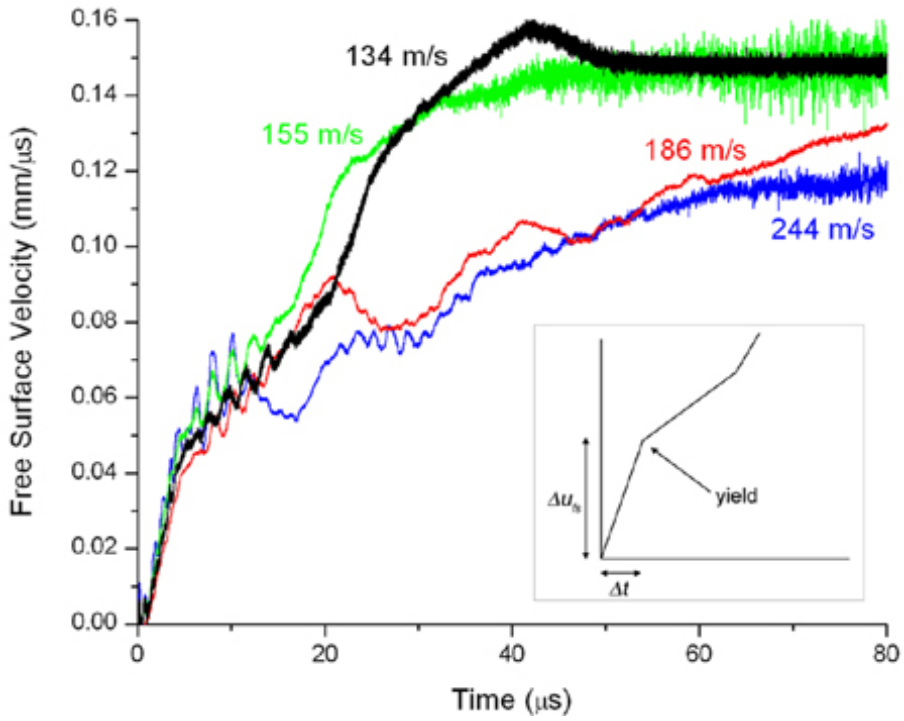

Figure 5.6: Free surface velocity traces (obtained using the VISAR system) from all experiments used for yield strength analysis. Notable features include the decreasing final free surface velocity with increasing impact velocity due to fracture. The values of free surface velocity and time that were taken from the first linear portion in each trace and used in calculations are indicated on the inset schematic.

Table 5.1: Dynamic material data including stress, strain, and strain rate at yield, determined from free surface velocity traces. Values were calculated using the analysis given by Rohr et al. [124].

Impact Velocity (m/s)	σ_y (GPa)	ε at yield (10^3)	$\frac{d\varepsilon}{dt}$ at yield (s^{-1})
134	1.47 ± 0.13	5.4	1114
155	1.61 ± 0.03	5.9	1282
186	1.33 ± 0.03	4.9	968
244	1.67 ± 0.03	6.1	1397

5.4.1.3 Incremental Strain and Fracture Initiation

Incremental areal and axial strains in the impacted samples were measured from each of the digital images captured and were plotted as a function of time after impact. These plots are shown in Figure 5.7(a, b, c) for the 134, 155, and 186 m/s impacts, respectively. During the 134 m/s impact experiment (Figure 5.7(a)), the areal strain steadily increased until a constant maximum strain of ~30% maximum areal strain was maintained, and fracture did not occur. A similar trend is seen when examining the axial strain, although some elastic recovery of the specimen length is observed, as will be seen more clearly in a later figure. The incremental areal and axial strain plots for the 155 and 186 m/s impact experiments (Figure 5.7(b & c)) show the effect of fracture, with the strains more abruptly reaching a threshold of ~4 to 5% areal strain and ~7% axial strain, following which fracture occurred. The final strain measurement in both of these plots is marked by an asterisk, indicating that fracture was evident in the corresponding high-speed image at those times. The specimen impacted at 244 m/s showed fracture even in the earliest image captured, so the incremental strain to fracture initiation could not be measured. Figure 5.7(a, b, c) also shows the sample back (free) surface velocities obtained for each experiment. The free surface velocity trace recorded during impact at 134 m/s (Figure 5.7(a)) shows a clean, stepped profile up to a constant free surface velocity. In the cases when fracture occurred (155 and 186 m/s impact experiments shown in Figure 5.7(b & c)) this stepped profile was disrupted due to creation of new surfaces and propagation of the failure front, resulting in a lower free surface velocity. In fact, the free surface velocity decreased with increasing impact velocity due to the increasing amount of energy/velocity lost as a result of fracture. Correlation of the incremental strains and free surface velocity provided information about the time of fracture initiation as well as the fracture initiation stress, which will be discussed later.

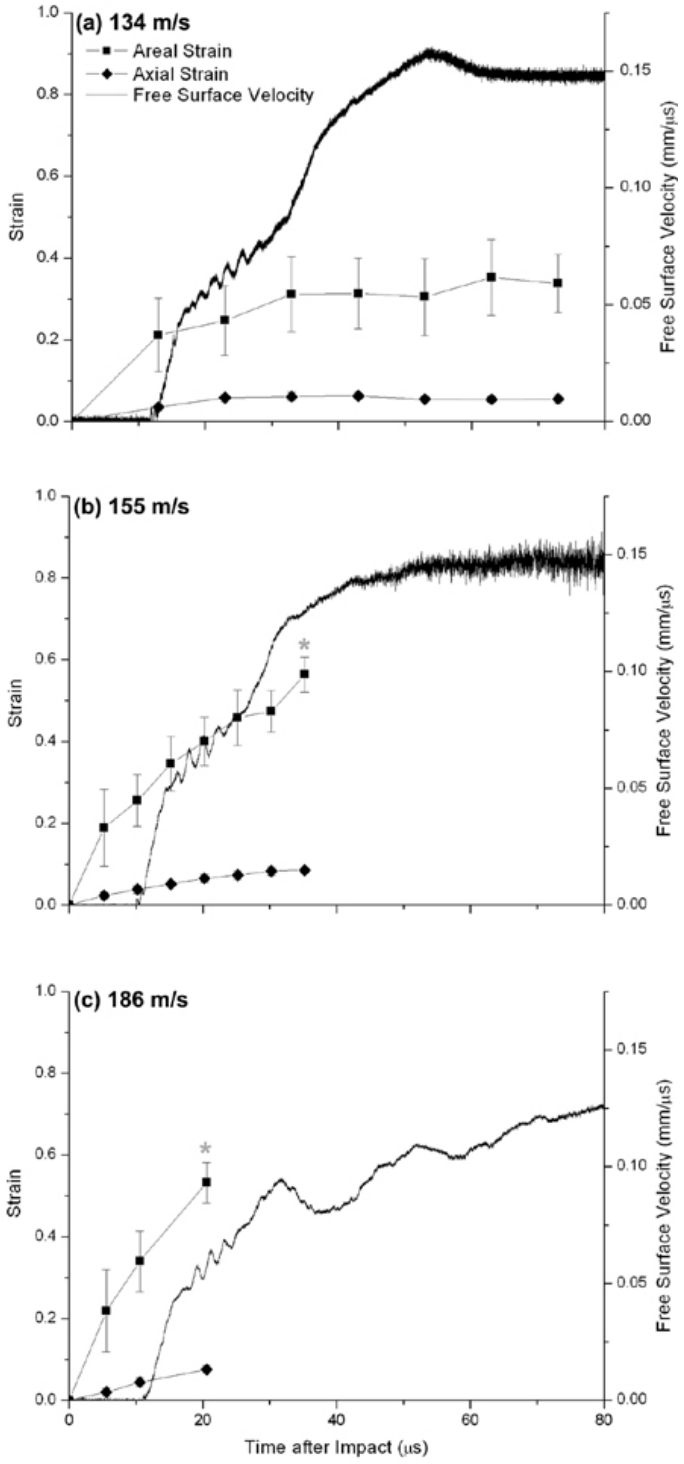

Figure 5.7: Incremental areal (ε = 1-A_0/A) and axial (ε = -ln(L/L_0)) strains as a function of time after impact for impacts velocities of (a) 134, (b) 155 and (c) 186 m/s. The strain was measured from the high-speed images captured during the experiment. Also shown are the free surface velocity traces recorded using VISAR during the experiment. The asterisk marks in the 155 and 186 m/s plots indicate that fracture was evident in the images at those corresponding times.

5.4.2 Constitutive Modeling

5.4.2.1 Model Validation

Figure 5.8 shows a comparison of the free surface velocity traces generated using various constitutive models (Stassi Drucker-Prager, von Mises, Steinberg-Guinan) and material properties, and their correlation with the experimentally measured free surface velocity trace from the 134 m/s impact experiment (black trace). It can be seen that the simulated traces based on Stassi Drucker-Prager and von Mises models for single-phase BMG (traces (b) &(c)) are quite different from the measured VISAR trace. The simulated traces based on Steinberg-Guinan and von Mises models for single-phase tungsten (traces (d) and (e)) show a better match, although with an earlier arrival of the wave at the back (free) surface and a four-step rise to peak velocity. Simulated traces based on von Mises and Drucker-Prager models with a rule of mixtures combination of properties of both constituents (traces (f) and (g)) predict the best correlation with the measured free surface velocity trace in terms of the arrival time and the stepped rise to peak velocity.

Figure 5.9 compares the simulated final shapes with those of the samples recovered after impact at 134 m/s. Again it can be seen that the simulated final profiles based on models using rule of mixtures combination of properties of both constituents (profiles (e) and (f)) provide the best correlation with imaged shape, in contrast to the models for single-phase monolithic glass (profiles (a) and (b)) or tungsten (profiles (c) and (d)).

The final dimensions (impact face radius and rod length) of the recovered impacted (mushroomed) rod and simulated sample profiles (based on rule of mixtures combination of properties) along with the percent differences in the corresponding dimensions are listed in Table 5.2. Values of the properties (experimentally determined or obtained from literature) are also listed in Table 5.2. The von Mises model yields a difference of 3.9% in final impact-face radius and 1.1% in final length and the Stassi Drucker-Prager model yields a slightly better match with a difference of 3.3% in final impact-face radius and 0.9% in final length.

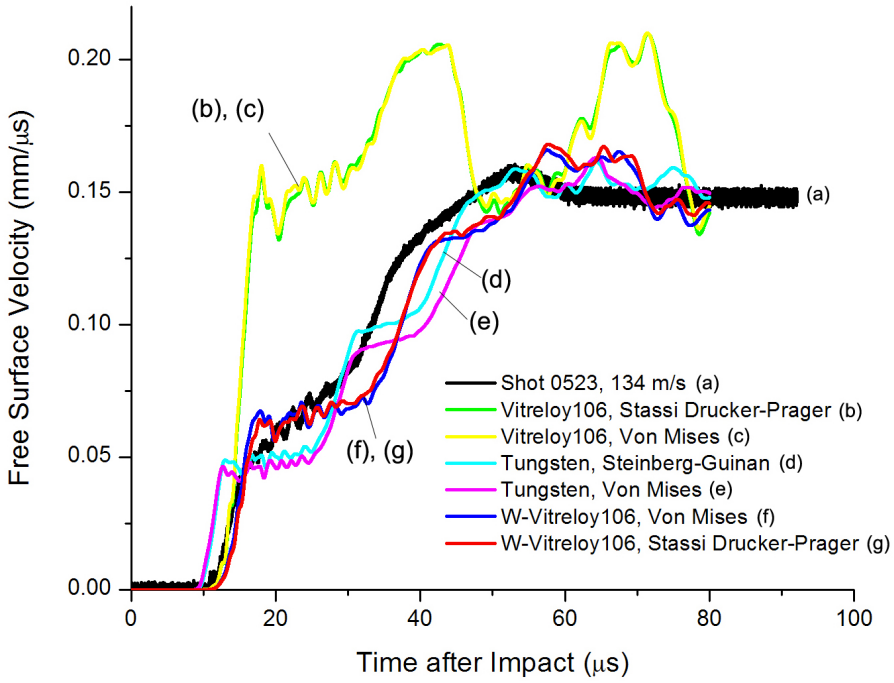

Figure 5.8: Comparison of experimental and simulated free surface velocity traces generated using different constitutive models and properties corresponding to the BMG, the W, or a rule-of-mixtures combination. The von Mises (f) and Stassi Drucker-Prager (g) models using the rule of mixtures properties of the composite provided the best fit to the free surface velocity data.

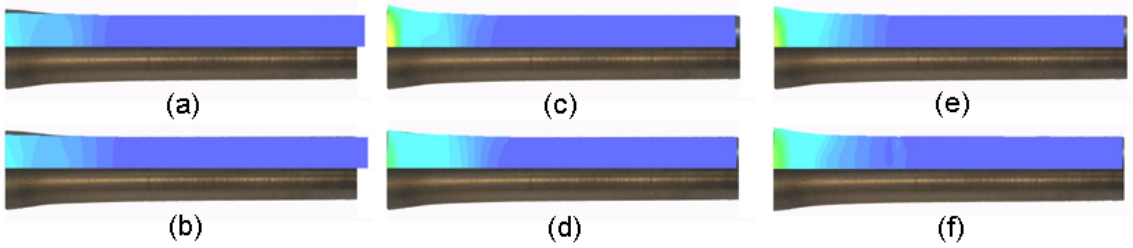

Figure 5.9: Comparisons of simulated final shapes (top) with the final shape of the specimen (bottom) recovered after impact at 134 m/s. Contours correspond to effective plastic strain: (a) von Mises model using properties of monolithic BMG; (b) Stassi Drucker-Prager model using properties of monolithic BMG; (c) von Mises model using properties of tungsten; (d) Steinberg-Guinan model using properties of tungsten; (e) von Mises model using properties of the composite obtained from rule-of mixtures and (f) Stassi Drucker-Prager model using properties of the composite obtained from rule-of mixtures. Qualitatively, the best match to the final shape was given by (f).

Table 5.2: Comparison of final (impact face) radius and length of recovered (mushroomed) rod with final dimensions of simulated profiles generated using von Mises or Drucker-Prager yield criterion with composite properties determined by a rule of mixtures (RofM). Values of model parameters (experimentally measured using quasi-static compression tests or obtained from literature [3]) are also listed.

Model	Model Parameters	R_f (mm)	% diff. radius	L_f (mm)	% diff. length
Recovered sample	N/A	5.45	N/A	48.70	N/A
von Mises: Vit106-70W composite	G=71 GPa (RofM)[1]	5.66	3.9	48.16	1.1
	YS=1789 MPa (comp. test)				
Drucker-Prager: Vit106-70W composite	G=71GPa (RofM)[1]	5.63	3.3	48.28	0.9
	CYS=1789 MPa (comp. test)				
	TYS=885 MPa (RofM)[2]				

[1]Reuss rule of mixtures (lower bound) with constant stress was used for shear modulus.
[2]Voigt rule of mixtures (upper bound) with constant strain was used for the strength.

Although the correlations reported in Table 5.2 reveal a good fit to the final (recovered) deformed state of the impacted sample, the applicability of the constitutive models was further validated by considering the transient deformation states in order to verify if the effects of the path-dependent deformation history were captured by the models. Plots of radial strain as a function of distance from the impact face at three different time intervals following impact - 12.99, 32.99, and 52.99 μs, are presented in Figure 5.10. Also shown are the simulated and experimental profiles at those same times. The plots and images show the match of the simulated transient shapes to those captured during the experiment. The simulations show the correct overall trend in deformation, although not a perfect match, as revealed by the profiles shown in Figure 5.9 and the comparison of dimensions reported in Table 5.2. Furthermore, no distinct differences between the von Mises and Drucker-Prager models were seen for this single experiment at 134 m/s (Figure 5.10).

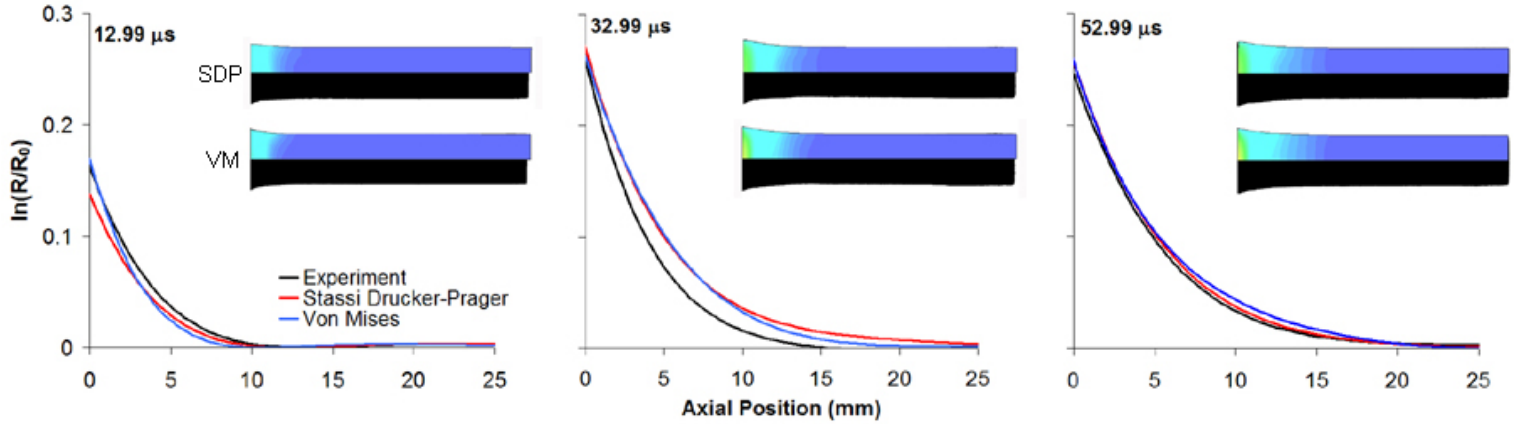

Figure 5.10: Radial strain as a function of axial position for experimental and simulated (von Mises and Stassi-Drucker-Prager) transient profiles at 12.99, 32.99 and 52.99 μs after impact. The simulation contours represent effective plastic strain. These comparisons show that both models provide a good fit to the experimental transient shapes, and that there is little difference in the transient shapes produced using von Mises versus Stassi-Drucker-Prager.

The results reveal that while the von Mises and Stassi Drucker-Prager constitutive models with a rule of mixtures combination of properties of the constituents can more accurately predict the final deformation states of the impacted composite sample, prediction of the transient states is less than perfect, illustrating the inability of the models to fully capture the path dependence. Likewise, the simulations do not completely describe the wave interactions, as evidenced from the correlations of the free surface velocity trace. The differences are not unexpected since the models considered in this work do not incorporate dependence of strain rate or any description of inhomogeneous flow. Nevertheless, the Drucker-Prager description of the deformation of the composite was considered to be the most reasonable (of existing models) based on the aforementioned results and the fundamental physical reasons that a Mohr-Coulomb-type model is applicable to metallic glasses (Section 2.4). Regardless of outcome, the results described illustrate the applicability of the instrumented anvil-on-rod impact experiments for validating constitutive models that can be used to predict the high strain-rate deformation response of metallic glasses and their composites.

5.4.3 Drucker-Prager Model

After initial numerical simulations [126] were concentrated on the 134 m/s impacted sample which did not undergo fracture, and the Drucker-Prager strength model was determined to provide the best description of the overall deformation history, the same simulation parameters were applied to the impact velocities of 155, 186, and 244 m/s until the point where fracture initiated in these specimens. The goal of this exercise was to deduce information about the fracture initiation process by comparison of experimental data to simulated results up to the point of fracture.

5.4.4 Model Validation at Transient Times

The applicability of the Drucker-Prager model at each impact velocity was further validated by considering the transient deformation states in order to verify if the effects of the

path-dependent (transient) deformation history were captured by the models. Composite images, consisting of a lower half from the experimental image and upper half from the simulated profile, of the deformed rod-shaped sample prior to fracture are presented in Figure 5.11(a-c). These images comparing experiments with simulations gave evidence of good agreement between the simulations and experiments. It can also be seen that once fracture was evident in the experimental image (35.21 μs in the 155 m/s impact and 20.56 μs in the 186 m/s impact), the simulations began to deviate from the experiments, which is expected since a failure model was not incorporated in the simulations. This comparison was not made for the 244 m/s experiment because even the earliest images captured during the experiment showed extensive fracture. Comparison between the simulations and experiments provided information relevant to understanding the initiation of fracture.

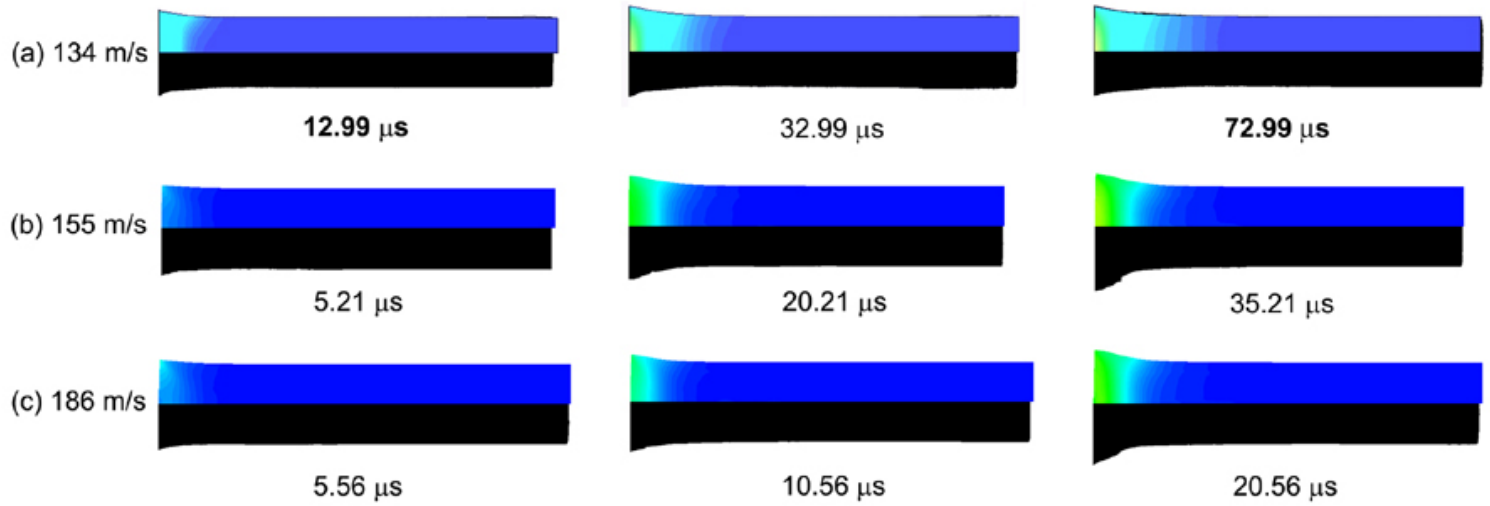

Figure 5.11: Images comparing the experimental (lower half) and simulated deforming sample at various times during impact at (a) 134 m/s, (b) 155 m/s, and (c) 186 m/s. The simulation contours represent effective plastic strain. These comparisons show that the model provides a good fit to the experimental transient shapes before fracture initiation, which is evident in the latest time of the 155 and 185 m/s impacts.

Simulated and experimental incremental areal and axial strains were also compared for each impact velocity to better analyze the correlation and assess the validity of the model for each impact velocity. These comparisons are shown as plots of incremental strain as a function of time in Figure 5.12. It can be seen that the Drucker-Prager simulations exhibit good agreement (within the pixel resolution of the camera) in length change and impact face area change for each of the impact velocities. For the plots of the 134 m/s impact, it can be seen that the amount of areal strain reaches a steady state around 32 μs after impact, which is below the threshold value of strain that leads to failure for this composite. The axial strain measurements and simulations of the specimen impacted at 134 m/s both show elastic recovery. The specimen decreases in length and then subsequently increases, recovering a small amount of strain. The strain data at 72 μs after impact at 134 m/s (Figure 5.12(a)) was measured at a point when the specimen had already separated from the flyer, so deformation was complete. Both the 155 m/s and 186 m/s impacts resulted in fracture. Because the simulations did not allow for fracture, the incremental strains from these experiments (Figure 5.12(b & c)) could only be compared during deformation until the point where fracture began and could be observed macroscopically. The last strain measurement for each of these two experiments was taken at a time when the sample had clearly begun to fracture, which is indicated by the asterisks in Figure 5.12(b & c). Comparisons of the measured strain values with the simulations provided another means of determining when fracture began. It can be seen from the measures of areal strain (Figure 5.12(b & c)) that after fracture the measured strain value suddenly deviates from the simulated strain value. From these graphs we can deduce that the threshold strain to failure values of areal and axial strain for this composite are ~4 to 5% and ~7%, respectively.

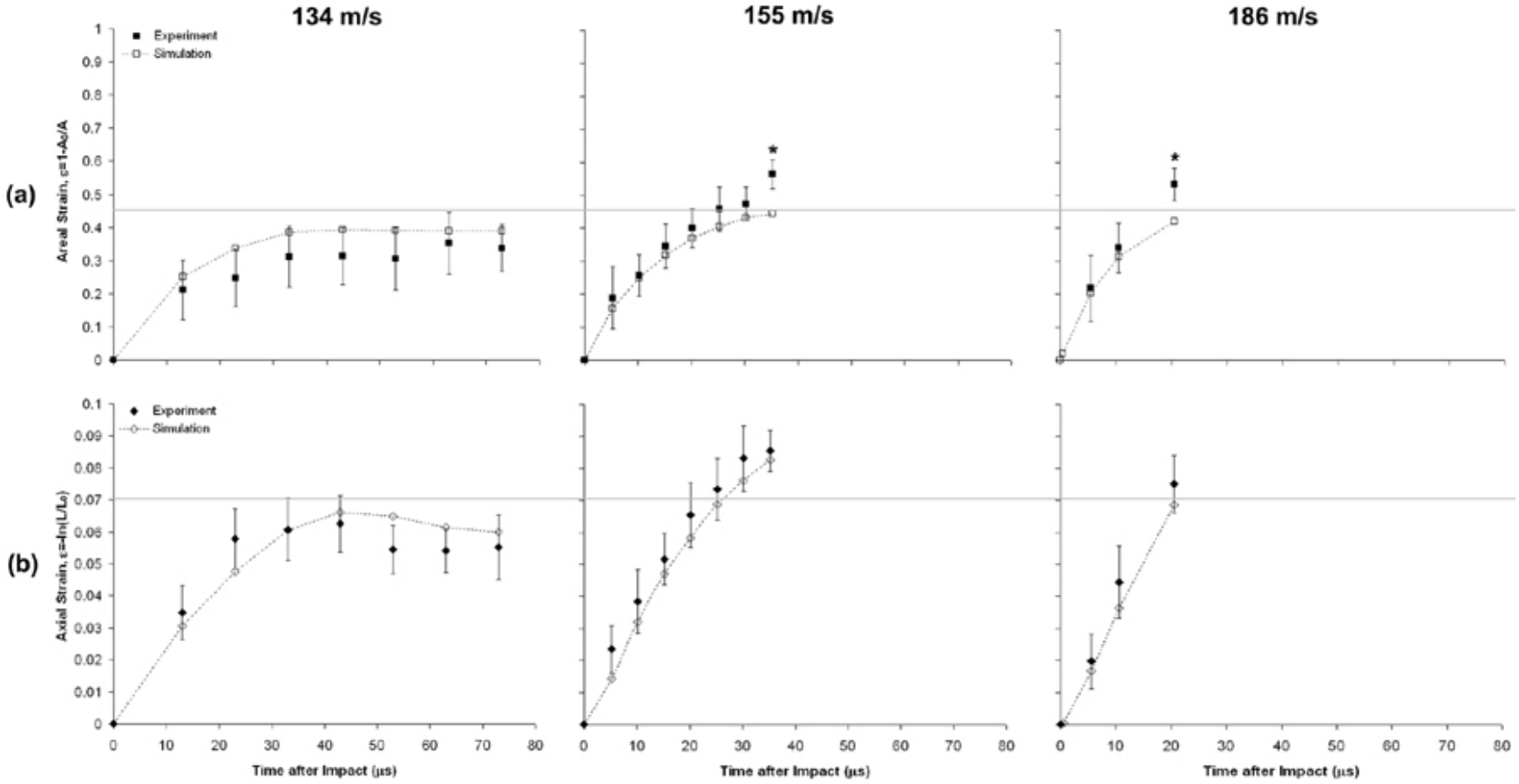

Figure 5.12: Comparison of incremental areal strains and incremental axial strains measured from high-speed images during experiments ((a) 134 m/s, (b) 155 m/s, (c) 186 m/s) and the corresponding incremental strains generated in the simulations. Error bars correspond to the pixel uncertainty when measuring strain from the high-speed images. Asterisks marked above the final incremental strain measurement for the 155 and 186 m/s experiments indicate measurements at a time when fracture had begun. The horizontal gray lines indicate thresholds to fracture of ~4 to 5% areal strain and ~7% axial strain.

5.4.4.1 Comparison of Experimental and Simulated Free Surface Velocities

Comparison of experimentally-obtained and numerically-simulated free surface velocity traces allowed for determination of fracture initiation stress based on quantification of the loss of velocity due to fracture. Figure 5.13 shows the free surface velocity traces obtained from the experiments (using VISAR) correlated with traces obtained from the Drucker-Prager simulations. The simulation of the 134 m/s impact experiment generated a free surface velocity trace that matched reasonably well [126] to the experimental trace (Figure 5.13(a)). Using this experiment as validation of the model describing the deforamtion response, simulations at other velocities were then compared to the corresponding experimental data. For the 155, 186, and 244 m/s impact experiments, significantly large discrepancies were observed after fracture initiated in the experiment (since a failure model was not incorporated in the simulations), but the simulated free surface velocities showed a reasonable fit until fracture initiation. Further work is needed to develop constitutive equations that include a failure model for validation at high velocities and strain rates.

The deviation between the experimental and simulated free surface velocity traces in these cases when fracture occurred can be used to obtain information about fracture initiation. The difference in free surface velocity between the simulations and experiments provides an indication of the velocity, and correspondingly the stress level, that would have been reached in the absence of fracture. This loss in free surface velocity (and stress) is indicated by the double-headed gray arrows in Figure 5.13. The magnitude of this stress, based on the velocity loss, can be quantified by $\sigma = \frac{1}{2}\rho_0 c_L u_{fs}$ [144], where ρ_0 and c_L are the density and sound speed of the material, respectively. The free surface velocity losses, Δu_{fs}, as a result of fracture were 51, 110, and 118 m/s in the 155, 186, and 244 m/s impact experiments, respectively. These Δu_{fs} values correspond to stresses of 1.66, 3.56, and 3.85 GPa. These values indicate the additional stress that the composites would have to endure in the absence of fracture, and these are clearly above the dynamic strength of this material.

If the time when the simulated free surface velocity trace deviates from the experimental free surface velocity trace is taken to be the approximate time of fracture initiation, then the fracture initiation stress can be calculated from the corresponding free surface velocity. The point on the free surface velocity trace at which this calculation was performed is indicated by the single-headed gray arrows in Figure 5.13. This calculation yields fracture initiation stresses of 4.50, 3.02, and 2.12 GPa for the impacts at 155, 186, and 244 m/s, respectively, which indicates that fracture initiation stress decreases with increasing impact velocity, which was also observed in the quasi-static to intermediate strain rate regimes (Section 4.4.1). The decrease in fracture stress with increase in impact velocity is consistent with the negative strain-rate sensitivity in the BMG [2, 8, 9], but is contrary to the data reported by Li et al. [9] who found positive strain-rate sensitivity for similar composite, albeit at a somewhat lower strain rate. It appears that since the failure primarily occurs in the BMG phase, as observed in the micrographs of recovered impacted samples (shown earlier in Figure 5.4), the negative strain-rate sensitivity of the glass matrix has a more dominant effect on the fracture response than the positive strain-rate sensitivity of the tungsten. While the strength of tungsten may be increasing at higher rates, that of the BMG is decreasing, which becomes the increasingly weaker phase permitting fracture at lower stresses. The mechanism for this negative strain-rate sensitivity in BMGs, as explained by Li et al. [8], is due to the tendency for the growth of shear bands to be increasingly more inhibited at high loading rates, which promotes micro-cracking. Whereas shear band growth and propagation can accommodate strain and allow the material to endure higher stresses, micro-cracks lead to immediate failure at lower stresses since there is no growth phase of the crack, just immediate failure, which explains the decrease in fracture initiation stress as impact velocity is increased. Additionally, as impact velocity increases, the degree of adiabatic heating increases, causing more softening of the W particles, which lessens their effectiveness as obstacles to crack propagation through the BMG, as explained by Jiao et al. [2].

This trend of decreasing fracture stresses with increasing impact velocities is presented

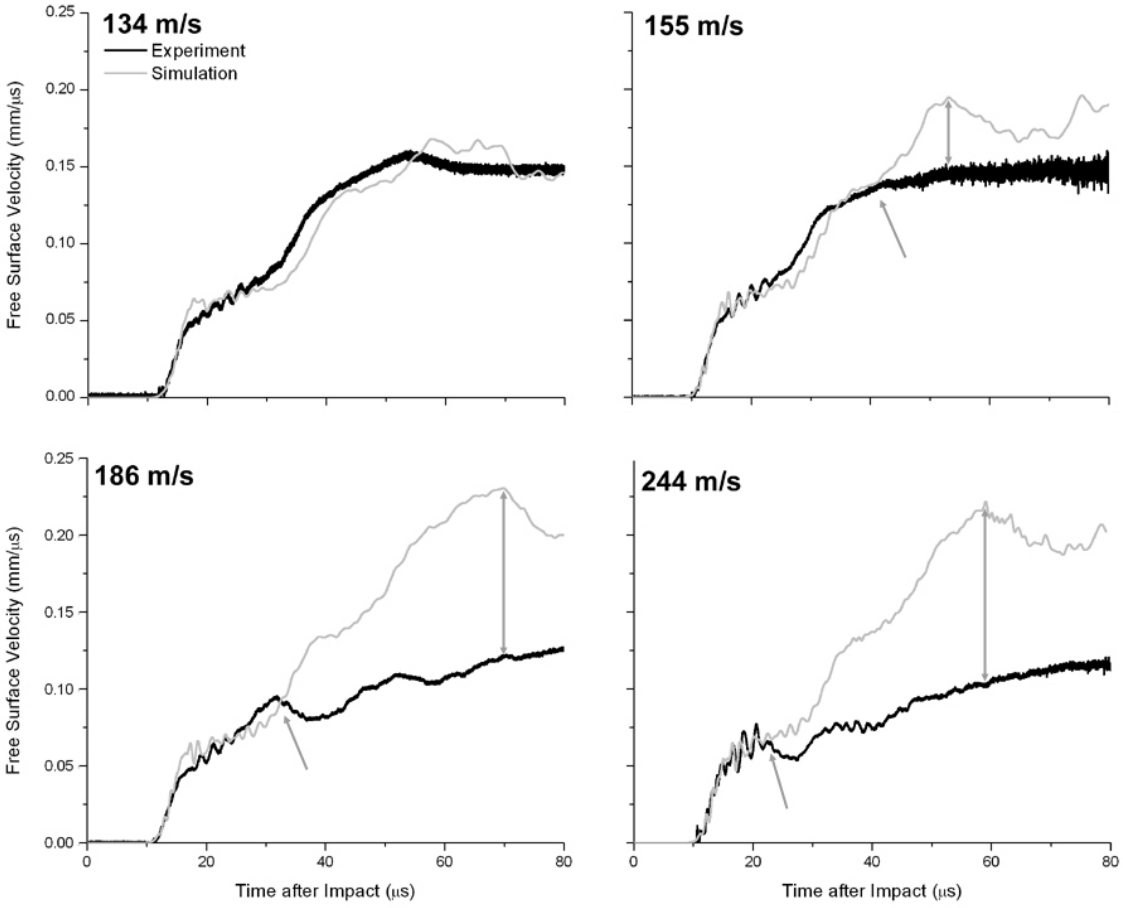

Figure 5.13: Experimental and Stassi Drucker-Prager simulated free surface velocity traces for impact at 134, 155, 186 and 244 m/s. The models show good agreement with the experiments until the occurrence of fracture. The single-headed arrows indicate the time/velocity at which fracture initiated and the double-headed arrows indicate the loss in free surface velocity due to fracture.

graphically in Figure 5.14. This figure shows a vertical dotted line at 134 m/s indicating an infinite fracture initiation stress since this specimen did not fail. It appears that the data points from the higher velocity impacts may asymptotically approach this line. The plot in Figure 5.14 also shows the yield stresses calculated from wave theory and VISAR data in Section 5.4.1.3. Yield stress increases with increasing impact velocity, as shown by the linear fit of the data. The linear fit to the yield stress data and the curve through the fracture stress data appear to be approaching one another, indicating that at even higher impact velocities, yield and fracture will happen simultaneously. Li et al. [8] suggested that shear bands initiate below the yield stress, and as strain rate increases, these shear bands immediately turn into micro-cracks due to the excess energy available, leading to failure below the yield stress.

5.5 Summary

Dynamic impact experiments performed on LM106 BMG and its composite with 70 vol% W particles have revealed microstructural deformation characteristics typical of BMGs, such as shear bands leading to cracking and evidence of localized melting caused by adiabatic heating and creation of free volume in the shear regions. The shear behavior which leads to catastrophic failure is restricted by the W particles, as evidenced by the deflection or termination of the shear bands and cracks. The W particles remained undeformed in some areas, and elongated in others, but generally did not fracture. It was observed that the W dominated the deformation response, however once the threshold of the failure regime of the BMG was reached, the fracture behavior of the composite was influenced by the BMG.

Simulations of the dynamic deformation of a W-LM106 metallic glass composite were performed using AUTODYN-2D with the Stassi Drucker-Prager model and validated by comparing simulated transient deformation profiles and sample back-surface velocity traces with those obtained from experiments. Comparison of the areal and axial strains measured

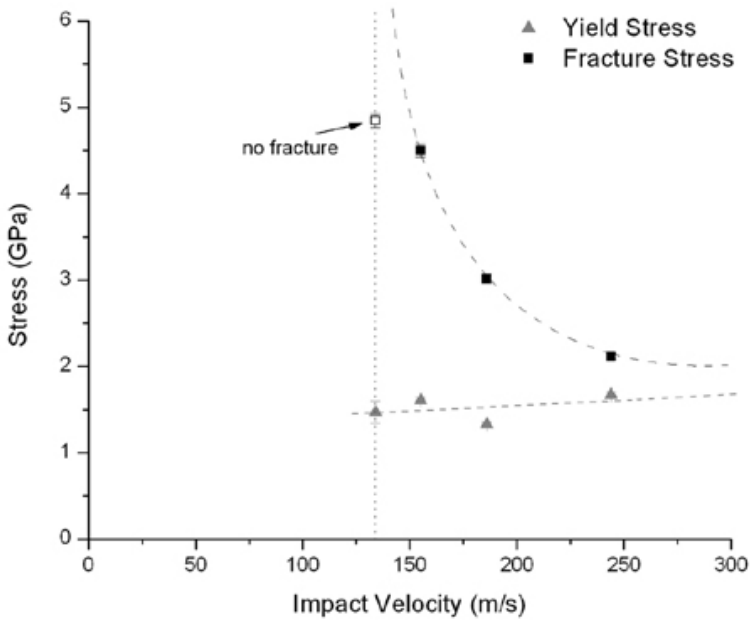

Figure 5.14: Yield stress and fracture initiation stress as a function of impact velocity. Yield stresses were obtained from wave theory and VISAR data (reported in Table 5.1). Fracture initiation stresses were measured from the point at which the simulated free surface velocity traces (no fracture) deviated from those which were experimentally measured (fracture). The value plotted for the 134 m/s experiment was the maximum stress experienced during that experiment, but fracture did not occur, so this is represented by an open symbol and dotted line, which the other data points would possibly approach asymptotically, as suggested by the dashed line (guide to the eye). It appears that as impact velocity increases, the yield stress and fracture stress approach one another.

from the experiments and the simulations showed good agreement up to the initiation of fracture, and revealed axial and areal strains to failure of ~45% and ~7%, respectively. Yield stress was found to increase with increasing impact velocity, with the deformation response being dominated by the positive strain-rate sensitivity of tungsten. However, the fracture initiation stresses were found to decrease with increasing impact velocity as a result of the fracture response being dominated by the negative rate sensitivity of the BMG matrix. Further increase in impact velocity causes fracture to occur at stresses below the yield point due to initiation of shear bands which propagate into cracks due to the large amount of available energy.

CHAPTER VI

DYNAMIC COMPRESSION OF LM106

6.1 Overview

Dynamic compression impact experiments were performed on zirconium-based bulk metallic glass (LM106) rods with a stainless steel confinement sleeve (described in Section 3.2.2). The experiments were conducted using reverse Taylor anvil-on-rod impact tests to generate strain rates on the order of 10^3 s^{-1}. High-speed digital photography was used to obtain transient images of the deformation history. VISAR velocity interferometry was used to determine the free surface velocity of the specimen's back surface during the impact event. These diagnostics provided quantitative and qualitative information about the transient deformation and failure response of the impacted specimens and allowed for correlation of the deformation path with the final, recovered geometry. The recovered, impacted specimens were analyzed using scanning electron microscopy. Numerical simulations using AUTODYN-2D finite element wave propagation code were used to elucidate the deformation and failure response of the bulk metallic glass and to better understand the effects of the altered stress states caused by the confinement sleeve. Experimental and simulated results showed a difference in deformation and failure behavior when comparing the sleeved and unsleeved specimens, with the unsleeved specimen showing catastrophic failure along many shear planes and the sleeved specimens showing failure along primarily a single shear plane.

6.2 Introduction and Motivation

The compressive behavior of BMGs has been investigated in a number of studies [19, 21, 22, 28, 31, 38, 42, 43, 72] that have shown that BMGs fail at ~43° from the loading axis,

which deviates from the maximum shear stress plane of 45°. This deviation has been the basis of the premises that BMGs exhibit a normal stress dependence [25, 31, 42–44] and that their failure does not follow the von Mises criterion [21, 28, 31, 38, 72–74], but instead a Mohr-Coulomb-type criterion [22, 31, 38, 72, 74, 75].

Because of the interest in understanding the failure criterion of metallic glasses, a few studies have investigated the effects of pressure or normal stress on yield in the quasi-static regime. Lu *et al.* [78] conducted experiments on $Zr_{41.2}Ti_{13.8}Cu_{12.5}Ni_{10}Be_{22.5}$ BMG and reported that critical shear stress is not necessarily a function of normal stress, but hydrostatic pressure (see Figure 2.27). In contrast, Lewandowski *et al.* [42, 72] reported evidence of a normal stress dependence, with no significant dependence on hydrostatic pressure, for the same BMG (see Figure 2.28). Further investigation of these effects is undoubtedly necessary; additionally, these effects have not yet been investigated in the high strain-rate regime.

The dynamic compressive behavior of BMGs has previously been explored using the Split Hopkinson Bar technique [2, 3, 8, 9, 45, 47, 49–54, 62] at strain rates up to 10^3 s^{-1}. The Taylor [57] rod-on-anvil and reverse Taylor [121, 122, 124, 126, 145, 146] anvil-on-rod impact experiments are other useful techniques for studying high-strain-rate mechanical behavior in the strain rate regime of 10^3-10^5 s^{-1}. The reverse configuration offers the advantage of simultaneous use of both high-speed photography to monitor transient deformation states and velocity interferometry to study elastic-plastic wave interactions. This combination of diagnostics allows for correlation between experiments and simulations based on strength and failure models. Additionally, Taylor test specimens are of larger bulk size than those used for Hopkinson Bar experiments, which allows for easier examination of recovered fragments and fracture surfaces. Taylor test experiments have previously been used to study the effects of radial confinement on dynamic deformation, utilizing a rod-shaped material surrounded by a metal sleeve [147, 148].

Taylor impact tests have only been used in a limited number of studies to evaluate the

dynamic mechanical behavior of bulk metallic glasses [55, 56]. Due to the limited plasticity of BMGs and the tendency for a single shear band to propagate to immediate failure, these tests did not yield any useful information about the dynamic deformation and failure mechanisms based on analysis of recovered, impacted samples. In the current work, anvil-on-rod impact experiments on BMG specimens with stainless steel confinement sleeves were used to examine the effects of the altered stress state, imposed by the surrounding sleeve, on deformation and fracture of the BMG. The confinement sleeve, which surrounds the BMG rod during deformation, provides a means of altering the stress state by imposing a radial confinement stress on the rod-shaped specimen. The sleeve also serves to "freeze" the fracture process and preserve failure planes to allow for post-impact observation and analysis.

6.3 Approach

6.3.1 Anvil-on-rod Impact Tests

Dynamic compression tests were performed using the reverse Taylor [57,121,122,124,145, 146] anvil-on-rod impact configuration instrumented with high-speed digital photography and velocity interferometry (Section 3.4.1). Sleeved specimens were impacted at 59, 98 and 131 m/s and the unsleeved BMG was impacted at 98 m/s. This choice of test conditions allowed for evaluation of the effects of impact velocity as well as those of the altered stress state caused by the confinement sleeve.

The confining stress, σ_c, imposed by the sleeve on the BMG specimen in the early stages of impact while both materials are elastically deforming can be calculated as [78]:

$$\sigma_c = \frac{\sigma\nu/E}{(\frac{b^2+a^2}{b^2-a^2}+\nu_s)/E_s+(1-\nu)/E}$$

where E and E_s are the elastic modulus of the specimen (84.7 GPa [3,4]) and sleeve, respectively, ν and ν_s are the Poisson's ratio of the specimen (0.38 [3,4]) and sleeve, respectively, a is the specimen diameter, b is the sleeve outer diameter, and σ is the axial stress in the

loading direction. The axial stresses calculated using the impedance matching technique were 0.96, 1.60, and 2.15 GPa for the 59, 98 and 131 m/s experiments, respectively. The resulting confinement stresses were calculated to be 100, 167, and 224 MPa for the 59, 98 and 131 m/s experiments, respectively. These confinement stresses are on the order of 10% of the axial stress, which is not insignificant, as will be seen later.

6.3.2 Numerical Simulations

Axisymmetric simulations of the impact experiments were performed using AUTODYN-2D. The sleeve and specimen were modeled as two separate parts with joined meshes to emulate the physical bond at the interface. This setup is believed to be representative of the interface properties. Other interface options, such as friction and creating the specimen and sleeve as one part containing two materials, were explored, but were found to misrepresent the interface properties. Use of friction only (no physical joining) between the parts led to their immediate separation, which was not representative of the events observed during the experiments, since the steel and BMG traveled at different velocities after impact. Creating the sleeve and specimen as one part filled with two different materials didn't allow for interfacial failure, as was seen in the experiments at some velocities. Thus, these two methods for describing the sleeve-specimen interface were deemed to be misrepresentative, and the physical bond at the interface was created by joining the nodes in the meshes of the sleeve and specimen.

The Al projectile and steel flyer plate were modeled using well-established parameters for the Johnson-Cook [110] and von Mises strength models, respectively. The stainless steel sleeve was modeled using the Steinberg-Guinan [142] constitutive model, for which parameters are also well-established.

The BMG was modeled using a linear equation of state (bulk modulus=118 GPa [3,4]) and the Stassi (pressure hardening) Drucker-Prager [79] strength model, owing to the

fact that many studies have shown amorphous metals to be better described by a Mohr-Coulomb-type yield criterion, as opposed to the von Mises yield criterion [21–23, 25, 28, 31, 38, 42, 45, 72–75]. The Stassi Drucker-Prager model, which was described earlier in more detail, is given as $J_{2Y} = \frac{Y_0}{3}[kY_0 + 3(k-1)p]$, where J_{2Y} is the second invariant of the deviatoric stress at yield, Y_0 is the strength in simple tension, k is the ratio between the yield strengths in compression and tension, and p is the pressure. The shear modulus, compressive strength and tensile strength were defined as 30.8 GPa, 1800 MPa, and 1200 MPa, respectively [3, 4]. The Drucker-Prager yield criterion was used with a non-associated, volume independent flow rule. Failure of the BMG was modeled using the Cumulative Damage (CD) failure criterion, in which the plastic strain at zero damage and the plastic strain at maximum damage (=1) were both defined to be 0.02. The same value of strain was chosen for both the minimum and maximum damage because it has been shown that this BMG has an elastic strain limit of 0.02 [3, 4], following which failure occurs immediately, with no plasticity. Although there is a difference in the type of strain, the 0.02 strain level was used as a descriptor for the failure threshold and was found to be an appropriate failure criterion, as will be discussed later. Finally, erosion was set for geometric strain of 1 to facilitate execution of the simulations without mesh entanglement.

The AUTODYN model setup is shown in Figure 6.1. The model utilizes an axisymmetric configuration; although the recovered specimens did not necessarily undergo symmetric failure, these simulations were used only as a tool to understand differences in stress and damage accumulation as a result of the confinement stress provided by the sleeve. A gauge placed on the back surface of the sample rod was used to monitor the free surface velocity. The deformed specimen profile generated by the simulations was captured at times corresponding to the images captured during each experiment. The simulated and experimental transient profiles and sample back (free) surface velocity traces were compared to verify the applicability of this model at all velocities and the resulting contour plots were used to better understand wave propagation and accumulation of damage in these materials.

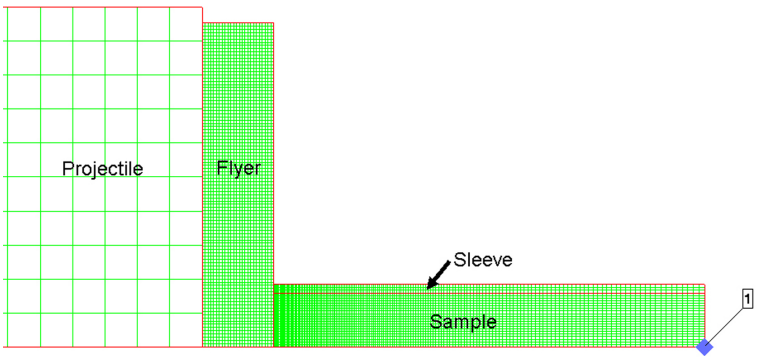

Figure 6.1: Axisymmetric problem setup and mesh in AUTODYN-2D showing the projectile, flyer, and sleeved sample. The gauge on the back (free) surface of the specimen tracks the free surface velocity.

6.4 Results and Discussion

6.4.1 Quasi-static Compression

As a baseline for comparison, the monolithic BMG was tested under uniaxial compression at a loading rate of 0.076 mm/sec, which corresponds to a strain rate of $\sim$1x10^{-4} s^{-1}. The unsleeved material showed a failure stress of 1600 MPa and an elastic limit of 1.7%. These values are slightly less than those measured by other researchers [3, 4]. The sleeved material exhibited a lower failure strength (1241 MPa) and a similar strain to failure. The reason for the failure of the sleeved material at a lower stress is likely due to defects in the material from the casting process, or from the instability of the intermetallic layer (see Figure 3.1) formed at the sleeve-specimen interface. Figure 6.2 shows photographs of LM106 specimens after failure under conditions of uniaxial quasi-static compression. The photograph on the left shows the shear failure of the unsleeved sample, whereas the photograph on the right shows failure of specimens that were tested with a steel confinement sleeve (which was removed after the compression to examine the fracture behavior). All specimens failed along one primary shear plane oriented at $\sim$43° to the loading axis, which was expected based on previous results in the literature [19, 21, 22, 28, 31, 38, 42, 43, 45, 72]. The unsleeved specimen showed some additional failure near the top of the specimen, whereas

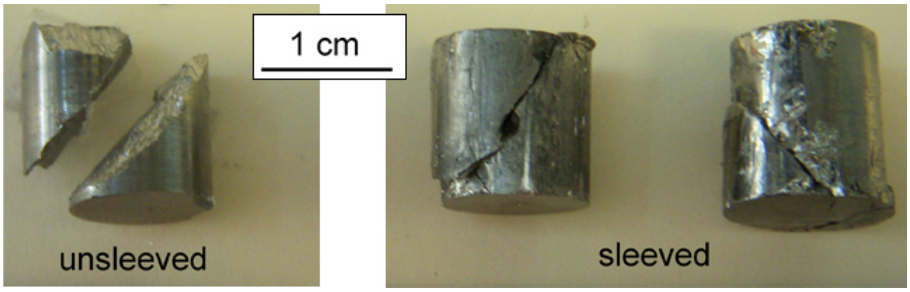

Figure 6.2: Photographs of unsleeved and sleeved (after sleeve removal) specimens showing failure along one primary shear plane oriented ~43° to the loading axis after quasi-static compression. The unsleeved specimen shows some additional failure aside from its primary failure plane, whereas all failure of the sleeved specimens was confined to one plane.

the failure in the sleeved specimens was confined to only the primary shear plane.

6.4.2 Imaging Transient Deformation

An Imacon-200 high-speed camera captured 16 images of transient deformation during each impact experiment. Examples of some of these images from three different experiments are shown in Figure 6.3, where the projectile and flyer are accelerating from the left to impact the rod-shaped specimen, which is centered in the image. The figure shows four of 16 images (at different times) from the sleeved 59 and 98 m/s experiments and the unsleeved 98 m/s experiment. These images allowed for evaluation of the effect of the confinement stress caused by the sleeve as well as the effect of impact velocity on deformation and failure of the BMG. Figure 6.3(a) shows images captured during 59 m/s impact of a sleeved specimen. These images show no noticeable deformation in the sleeve. As seen in Figure 6.3(b), impact of a sleeved BMG at 98 m/s produces a bulge (indication of deformation in the BMG) in the sleeve as early as 13 μs after impact. The bulge only protrudes on one side (top side of specimen in images) of the rod, which indicates that the BMG is failing by shear deformation at ~45° to the loading axis, as has been seen during quasi-static compression tests of BMGs with imposed pressure [42,72]. Figure 6.3(c) clearly shows the failure of the unsleeved BMG (also impacted at 98 m/s) since there is no sleeve obstructing

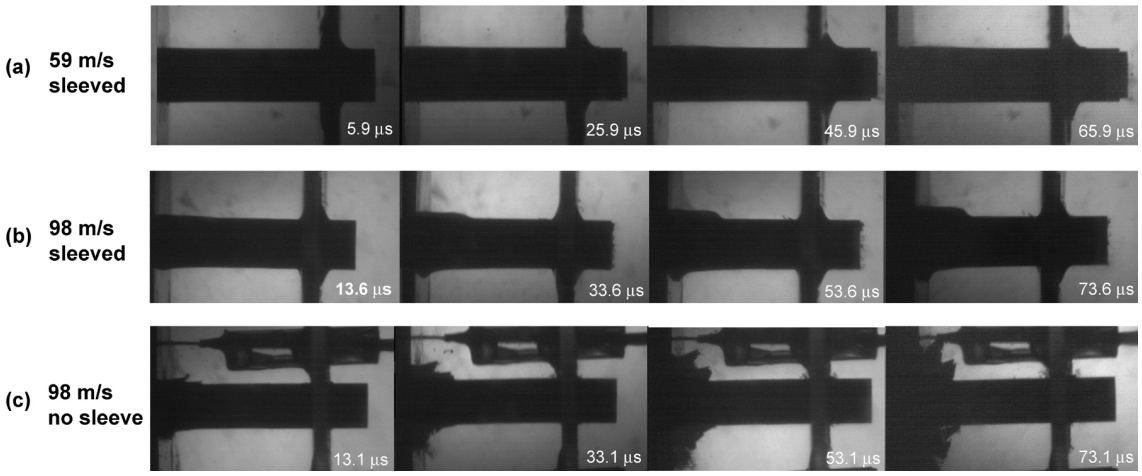

Figure 6.3: Four of 16 high-speed images captured during reverse Taylor impact experiments. (a) Sleeved specimen impacted at 59 m/s, showing no noticeable deformation in the sleeve. (b) Impact of a sleeved BMG at 98 m/s produces a bulge (indication of deformation in the BMG) in the sleeve as early as 13 μs after impact. The bulge only protrudes on one side (top side of specimen in images) of the rod, which indicates that the BMG is failing by shear deformation at ~45° to the loading axis, as has been seen during quasi-static compression tests of BMGs with imposed pressure [42, 72]. (c) Impact of unsleeved specimen at 98 m/s showing failure since there is no sleeve obstructing the view. Fractured fragments appear to have formed by shear on multiple planes, revealing that without the confinement of the steel sleeve, impact at 98 m/s results in catastrophic failure.

the view. Fractured fragments appear to have formed by shear on multiple planes, revealing that without the confinement of the steel sleeve, impact at 98 m/s results in catastrophic failure.

6.4.3 Characterization of Recovered, Impacted Specimens

Photographs of the recovered, impacted specimens are shown in Figure 6.4. Figure 6.4(a) shows all three sleeved specimens, clearly illustrating the effects of impact velocity on deformation and failure. The sleeved specimens were used to learn about the failure of the BMG under dynamic conditions since the sleeves provide a means of "freezing" the fracture of the BMG, giving insight into its failure mechanisms. At 59 m/s, the steel sleeve remained essentially undeformed, and the BMG fractured near the impact end along one primary shear plane. As a result of 98 m/s impact, the steel sleeve showed a bulge and a

tear. The BMG fractured, which was evident from the bulge in the sleeve. At 131 m/s, the steel sleeve tore and peeled back, and the impact end of the BMG was completely fractured. The impact face of the specimen fractured off in a cone shape (fragment marked by arrow in Figure 6.4(a)). Figure 6.4(b) shows a side-by-side comparison of the sleeved and unsleeved specimens that were impacted at 98 m/s. In contrast to the sleeved sample, the unsleeved specimen shows that the impact end completely fractured into many pieces and the length of the rod showed several fracture planes perpendicular to the loading axis. This difference was seen to a lesser extent with the quasi-statically compressed specimens shown in Figure 6.2, with the failure of the sleeved specimens confined completely to a single plane and the unsleeved specimen showing only minor additional failure aside from its primary failure plane.

Figure 6.5 shows schematics and corresponding photographs of the deformation and failure of the sleeved specimens. In Figure 6.5(a), which shows the deformation caused by the 59 m/s impact, it can be seen that the steel sleeve remained undeformed, but the BMG inside the sleeve fractured. This fracture occurred primarily along a single plane oriented at 42.5° to the loading axis, which is the same as the failure angle in static tests and is comparable to the failure angle that has been observed in other studies of BMGs under compression [25, 31, 42–44]. A photograph of the corresponding fractured piece is also shown in Figure 6.5(a). Figure 6.6 shows SEM micrographs of the fracture surfaces of the sleeved BMG which was impacted at 59 m/s. Figure 6.6(a) shows the fracture surface which was oriented 42.5° from the loading axis; this fracture surface reveals the uniform veinal pattern which is typical of BMG failure in compression [28]. This veinal pattern is very well-developed and highly organized, in contrast to that observed on the fracture surface of the specimen impacted at 131 m/s (Figure 6.7). Figure 6.6(b) shows the fracture surface that was oriented parallel to the impact surface of the specimen. This surface shows a dimple structure, which is an indication of ductility [149]. Although this material is quite brittle, there are signs of localized plasticity. It cannot be stated conclusively whether this

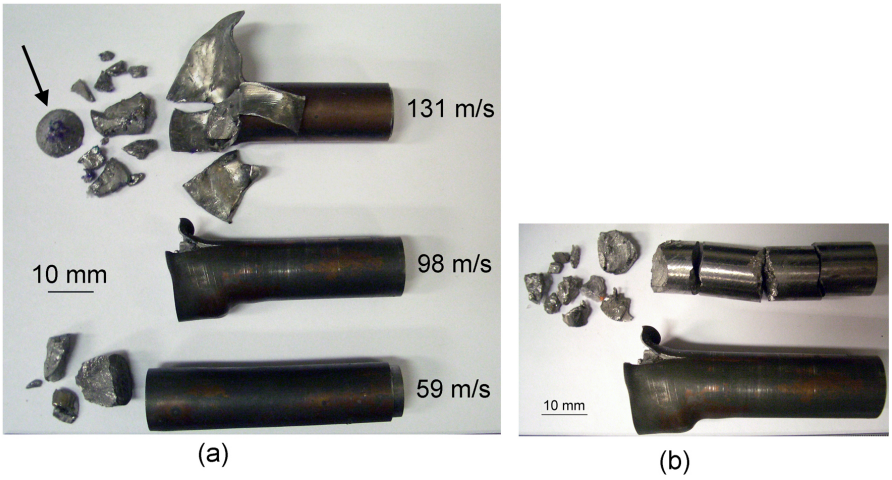

Figure 6.4: (a) Sleeved specimens recovered after Taylor impact of all three sleeved specimens, clearly illustrating the effects of impact velocity on deformation and failure. At 59 m/s, the steel sleeve remained essentially undeformed, and the BMG fractured near the impact end along one primary shear plane. As a result of 98 m/s impact, the steel sleeve showed a bulge and a tear. The BMG fractured, which was evident from the bulge in the sleeve. At 131 m/s, the steel sleeve tore and peeled back, and the impact end of the BMG was completely fractured. The impact face of the specimen fractured off in a cone shape (fragment marked by arrow). (b) Sleeved and unsleeved specimens impacted at 98 m/s, showing a side-by-side comparison of the sleeved and unsleeved specimens that were impacted at 98 m/s. In contrast to the sleeved sample, the unsleeved specimen shows that the impact end completely fractured into many pieces and the length of the rod showed several fracture planes perpendicular to the loading axis.

fracture surface (parallel to impact face) was created as a result of the wave propagation within the rod after impact or whether it fractured as a result of secondary impact in the catch tank. This will be discussed further in a later section in conjunction with simulation results.

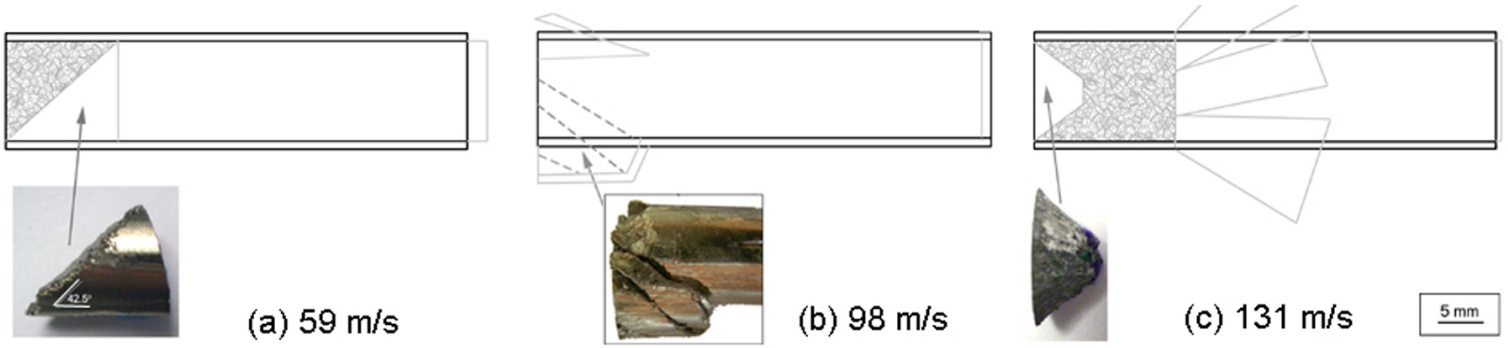

Figure 6.5: Schematics of the deformation of the sleeved specimens impacted at (a) 59, (b) 98 and (c) 131 m/s. Also shown are corresponding photographs of portions of the fractured BMG rods. Black lines indicate starting sleeve/specimen configurations and gray lines indicate fracture and final/recovered configurations. In (a), it can be seen that the steel sleeve remained undeformed, but the BMG inside the sleeve fractured. This fracture occurred primarily along a single plane oriented at 42.5° to the loading axis. 98 m/s impact (b) resulted in three parallel shear planes, and 131 m/s impact (c) resulted in formation of a cone at the impact face and many small fragments behind it.

The schematic and corresponding photograph of the deformation and failure of the sleeved specimen impacted at 98 m/s is shown in Figure 6.5(b). The solid gray lines indicate the tearing in the steel sleeve and the dashed gray lines indicate the approximate locations of the shear planes in the BMG rod. The photograph of the impact end of the rod (after the sleeve was removed) is shown below the schematic. Because the steel sleeve held the BMG in place, the shear planes were preserved for recovery and analysis. There were found to be three dominant shear planes, all at approximately 45° to the loading axis.

Figure 6.5(c) shows the schematic outline of the cone-shaped piece that fractured off the impact face of the BMG during impact at 131 m/s. The symmetry of the failure is not unexpected and is a result of the buildup of shear stresses originating at the BMG-sleeve interface. This does bring up the question of why, then, did the other specimens not fail symmetrically? It can be theorized that all shear bands have an equal opportunity to propagate in order to accommodate strain, and the first one to successfully propagate often provides adequate strain accommodation. Since compressive failure along one plane (~42-46° to the loading direction [25, 31, 42–44]) has been commonly seen during mechanical testing of BMGs, this would then suggest that BMGs respond inhomogeneously, allowing for propagation of one shear band to be more favorable than the propagation of any other. It appears that the specimen impacted at 131 m/s was subjected to large strain such that a single shear plane was not sufficient, and shear along multiple planes began propagating simultaneously, resulting in cone formation. This rationale then does not explain why the sleeved specimen impacted at 98 m/s fractured along three parallel planes. It is likely that the deformation of bulk metallic glasses and the number and orientation of shear bands is highly sensitive to the subtle, localized variations in free volume distribution or atomic arrangements, different combinations of which could promote or inhibit shear band nucleation and propagation in different orientations. However, this issue requires further investigation and possibly additional experiments.

The fracture surface of the convex conical fracture surface at the impact face of the

specimen impacted at 131 m/s was examined with SEM to gain insight into the failure mechanism. Figure 6.7(a) shows the veinal pattern typical of compressive deformation in BMGs and Figure 6.7(b) shows ductile features (dimple pattern), both of which were observed on the surface of this cone-shaped fractured piece, but at two different locations. Again, we see evidence of the large amount of localized plasticity although the BMG is a macroscopically brittle material. It should be noted that in comparison with the fracture surfaces from the 59 m/s experiment (Figure 6.6), these fracture surfaces show less homogeneity, and the veinal structures are not as well developed. This trend was also observed in other work on dynamically tested specimens that failed along multiple planes [45, 47, 50]. Under dynamic conditions, more rough fracture surfaces (in comparison to fracture surfaces generated under static conditions) containing disorganized and randomly oriented veinal patterns and liquid droplets were observed. Subhash et al. [47] explained the lesser degree of homogeneity during more rapid loading by the minor fluctuations in the stress and temperature fields which are associated with the inherent defects (voids or impurities) in the material or the minor variations in chemical composition within the microstructure. This theory could also explain the differences in macroscopic failure between different specimens.

6.4.4 Correlation of Simulations with Experimental Results

Figure 6.8 shows results of simulations performed with AUTODYN-2D illustrating pressure, shear stress, and damage contour plots (impact end, axisymmetric sections) at three times during impact of unsleeved BMG at 98 m/s and sleeved BMG at 98 and 131 m/s. The images show the evolution of pressure/shear stress/damage (strain), and subsequent failure. Comparison of the two 98 m/s simulations performed on sleeved and unsleeved samples shows the effect of the confinement stress imposed by the steel sleeve on the strain experienced by the BMG. It is clear from these countour plots that the sleeve is changing the stress distribution within the specimen rod, thus changing the location and orientation of failure

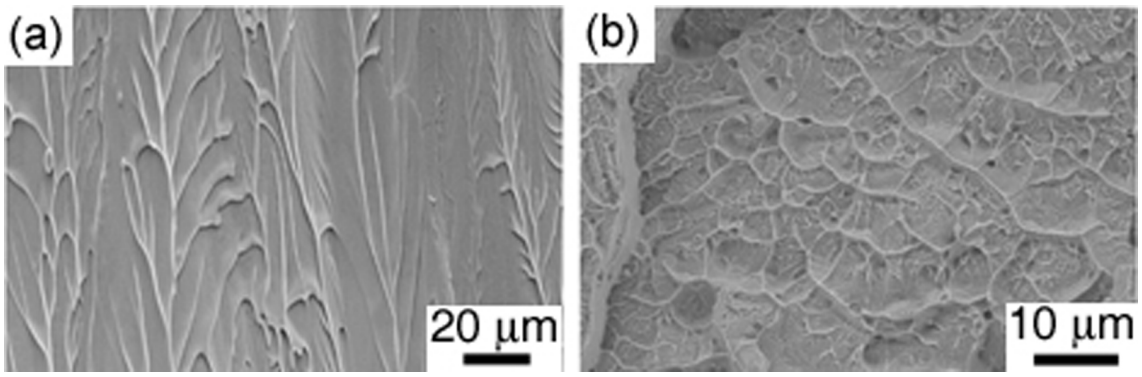

Figure 6.6: Micrographs of fracture surfaces created during impact at 59 m/s. (a) Shear fracture plane created at 42.5° to the loading axis showing veinal pattern typical of compressive failure. (b) Fracture surface perpendicular to the loading axis showing dimple structure. Rough fracture surfaces, containing disorganized and randomly oriented veinal patterns and liquid droplets, are often observed under dynamic conditions due to more rapid loading by the minor fluctuations in the stress and temperature fields which are associated with the inherent defects (voids or impurities) in the material or the minor variations in chemical composition within the microstructure [47].

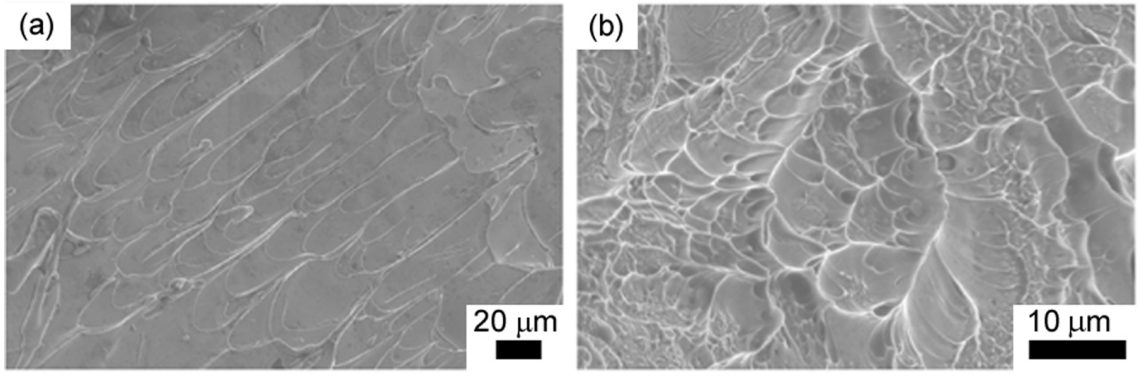

Figure 6.7: Micrographs of two different locations on the conical fracture surface created during impact at 131 m/s showing (a) veinal pattern and (b) dimple structure.

plane(s). It can be seen from the shear stress and damage contours (Figure 6.8 (b) and (c)) that the sleeved specimen primarily fractures at approximately 45° to the loading axis (as seen in the recovered specimen shown in Figure 6.5(b)), whereas the unsleeved specimen has multiple fracture planes and the entire impact end of the rod essentially crumbles, as seen in the recovered specimen in Figure 6.4(b). The unsleeved specimen shows accumulation of damage on several planes perpendicular to the loading axis since the tension generated from the radial release is not counteracted by radial confinement. The locations and orientations of this accumulation of strain/damage correspond to the fracture observed on the recovered specimen, which had fractured along many planes perpendicular to the loading direction. The specimen recovered after the 131 m/s impact showed the formation of a cone at the impact face. This is also seen in the corresponding simulation, which shows high shear stress and damage zones originating at the sleeve-specimen interface at the impact face and propagating toward the center of the specimen rod at an angle of ~45° and eventually cracking along these zones of maximum damage. The overlay of the simulation on the photograph of the recovered sample in Figure 6.8 provides a clear illustration of damage resulting in the cone-shaped failed section at the impact face of the rod-shaped specimen.

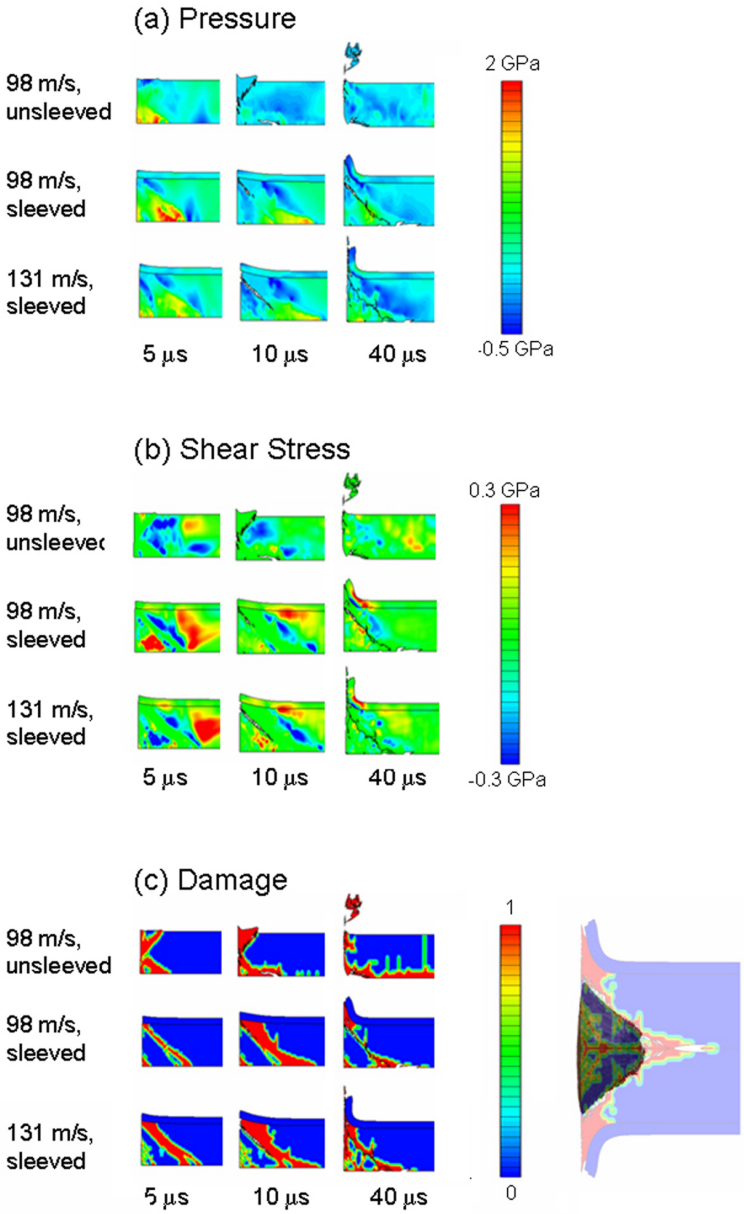

Figure 6.8: Simulated axisymmetric half-sections of the impact end of the rod showing (a) pressure, (b) shear stress, and (c) damage (strain) at 5, 10 and 40 μs after impact of sleeved and unsleeved BMG at 98 m/s and sleeved BMG at 131 m/s. Contours show the development of the respective variables with time and indicate the locations where shear stress is at a maximum. Also shown in (c) is a damage plot (using symmetry to get the full diameter of the rod) of the sleeved specimen impacted at 131 m/s overlayed on a photograph of the cone-shaped fragment recovered after impact. These show agreement in fracture location and angle between experiments and simulations.

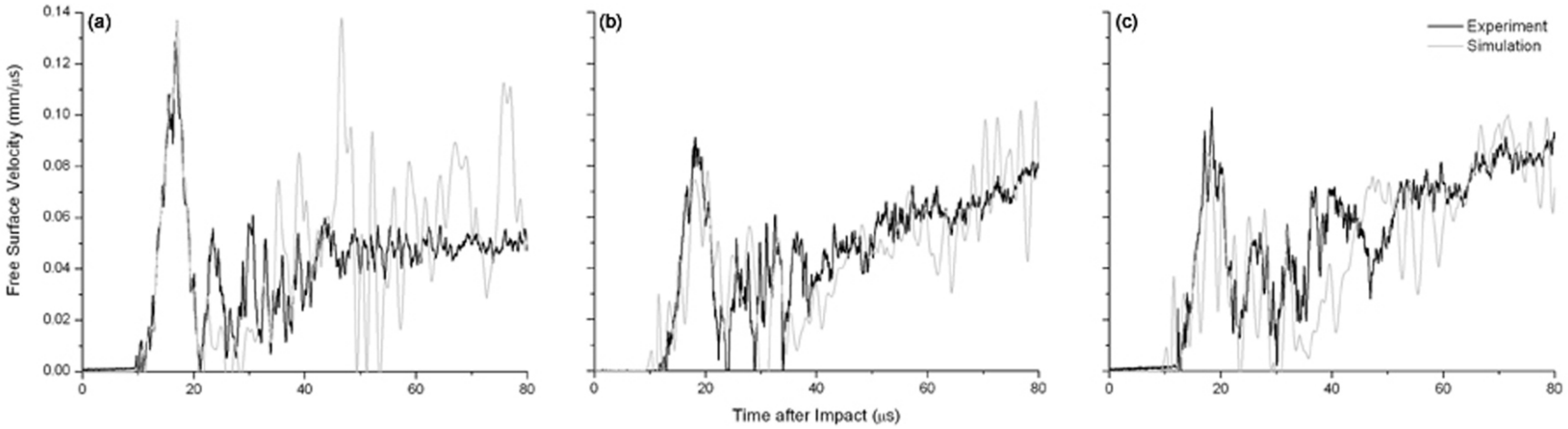

Figure 6.9: Experimental (black) and simulated (gray) free surface velocity traces from (a) impact of unsleeved BMG at 98 m/s, (b) sleeved BMG at 98 m/s and (c) sleeved BMG at 131 m/s. These traces show a steep rise to peak free surface velocity, followed by a steep drop. The drop in free surface velocity is due to fracture of the specimen. It can be seen that use of the Cumulative Damage failure criterion with a strain threshold of 0.02 was able to reproduce the measured free-surface velocity traces fairly well. Although the match beyond the initial peak velocity and subsequent drop is not perfect, the main features, including the arrival time, steep rise, peak magnitude and steep drop, are evident in the simulation. These correlations indicate agreement in elastic-plastic properties and fracture initiation time as well as strain level at fracture initiation. The differences at later times are due to differences in wave reverberations within the fractured specimen, but this can be a factor of erosion, mesh size, and other such non-physical variables, refinement of which was beyond the focus of this work.

The sample back (free) surface velocity trace obtained from VISAR during impact of the sleeved and unsleeved BMGs at 98 m/s as well as the sleeved BMG at 131 m/s and the corresponding simulated traces are shown in Figure 6.9. These traces show a steep rise to peak free surface velocity, followed by a steep drop. The drop in free surface velocity is due to fracture of the specimen, much like that seen in a VISAR trace from a spall experiment [150]. The failure in these experiments was compressive, however, and use of the Cumulative Damage failure criterion with strain threshold of 0.02 was able to reproduce the measured free-surface velocity traces fairly well, as shown in Figure 6.9. Although the match beyond the initial peak velocity and subsequent drop is not perfect, the main features, including the arrival time, steep rise, peak magnitude and steep drop, are evident in the simulation. These correlations indicate agreement in elastic-plastic properties and fracture initiation time as well as strain level at fracture initiation. The differences at later times are due to differences in wave reverberations within the fractured specimen, but this can be a factor of erosion, mesh size, and other such non-physical variables, refinement of which was beyond the focus of this work. Overall, the qualitative match of the simulations in terms of fracture path and free surface velocity was quite good, indicating that the pressure-hardening Drucker-Prager yield criterion coupled with the Cumulative Damage failure criterion (strain threshold of 0.02) describes the deformation and failure of the monolithic BMG reasonably well.

6.5 Summary

Reverse Taylor anvil-on-rod impact experiments were performed on LM106 BMG specimens, both with and without a 316 stainless steel confinement sleeve. Analysis of recovered specimens showed compressive failure on shear planes oriented approximately 42-43° from the loading axis in sleeved specimens impacted at 59 and 98 m/s. The unsleeved BMG underwent catastrophic failure near the impact end as a result of impact at 98 m/s. The sleeved specimen impacted at 131 m/s fractured in a cone shape due to the stress from the sleeve;

this fracture was symmetrical, as may have been expected in all experiments, but was not seen possibly due to localized inhomogeneities in the material. The differing shear band configurations (symmetrical vs. parallel bands) from one specimen to another is a topic which requires further investigation, but is most likely due to variations in local structure. Numerical simulations showed the differences in accumulation of pressure, shear stress, and strain, which led to varying degrees of damage in sleeved and unsleeved specimens. In the sleeved specimens, cracks formed primarily along one shear plane at approximately 43° to the loading axis, which was seen in the recovered specimens. Simulation of impact of the unsleeved specimen showed greater amounts of damage and fracture along multiple directions at the impact end of the rod, as was seen in the experiment. Simulated free surface velocity traces matched well with those from experiments, providing additional validation of the failure criterion and simulated images of the transient state deformation and failure response of bulk metallic glasses.

CHAPTER VII

HIGH PRESSURE EQUATION OF STATE AND PHASE STABILITY OF LM106

7.1 Overview

This chapter reports and discusses investigations aimed at determining the equation of state of monolithic $Zr_{57}Nb_5Cu_{15.4}Ni_{12.6}Al_{10}$ BMG and understanding its phase stability and possibility of stress-induced transformations at high stresses [151]. The phase stability of this, or any, BMG has not previously been studied under these extreme conditions. The high pressure U_s-U_p Hugoniot equation of state of LM106 BMG was determined using plate impact experiments on disk-shaped samples of 10 mm diameter and 2 mm thickness. The National Institute for Materials Science (NIMS) two-stage light-gas gun was utilized for the high stress measurements (~26-123 GPa) and the Georgia Institute of Technology (GT) single-stage gas gun was utilized for the measurements at lower stresses (~5-26 GPa). NIMS experiments were instrumented with streak photography and utilized the inclined mirror method to simultaneously measure shock velocity and particle velocity obtained from free surface velocity measurements. GT experiments utilized polyvinylidene fluoride (PVDF) stress gauges and velocity interferometry (VISAR) to simultaneously measure the input stress, shock velocity, and free surface velocity. Results from the streak camera records and PVDF gauges combined with VISAR traces, as well as impedance matching calculations, were used to generate the U_s-U_p Hugoniot equation of state for the bulk metallic glass over a wide range of stresses up to ~123 GPa. The U_s-U_p data shows evidence of a low pressure phase, a transition to a mixed phase region at ~26 GPa, followed by transition at ~67 GPa to a high pressure phase of bulk modulus of 288 GPa, which is higher than that

of the starting material.

7.2 Introduction and Motivation

Several previous studies have investigated stress and strain-rate induced crystallization (discussed in Section 2.5.2) and possibilities of high-pressure phase transformations in BMGs (Section 2.5.3). The current work aims to investigate the shock wave response, phase stability and U_s-U_p equation of state of LM106 bulk metallic glass up to pressures far exceeding those previously investigated for any amorphous metal system. In order to determine the relationship between pressure, P, particle velocity, U_p, shock velocity, U_s, specific volume, V, and density, ρ, an equation of state relating U_p and U_s must be determined and evaluated along with the expressions for conservation of mass, momentum, and energy. Determination of this EOS data and changes in the observed $U_s - U_p$ trend will provide evidence of phase transformations occurring in this BMG under high pressure conditions.

7.3 Experimental Approach and Results

Equation of state experiments performed at Georgia Tech were instrumented with PVDF gauges and VISAR, as described in Section 3.5.1.1. Experimetns performed at NIMS were instrumented with streak photography and the inclined mirror method, as described in Section 3.5.1.2. The details of the setup for each experiment are given in Table 7.1, and the equation of state data obtained from each corresponding experiment is summarized in Table 7.2.

Table 7.1: Summary of experimental details including shot number, impact velocity, measurement techniques utilized, and flyer and driver materials for equation of state experiments.

Shot No.	Impact Velocity (m/s)	Measurement Technique[1]	Flyer Material	Driver Material
0706	0.346	PVDF(i,p)+VISAR	Cu	Cu
0675	0.412	PVDF(i)+VISAR	WHA	304SS
0701	0.677	PVDF(i,p)+VISAR	WHA	304SS
0676	1.047	PVDF(i)+VISAR	WHA	304SS
202	3.015	streak camera	304SS	304SS
201	3.149	streak camera	304SS	Al
209	3.583	streak camera	304SS	304SS
206	4.125	streak camera	304SS	304SS
208	4.664	streak camera	304SS	304SS

[1]Some experiments instrumented with PVDF gauges utilized a gauge to measure the input stress and another to measure the propagated stress (i,p), whereas other experiments utilized only an input gauge (i). When both input and propagated gauges were used, the travel time of the shock wave through the sample was obtained from the activation time of each of the two gauges; when only an input gauge was used, the VISAR trace was used to determine the arrival time of the shock wave at the back of the sample.

Table 7.2: Summary of equation of state data (pressure, showck velocity, particle velocity, and density). Both experimentally measured values and those calculated using impedance matching are reported (in separate columns). Experiments showing a two-wave structure have two sets of data listed. Impedance matching calculations were done for the second wave in the case of experiments showing a two-wave structure. Error was calculated using maximum possible deviations for U_s and U_p and error propagation analysis [152, 153] (derived in Appendix B.2 for P, ρ and impedance matching calculations.

Shot No.	P (GPa)		[1] U_s (km/s)	U_p (km/s)		ρ (g/cm^3)	
	Expt.	Imp. Match	Expt.	Expt.	Imp. Match	Expt	Imp. Match
0706	5.39±0.29	6.18±0.13	5.10±0.10	0.18±0.01	0.18±0	6.95±0.02	6.95±0.14
0675[2]	6.61±0.29	N/A	4.68±0.1	0.22±0.01	N/A	7.04±0.03	N/A
	8.02±0.29	8.62±0.21	4.30±0.10	0.27±0.01	0.30±0.01	7.03±0.03	7.20±0.17
0701[2]	7.10±0.29	N/A	4.99±0.10	0.24±0.01	N/A	7.04±0.03	N/A
	12.76±0.29	14.67±0.44	4.58±0.10	0.43±0.01	0.48±0.01	7.20±0.03	7.48±0.23
0676	21.21±0.29	26.52±0.45	5.97±0.10	0.72±0.01	0.63±0.01	7.62±0.03	7.54±0.13
202[3]	50.79±8.10	N/A	5.90±0.20	1.28±0.20	N/A	8.56±0.30	N/A
	74.07±9.00	*67.46±2.39*	*5.74±0.20*	*1.93±0.20*	*1.71±0.06*	*10.08±0.50*	*9.42±0.33*
201	26.06±7.86	42.53±1.48	5.83±0.20	0.67±0.20	1.09±0.04	7.57±0.38	8.24±0.29
209	115.11±9.83	84.57±2.76	6.22±0.20	2.76±0.20	2.03±0.07	12.04±0.55	9.94±0.32
206	114.28±9.13	104.2±3.14	6.73±0.20	2.55±0.20	2.31±0.07	10.77±0.45	10.20±0.31
208	105.55±9.82	122.51±3.56	6.96±0.20	2.26±0.20	2.63±0.08	9.92±0.76	10.75±0.31

[1] Stress was measured using PVDF/VISAR experiments and calculated from U_s and U_p for the streak camera experiments.

[2] These experiments showed the HEL in the VISAR trace, so a two wave structure was considered, and thus there are two sets of data for these shots.

[3] This experiment showed a change in slope indicative of a phase transformation in the streak record, thus there are two sets of data for this experiment. The data from the second wave is italicized because this is the only experiment which showed an apparent phase change in the high stress regime, thus it cannot be stated conclusively that this second phase exists and it is not included in the plot in Figure 7.5.

7.3.1 PVDF Stress Gauge + VISAR Velocity Interferometry Data

The stress traces obtained by the input PVDF gauges from each experiment are shown in Figure 7.1. It can be seen that these stress traces show considerable dispersion in the shock front in the rising part of the waveform, and this is expected in amorphous materials due to the negative first pressure derivative of elastic modulus [67], as discussed in Section 2.5.3. Because of this dispersion, however, the magnitude of the input stress could not be precisely determined using this method. Instead, the shock stress was estimated from the U_{fs} ($\sigma = \frac{1}{2}\rho_0 C_0 U_{fs}$ [150]) obtained from the VISAR traces as well as from impedance matching calculations. The stress values calculated using impedance matching, are indicated with arrows on the y-axis of Figure 7.1. The travel time of the shock wave through the thickness of each sample was determined using the activation times of the input and propagated voltage traces (less time of travel through PVDF gauge package), where applicable, or the activation times of the input voltage and VISAR trace (shown in Figure 7.2). This travel time was used with sample thickness to determine shock velocity (U_s). The experimentally determined values of U_s, U_p, and P are listed in Table 7.2.

Velocity interferometry using the VISAR was utilized to measure the free surface velocity of the BMG specimens in order to monitor the free surface velocity and determine the shock response of the BMGs. The free surface velocity traces for Shots 0675, 0676, 0701 and 0706 are shown in Figure 7.2. The particle velocities (U_p) obtained from free surface velocity (U_{fs}) traces according to Equation 16 are listed in Table 7.2.

The free surface velocity traces from Shots 0675 and 0701 also show the existence of a distinct two-wave structure indicative of a possible elastic-plastic transition in the response. These two traces show an elastic precursor, corresponding to the Hugoniot Elastic Limit (HEL), and a peak at the elastic front. The stress at the HEL represents the maximum normal stress that a material can withstand under one-dimensional compressive strain without internal rearrangement taking place at the shock front [134]. The elastic peaks are followed by a steeply rising plastic wave and a transition to the final plateau. The

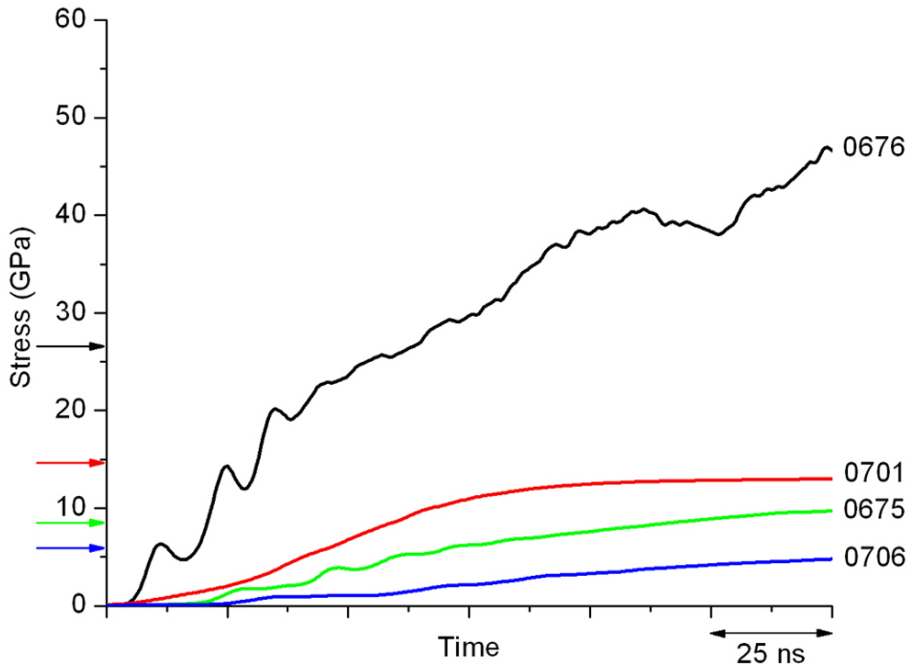

Figure 7.1: PVDF stress traces from Georgia Tech EOS experiments. These stress traces show considerable dispersion in the shock front in the rising part of the waveform due to the negative first pressure derivative of elastic modulus of amorphous materials [67]. Corresponding stress values calculated using impedance matching are indicated with arrows on the y-axis.

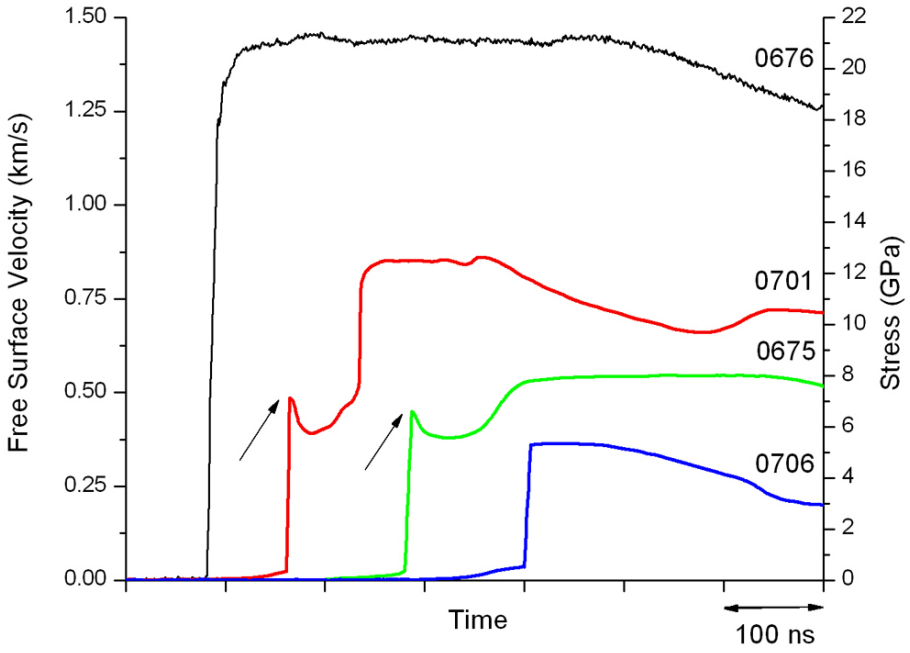

Figure 7.2: VISAR free surface velocity traces traces from Georgia Tech EOS experiments. The free surface velocity traces from Shots 0675 and 0701 show the existence of a distinct two-wave structure indicative of a possible elastic-plastic transition in the response. These two traces show an elastic precursor, corresponding to the Hugoniot Elastic Limit (HEL), and a peak at the elastic front. HEL points are indicated with arrows. The elastic peaks are followed by a steeply rising plastic wave and a transition to the final plateau. The σ_{HEL} values obtained from the free surface velocity traces ($\sigma = \frac{1}{2}\rho_0 C_0 U_{fs}$ [150]) from these two experiments were 6.61 GPa and 7.10 GPa, respectively, with an average value of 6.86 GPa.

σ_{HEL} values obtained from the free surface velocity traces ($\sigma = \frac{1}{2}\rho_0 C_0 U_{fs}$ [150]) from these two experiments were 6.61 GPa and 7.10 GPa, respectively, with an average value of 6.86 GPa. This is comparable to the values reported by Turneaure et al. [66] and Yuan et al. [64] for similar BMGs. The measured stress values correspond to ~4.8% elastic strain, which is in agreement with the ~4% elastic strain reported by Turneaure et al. [66]. These VISAR traces show characteristics typical of an ideal elasto-isotropic solid, in which shear strength is catastrophically lost above the HEL [67]. Similar to what was observed by Yuan et al. [64], the peak at the elastic precursor front seen in the VISAR traces (Figure 7.2) becomes sharper with increasing impact velocity (from 412 m/s to 677 m/s), as is typical for shock wave measurements on elasto-isotropic solids lacking strain-hardening capability [64, 67], as has been previously discussed in Section 2.3.2.6.

7.3.2 Streak Camera Images

The streak camera images obtained from the high stress experiments performed at NIMS are shown in Figure 7.3. A schematic of the setup showing the mirrors mounted on the specimen, and the streak image from Shot 202, aligned with the schematic as an example, is shown in Figure 7.3(a). It can be seen that the extinction times of the flat mirrors can be clearly measured. Close examination of the streak from the inclined mirror (IM) shows that there are two slopes, as indicated in the inset. The change in slope is indicative of a phase transformation. The streak images from Shots 201, 206, 208 and 209 are shown in Figure 7.3(b), (c), (d) and (e), respectively. The $U_s$and U_p values determined from these images are reported in Table 7.2.

7.3.3 Analysis of Data

All experimental data are summarized in Table 7.2. Also reported in the table are values of density and pressure which were calculated using the Rankine-Hugoniot conservation equations [103]. (Pressure values were calculated for the streak camera experiments and measured in the PVDF/VISAR experiments.) Experiments which showed a two-wave

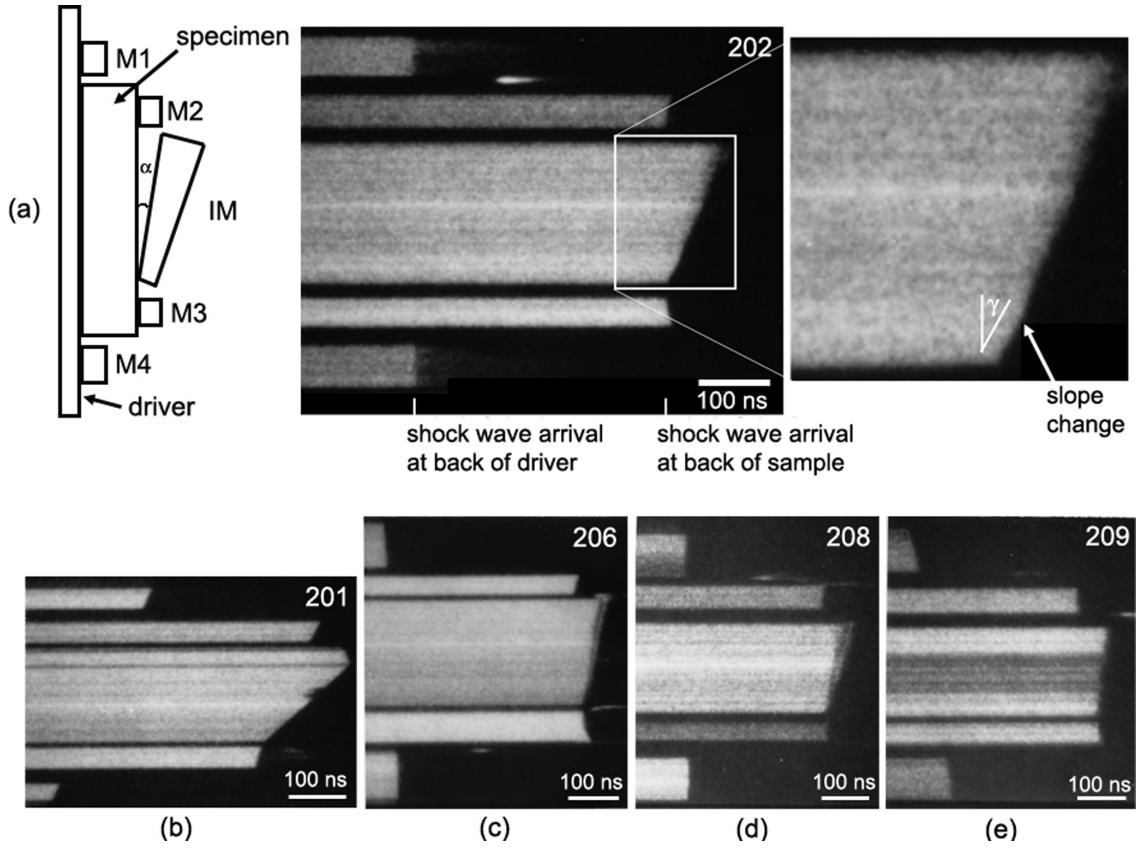

Figure 7.3: Streak camera images. (a) Schematic of driver plate+specimen+mirror setup showing flat mirrors (M1-M4) and an inclined mirror (MI). The corresponding streak image from Shot 202 is also shown. The inset shows a change in slope in the streak image, which is indicative of a phase transition. (b) Streak record from Shot 201, (c) Streak record from Shot 206, (d) Streak record from Shot 208, and (e) Streak record from Shot 209.

structure in the form of an HEL (Shots 0675 and 0701) or possible phase transformation (Shot 202) have two sets of data listed. Each final-state data point also has a corresponding value determined using the impedance matching method [103, 135]. The impedance matching calculations were performed by calculating the pressure at the flyer/driver interface according to:

$$P = \rho_0[C_0 + S(V - U_p)](V - U_p), \tag{22}$$

which is derived from the conservation equations (Equations 11,12,14). In this equation, V is impact velocity. Next, pressure at the driver/sample interface was calculated over a range of particle velocities according to:

$$P = \rho_0[C_0 + S\,U_p]U_p, \tag{23}$$

Values for C_0 and S are well-known for commonly used flyer and driver materials including Al, steel, tungsten, etc. Next, the pressure in the specimen was calculated according to:

$$P = \rho_0 U_s U_p, \tag{24}$$

with only the shock velocity and impact velocity being measured quantities from the current experiment. The resulting P-U_p relationships were plotted, along with the reflection (when P=0 and U_p=V) of the P-U_p relationship for the flyer material. The intersection of the reflected curve for the flyer material and the curve for the specimen material was calculated using the quadratic formula, yielding the calculated pressure and particle velocity at impact. An example graphical representation of impedance matching calculations is shown in Figure 7.4. The pressure-particle velocity data of interest for use in data analysis is the intersection of the BMG curve (green) and the reflected steel flyer curve (dashed red).

The shock velocity (U_s) versus particle velocity (U_p) Hugoniot results are shown in Figure 7.5(a). In the high stress regime (≥67 GPa), where single wave structures are assumed, the U_p values determined using the impedance matching method are plotted since these

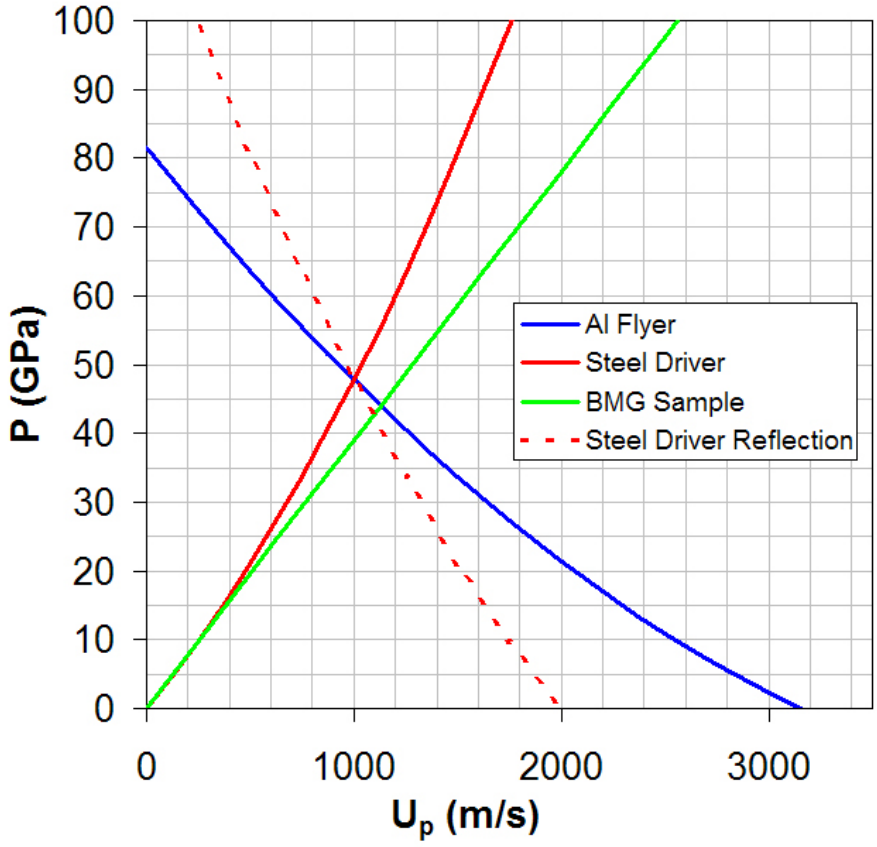

Figure 7.4: Example of graphical solution of impedance matching calculation for Shot 201. The pressure-particle velocity data of interest is the intersection of the BMG curve (green) and the reflected steel flyer curve (dashed red). Impedance matching calculations were performed using Equations 22-24.

are more precise. The U_s-U_p plot shows four regions as a function of increasing particle velocity; (1) HEL region (U_p = 0.24 km/s), (2) the low pressure plastic region (0.27 ≤ U_p ≤ 0.72 km/s) (Shots 0675, 0701, and 0676), (3) the mixed phase region (0.72 ≤ U_p ≤ 1.71 km/s) (Shots 0676, 0201, and 0202), and (4) the high pressure plastic region (U_p ≥ 1.71 km/s) (Shots 202, 209, 206, and 208). The onset stress for the phase transition corresponding to U_p = 1.71 km/s is approximately 26 GPa, which is higher than the corresponding phase transition observed by Mashimo et al. [68] on $Zr_{55}Al_{10}Ni_5Cu_{30}$ at ~14 GPa (shown in Figure 2.36).

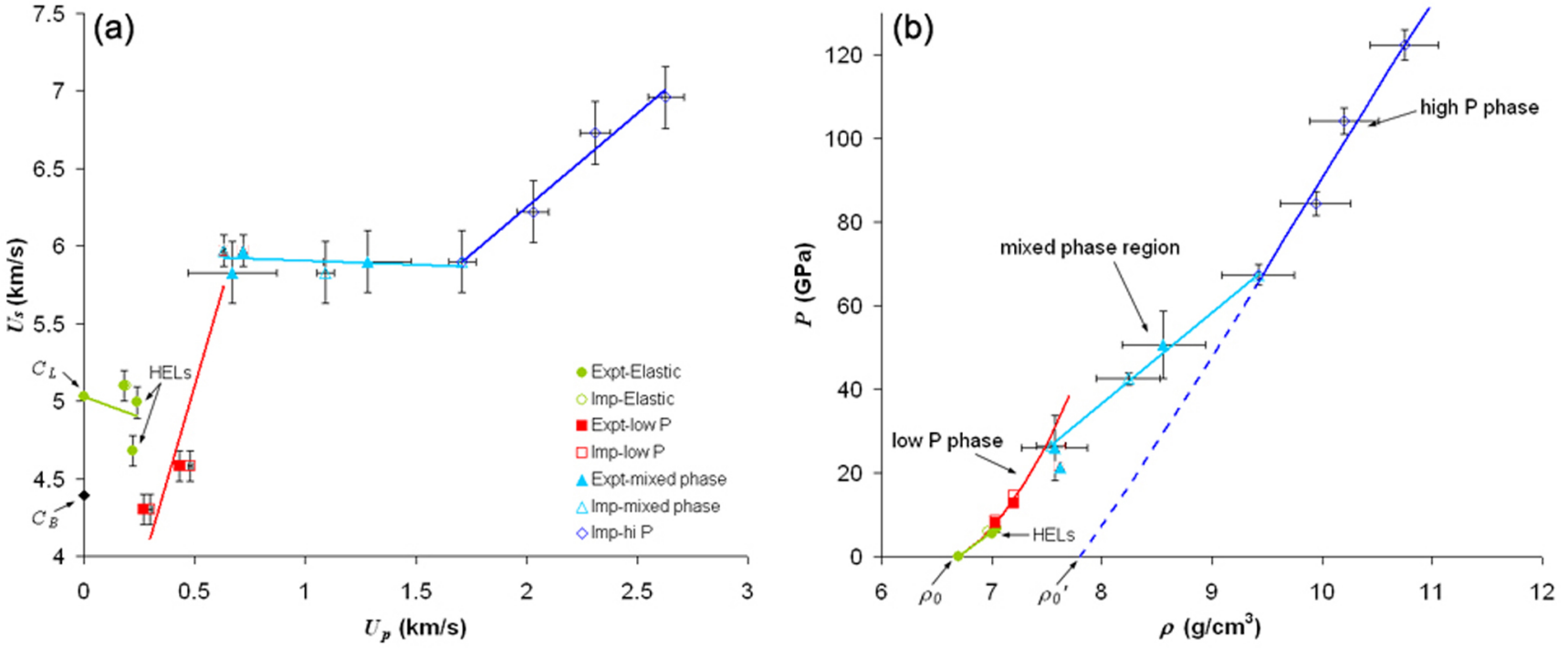

Figure 7.5: (a) U_s-U_p data obtained from PVDF+VISAR experiments at Georgia Tech and streak camera experiments at NIMS. Bulk sound speed (C_B) and longitudinal sound speed (C_L) are calculated from elastic properties data in [3]. U_p values obtained using impedance matching are plotted in the high pressure regime (≥67 GPa), and both experimentally determined and impedance matching calculated U_p values are plotted in the mixed phase a low pressure regions. All lines are linear fits to the corresponding data. (b) Pressure as a function of density. The lines in the elastic and mixed phase regions are linear fits and the lines in the low and high pressure regions are Birch-Murnaghan fits. For the low pressure phase, the Birch-Murnaghan Equation is plotted using the known bulk modulus (K_0) value [3] and K_0' is taken as *4S-1* [154]. For the high pressure phase, the best fits of K_0, K_0' and ρ_0 were determined using least squares regression.

The U_s-U_p relation in the elastic region is given by U_s=5.03-0.54U_p (U_p=0.24 km/s). Although the slope in this region is negative, which is in contrast to the work by Mashimo et al. [68] performed on another BMG, this negative slope is not unexpected due to the aforementioned (Section 2.5.3) existence of dispersed elastic fronts in amorphous materials because of the negative first pressure derivative of elastic modulus [67]. However, since the negative trend is due to only one point (Shot 0675), it is not possible to draw a conclusion either way. The U_s-U_p relations in the plastic regions are given by U_s=2.63+4.95U_p (0.27≤U_p≤0.72 km/s), U_s=5.96-0.05U_p (0.72≤U_p≤1.71 km/s), and U_s=3.83+1.21U_p (U_p≥1.71 km/s).

The data plot in the form of pressure as a function of density is shown in Figure 7.5(b). This plot again shows four distinct regions: an elastic region, a low pressure phase, a mixed phase region and a high pressure phase. The transition in the plastic range occurs at ~26 GPa, which is again higher than the corresponding phase transition observed by Mashimo et al. [68] at ~13.6 GPa (shown in Figure 2.36). The Birch-Murnaghan equation [155] was used to calculate the pressure (P_S)-density relationship of the LM106 BMG assuming no phase changes in the stress range of interest. The B-M equation is given as:

$$P_s = \frac{3K_0}{2}\left[\left(\frac{\rho}{\rho_0}\right)^{\frac{7}{3}} - \left(\frac{\rho}{\rho_0}\right)^{\frac{5}{3}}\right]\left\{1 + 3\left(\frac{K_0'}{4} - 1\right)\left[\left(\frac{\rho}{\rho_0}\right)^{\frac{2}{3}} - 1\right]\right\} \tag{25}$$

where P is pressure, ρ is the density of the material at pressure and ρ_0 is the volume of the material at zero stress. K_0 is the bulk modulus and K_0' is the pressure derivative of the bulk modulus. For the low pressure phase, this equation was plotted using the known value of K_0 (118 GPa [3]) and K_0' was taken to be *4S-1* [154], where S was determined from the U_s-U_p plot in Figure 7.5(a). For the high pressure phase, the values of K_0, K_0' and ρ_0' (zero pressure density of the high pressure phase) were determined using least squares regression to determine the best fit to the experimental data, as described in Appendix C.2. The values of these parameters were determined to be 288 GPa, 2.3, and 7.8 g/cm^3,

respectively. The best fit of the Birch-Murnaghan Equation to the experimental data in the high pressure region illustrates a shock-induced transition to a high pressure phase having a bulk modulus of 288 GPa, which is ~144% higher than the bulk modulus of this BMG at ambient pressure [3]. A similarly high value of bulk modulus has also been reported for the high pressure phase of $Pd_{39}Ni_{10}Cu_{30}P_{21}$ [85]. The authors of that work have noted that this value is not unreasonably large, citing that some metals have similar or larger bulk moduli at ambient pressures [156]. Although the current work shows evidence of a high pressure phase transition, the structural characteristics of the high pressure phase are yet to be determined.

7.3.4 Recovery Experiments

Five recovery experiments were performed on the BMG at high pressures. The experiments were performed at impact pressures ranging from ~8-60 GPa under the conditions listed in Table 7.3. A photograph of the recovered capsules can be seen in Figure 7.6(a). The BMG specimens were removed from the capsules post-impact using a lathe and analyzed using x-ray diffraction and SEM to determine if any high-pressure phases were formed or if the material had undergone any detectable changes. The specimens impacted at 8, 20 and 35 GPa could easily be removed from their respective capsules, but those impacted at 45 and 60 GPa appeared to have undergone melting or bonding of some sort and could not be separated from the steel, as can be seen in Figure 7.6. Results of shock and particle velocity measurements described in the previous section revealed transition to a mixed phase region at ~27 GPa in the U_s-U_p data and the transition to the high-pressure phase at 67 GPa. The recovered experiments were performed at a maximum pressure of 60 GPa, so we would not expect to observe a fully-transformed state in any of these recovered specimens, but specimens impacted at a pressure exceeding 27 GPa had the possibility to show some evidence of phase change if the transition was irreversible. X-ray diffraction analysis of the specimens impacted at 8, 20 and 35 GPa showed a completely amorphous structure,

Table 7.3: Experimental setup conditions (shot number, impact velocity, flyer material, and impact pressure) corresponding estimates of impact pressure, which were obtained using numerical simulations, for recovery experiments.

Shot No.	Impact Velocity (m/s)	Flyer Material	Impact Pressure (GPa)
BMG1	794	Al	8
BMG2	1014	304SS	20
BMG3	1627	304 SS	35
BMG4	1974	304SS	45
BMG5	1894	W	60

as shown in Figure7.7(a). The x-ray diffraction pattern of the as-received material is also shown in the figure, and no change was detected between the as-received and impacted materials. It should be noted, however, that x-ray diffraction may not be sensitive enough to detect any subtle changes that may be occurring. X-ray diffraction patterns obtained for the 45 and 60 GPa impacted samples are shown in Figure 7.7(b). Although these traces show peaks representing crystallinity, the peaks correspond to NiFe impurities from the steel capsules. There are a couple of unidentified peaks, but these did not correspond to any crystalline compounds of the constituents of the BMG. It is believed that all of these peaks are due to the steel capsules. Thus, x-ray diffraction did not lead to any information about what sort of changes are taking place in LM106 to cause the high-pressure phase transformation that was shown in Figure 7.5. This observation corresponds to that made by Mashimo et al. [68] that recovered specimens showed no sign of phase transformation using through XRD analysis on recovered specimens shocked up to 40 GPa although U_s-U_p data showed a very distinct kink. This discrepancy could perhaps be due to high-pressure polyamorphism, as has been observed in BMG under static high pressure conditions [89]. Since polyamorphism is a transition to another amorphous phase with a different structure, the transition would still be observed in U_s-U_p data, although XRD would not be useful in identifying the second phase since both phases are amorphous.

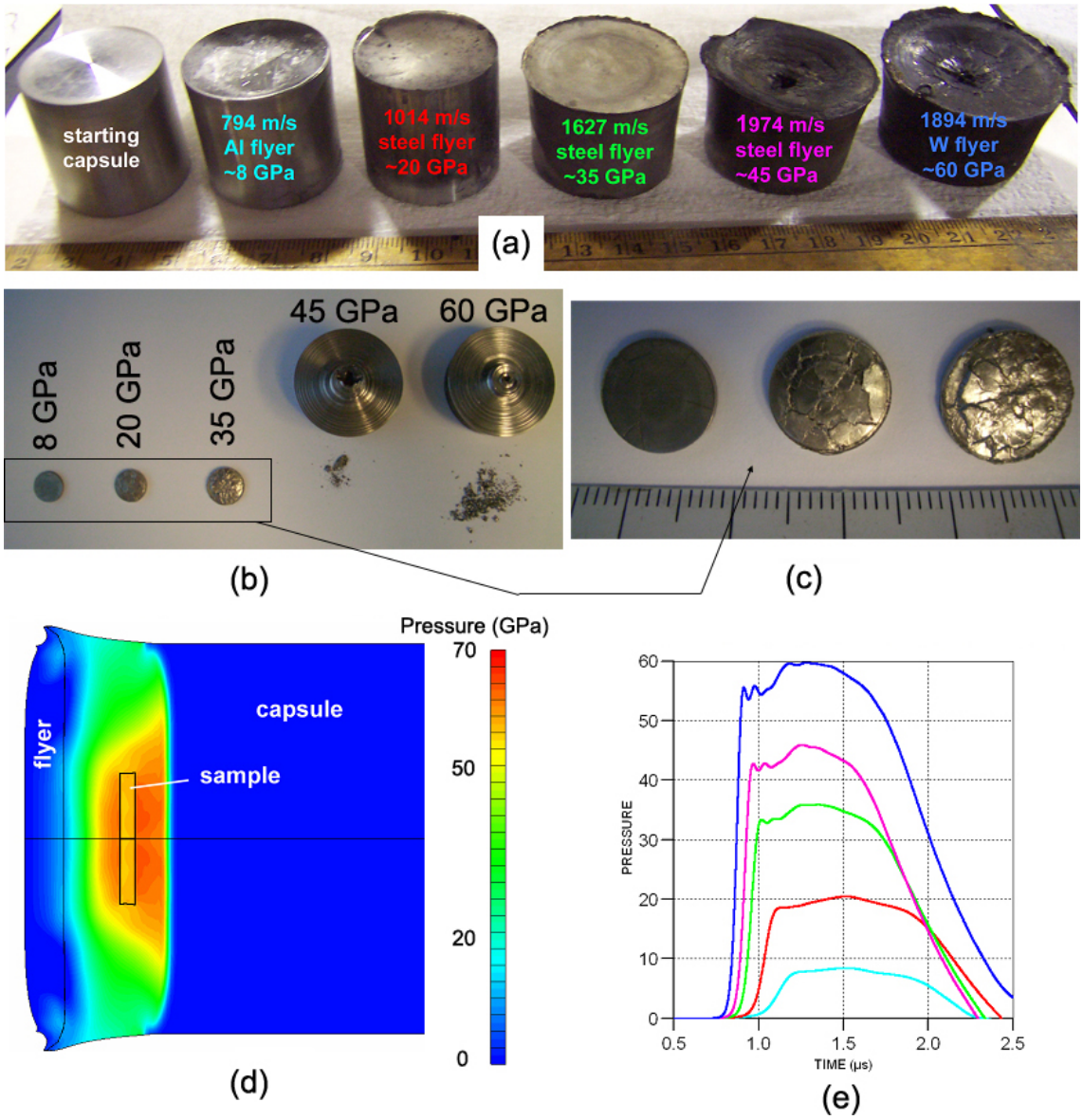

Figure 7.6: (a) Deformed capsules recovered after experiments. The BMG sample material is inside the capsules. (b) Samples recovered after impact experiments. The three impacted at the relatively lower pressures were easily removed from their capsules, but the two at the highest pressures had bonded with their capsules. (c) Closer view of the three samples impacted at 8-35 GPa. The increasing degrees of damage are evident as impact pressure increased. (d) AUTODYN simulation of BMG5 recovery experiment (W flyer, 1894 m/s) at 0.5 μs after impact. Pressure contours are shown and the pressure of interest is that within the box marking the sample location. (e) Pressure traces generated by AUTODYN to estimate the impact pressure.

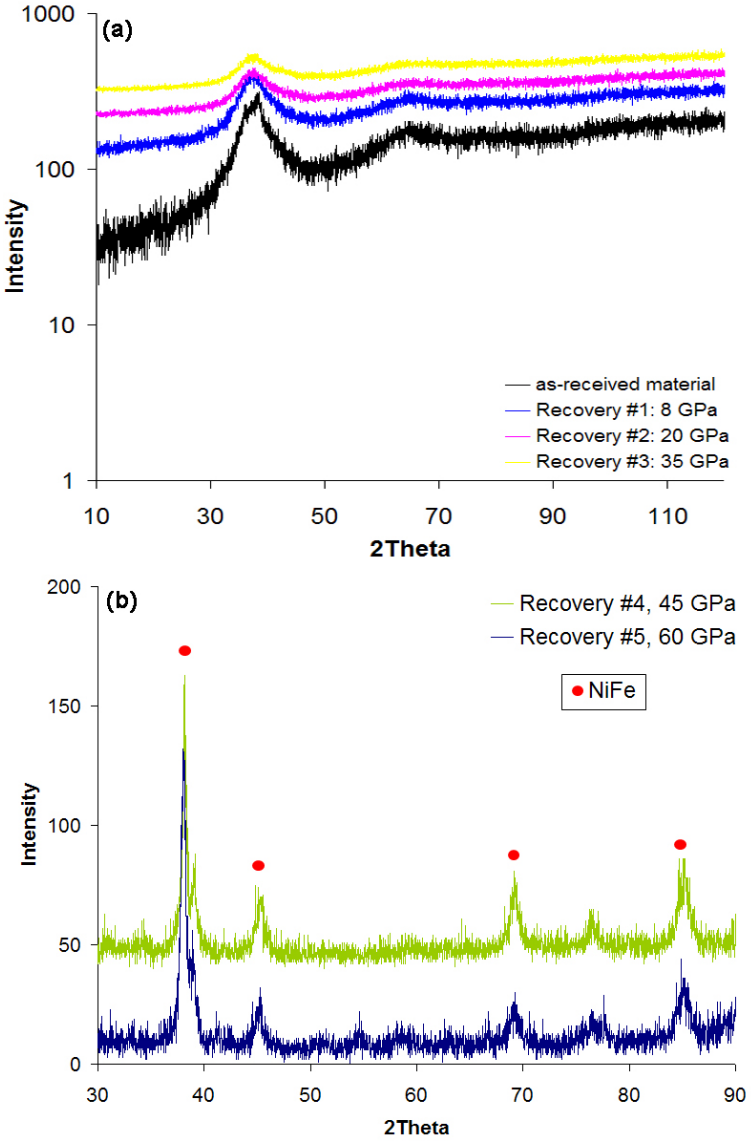

Figure 7.7: (a) XRD traces of the material recovered after the first three recovery experiments (8-35 GPa). These show the sample amorphous structure as the starting material. (b) XRD traces of the material recovered after recovery experiments at 45 and 60 GPa. Although these show some crystallinity, the peaks correspond to NiFe in the steel capsule. Traces are shifted in intensity for clarity.

7.4 Summary

Equation of state experiments were performed on $Zr_{57}Nb_5Cu_{15.4}Ni_{12.6}Al_{10}$ BMG using parallel plate impact experiments instrumented either with PVDF stress gauges + VISAR velocity interferometry, or streak photography and the inclined mirror method. Shock velocity and particle velocity were measured in all experiments and stress was also measured in the PVDF + VISAR experiments. These experiments explored a stress regime higher than has been investigated previously and on a BMG of a composition different than those which have previously been explored. The Rankine Hugoniot equations were then used to calculate additional parameters, and impedance matching technique was used for comparison with experimental results. The HEL of the BMG was determined to be 6.86 GPa, which is in agreement with other work [64, 68]. The U_s-U_p data shows evidence of a low pressure phase, a transition to a mixed phase region at ~26 GPa, followed by transition to a high pressure phase at ~67 GPa. Comparisons of the experimental data with the Birch-Murnaghan Equation of State reveals that the bulk modulus value which provides the best fit to the data for the high-pressure pahse is 288 GPa, which differs by ~144% from the ambient bulk modulus of 118 GPa [3]. Analysis of recovery specimens yielded amorphous x-ray diffraction patterns and did not lead to any further information about the high-pressure phase transformation.

CHAPTER VIII

SUMMARY AND DISCUSSION OF RESULTS

8.1 Summary of Results

In this work, the high-strain-rate mechanical properties, deformation mechanisms, and fracture characteristics of LM106 Zr-based bulk metallic glass and its composite with tungsten were investigated. A summary of the key results and findings is listed below.

In the case of the composite:

1. Mechanical testing revealed positive strain-rate sensitivity of yield stress and negative strain-rate sensitivity of failure stress over the range of strain rates evaluated. Work-hardening decreased as strain-rate increased.

2. The deformation mode was found to transition from heterogeneous deformation below the glass transition temperature (of the BMG), to homogeneous deformation between the glass transition and crystallization temperatures, and then back to heterogeneous deformation behavior above the crystallization temperature.

3. A large susceptibility to shear failure was observed, as evidenced by much decreased strain-to-failure in biaxial (compression-shear) specimens as compared to that in uniaxial (compression) specimens.

4. Failure took place primarily in the glass matrix and at the tungsten particle interfaces at all strain rates.

5. Overall, the deformation and failure behavior of the composite is dominated by that of tungsten, but characteristics of BMG deformation and failure are evident, especially between the glass transition and crystallization temperatures, and at extremely

high strain rates.

In the case of the monolithic BMG:

1. Fracture surfaces became increasingly more disorganized as strain rate increased, with evidence of melting due to temperature rise during fracture.

2. The deformation and elastic-plastic wave propagation and interaction response based on measured free surface velocity traces of the monolithic glass were well described by the pressure-hardening Drucker-Prager model. Likewise, the deformation response of the composite was described reasonably well considering a rule of mixtures combination of properties of the BMG and W.

3. High-pressure equation of state experiments provided evidence of transition to a mixed phase region (at ~26 GPa) and then to a high-pressure phase (at ~67 GPa) with a bulk modulus of 288 GPa, 144% higher than that of the bulk modulus of the ambient pressure. Specimens obtained from recovery experiments did not reveal any transformation, indicating that the transformation is likely reversible or polymorphic.

The key results summarized above illustrate that strain-rate and high-pressure phase stability are the two main parameters that play an important role in distinguishing the overall mechanical behavior of the BMG and its composite with W. Hence, the two effects are discussed further in the following sections.

8.2 Mechanical Properties of LM106 and LM106-70W over a Range of Strain Rates

During the course of this work, mechanical testing was performed in strain-rate regimes ranging from quasi-static to the high-pressure dynamic regime. The strain rates investigated ranged from approximately 10^{-4} s^{-1} to 10^{6} s^{-1}. Data from all experiments was compiled together using an analysis described by Rohr et al. [124, 157–160] which describes

a procedure for converting VISAR free surface velocity traces from Taylor test and plate impact experiments into stresses in a state that can be compared with measured stress-strain data from the quasi-static and intermediate strain-rate regimes.

For the Taylor test analysis, the stress, strain, and strain rate at yield are defined as follows [124]:

$$\sigma_y = \tfrac{1}{2}\rho c_L u_{fs}$$
$$\varepsilon_y = \frac{u_{fs}}{2c_L}$$
$$\dot{\varepsilon}_y = \frac{\Delta\varepsilon_{elastic}}{\Delta t_{elastic}}$$

where ρ is density, c_L is the longitudinal wave speed, u_{fs} is the free surface velocity at the elastic-plastic transition (first change in slope of the free surface velocity trace), and $\Delta\varepsilon$ and Δt are the incremental values of strain and time, respectively, at the first change in slope of the free surface velocity curve. This analysis was used for the Taylor Test data previously presented in Section 5.4.1.2. The values obtained from this series of equations could be directly compared with those obtained from uniaxial compression, drop weight, and SHPB tests, which all yielded true stress-strain curves, since Taylor tests are performed under a 1-D state of stress.

For plate impact tests, the stress, strain, and strain rate at yield, are determined at the HEL from the free surface velocity traces [124]. Stresses were corrected for the differences in stress state such that comparisons could be made across the whole range of strain rates. The relations for these parameters are as follows:

$$\sigma_y = \frac{1-2\nu}{1-\nu}\sigma_{HEL}$$

where

$$\sigma_{HEL} = \tfrac{1}{2}\rho c_L u_{HEL}$$

$$\varepsilon_{el} = \frac{1}{2}\frac{u_{HEL}}{c_p}$$

$$\dot{\varepsilon}_{HEL} = \frac{1}{2}\frac{u_{HEL}}{2c_p\Delta t_{el}}$$

where ν is Poisson's ratio, c_p is the plastic wave speed, which is defined as $\sqrt{\frac{K+4/3G}{\rho}}$ where K is bulk modulus and G is shear modulus, Δt_{el} is the rise time to the HEL. The resulting data from this analysis on all Taylor Test and plate impact experiments is provided in tabular form in Tables 8.4, 8.5 for the composite and monolithic BMG, respectively.

Failure stresses from Taylor experiments were determined by comparison with simulations, as described in Section 5.4.4.1. Failure stress, strain, and strain rate from plate impact experiments were calculated according to [124]:

$$\sigma_{fail} = \frac{1-2\nu}{1-\nu}\sigma_{max}$$

where

$$\sigma_{max} = \frac{1}{2}\rho c_p u_{HEL} + \frac{1}{2}u_s\rho(u_{max} - u_{HEL})$$

$$\varepsilon_{fail} = \varepsilon_{elastic} + \varepsilon_{plastic}$$

where

$$\varepsilon_{elastic} = \frac{1}{2}\frac{u_{HEL}}{c_p}$$

and

$$\varepsilon_{plastic} = \frac{1}{2}\frac{(u_{max}-u_{HEL})}{u_s}$$

$$\dot{\varepsilon}_{fail} = \frac{\Delta\varepsilon_{elastic+plastic}}{\Delta t_{elastic+plastic}}$$

The conversion from σ_{max} to σ_{fail} is valid with the assumption that the solid behaves elastically up to failure [161], which is valid for BMGs, which exhibit almost no plasticity. Use of the above equations allowed for comparison of yield and failure stress over strain rates ranging eleven orders of magnitude and obtained using varying testing techniques.

Figure 8.8 shows the compilation of (a) yield and (b) failure stress data from quasi-static compression tests, drop weight tests, SHPB tests, Taylor tests, and plate impact tests for LM106-70W composite and LM106 monolithic BMG. The yield stress data shown in Figure 8.8(a) reveals that the composite clearly exhibits positive strain-rate sensitivity up to strain rates on the order of 10^3 s^{-1}, as was discussed in Section 4.4.1, and the added Taylor Test data from Chapter V supports this trend and possibly displays an increase in strain-rate sensitivity at $\sim 10^3$ s^{-1}. The monolithic BMG shows positive strain-rate sensitivity over the entire range of strain rates, but there is only one data point at a strain rate between 10^{-4} and 10^6 s^{-1}, so more data is necessary to confirm this trend, especially given that slightly negative strain-rate sensitivity has been observed by other researchers (see Section 2.3.2.4). The plate impact experiments ($\dot{\varepsilon} \approx 10^6$ s^{-1}) on the monolithic BMG show much higher yield stresses (obtained from the HEL) than are seen at lower strain rates, indicating a possible transition in the strain-rate effect on yield stress. Figure 8.8(b) shows the corresponding failure stress trends as a function of strain rate. Whereas the composite has been shown to exhibit negative strain-rate sensitivity in failure stress up to $\sim 10^3$ s^{-1} (Section 4.4.1), the addition of failure stress results from current Taylor Test data add some scatter near $\sim 10^3$ s^{-1}, indicating either the beginning of an increase in failure strength with strain rate, or possibly just scatter and no obvious strain-rate sensitivity effect within that range of strain rates. The trend in failure stress of the monolithic BMG shows a clear, significant increase above strain rates on the order of 10^4 s^{-1}.

In order to make a more complete comparison and analysis of the mechanical behavior of LM106 BMG and LM106-70W composite, literature data was also collected and analyzed using Rohr's method. This data is also presented in Table 8.5 for the monolithic glass and an additional table (Table 8.6) reports data tabulated from literature results on tungsten. The addition of data on tungsten the monolithic glass provided a more complete data set for analysis of the influence of strain rate on the mechanical behavior. Additionally, all data was normalized in order to remove material-inherent effects (i.e. density and

elastic properties) such that direct comparisons could be made between the three materials. Figure 8.9 shows the compilation of (a) yield and (b) failure stress data normalized by ρc_L^2 or ρc_P^2, respectively, where ρ is density, c_L is elastic wave speed, and c_P is plastic wave speed $\left(= \sqrt{\frac{K+4/3G}{\rho}}\right)$. The product ρc_L^2 provides an elastic modulus equivalent $\left(c_L = \sqrt{\frac{E}{\rho}}\right)$ and ρc_P^2 is likewise the plastic modulus equivalent. In Figure 8.9, data from the present work is plotted along with data calculated from results in the literature for LM106 [2, 9] and W [2, 9, 162–164], resulting in data for all three materials spanning strain-rates ranging approximately eleven orders of magnitude.

Table 8.4: Tabular yield and failure stresses and strain rates data for LM106-70W composite corresponding to Figures 8.8 and 8.9.

Material	$\dot{\varepsilon}_y$ (s^{-1})	σ_y (MPa)	$\sigma_y/\rho c_L^2$	$\dot{\varepsilon}_{fail}$ (s^{-1})	σ_{fail} (MPa)	$\sigma_{fail}/\rho c_P^2$	Source
LM106-70W	0.0007	1067	0.0028	0.0007	2318	0.0062	this work, Instron
LM106-70W	0.0007	1096	0.0029	0.0007	2252	0.0060	this work, Instron
LM106-70W	0.036	1285	0.0034	0.036	2286	0.0061	this work, Instron
LM106-70W	0.037	1271	0.0034	0.037	2237	0.0059	this work, Instron
LM106-70W	0.78	1359	0.0036	0.78	–	–	this work, Instron
LM106-70W	0.78	1283	0.0034	0.78	–	–	this work, Instron
LM106-70W	0.79	1307	0.0035	0.79	–	–	this work, Instron
LM106-70W	152	1586	0.0042	152	1772	0.0047	this work, DW
LM106-70W	153	1642	0.0043	153	1758	0.0047	this work, DW
LM106-70W	1041	1574	0.0042	185	5228	0.0139	this work, Taylor Test
LM106-70W	1209	1732	0.0046	–	–	–	this work, SHPB
LM106-70W	1390	1455	0.0039	1390	2057	0.0055	this work, SHPB
LM106-70W	1416	1894	0.0050	360	5692	0.0151	this work, Taylor Test
LM106-70W	1430	1656	0.0044	1430	2093	0.0056	this work, SHPB
LM106-70W	1570	1964	0.0052	185	4520	0.0120	this work, Taylor Test

Table 8.5: Tabular yield and failure stresses and strain rates data for LM106 corresponding to Figures 8.8 and 8.9. Data is from this work as well as calculated from results reported in literature [2, 9].

Material	$\dot{\varepsilon}_y$ (s^{-1})	σ_y (MPa)	$\sigma_y/\rho c_L^2$	$\dot{\varepsilon}_{fail}$ (s^{-1})	σ_{fail} (MPa)	$\sigma_{fail}/\rho c_P^2$	Source
LM106	0.0001	1650	0.0102	0.0001	1650	0.0104	this work, Instron
LM106	0.0001	1700	0.0106	0.0001	1700	0.0107	Jiao [2]
LM106	0.0001	1800	0.0112	0.0001	1800	0.0113	Li [9]
LM106	2313	2112	0.0131	2451	2106	0.0132	this work, Taylor Test
LM106	2500	1400	0.0087	2500	1400	0.0088	Jiao [2]
LM106	4000	1420	0.0088	4000	1420	0.0089	Li [9]
LM106	2.3e6	2838	0.0176	4.02e5	3298	0.0207	this work, plate impact
LM106	2.59e6	3033	0.0188	1.04e6	5067	0.0319	this work, plate impact
LM106	–	–	–	6.78e6	8483	0.0533	this work, plate impact
LM106	–	–	–	4.3e6	2320	0.0146	this work, plate impact
Sleeved LM106	0.0001	1241	0.0077	0.0001	1241	0.0078	this work, Instron
Sleeved LM106	1956	1465	0.0091	1868	1471	0.0092	this work, Taylor Test
Sleeved LM106	2268	1534	0.0095	1805	1665	0.0105	this work, Taylor Test

Table 8.6: Tabular yield and failure stresses and strain rates data for tungsten corresponding to Figure 8.9. Data is from this work as well as calculated from results reported in literature [2, 9, 162–164].

Material	$\dot{\varepsilon}_y$ (s^{-1})	σ_y (MPa)	$\sigma_y/\rho c_L^2$	$\dot{\varepsilon}_{fail}$ (s^{-1})	σ_{fail} (MPa)	$\sigma_{fail}/\rho c_P^2$	Source
W	0.0001	1200	0.0023	–	–	–	Jiao [2]
W	0.0001	1620	0.0031	–	–	–	Li [9]
W	0.001	1575	0.0030	–	–	–	Zurek [164]
W	1	1200	0.0023	–	–	–	Lennon [163]
W	1	2250	0.0043	–	–	–	Zurek [164]
W	2000	1950	0.0038	–	–	–	Zurek [164]
W	4000	1800	0.0035	2200	0.0035	0.0042	Li [9]
W	5600	2200	0.0042	–	–	–	Jiao [2]
W	50000	1900	0.0037	–	–	–	Lennon [163]
W	100000	2250	0.0043	–	–	–	Lennon [163]
W	1.40e4	2078	0.0040	4.88e4	6019	0.0116	Asay [162]
W	1.40e4	2322	0.0045	4.93e4	6074	0.0117	Asay [162]
W	2.33e4	2261	0.0044	8.48e4	5974	0.0115	Asay [162]
W	2.33e4	2139	0.0041	8.65e4	6082	0.0117	Asay [162]
W	2.33e4	2689	0.0052	8.42e4	5940	0.0115	Asay [162]
W	7.75e3	2078	0.0040	2.83e4	5974	0.0115	Asay [162]
W	7.75e3	1894	0.0037	2.85e4	6003	0.0116	Asay [162]

The normalized data plots shown in Figure 8.9 reveal more information regarding the yield and failure trends of all three materials (LM106, LM106-70W, and W). It is obvious that normalizing eliminates the material-inherent properties and effects of the three materials, providing a more generalized comparison and demonstrating the differences in behavior between the W metal (BCC), the BMG, and the tungsten-containing BMG composite. In Figure 8.9(a), the strain-rate strengthening effect seen in the composite is similar to that seen in W up to strain rates of $\sim 10^3$ s^{-1}, which is not unexpected given the large volume fraction of tungsten. The BMG data is significantly different, both in terms of overall strength as well as the rate of the the significant strength increase at $\dot{\varepsilon} > 10^3$ s^{-1}. The monolithic glass shows slight negative strain-rate sensitivity at strain rates up to 10^4 s^{-1}, as previously discussed (Section 2.3.2.4), followed by a drastic increase in strength above strain rates of approximately 10^4 s^{-1}, which will be discussed further later. Tungsten, however, does not show any transition or drastic increase in yield stress at strain rates as high as 10^5 s^{-1}. It is not certain if the composite data at $\dot{\varepsilon} \approx 10^3$ s^{-1} shows the beginnings of an abrupt increase in strength or is simply scatter, similar to what is seen in the W data between 10^3 and 10^5 s^{-1}. Further tests on the composite at higher rates are needed to investigate the possibility of the drastic increase in its yield stress similar to the observed behavior of the glass. The plot of failure stress as a function of strain rate (Figure 8.9 (b)) shows a clear drastic increase in failure strength of both the tungsten and the monolithic glass above a strain rate of $\sim 10^4$ s^{-1}. The composite data at $\sim 10^4$ s^{-1} remains within scatter and additional data at higher strain rates is necessary to confirm the possibility of obvious increase in its failure strength as was found in both of its constituents.

Curves drawn on the plots in Figures 8.8 and 8.9 are simply guides to they eye to help illustrate the trends. In general, these curves show that the composite's deformation (yield) behavior is largely dominated by tungsten up to intermediate strain rates, but may slightly deviate more toward the behavior of the monolithic glass as strain rate increases. No strengthening transition is observed in the composite behavior, although the

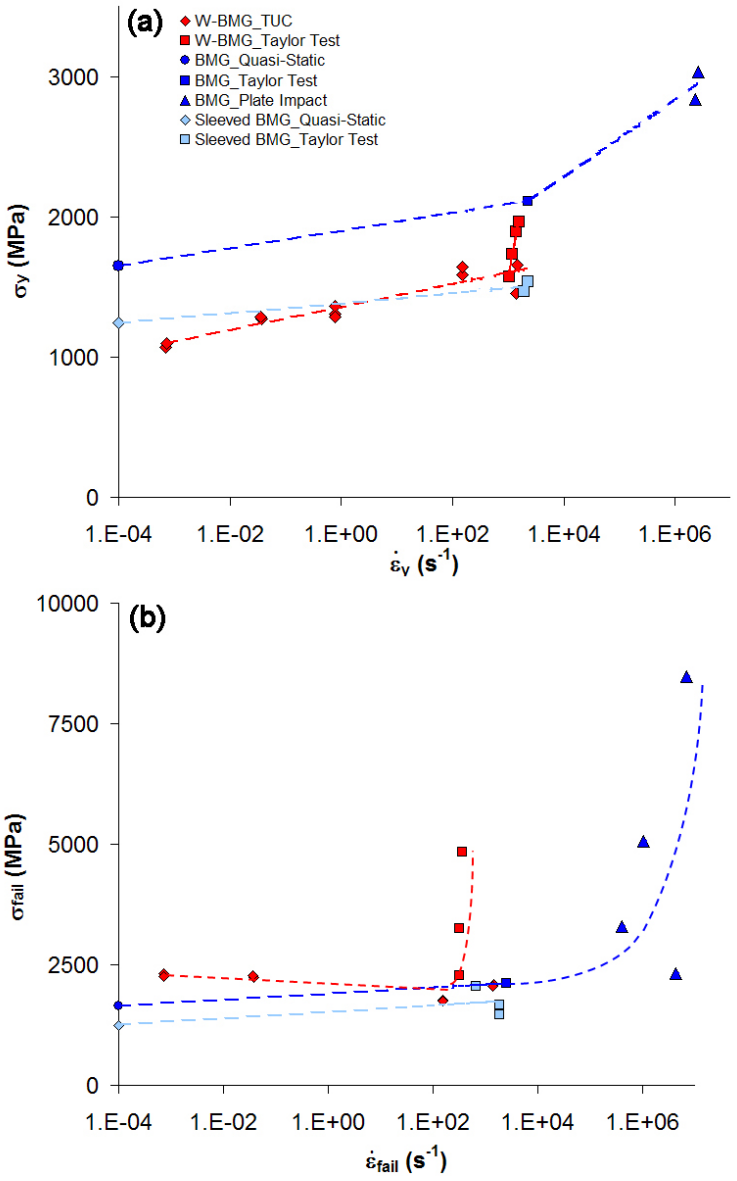

Figure 8.8: (a) Yield stress and (b) failure stress as a function of strain rate for LM106 and LM106-70W from experiments ranging from strain rates of 10^{-4} to 10^{6} s^{-1} performed in the present work. Curves are simply guides to the eye to aid in visualization of the trends. Data shows positive strain-rate sensitivity in yield stress in all materials, with a significant strengthening observed in the BMG above strain rates of $\sim 10^{4}$ s^{-1} (a). Failure stress of the BMG also shows a drastic increase above strain rates of $\sim 10^{4}$ s^{-1} and the composite is possibly also exhibiting a transition in toughening behavior (b).

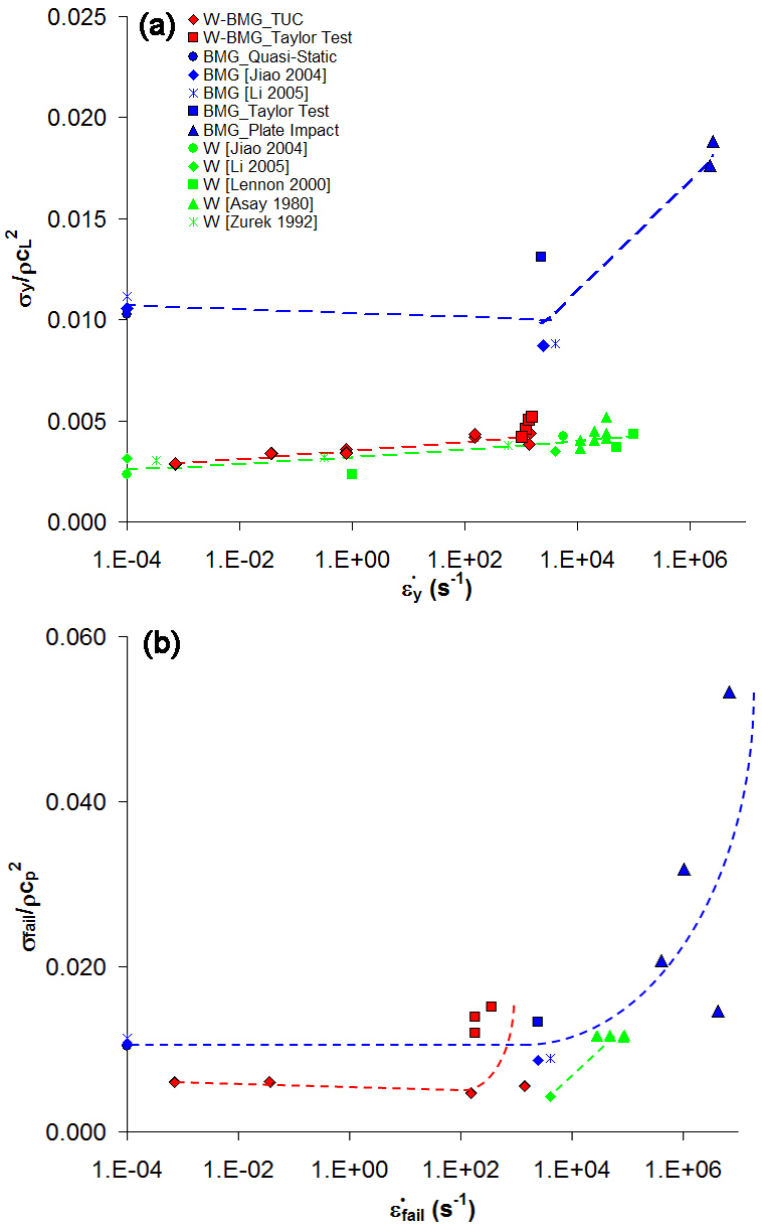

Figure 8.9: (a) Yield stress and (b) failure stress as a function of strain rate for LM106, LM106-70W, and W from 10^{-4} to 10^{6} s^{-1}. LM106-70W data is from this work, LM106 data is from this work as well as from [2, 9] and data on tungsten is from [2, 9, 162–164]. Yield stress data is normalized by ρc_L^2 (elastic modulus) and failure stress data is normalized by ρc_P^2 (plastic modulus) to remove material inherent effects of density and elastic properties and allow for direct comparison. Curves are simply guides to the eye to aid in visualization of the trends. Data shows distinct strengthening (a) and toughening (b) in the BMG above strain rates of $\sim 10^4$ s^{-1}. The composite shows possible beginnings of toughening effects.

un-normalized data (Figures 8.8(a)) shows possibility of the beginning of a strengthening transition. There appears to be the beginning of a toughening transition in the composite, as seen in Figure 8.9(b). However, it is of interest to test the composite at higher rates to determine if the observed beginnings of a toughening transition in the BMG is in fact a trend, and not just scatter. It is expected that the transition in strain-rate sensitivity response would be observed in the failure stress (toughening) of the composite since LM106 shows the sudden fracture strength increase at strain rates $>10^4$ s^{-1}. More experiments are necessary to investigate both the strengthening and toughening effects of strain rate on the composite at strain rates exceeding 10^4 s^{-1}.

The increase in both yield and failure strengths of tungsten with increasing strain rate can be explained by well-known dislocation theory. Increased strain-rate sensitivity in BCC metals has been attributed to a transition in rate-controlling mechanism from thermal activation at low strain rates to dislocation drag due to interaction with phonons at high strain rates ($> 10^3$ s^{-1}) [165, 166]. This same explanation does not apply to amorphous materials, however, and as bulk metallic glasses have not previously been well characterized in the high strain rate regime ($> 10^6$ s^{-1}), the strengthening mechanism is unknown. A drastic increase in dynamic fracture toughness at crack initiation of LM1 has nevertheless been observed by Owen et al. [48] above loading rates of $\sim 10^6$ s^{-1}, as was discussed in Section 2.3.2.2. This increase was attributed to effects of inertia and thermal softening on the dynamic crack initiation process, which would effectively cause crack blunting. These theories would explain toughening in BMGs at high strain rates, but not the observed strengthening effects.

With respect to polymers, another class of amorphous materials, other types of strengthening mechanisms have been proposed. Kauzmann [167] described units of flow in a material as: "structures in a body whose motions past one another make up the unit shear stress process...the unit of flow may be a single molecule or a group of many molecules, and the barrier may arise directly from the repulsion between a few molecules or from some more

complicated mechanism." For polymers, Zerilli [168] has suggested units of flow analogous to dislocations in crystalline materials, where a line defect is the boundary between slipped and unslipped regions. The application of dislocation theory to amorphous materials by replacing the constant Burgers displacement vector in crystalline materials with the average of a fluctuating Burgers displacement in the amorphous material has also been proposed [169]. In agreement with these analogies, increased strain hardening with strain in polymers is logical since the probability for immobilization of flow units increases with increasing strain and strain rate [168]. If the unit of flow in a BMG is the shear transformation zone, a similar analogy could apply. Similarly, it would follow that yield stress and ultimate stress increase with strain rate because at high rates there is not enough time for the shear transformation zones to operate in the typical deformation mode of BMGs (shear banding), so there is effectively a shear transformation zone drag, analogous to dislocation drag. While an argument of this type may explain strengthening in BMGs, it does not explain the observed toughening effect. A third possible argument, however, offers explanations fro both strengthening and toughening in BMGs at high-strain rates.

8.3 Phase Transformation Effect on Strain-Rate Sensitivity

The high pressure phase stability of monolithic LM106 was discussed in detail in Chapter VII. The results from this work showed clear evidence of transformation to a mixed phase region at 26 GPa and to a completely new second phase at 67 GPa [151]. For these phase changes to be detectable on the bulk scale during the nanosecond time scale of shock experiments, a significant portion of the specimen would have to have undergone the transition. However, the onset of this transition is likely to occur locally at lower pressures than were observed on the bulk scale. In this case, as the phase transformation begins to occur locally in the BMG, the mechanical work and stress-strain energy is dissipated in causing the phase change rather than in producing deformation and failure. As a result of this energy dissipation, the material would be able to withstand higher stresses. The BMG data presented in

Figures 8.8 and 8.9 span the pressure range up to the observed transition to the mixed phase (experiments at higher pressures did not utilize VISAR and thus could not be included in this analysis). Local energy dissipation within the BMG as a result of the phase transformation that is beginning to occur can therefore also account for the increase in strength that is observed in the BMG above 10^4 s^{-1}. Additionally, the Birch-Murnaghan EOS provided information about the high-pressure phase and revealed that it has a bulk modulus of 288 GPa, which is significantly higher than the ambient pressure modulus. Transition to a phase with a higher modulus explains the observed strengthening effects.

The possible explanation linking the phase transformation to toughening observed at high strain rates is analogous to the mechanism that occurs in transformation-toughening in ceramics such as zirconia (TTZ). In the case of TTZ, an advancing crack provides the necessary space and stress for the transformation to occur from the metastable tetragonal to the more voluminous (and more energetically favorable) monoclinic phase. Hence, in addition to the dissipation of energy in causing the phase transition, the resulting cumulative increase in volume of the material leads to closing of the crack, thus resulting in a higher strength material. Although the specific details of the possible analogous transformation-toughening mechanism are unclear in this BMG, and a subject of further study, the occurrence of phase transition at high-strain rates and pressure in this BMG can be an important factor contributing to the observed strengthening and toughe ning effects.

CHAPTER IX

CONCLUSIONS AND SUGGESTIONS FOR FUTURE WORK

9.1 Conclusions

An investigation was conducted to study the high-strain-rate mechanical properties of LM106 BMG and its composite with tungsten to determine their deformation and failure responses at high strain rates. For the composite, mechanical testing revealed positive strain-rate sensitivity of its yield stress and negative strain-rate sensitivity of its failure stress over the range of strain rates evaluated, and work-hardening decreased as strain-rate increased. The deformation mode in the composite was found to transition from heterogeneous deformation below the glass transition temperature (of the BMG), to homogeneous deformation between the glass transition and crystallization temperatures, and then back to heterogeneous deformation behavior above the crystallization temperature. The composite exhibited a large susceptibility to shear failure, as evidenced by much decreased strain-to-failure in biaxial (compression-shear) specimens as compared to that in uniaxial (compression) specimens. Failure took place primarily in the glass matrix and at the tungsten particle interfaces at all strain rates. Overall, the deformation and failure behavior of the composite is dominated by that of tungsten, but characteristics of BMG deformation and failure are evident, especially between the glass transition and crystallization temperatures, and at extremely high strain rates.

For the monolithic BMG, fracture surfaces became increasingly more disorganized as strain rate increased, with evidence of melting due to temperature rise during fracture. The deformation and elastic-plastic wave propagation and interaction response based on

measured free surface velocity traces of the monolithic glass were quite well described by the pressure-hardening Drucker-Prager model. Likewise, the deformation response of the composite was described reasonably well considering a rule of mixtures combination of properties of the BMG and W. High-pressure equation of state experiments provided evidence of transition to a mixed phase region (at ~26 GPa) and then to a high-pressure phase (at ~67 GPa) with a bulk modulus of 288 GPa, 144% higher than that of the bulk modulus of the ambient pressure. Specimens obtained from recovery experiments did not reveal any transformation, indicating that the transformation is likely reversible or polymorphic.

In the present work, mechanical testing was performed on the BMG and composite over eleven orders of magnitude. A transition in the effect of strain-rate sensitivity was observed at strain rates exceeding 10^4 s^{-1}. The yield and failure stresses of LM106 increased drastically as a function of strain rate above this transition point. The transition in yield strength (strengthening) is believed to be due to transition to a higher modulus phase and the transition in failure stress (toughening) is believed to be due to effects of energy dissipation associated with the high-pressure phase transition.

9.2 Suggestions for Future Work

There are several areas where further investigation is necessary to answer some questions which were revealed during the course of this work.

Although recovery experiments were performed on the monolithic BMG up to ~60 GPa, no evidence of phase changed was observed in the recovered material to verify the phase change observed in the U_s-U_p data. According to the experimental data, 60 GPa is only in the mixed phase region and is not quite a high enough pressure to cause formation of the second phase. This may mean that the transformation is reversible, not enough of the material had transformed such that it could be detected, or that the transformation is polymorphic. To verify this, recovery experiments should be done to higher impact pressures

such that the impact conditions are well within the second phase (>67 GPa). X-ray diffraction and transmission electron microscopy analysis can then be conducted on the recovered samples. However, if the fraction of crystals formed is too small to be detected by XRD, or if the phase change is from one amorphous state to another (polyamorphism), then elucidation of the dynamic high-pressure phase may be unattainable. It may also be interesting to perform static high-pressure experiments combined with *in situ* x-ray diffraction analysis. However, the effects of the different state of stress (hydrostatic pressure vs. 1-dimensional stress) may alter the observation of a phase transition. Collaborating work is currently in progress at the University of Alabama, Birmingham to study the monolithic BMG under static high pressure with in situ XRD. Molecular Dynamics simulations of high-pressure impact/phase change also need to be performed (currently in progress in Dr. Mo Li's group at Georgia Tech) and may provide insight into this phenomenon.

As was discussed in the previous section, mechanical properties seem to be drastically changing as the phase transition is approached. As such, once the nature of the high pressure phase has been determined, its mechanical response should be investigated such that this BMG can be used in design of composites for high strain rate applications and the material behavior upon high pressure impact will be fully understood.

The compilation of mechanical properties (yield stress and strain, failure stress) results ranging over eleven orders of magnitude provided valuable information about the monolithic BMG and the composite. However, the results would be more complete with additional plate impact experiments on the composite since there are currently no data points from the very high strain rate regime ($>10^4$ s^{-1}) and the apparent transition in yield and failure stress behavior at high rates needs to be investigated. This data could be obtained from plate impact experiments. As plate impact experiments are being conducted, it would be of interest to measure the high pressure equation of state for the composite material as was done for the monolithic BMG. Equation of state parameters are often needed for calculations (i.e. conversion of VISAR data to stress-strain curves for determination of 0.2%

YS) so without these values, estimates must be used, which is not ideal or accurate. However, a complete understanding of the high pressure phase change taking place in the BMG may be necessary before the composite can be fully understood.

Although constitutive modeling was done as a supplement to experiments in this work, it is clear that none of the models used really provided an accurate description of the material behavior over the entire range of strain rates investigated. This is a difficult problem given that there really isn't an appropriate model even for the monolithic glass, although there are several investigators working on this. It is desirable to develop a constitutive model that would describe the mechanical behavior of both the monolithic glass as well as the composite such that finite element modeling could be used in correlation with experiments to learn more about deformation and failure behavior. Additionally, the dependence of shear stress on temperature and strain rate should be incorporated into such a model since it was shown in this work that this material is quite susceptible to shear failure under biaxial loading conditions.

APPENDIX A

ANALYSIS OF STRESS-STRAIN DATA USING FAMOS SOFTWARE

This appendix describes the data analysis from the mechanical testing performed at TU Chemnitz.

A.1 Quasi-static Data Analysis

This section describes the data analysis for the quasi-static experiments performed on the Instron. Initially, the displacement data measured from the inductive sensors and the voltage data measured from the strain gauges was zeroed. Next, the data was smoothed to decrease the noise in the signal that was a result of the hydraulic machine attempting to keep a constant level. The stress was the calculated according to:

$$\sigma = P/A_0$$

and the displacement measured by the inductive sensors was converted to strain:

$$\varepsilon_{cross-head} = \frac{\Delta l}{l_0} = \frac{displacement}{l_0}$$

The strain gauge signal was converted to strain according to:

$$\varepsilon_{SG} = \frac{B \cdot U_b \cdot 100\%}{U_i \cdot K_{amp} \cdot K_{SG}}$$

where B is the type of the Wheatstone Bridge (in this case, value of 2 for 1/2 bridge), U_b is the measured voltage signal, U_i is the voltage running through the circuit immediately

before the start of the test, K_{amp} is the amplification (100 X), and K_{SG} is the K-factor of the strain gauge, which is the proportionality factor between the relative change of the resistance (K_{SG}=1.98). The excess data which was recorded after specimen failure was then removed and the stress-strain data was plotted. The strain data from the inductive sensors was then corrected for the machine compliance. Finally, the 0.2% offset yield stress was determined. The script used in FAMOS is given below for specimen W-BMG ♯3 which was tested in uniaxial compression:

;zero displacements, enter offsets from zero

displacement_WBMG_comp3=displacement_WBMG_comp3+6.365

sg_WBMG_comp3=sg_WBMG_comp3+4.031

;smooth data, enter smoothing values s.t. initial portion of curve, as well as yield and fracture data are not altered

load_WBMG_comp3_smooth=smo(load_WBMG_comp3,150)

displacement_WBMG_comp3_smooth=smo(displacement_WBMG_comp3,200)

sg_WBMG_comp3_smooth=smo(sg_WBMG_comp3,150)

;calc stress and strain, enter initial dimensions

stress_WBMG_comp3=load_WBMG_comp3_smooth/(pi/4)/sqr(5.998)

strain_WBMG_comp3=displacement_WBMGcomp3_smooth/6.015*100

strain_sg_WBMG_comp3=2*sg_WBMG_comp3_smooth*100/(1.276*100*1.98)

;clip excess data, enter limits

stress_WBMG_comp3_cut=cut(stress_WBMG_comp3,0,14360)

strain_sg_WBMG_comp3_cut=cut(strain_sg_WBMG_comp3,0,10740)

strain_WBMG_comp3_cut=cut(strain_WBMG_comp3,0,14400)

;plot stress-strain curve

stress_strain_sg_WBMG_comp3=

xy(strain_sg_WBMG_comp3_cut,stress_WBMG_comp3_cut)

stress_strain_WBMG_comp3=xy(strain_WBMG_comp3_cut,stress_WBMG_comp3_cut)

```
;compliance data
displacement_instron_compliance=displacement_instron_compliance+0.3785
load_displacement_instron_compliance=
xy(displacement_instron_compliance,load_instron_compliance)
;compliance correction, enter specimen initial length, machine stiffness, and limits for data
clipping and shifting
corrected_displacement_WBMG_comp3_smooth=displacement_WBMG_comp3_smooth-
(1.6e-6)*load_WBMG_comp3_smooth
corrected_strain_WBMG_comp3=
corrected_displacement_WBMG_comp3_smooth/6.016*100
corrected_strain_WBMG_comp3_cut=cut(corrected_strain_WBMG_comp3,0,9120)
corrected_stress_strain_WBMG_comp3=
xy(corrected_strain_WBMG_comp3_cut,stress_WBMG_comp3_cut)
shift_corrected_strain_WBMG_comp3_cut=corrected_strain_WBMG_comp3_cut-0.5
shift_corrected_stress_strain_WBMG_comp3=
xy(shift_corrected_strain_WBMG_comp3_cut,stress_WBMG_comp3)
cut_shift_corrected_stress_strain_WBMG_comp3=
cut(shift_corrected_stress_strain_WBMG_comp3,0,59.6)
;0.2% offset YS line, input elastic modulus (2200) and y intercept (-440)
X=ramp(0.2,0.1,100)
Y=2200*X-440
YS=xy(X,Y)
```

A.2 Drop Weight Testing Data Analysis

This section describes the FAMOS script used to analyze the data obtained using the drop weight testing apparatus. The following scripts were adapted from those written by Mr.

Muth. The raw data was obtained from the optical sensor, and the strain gauges on the machine and on the specimen were converted from voltage to stress or strain using sequences, which are given in the Sections A.2.3,A.2.1, and A.2.2. The sampling rates of each data channel were then made to be the same and the data was smoothed to remove noise and the zero points were adjusted.

```
;DROP WEIGHT TESTING
;convert raw data to stress and strain
sequence dw_stress WBMG_C16_stress 5.999 9.485 0.002 0.005
sequence dw_strain WBMG_C16_strain 5.988 WBMG_C16_stress
sequence dw_sg WBMG_C16_sg 2 1.270 1.98 tds_ch3
;make all data have same sampling rate
WBMG_C16_sg=rsamp(WBMG_C16_sg,WBMG_C16_stress)
;smooth stress data
WBMG_C16_stress=smo(WBMG_CS16_stress,2e-5)
;zero stress and strain data, input offset from zero
WBMG_C16_stress=WBMG_C16_stress-2
WBMG_C16_strain=WBMG_C16_strain-55.15
WBMG_C16_sg=WBMG_C16_sg-0.098
WBMG_C16_sg_cut=cut(WBMG_C16_sg,0.002706,0.003529)
WBMG_C16_stress_cut=rsamp(WBMG_C16_stress,WBMG_C16_sg_cut)
```

The machine compliance was corrected and the strain measured from the optical sensor was adjusted such that the elastic modulus measured from this data was the same as that measured using the strain gauge on the specimen. Next, the stress-strain data was plotted and cut to remove excess data.

```
;compliance correction
WBMG_C16_force=WBMG_C16_stress*(sqr(5.999)*PI/4)
```

WBMG_C16_displacement=WBMG_C16_strain*5.988/100

WBMG_C16_disp_corrected=WBMG_C16_displacement-WBMG_C16_force*0.0000029

WBMG_C16_disp_corrected%=100/5.988*WBMG_C16_disp_corrected

WBMG_C16_disp_corrected%=smo(WBMG_C16_disp_corrected%,3e-5)

;plot stress-strain curve and cut

stress_strain_WBMG_C16=xy(WBMG_C16_disp_corrected%,WBMG_C16_stress)

stress_strain_sg_WBMG_C16=xy(WBMG_C16_sg_cut,WBMG_C16_stress_cut)

stress_strain_WBMG_C16_cut=cut(stress_strain_WBMG_C16,0,17)

The 0.2% yield stress and failure stress were then determined as follows:

;0.2% offset YS line, input elastic modulus (2200) and y intercept (-440)

X=ramp(0.2,0.1,100)

Y=2200*X-440

YS=xy(X,Y)

;Ultimate (failure) stress

UFS=max(stress_strain_WBMG_C16_cut)

A.2.1 Sequence for Calculation of Stress from Strain Gauge on Machine

This section gives the sequence used for calculating stress from the voltage measured using the strain gauge on the machine.

; NAME: dw_stress

; Stress calculation for Drop Weight Test

; 2 strain gages measure stress, 350 ohm each

; Amplification = 100

; 1.PARAMETER: name of result file

; 2.PARAMETER: specimen diameter (mm)

; 3.PARAMETER: machine strain gage voltage [V]

; 4.PARAMETER: begin time [sec]

; 5.PARAMETER: end time [sec]

FAMOS

PA1=tds_ch2

PA1=smo(PA1,1e-5)

C=cut(PA1,xoff?(PA1),(xdel?(PA1)*600))

A=mean(C)

B=PA3*0.001555

AREA=sqr(PA2)*PI/4

PA1=((PA1-A)/B/AREA)*1000

PA1=cut(PA1,PA4,PA5)

Yunit PA1 MPa

delete A

delete B

delete C

delete AREA

A.2.2 Sequence for Calculation of Strain from Optical Sensor

This section gives the sequence used for calculating strain from the voltage measured using the optical sensor on the machine. The sTri function cuts the data with the given upper and lower y limits. The peaks function then counts the number of peaks recorded in the data. Each peak corresponds to an increment in displacement.

; NAME: dw_strain

; Strain calculation for Drop Weight Test

; strain measured using optical system on machine

; 1.PARAMETER: name of result file

; 2.PARAMETER: sample height (mm)

; 3.PARAMETER: stress file name (used as a reference)

FAMOS

PA1=tds_ch1

A=sTri(PA1,2,1.5)

C=(peaks(A))*2

A=all0(A)

B=ramp(0,1,C)

PA1=xy(A,B)

PA1=PA1*0.002

PA1=100/PA2*PA1

PA1=smo(PA1,1e-5)

PA1=rsamp(PA1,PA3)

Yunit PA1 %

delete A

delete B

delete C

A.2.3 Sequence for Calculation of Strain from Strain Gauge on Specimen

This section gives the sequence used for calculating strain from the voltage measured using the strain gauge on the specimen.

; NAME: dw_sg

; Strain Gauge calculation for Drop Weight Test

; strain measured using strain gauge on specimen

; Amplification = 100

; 1.PARAMETER: name of result file

; 2.PARAMETER: bridge factor (=2 for half bridge)

; 3.PARAMETER: voltage (V)

; 4.PARAMETER: strain gauge k factor

; 5.PARAMETER: input strain gauge file name

FAMOS

PA1=(PA2*PA5*100)/(PA3*100*PA4)

PA1=smo(PA1,2e-5)

Yunit PA1 %

A.3 Split Hopkinson Pressure Bar Data Analysis

This section describes the data analysis for the Split Hopkinson Pressure Bar experiments. The FAMOS script is given below for compression specimen number 10.

;SHPB stress-strain

The reflected wave was isolated from the data recorded from the strain gauge on the incident bar.

;cut incident bar data to only include reflected wave, input time window

IncBar_WBMG_C10_cut=cut(IncBar_WBMG_C10,0.00027031,0.0005841)

A sequence was used to calculate strain from the incident bar reflected wave. The sequence is given below in Section A.3.1 and the inputs correspond to the specimen height, input voltage, file containing incident bar reflected wave, and name for new file containing strain data.

;incident bar: voltage->displacement->strain

sequence displacement 6.006 5.098 IncBar_WBMG_C10_cut strain_WBMG_C10

Next, a sequence was used to calculate stress from the signal recorded by the strain

gauge on the transmitted bar. This sequence is given in Section A.3.2 and the inputs correspond to new file name for stress data, specimen diameter, output voltage, and file containing raw data.

;transmitted bar: voltage->stress

sequence stress stress_WBMG_C10 6.005 5.123 TransBar_WBMG_C10

The stress trace needed to be zeroed:

;zero stress, input offset from zero

stress_WBMG_C10_zero=stress_WBMG_C10-210

and the data was smoothed to reduce the noise:

;smooth stress data

stress_WBMG_C10_zero_smooth=smo(stress_WBMG_C10_zero,3e-6)

A third sequence was required for specimens which utilized strain gauges. This sequence converted the strain gauge voltage signal to strain, as described for quasi-static tests. This sequence is given in Section A.3.3 and the input values correspond to the value of the Wheatstone Bridge (2 for half bridge), name of file containing raw data, voltage running through strain gauge, k-factor of strain gauge, and name for new file containing strain data.

;strain gauge: voltage->strain

sequence straingauge 2 SG_WBMG_C10 1.790 1.98 strain_gauge_WBMG_C10

Next, all three traces (stress and both strain) needed to be transferred to the same time scale, using the strain calculated from the specimen strain gauges as a reference. Once all three traces were starting at the same time, they were grouped together and the sampling rates were adjusted such that they were all the same for plotting purposes.

;move incident bar strain data and stress data to strain gauge->change X0

;group 3 traces together under name data

;make all data have same sampling rate

data_edit=rsamp(data,data:stress_WBMG_C10_zero_smooth)

The two strain traces were combined such that the strain gauge data was used during the beginning of deformation until it was damaged (~2%) and then the strain data from the incident bar was used thereafter.

;combine strain data from strain gauge and from incident bar

strain_gauge_WBMG_C10_cut=cut(data_edit:strain_gauge_WBMG_C10,0,0.000175)

strain_WBMG_C10_cut=cut(data_edit:strain_WBMG_C10,0.000175,0.000427)

strain_WBMG_C10_combo=

join(strain_gauge_WBMG_C10_cut,strain_WBMG_C10_cut)

The data was cut to only include the relevant time window, and then plotted and cut further, if necessary.

;cut data

stress_WBMG_C10_zero_smooth_cut=

cut(data:stress_WBMG_C10_zero_smooth,0,0.000427)

strain_WBMG_C10_cut=cut(strain_WBMG_C10_combo,0,0.000427)

;plot stress-strain curve

stress_strain_WBMG_C10=

xy(strain_WBMG_C10_cut,stress_WBMG_C10_zero_smooth_cut)

;cut

stress_strain_WBMG_C10_cut=cut(stress_strain_WBMG_C10,0,28.8)

Finally, the 0.2% yield stress was determined by plotting a line:

;0.2% offset YS line, input elastic modulus (2200) and y intercept (-440)

X=ramp(0.2,0.1,100)

Y=2200*X-440

YS=xy(X,Y)

and the ultimate/failure stress was determined:

;Ultimate (failure) stress

UFS=max(stress_WBMG_CS7_zero_smooth_cut)

A.3.1 Sequence for Calculation of Strain from Incident Bar

The following sequences were adapted from those written by Stefan Syla. This section describes the calculation of strain from the strain gauge on the incident bar, as was described in Section 3.3.4.

; NAME: Displacement_IncBar

;15.05.2000 / Stefan Syla

;calculate the displacement from the reflected wave of the input bar

;Displacement calculation

; bar (2X2) active strain gauge (350 Ohm) k=3.22

; Amplification 100

; 1.PARAMETER: sample height (mm)

; 2.PARAMETER: input voltage (V)

; 3.PARAMETER: name of cut IncBar file

; 4.Parameter: new file name

FAMOS

A=PA3*(-1)

B=(2*A*100)/(PA2*100*3.22)

er=INT(HILF2)

PA4=((2*4772000)/PA1)*er

;actual value 4772000 m/s

Yunit PA4 %

delete A

delete B

delete er

A.3.2 Sequence for Calculation of Stress from Transmitted Bar

This section describes the calculation of stress from the strain gauge on the transmitted bar, as was described in Section 3.3.4.

; NAME:stress_TransBar

; Stress calculation for Hopkinson bar 20mm (corrected Sequence, without factor)

; effective from 8.11.2000

; 1.PARAMETER: name of result file

; 2.PARAMETER: specimen diameter (mm)

; 3.PARAMETER: output voltage [V]

; 4.PARAMETER: measurement file name (channel 2)

;————————Bridge factor————————————

B=2

;————————Measured signal————————————

ub=PA4

;————————Elastic modulus of bar————————-

;calculated using measured value of sound speed vc=4772000 mm/s

;and density 7.97 g/cm^3

;em=roh*vc^2

em=181500

;————————Bar diameter————————————

dbar=19.66

;————————input terminal voltage————————

us=PA3

;————————Amplification factor————————-

```
ktex=100
;————————————k-factor of strain gauge on bar————————————
ksg=3.22
;————————————————————————————————————————
FAMOS
;————————————————-sample area and bar area calculation————————-
s0 = sqr (PA2) * PI / 4
sk = sqr (dbar) * PI / 4
;————————————————-stress calculation————————————————-
PA1 = (b*ub*em*sk)/(us*ktex*ksg*s0)
;————————————————-set units————————————————————-
Yunit PA1 MPa
;————————————————-clean up————————————————————
delete s0
delete b
delete ub
delete em
delete sk
delete us
delete ktex
delete kdms
delete dbar
```

A.3.3 Sequence for Calculation of Strain from Strain Gauges on Specimen

This section describes the calculation of strain from the strain gauges on the specimen, as was described for quasi-static tests in Section 3.3.2.

```
    ;NAME:strain_strain-gauge
;Strain calculation strain gauge
;09.05.2000 Stefan Syla
; 1.PARAMETER: Bridge factor B (2=half bridge,4=quarter bridge,1=full bridge)
; 2.PARAMETER: file name
; 3.PARAMETER: voltage over strain gauge
; 4.PARAMETER: K-Factor of strain gauge
; 5.PARAMETER: new file name
; fixed amplification value of 100 !!!
FAMOS
PA5=(PA1*PA2*100)/(PA3*PA4*100)
Yunit PA5 %
```

APPENDIX B

ERROR PROPAGATION ANALYSIS

The following error propagation analyses were derived based on the theory described by Taylor [153]. This analysis was used to insure that in as much as possible all error associated with these experiments was captured accurately as it propagated throughout calculations to yield final results. In all of the following equations, δ_z is the value of error associated with the measurement of each respective parameter, z, which is notated as a the subscript of δ. The error has units corresponding to those of parameter z.

B.1 Error in Measurements Taken from High-Speed Images during Taylor Tests

Much of the data from Taylor impact experiments is derived from measurements taken on the high-speed camera images. This error propagation analysis helps to quantify the error derived from the resolution of the camera and the human factor of making repeated measurements. The variables relevant to the measurements made on the high-speed camera images are given in Table B.1.

The specimen diameter was measured according to:

$$d = \frac{D}{R_D} = \frac{D}{D_0/d_0} = \frac{Dd_0}{D_0}$$

As such, the error associated with measurement of the specimen diameter is:

$$\delta_d = d\sqrt{\left(\frac{\delta_D}{D}\right)^2 + \left(\frac{\delta_{d_0}}{d_0}\right)^2 + \left(\frac{\delta_{D_0}}{D_0}\right)^2}$$

Correspondingly, specimen radius is measured according to:

$$r = \frac{D}{2R_D} = \frac{D}{2(D_0/d_0)} = \frac{Dd_0}{2D_0}$$

and error associated with measurement of the specimen radius is:

$$\delta_r = r\sqrt{\left(\frac{\delta_D}{D}\right)^2 + \left(\frac{\delta_{d_0}}{d_0}\right)^2 + \left(\frac{\delta_{D_0}}{D_0}\right)^2}$$

Table B.1: Variables associated with error propagation originating with measurements taken on high-speed images captured during Taylor impact tests.

Variable	Definition	Units
A_0	initial cross-sectional area of impact face	m^2
A	cross-sectional area of impact face at time when strain is measured	m^2
d_0	initial diameter of impact face	m
d	diameter of impact face at time when strain is measured	m
D_0	initial diameter of impact face measured from static image	px
D	diameter of impact face at time when strain is measured	px
ε_{areal}	areal strain, as defined by Taylor [57]	none
ε_{axial}	areal strain, as defined by Wilkins [58]	none
l_0	initial length of sample	m
l	length of sample at time when strain is measured	m
L_0	initial length of sample measured from static image	px
L	length of sample at time when strain is measured	px
r_0	initial radius of impact face	m
r	radius of impact face at time when strain is measured	m
R_D	image resolution over sample diameter ($= \frac{D_0}{d_0}$)	px/m
R_L	image resolution over sample length ($= \frac{L_0}{l_0}$)	px/m

Specimen length was measured according to:

$$l = \frac{L}{R_L} = \frac{L}{L_0/l_0} = \frac{Ll_0}{L_0}$$

Error associated with measurement of the specimen length is as follows:

$$\delta_l = l\sqrt{\left(\frac{\delta_L}{L}\right)^2 + \left(\frac{\delta_{l_0}}{l_0}\right)^2 + \left(\frac{\delta_{L_0}}{L_0}\right)^2}$$

Areal strain, as defined by Taylor [57], was determined according to:

$$\varepsilon_{areal} = 1 - \frac{A}{A_0} = 1 - \frac{r_0^2}{r^2} = 1 - \frac{d_0^2}{d^2} = 1 - \frac{d_0^2}{(D/R_D)^2} = 1 - \frac{d_0^2}{\left(\frac{D}{D_0/d_0}\right)^2} = 1 - \frac{D_0^2}{D^2}$$

and the error associated with that measurement is:

$$\delta_{\varepsilon_{areal}} = \sqrt{\left(\frac{\partial\varepsilon}{\partial D_0}\right)^2 \delta_{D_0}^2 + \left(\frac{\partial\varepsilon}{\partial D}\right)^2 \delta_D^2} = \sqrt{\left(\frac{-2D_0}{D^2}\right)\delta_{D_0}^2 + \left(\frac{2D_0^2}{D^3}\right)^2 \delta_D^2} = 2\sqrt{\frac{D_0^2}{D^4}\delta_{D_0}^2 + \frac{D_0^4}{D^6}\delta_D^2}$$

Similarly, axial strain, as defined by Wilkins [58], was measured according to:

$$\varepsilon_{areal} = -\ln\left(\frac{l}{l_0}\right) = -\ln\left(\frac{L/R_L}{l_0}\right) = -\ln\left(\frac{\frac{L}{(L_0/l_0)}}{l_0}\right) = -\ln\left(\frac{L}{L_0}\right)$$

and the error associated with this measurement is defined as:

$$\delta_{\varepsilon_{axial}} = \sqrt{\left(\frac{\partial\varepsilon}{\partial L}\right)^2 \delta_L^2 + \left(\frac{\partial\varepsilon}{\partial L_0}\right)^2 \delta_{L_0}^2} = \sqrt{\left(\frac{-1/L_0}{L/L_0}\right)^2 \delta_L^2 + \left(\frac{-\left(-L/L_0^2\right)}{L/L_0}\right)^2 \delta_{L_0}^2} = \sqrt{\frac{1}{L^2}\delta_L^2 + \frac{1}{L_0^2}\delta_{L_0}^2}$$

Table B.2: Variables associated with error propagation originating with measurements taken on high-speed images captured during Taylor impact tests.

Variable	Definition	Units
α	angle between the inclined mirror and the sample	radians
d	distance between the outer mirrors measured from the image	px
D	physically measured distance between the outer mirrors	m
γ	streak angle measured from the streak image	radians
h	sample thickness	m
M	image magnification	none
P	pressure	Pa
r	resolution of the streak image	px/m
R	resolution if the image of the mirrors	px/m
ρ	current material density	g/cm^3
ρ_0	starting material density	g/cm^3
t	travel time of shock wave through sample	s
t_f	time shock wave arrives at front of sample	s
t_b	time shock wave arrives at back of sample	s
Δt	travel time of shock wave between first phase and second phase	s
U_{fs}	free surface velocity	m/s
U_p	particle velocity	m/s
U_s	shock velocity	m/s
V	current material volume	m^3
V_0	starting material volume	m^3
W	streak rate	s/m
x	travel time of the shock wave through the sample	px
X	travel time of the shock wave between first and second phase	px

B.2 Error Propagation in Equation of State Measurements

Determination of equation of state data also required measurement from images (streak camera), which was one source of error, and additionally, there was error associated with the inclined mirror method for determining U_p and U_{fs}, as well as with the PVDF gauge and VISAR measurements. The variables relevant to the equation of state experiments (both experimental setups) in Table B.2:

Streak image magnification is defined as:

$M = \frac{d}{RD}$

The error associated with determination of the image magnification is:

$\delta_M = M\sqrt{\left(\frac{\delta_d}{d}\right)^2 + \left(\frac{\delta_R}{R}\right)^2 + \left(\frac{\delta_D}{D}\right)^2}$

For the streak camera experimental setup, the travel time of the shock wave through the thickness of the specimen is measured as:

$t = \frac{xW}{r}$

and the error associated with this measurement is:

$\delta_t = t\sqrt{\left(\frac{\delta_x}{x}\right)^2 + \left(\frac{\delta_W}{W}\right)^2 + \left(\frac{\delta_r}{r}\right)^2}$

When using PVDF gauges, the travel time of the shock wave through the specimen thickness is measured as:

$t = t_b - t_f$

and the corresponding error is:

$\delta_t = \sqrt{(\delta_{t_b})^2 + \left(\delta_{t_f}\right)^2}$

In the case when a phase transition was observed as a kink in the streak camera image, the travel time of the shock wave between the first and second phases is:

$\Delta t = \frac{XW}{r}$

and the associated error is:

$\delta_{\Delta t} = \Delta t\sqrt{\left(\frac{\delta_X}{X}\right)^2 + \left(\frac{\delta_W}{W}\right)^2 + \left(\frac{\delta_r}{r}\right)^2}$

Particle velocity was measured from streak camera images using the inclined mirror method according to:

$U_{p1} = \frac{1}{2}U_{fs1} = \frac{1}{2}\frac{W}{M}\frac{\tan\alpha}{\tan\gamma_1}$

The error associated with measurement of particle velocity is:

$\delta_{U_{p1}} = U_{p1}\cdot\frac{1}{2}\sqrt{\left(\frac{\delta_W}{W}\right)^2 + \left(\frac{\delta_{\tan\alpha}}{\tan\alpha}\right)^2 + \left(\frac{\delta_M}{M}\right)^2 + \left(\frac{\delta_{\tan\gamma_1}}{\tan\gamma_1}\right)^2}$

If applicable, the particle velocity of the second phase is:

$U_{p2} = \frac{1}{2}U_{fs1} = \frac{1}{2}\frac{W}{M}\frac{\tan\alpha}{\tan\gamma_2}$

and its associated error is: $\delta_{U_{p2}} = U_{p2}\cdot\frac{1}{2}\sqrt{\left(\frac{\delta_W}{W}\right)^2 + \left(\frac{\delta_{\tan\alpha}}{\tan\alpha}\right)^2 + \left(\frac{\delta_M}{M}\right)^2 + \left(\frac{\delta_{\tan\gamma_2}}{\tan\gamma_2}\right)^2}$

When using the streak camera experimental setup, the shock velocity was measured as:

$U_{s1} = \frac{hr}{xW}$

and the associated error is given as:

$\delta_{U_{s1}} = U_{s1}\sqrt{\left(\frac{\delta_h}{h}\right)^2 + \left(\frac{\delta_r}{r}\right)^2 + \left(\frac{\delta_x}{x}\right)^2 + \left(\frac{\delta_W}{W}\right)^2}$

In the case of a phase transition, the shock velocity of the second phase is measured as:

$$U_{s2} = \frac{h+U_{fs1}\Delta t}{t+\Delta t}$$

and the error is defined as:

$$\delta_{U_{s2}} = \sqrt{\left(\frac{\partial U_{s2}}{\partial h}\right)^2 \delta_h^2 + \left(\frac{\partial U_{s2}}{\partial U_{fs1}}\right)^2 \delta_{U_{fs1}}^2 + \left(\frac{\partial U_{s2}}{\partial \Delta t}\right)^2 \delta_{\Delta t}^2 + \left(\frac{\partial U_{s2}}{\partial t}\right)^2 \delta_t^2}$$

$$= \sqrt{\left(\frac{1}{t+\Delta t}\right)^2 \delta_h^2 + \left(\frac{\Delta t}{t+\Delta t}\right)^2 \left(2\delta_{U_{p1}}\right)^2 + \left(\frac{(t+\Delta t)U_{fs1}-\left(h+U_{fs1}\Delta t\right)}{(t+\Delta t)^2}\right)^2 \delta_{\Delta t}^2 + \left(\frac{-\left(h+U_{fs1}\Delta t\right)}{(t+\Delta)^2}\right)^2 \delta_t^2}$$

$$= \sqrt{\frac{\delta_h^2+\left(2\Delta t\delta_{U_{p1}}\right)^2}{(t+\Delta t)^2} + \frac{\left(tU_{fs1-h}\right)^2\delta_{\Delta t}^2+\left(h+U_{fs1}\Delta t\right)^2\delta_t^2}{(t+\Delta t)^4}}$$

The shock velocity measurement when using PVDF gauge instrumentation is done according to:

$$U_s = \frac{h}{t}$$

and the associated error is:

$$\delta_{U_s} = U_s \sqrt{\left(\frac{\delta_h}{h}\right)^2 + \left(\frac{\delta_t}{t}\right)^2}$$

Pressure was calculated from measured quantities according to:

$$P_1 = \rho_0 U_{s1} U_{p1}$$

with associated error of:

$$\delta_{P_1} = P_1 \sqrt{\left(\frac{\delta_{\rho_0}}{\rho_0}\right)^2 + \left(\frac{\delta_{U_{s1}}}{U_{s1}}\right)^2 + \left(\frac{\delta_{U_{p1}}}{U_{p1}}\right)^2}$$

The pressure of the second phase, if applicable, and its associate error were calculated in a similar manner.

Compressibility was also a calculated quantity and was calculated by:

$$\left(\frac{V}{V_0}\right)_1 = 1 - \frac{U_{p1}}{U_{s1}}$$

with error of:

$$\delta_{(V/V_0)_1} = \sqrt{\left(\frac{\partial (V/V_0)_1}{\partial U_{p1}}\right)^2 \delta_{U_{p1}}^2 + \left(\frac{\partial (V/V_0)_1}{\partial U_{s1}}\right)^2 \delta_{U_{s1}}^2} = \sqrt{\left(\frac{-1}{U_{s1}}\right)^2 \delta_{U_{p1}}^2 + \left(\frac{U_{p1}}{U_{s1}^2}\right) \delta_{U_{s1}}^2}$$

and similarly for the compressibility of the second phase.

Density is derived from measured quantities according to:

$$\rho_1 = \frac{\rho_0}{1-\left(\frac{U_{p1}}{U_{s1}}\right)}$$

with associated error of:

$$\delta_{\rho_1} = \sqrt{\left(\frac{\partial \rho_1}{\partial \rho_0}\right)^2 \delta_{\rho_0}^2 + \left(\frac{\partial \rho_1}{\partial Up1}\right)^2 \delta_{U_{p1}}^2 + \left(\frac{\partial \rho_1}{\partial U_{s1}}\right)^2 \delta_{U_{s1}}^2}$$

$$= \sqrt{\left(\frac{1}{1-\left(U_{p1}/U_{s1}\right)}\right)^2 \delta_{\rho_0}^2 + \left(\frac{U_{s1}\rho_0}{\left(U_{s1}-U_{p1}\right)^2}\right)^2 \delta_{U_{p1}}^2 + \left(\frac{\left(U_{s1}-U_{p1}\right)\rho_0 - U_{s1}\rho_0}{\left(U_{s1}-U_{p1}\right)^2}\right)^2 \delta_{U_{s1}}^2}$$

$$= \sqrt{\frac{\left(U_{s1}\delta_{\rho_0}\right)^2\left(U_{s1}-U_{p1}\right)^2 + \left(U_{s1}\rho_0\delta_{U_{p1}}\right)^2 + \left(U_{p1}\rho_0\delta_{U_{s1}}\right)^2}{\left(U_{s1-U_{p1}}\right)^4}}$$

and similarly for the density of the second phase.

APPENDIX C

MATLAB SCRIPTS USED FOR DATA ANALYSIS

The following scripts were used in MATLAB to assist with data analysis.

C.1 MATLAB Script for Creating Contour Plots of Hardness Data on Impact Face of Recovered Taylor Specimen

This script was used to create a contour plot from the hardness data that was measured by doing indentations in a grid on a quarter of the impact face of a recovered impacted specimen.

function data = contourHalf(excelfile,sheet,contoursVec)

%takes in an excel file of one quadrant of a sample and returns a contour map of the hardness of that sample.

%excelfile = 'filename', sheet ='sheet name', and contoursVec = [vector of lines to be shown]

%example: contourHalf('justHalfData.xls','quarter',[300 350 400 430 440 450 460 470 480 490 500 505]) would return a contour from the given inputs; origData = xlsread(excelfile,sheet);

[*col*, *row*] = size(origData)

data = zeros(2*col,2*row);

%horizontal Mirror

for k = 1:col

for j = 1:row

data(k,j)=origData(k,j);

data(k,2*row+1-j)=origData(k,j);

```
data(2*col+1-k,j)=origData(k,j);
data(2*col+1-k,2*row+1-j)=origData(k,j);
end
end
[C, h1] = contour(interp2(data,4),contoursVec);
%text_handle = clabel(C,h1);
%set(text_handle,'BackgroundColor',[1 1 .6],...
% 'Edgecolor',[.7 .7 .7])
legend('Hardness')
end
```

C.2 MATLAB Script for Regression Fitting of Birch-Murnaghan Equation

The following is the MATLAB script that was applied to use least-squares regression to determine the values of the variables K_0 (bulk modulus), K_0' (pressure derivative of bulk modulus) and ρ_0' (zero pressure density of the high pressure phase) in the Birch-Murnaghan Equation of State for the high pressure phase:

First, three data sets were loaded:

```
load k.txt
load p.txt
load v.txt
```

The 'k' data set is approximate starting values for the bulk modulus and pressure derivative of bulk modulus, and 'p' and 'v' are pressure and corresponding volume (current volume normalized by initial volume) data obtained from experiments, respectively. Next, the function was defined:

```
function p = birch(K,V)
```

k1 = K(1);

k2 = K(2);

v1 = V(:,1);

$p = 1.5. * k(1). * (v(:,1).^(7/3) - (v(:,1)).^(5/3)). * (1 + 3. * (k(2)./4 - 1). * (v(:,1).^(2/3) - 1));$

Finally, the non-linear regression was performed to find the values of bulk modulus, pressure derivative of bulk modulus, and zero-pressure density of the high pressure phase that provided the best fit to the experimental data:

kfit=nlinfit(v,p,'birch',k)

REFERENCES

[1] Inoue, A. *Acta Mater* **48**, 279 (2000).

[2] Jiao, T., Kecskes, L., Hufnagel, T., and Ramesh, K. *Metall Mater Trans* **35A**, 3439–3444 (2004).

[3] Conner, R., Choi-Yim, H., and Johnson, W. *Journal of Materials Research* **14**(8), 3292–3297 (1999).

[4] Choi-Yim, H., Conner, R., Szuecs, F., and Johnson, W. *Acta Materialia* **50**, 2737–2745 (2002).

[5] Choi-Yim, H., Schroers, J., and Johnson, W. *Appl Phys Lett* **80**(11), 1906–1908 (2002).

[6] Choi-Yim, H., Conner, R., Szuecs, F., and Johnson, W. *Scripta Materialia* **45**, 1039–1045 (2001).

[7] Choi-Yim, H., Busch, R., Koster, U., and Johnson, W. L. *Acta Materialia* **47**(8), 2455–2462 (1999).

[8] Li, H., Subhash, G., Gao, X.-L., Kecskes, L., and Dowding, R. *Scripta Mater* **49**, 1087–1092 (2003).

[9] Li, H., Subhash, G., Kecskes, L., and Dowding, R. *Materials Science and Engineering* **A403**, 134–143 (2005).

[10] Klement, W. I., Willens, R. H., and Duwez, P. *Nature* **187**, 869 (1960).

[11] Johnson, W. *Progress in Materials Science* **30**, 81 (1986).

[12] Yeh, X. L., Samwer, K., and Johnson, W. L. *Applied Physics Letters* **42**, 242 (1983).

[13] van Diepen, A. M. and Buschow, K. H. J. *Solid State Communications* **22**, 113 (1977).

[14] Aning, A. O., Wang, Z., and Courtney, T. H. *Acta Metallurgica Materialia* **41**(1), 165–174 (1993).

[15] Schwarz, R. B. and Johnson, W. L. *Physics Review Letters* **51**, 415 (1983).

[16] Conner, R. D., Dandliker, R. B., and Johnson, W. L. *Acta Materialia* **46**(17), 455–468 (1998).

[17] Peker, A. and Johnson, W. L. *Applied Physics Letters* **63**, 2342 (1993).

[18] Telford, M. *Materials Today* , 36–43 (2004).

[19] Liu, C., Heatherly, L., Easton, D., Carmichael, C., Schneiberl, J., and Chen, C. *Metallurgical and Materials Transactions A* **29**(7), 1811 (1998).

[20] A. Inoue, C. Fan, J. S. and Zhang, T. *Science and Technology of Advanced Materials* **1**, 73–86 (2000).

[21] Li, J., Shan, G., Gao, K., Qiao, L., and Chu, W. *Materials Science and Engineering* **A354**, 337–343 (2003).

[22] Lund, A. and Schuh, C. *Intermetallics* **12**, 1159–1165 (2004).

[23] Donovan, P. *Acta Materialia* **37**, 445 (1988).

[24] Spaepen, F. *Acta Materialia* **25**, 407–415 (1977).

[25] Wright, W., Schwarz, R., and Nix, W. *Materials Science and Engineering* **A319-321**, 229–232 (2001).

[26] Jiang, W. H. and Atzmon, M. *Acta Materialia* **51**, 4095 (2003).

[27] Li, J., Spaepen, F., and Hufnagel, T. C. *Philosophical Magazine* **A82**, 2623–2630 (2002).

[28] Zhang, Z., Eckert, J., and Schultz, L. *Acta Materialia* **51**, 1167–1179 (2003).

[29] Lu, J. *Mechanical behavior of a bulk metallic glass and its composite over a wide range of strain rates and temperatures*. PhD thesis, California Institute of Technology, (2002).

[30] Heilmaier, M. and Eckert, J. *Advanced Engineering Materials* **7**(9), 833–841 (2005).

[31] Donovan, P. *Acta Materialia* **37**(2), 445–456 (1989).

[32] Leamy, H. J., Chen, C. H., and Wang, T. T. *Metallurgical and Materials Transaction* **A3**, 699 (1972).

[33] Pampillo, C. A. and Reimschuessel, A. C. *Journal of Materials Science* **9**(5), 718 (1974).

[34] Spaepen, F. and Turnbull, D. *Scripta Metallurgica* **8**, 563 (1974).

[35] Saffman, P. G. and Taylor, G. I. *Proceedings of the Royal Society of London* **A245**, 312 (1958).

[36] Lewandowski, J. and Greer, L. *Nature Materials* **5**, 15 (2006).

[37] Zhang, Y., Stelmashenko, N., Barber, Z., Wang, W., Lewandowski, J., and Greer, A. *Journal of Materials Research* **22**(2), 419–427 (2003).

[38] Schuh, C. and Nieh, T. *Acta Mater* **51**, 87–99 (2003).

[39] Xing, L. Q., Hufnagel, T. C., and Ramesh, K. T. In *International Journal of Impact Engineering*, L11.7.1–L11.7.6, (2001).

[40] Davis, L. A. *Mechanical Behavior of Rapidly Solidified Materials*. Metall. Soc., (1989).

[41] Wright, W. J., Saha, R., and Nix, W. D. *Mater Trans JIM* **42**, 642 (2001).

[42] Lowhaphandu, P., Montgomery, S., and Lewandowski, J. *Scripta Mater* **41**(19), 19–24 (1999).

[43] Lowhaphandu, P., Ludrosky, L., Montgomery, S., and Lewandowski, J. *Intermetallics* **8**, 487–492 (2000).

[44] He, G., Lu, J., Bian, Z., Chen, D., Chen, G., and Tu, G. *Mater Trans* **42**(2), 356 (2001).

[45] Mukai, T., Nieh, T., Kawamura, Y., Inoue, A., and Higashi, K. *Intermetallics* **10**, 1071–1077 (2002).

[46] Takayama, S. *Scripta Materialia* **13**, 463 (1979).

[47] Subhash, G., Dowding, R., and Kecskes, L. *Materials Science and Engineering A* **334**, 33–40 (2002).

[48] Owen, D. M., Rosakis, A. J., and Johnson, W. L. In *Materials Research Society Symposium Proceedings*, volume 554, 419–430, (1999).

[49] Bruck, H., Rosakis, A., and Johnson, W. *J Mater Res* **11**(2), 503–511 (1996).

[50] Sun, J.-F., Yang, M., and Shun, J. *Trans Nonferrous Met Soc China* **15**(2), 115–119 (2005).

[51] Sunny, G., Yuan, F., Lewandowski, J., and Prakash, V. In *Proceedings of the 2005 SEM Annual Conference and Exposition on Experimental and Applied Mechanics*, volume 324, 157–164 (, Celevland, OH, 2005).

[52] Torre, F. D., Dubach, A., Siegrist, M., and Loffler, J. *Applied Physics Letters* **89**, 092928–1–3 (2006).

[53] Hufnagel, T., Jiao, T., Li, Y., Xing, L., and Ramesh, K. *Journal of Materials Research* **17**, 1441–1445 (2002).

[54] Gu, X., Jiao, T., Kecskes, L., Woodman, R., Fan, C., Ramesh, K., and Hufnagel, T. *Journal of Non-Crystalline Solids* **317**, 112–117 (2003).

[55] Cline, C. and Reaugh, J. *Journal De Physique. IV* **7**, C3–493–496 (1997).

[56] Cline, C. and Reaugh, J. *Journal De Physique. IV* **1**, C3–139–146 (1991).

[57] Taylor, G. I. *Proc. Roy. Soc. London* **A-194**, 289–299 (1948).

[58] Wilkins, M. L. and Guinan, M. W. *Journal of Applied Physics* **44**(3), 1200–1206 (1973).

[59] Liu, L., Dai, L., Bai, Y., Wei, B., and Yu, G. *Intermetallics* **13**, 827–832 (2005).

[60] Kawamura, Y., Shibata, T., Inoue, A., and Masumoto, T. *Acta Metallurgica* **37**(4), 431–436 (1997).

[61] Masumoto, T. and Maddin, R. *Acta Metallurgica* **19**, 725–741 (1971).

[62] Lu, J., Ravichandran, G., and Johnson, W. *Acta Mater* **51**, 3429–3443 (2003).

[63] Zhuang, S., Lu, J., and Ravichandran, G. *Applied Physics Letters* **80**(24), 4522–4524 (2002).

[64] Yuan, F., Prakash, V., and Lewandowski, J. *Journal of Materials Research* **22**(2), 402–411 (2007).

[65] Antoun, T., Seaman, L., Curran, D., Kanel, G., Razorenov, S., and Utkin, A. *Spall Fracture*. High-Pressure Shock Compression of Condensed Matter. Springer, (2003).

[66] Turneaure, S. J., Winey, J. M., and Gupta, Y. M. *Applied Physics Letters* **84**(10), 1692–1694 (2004).

[67] Mashimo, T. *High-Pressure Shock Compression of Solids III*, chapter Effect of shock compression on ceramic materials, 101–146. Springer-Verlag, New York (1998).

[68] Mashimo, T., Togo, H., Zhang, Y., Uemura, Y., Kinoshita, T., and Kawamura, Y. *Applied Physics Letters* **89**, 241904–1–241904–3 (2006).

[69] de Hey, P., Sietsma, J., and den Beukel, A. V. *Acta Materilia* **46**, 5873 (1998).

[70] Wang, G., Shen, J., Sun, J., Lu, Z., Stachurski, Z., and Zhou, B. *Materials Science and Engineering* **A398**, 82–87 (2005).

[71] Wang, Q., Pelletier, J., Blandin, J., and Suery, M. *Journal of Non-Crystallien Solids* **351**, 2224–2231 (2005).

[72] Lewandowski, J. and Lowhaphandu, P. *Philosophical Magazine* **A82**(17/18), 3427–3441 (2002).

[73] Davis, L. and Kavesh, S. *J Mater Sci Lett* **10**(3), 453–459 (1975).

[74] Patnaik, M., Narasimhan, R., and Ramamurty, U. *Acta Mater* **52**, 3335–3345 (2004).

[75] Vaidyanathan, R., Dao, M., Ravichandran, G., and Suresh, S. *Acta Materialia* **3781-3789**, 3781–3789 (2001).

[76] Rottler, J. and Robbins, M. O. *Physical Review* **E64**(051801), 1–8 (2001).

[77] Flores, K. M. and Dauskardt, R. H. *Acta Materialia* **49**, 2527 (2001).

[78] Lu, J. and Ravichandran, G. *J Mater Res* **18**(9), 2039–2049 (2003).

[79] Drucker, D. and Prager, W. *Quarterly of Applied Mathematics* **10**(2), 157–165 (1952).

[80] Kim, J.-J., Choi, Y., Suresh, S., and Argon, A. S. *Science* **295**(5555), 654 (2002).

[81] Boucharat, N., Hebert, R., Rosner, H., Valiev, R., and Wilde, G. *Scripta Materialia* **53**, 823–827 (2005).

[82] Lohwongwatana, B., Schroers, J., and Johnson, W. L. *Physical Review Letters* **96**, 075503(4) (2006).

[83] Jiang, J., Zhou, T., Rasmussen, H., Kuhn, U., Eckert, J., and Lathe, C. *Applied Physics Letters* **77**(22), 3553–3555 (2000).

[84] Pan, M., Wang, W., Zhao, D., Bao, Z., Zhang, W., and Zhang, S. *Journal of Physics: Condensed Matter* **14**, 5665–5670 (2002).

[85] Wang, L., Zhan, Z., Liu, J., Sun, L., Li, G., and Wang, W. *Journal of Physics Condensed Matter* **13**, 5743–5748 (2001).

[86] Gong, L., Zhan, Z.-J., Wang, L.-M., Sun, L.-L., Liu, J., and Wang, W.-K. *Chinese Physical Letters* **21**(5), 898–900 (2004).

[87] Togo, H., Zhang, Y., Kawamura, Y., and Mashimo, T. *Materials Science and Engineering A* **449-451**, 264–268 (2007).

[88] Wackerle, J. *Journal of Applied Physics* **33**(3), 922–937 (1963).

[89] Sheng, H., Liu, H., Cheng, Y., adn P.L. Lee, J. W., Luo, W., Shastri, S., and Ma, E. *Nature Materials* **6**, 192–197 (2007).

[90] Inoue, A. and Fan, C. *NanoStructured Materials* **12**, 741–749 (1999).

[91] C. Fan, D. V. Louzguine, C. L. and Inoue, A. *Applied Physics Letters* **75**(3), 340–342 (1999).

[92] Fan, C. and Inoue, A. *Applied Physics Letters* **77**(1), 46–48 (2000).

[93] Xing, L. Q., Eckert, J., Loser, W., and Schultz, L. *Applied Physics Letters* **74**(5), 664 (1999).

[94] Inoue, A. *Intermetallics* **8**, 455–468 (2000).

[95] Hays, C. C., Kim, C. P., and Johnson, W. L. *Physical Review Letters* **84**(13), 1087–1092 (2003).

[96] Choi-Yim, H., Busch, R., and Johnson, W. In *Materials Research Society Symposium Proceedings*, 393–398, (1999).

[97] Choi-Yim, H., Conner, R. D., and Johnson, W. L. In *Materials Research Society Symposium Proceedings*, L9.1.1–L9.1.6, (2001).

[98] Conner, R. D., Dandliker, R. B., Scruggs, V., and Johnson, W. L. *International Journal of Impact Engineering* **24**, 435–444 (2000).

[99] Loffler, J., Bossuyt, S., Glade, S., Johnson, W., Wagner, W., and Thiyagarajan, P. *Applied Physics Letters* **77**(4), 525 (2000).

[100] Meyer, L. and Krueger, L. *ASM Handbook*, volume 8, chapter High strain rate shear testing, 452–454. ASM International, Materials Park, OH (2000).

[101] http://www.sensorland.com/HowPage002.html. (October 2007).

[102] Hopkinson, B. *Roy Soc Phil Trans* **A213**, 437 (1914).

[103] Meyers, M. *Dynamic Behavior of Materials*. John Wiley and Sons, Inc., New York, (1994).

[104] Gray, G. In *Mechanical Testing and Evaluation Handbook*, volume 8, 462–476 (, Materials Park, OH, 2000).

[105] Sunny, G. *Journal of Materials Research* **22**(2), 389–401 (2007).

[106] Hawkyard, J., Eaton, D., and Johnson, W. *International Journal of Mechanical Sciences* **10**, 929–948 (1968).

[107] House, J., Lewis, J., Gillis, P., and Wilson, L. *International Journal of Impact Engineering* **16**(2), 189–200 (1995).

[108] Gillis, P. and Jones, S. *Journal of Engineering Materials and Technology* **111**, 327–330 (1989).

[109] Jones, S., Drinkard, J., Rule, W., and Wilson, L. *International Journal of Impact Engineering* **21**(1-2), 1–13 (1998).

[110] Johnson, G. and Cook, W. In *seventh International Symposium on Ballistics*, 541–547 (, Den Haag, Netherlands, 1983).

[111] Zerilli, F. and Armstrong, R. *Journal of Applied Physics* **61**, 1816–1825 (1987).

[112] Hawkyard, J. *International Journal of Mechanical Sciences* **11**(3), 313–333 (1969).

[113] Gust, W. *Journal of Applied Physics* **53**(5), 3566–3575 (1982).

[114] Maudlin, P., Bingert, J., House, J., and Chen, S. *International Journal of Plasticity* **15**, 139–166 (1999).

[115] Rule, W. *International Journal of Impact Engineering* **19**(9-10), 797–810 (1997).

[116] Buchar, J., Forejt, M., Jopek, M., and Krivanek, I. *Journal of Physics IV* **10**(Pr9), 5–80 (2000).

[117] Allen, D., Rule, W., and Jones, S. *Experimental Mechanics* **37**(3), 333–338.

[118] Johnson, G. and Holmquist, T. *Journal of Applied Physics* **64**(8), 3901–3910 (1988).

[119] Maudlin, P., Bingert, J., and Gray, G.T., I. *International Journal of Plasticity* **19**, 483–515 (2003).

[120] Plunkett, B., Cazacu, O., Lebensohn, R., and Barlat, F. *International Journal of Plasticity* **23**, 1001–1021 (2007).

[121] Eakins, D. and Thadhani, N. *J Appl Phys* **100**(7), 073503 (2006).

[122] Martin, M., Mishra, A., Meyers, M., and Thadhani, N. *Mater Sci Eng A* **464**, 202–209 (2007).

[123] Eakins, D. and Thadhani, N. *International Journal of Impact Engineering* (2006).

[124] Rohr, I., Nahme, H., and Thoma, K. *Int J Impact Eng* **31**(4), 401–433 (2005).

[125] Rohr, I., Nahme, H., and Thoma, K. *Journal de Physique IV* **10**, 513–518 (2003).

[126] Martin, M., Thadhani, N., Kecskes, L., and Dowding, R. *Scripta Materialia* **55**, 1019–1022 (2006).

[127] Barker, L. In *Proceedings of SPIE- The International Society for Optical Engineering*, 116–126, (1983).

[128] McQueen, G., Marsh, S., Taylor, J., Fritz, J., and Carter, W. *The Equation of State of Solids from Shock Wave Studies, High Velocity Impact Phenomena*, 230. Academic, New York (1970).

[129] Bridgman, P. *Proc Am Acad Arts Sci* **77**, 189 (2006).

[130] Eakins, D. *Roke of heterogeneity in the chemical and mechanical shock-reponse of nickel and aluminum powders*. PhD thesis, Georgia Institute of Technology, (2007).

[131] Bauer, F. In *Shock Waves in Condensed Matter,* Gupta, Y., editor, 483–496. Plenum, (1986).

[132] Graham, R., Anderson, M., Bauer, F., and setchell, R. In *Shock Waves in Condensed Matter,* Schmidt, S., Dick, R., Forbes, J., and Tasker, D., editors, 883–886, (1992).

[133] Sandia National Laboratories. *PlotData*, 2.3 edition, (2005).

[134] Ahrens, T., Gust, W., and Royce, E. *Journal of Applied Physics* **39**, 4610 (1968).

[135] Rice, M., McQueen, R., and Walsh, J. *Solid State Physics*, volume 6. Academic Press, Inc., New York, (1958).

[136] Eakins, D. and N.N.Thadhani. In *Shock Compression of Condensed Matter*, volume 845, 1153. American Institute of Physics, (2005).

[137] Xu, X. and Thadhani, N. *Journal of Applied Physics* **96**, 2000 (2004).

[138] Sekine, T., Tashiro, S., Kobayashi, T., and Matsumura, T. In *Shock Compression of Condensed Matter,* of Physics, A. I., editor, 1201–1204, (1995).

[139] Gumbsch, P. *Journal of Nuclear Materials* **323**, 304–312 (2003).

[140] Islam, S., Tufail, M., and Qu, X. *Materials Science Forum* **561-565**, 647–650 (2007).

[141] Martin, M., Kecskes, L., and Thadhani, N. *Journal of Materials Research* **in press** (2008).

[142] Steinberg, Cochran, and Guinan, M. *Journal of Applied Physics* **51**(3), 533–535 (1949).

[143] *AUTODYN Manual*.

[144] Novikov, S., Divnov, I., and Ivanov, A. *Phys. Metals Metal Science* **21**, 608–615 (1966).

[145] Martin, M., Hanagud, S., and Thadhani, N. *Mater Sci Eng A* **443**, 209–218 (2007).

[146] Eakins, D. and Thadhani, N. *Int J Impact Eng* **34**(11), 1821–1834 (2007).

[147] Gilmore, M., Foster, J.C., J., and Wilson, L. In *Shock Compression of Condensed Matter,* Furnish, M., Thadhani, N., and Horie, Y., editors, 519–522. American Institute of Physics, (2002).

[148] Rule, W. In *PVP Problems Involving Thermal-Hydraulics, Liquid Sloshing, and Extreme Loads on Structures*, volume 454, 117–122, (2003).

[149] Xi, X., Zhao, D., Wang, W., Wu, Y., and Lewandowski, J. *Phys Rev Lett* **94**(12), 125510 (2005).

[150] Cochran, S. and Banner, D. *J Appl Phys* **48**(7), 2729–2737 (1977).

[151] Martin, M., Sekine, T., Kobayashi, T., Kecskes, L., and Thadhani, N. *Met Trans* **38A**, 2689–2696 (2007).

[152] Jackson, I. and Ahrens, T. *Journal of Geophysical Research* **84**(B6), 3039–3048 (1979).

[153] Taylor, J. *An Introduction to Error Analysis: The Study of Uncertainties in Physical Measurements*. A Series of Books in Physics. University Science Books, Mill Valley, CA, (1982).

[154] Graham, R., Anderson, M., Horie, Y., You, S.-K., and Holman, G. *Shock Waves* **3**(2), 79–82 (1993).

[155] Birch, F. *Physical Review* **71**(11), 809–824 (1947).

[156] Raju, S., Mohandas, E., and Raghunathan, V. *Journal of Physics and Chemical Solids* **58**(9), 1367–1373 (1997).

[157] Barker, L. and Hollenbahc, R. *J Appl Phys* **43**, 4669–4675 (1972).

[158] Nahme, H. and Hiltl, M. In *Metallurgical and materials applications of shock-wave and high-strain-rate phenomena,* Murr, L., Staudhammer, K., and Meyers, M., editors. Elsevier, (1995).

[159] Romanchenko, V. and Stepanov, G. *J Appl Mech Tech Phys* **21**, 555–561 (1990).

[160] Jones, O. E. *Metallurgical effects at high strain rates*, 33–55. Plenum Press (1973).

[161] Duvall, G. and Fowles, G. *High Pressure Physics ahd Chemistry*, volume 2, chapter Chapter 9- Shock Waves, 268. Academic Press (1963).

[162] Asay, J., Chhabildas, L., and Dandecar, D. *Journal of Applied Physics* **51**(9), 4774–47833 (1980).

[163] Lennon, A. and Ramesh, K. *Materials Science and Engineering A* **276**, 9–21 (2000).

[164] High strain rate behavior of refractory metals and alloys, 179–191. The Minerals, Metals & Materials Society, TMS, (1992).

[165] Granato, A. *Metallurgucal effects at high strain rates*, chapter Microscopic mechanisms of dislocaion drag. Plenum Press, New York (1973).

[166] Follansbee, P. *Metallurgucal applications of shock wave and high strain rate phenomena*, chapter High-strian-rate deformation of FCC metals and alloys. Marcel Dekker, New York (1986).

[167] Kauzmann, W. *Trans Am Inst Min Metall Eng* **143**, 57 (1941).

[168] Zerilli, F. *Metallurgical and Materials Transactions* **35A**(9), 2547–2555 (2004).

[169] Gilman, J. *Journal of Applied Physics* **44**, 675 (1973).